A Study of Non-linear Acoustic Flows at the Open End of a Tube using Particle Image Velocimetry



David John Skulina

A thesis submitted in fulfilment of the requirements
for the degree of Doctor of Philosophy
to the
University of Edinburgh
2005

Abstract

The radiation of sound from the open end of a resonant tube is relatively well understood at low acoustic amplitudes in terms of linear acoustics. At high acoustic amplitudes, hovever, additional non-linear loss mechanisms such as vortex shedding and jet streaming are known to affect the sound field at the open end and the efficiency with which a standing wave is maintained within a tube. This has implications in a number of fields, notably in musical instrument design and in the automotive industry. Particle Image Velocimetry (PIV) is used to acquire full-field instantaneous velocity information of the acoustic particle velocity field at the open end of a cylindrical tube in which a high amplitude sound field has been generated by a loudspeaker. Five different tube terminations are used to examine the effect of varying the geometry of the open end on the flow phenomena observed. A qualitative identification of number of flow regimes is made and two different techniques are used to evaluate the non-linear losses numerically. PIV results are used in combination with pressure measurements to evaluate the termination impedance and a comparison is drawn with results made by conventional methods. Vortex sound theory is then used to measure the acoustical losses caused by boundary layer separation and the resultant generation of vortex structures.

Declaration

I do hereby declare that this thesis was composed by myself and that the work described within is my own, except where explicitly stated otherwise.

David J. Skulina
September 2005

Acknowledgements

I would like to thank my supervisors Murray Campbell and Clive Greated for thier continued support and encouragement throughout the course of this study. The assistance of Joel Gilbert and Meroanne Atig has been invaluable. Thanks also go to Dawn Rockliff for getting me started in the early days of my PhD and to Ted Schlicke for helping with all my computer programming problems. Thanks to Allan Marson for the distracting games of pool and some interesting games of extreme catch. Thanks to all the other members of the Acoustics and Fluid Dynamics Research Group at the University of Edinburgh. Thanks to Orlando Richards, Steve Tonge and Darren Hendrie for their work (with varying degrees of enthusiasm) in keeping my computer alive. Thanks to everybody in the workshop, especially Frank Morris and Vince Devine, for the valuable technical help and advice.

The Financial support of ESPRC is gratefully acknowledged.

Special thanks and big slobbery smooches go to my fiancèe Seona Bromage for everything including her calming influence, general encouragement and for making me laugh. Finally, I would like to thank my mum and dad for everything they have ever done and for making me a nice family.

Contents

Abstract i

Declaration iii

Acknowledgements v

Contents vii

List of figures xi

List of tables xv

1 Introduction 1
- 1.1 Context . . . 1
- 1.2 Aims . . . 1
- 1.3 Content . . . 2

2 Background Acoustics 5
- 2.1 Introduction . . . 5
  - 2.1.1 Acoustic Intensity . . . 5
  - 2.1.2 Impedance . . . 6
  - 2.1.3 Acoustic velocity and pressure . . . 8
- 2.2 Resonance in an open ended cylindrical tube . . . 8
- 2.3 Useful dimensionless parameters . . . 9
- 2.4 Potential Flow . . . 11
- 2.5 Non-linearity . . . 12
  - 2.5.1 Boundary layers . . . 12
  - 2.5.2 Flow Separation . . . 13
  - 2.5.3 Vorticity . . . 14
- 2.6 Vortex Sound Theory . . . 14
  - 2.6.1 The Powell-Howe analogy . . . 15
  - 2.6.2 Howe's energy corollary . . . 18

3 Particle Image Velocimetry 21
- 3.1 Introduction . . . 21
- 3.2 PIV Principle . . . 22
- 3.3 Image acquisition . . . 23

3.3.1 Flow illumination 24
3.3.2 Seeding Particles 25
3.3.3 Image capture 27
3.4 Image analysis 28
3.4.1 Cross-correlation 28
3.4.2 Peak detection 29
3.4.3 Sources of error 30
3.4.4 Post processing - vector validation 30
3.5 Summary 30

4 PIV Apparatus and Experimental Procedures 33
4.1 Introduction 33
4.2 PIV System Apparatus 33
4.2.1 Copper Vapour Laser 33
4.2.2 Digital Camera - PCO Sensicam 35
4.2.3 PIV Enclosure Design 35
4.2.4 PIV Timing and Synchronisation 37
4.3 Experimental method 40
4.3.1 Loudspeaker 40
4.3.2 Copper tube and terminations 41
4.3.3 Monitoring the acoustic field within the tube 43
4.3.4 Optical alignment 44
4.3.5 Seeding particles 45
4.3.6 PIV measurement procedure 46
4.4 Microphone Calibration 47
4.4.1 Experimental Method 47

5 PIV Measurements of the Acoustic Behaviour of Open Ended Pipes 51
5.1 Introduction 51
5.2 Background 52
5.2.1 Non-linear acoustic flows 52
5.2.2 Recent use of PIV in the field of musical acoustics 53
5.3 PIV Results 54
5.3.1 Low amplitude measurements 54
5.3.2 Sharp (Unflanged) termination 60
5.3.3 R=0mm termination 93
5.3.4 R=0.3mm and R = 1mm terminations 117
5.3.5 R=4mm termination 122
5.4 Conclusions 122

6 Termination impedance measurements of open ended pipes with PIV 125
6.1 Introduction 125
6.2 Background 126
6.2.1 Linear radiation impedance 126
6.2.2 Non-linear radiation impedance 127
6.2.3 Recent work with tube terminations 127

6.3 Termination impedance measurement technique 129
6.3.1 Pressure measurements 131
6.3.2 Volume velocity measurements 136
6.3.3 Termination impedance error analysis 149
6.4 Termination impedance results 150
6.5 Comparison with two microphone method results 152
6.6 Comparison with PIV streaming vector maps 158
6.7 Conclusions 162

7 Evaluation of Acoustical Losses using Vortex Sound Theory 163
7.1 Introduction 163
7.2 Vortex sound analysis of PIV maps 165
7.2.1 Analysis method 165
7.2.2 Potential velocity field - PIV 167
7.2.3 Potential velocity model - Pistonic flow 168
7.3 Results and discussion 170
7.3.1 Velocity amplitude dependence 172
7.3.2 Time dependence 175
7.3.3 Interpretation of vortex sound theory 183
7.4 Conclusions 184

8 Conclusions 185
8.1 Non-linear effects in acoustically generated flows at the open ends of tubes 185
8.2 Termination impedance measurements at high acoustic amplitudes . . . 186
8.3 Losses associated with acoustically generated vortex structures 186
8.4 Future work 187

A Limitations of PIV in acoustic particle displacement measurement 189
A.1 Maximum Displacement: Nyquists Theorem 189
A.2 Acoustic Particle Displacement and Frame Capture Rate 190
A.3 PIV Measurement of Resonant Tubes 192
A.4 Errors 194

Bibliography 196

Publications 201

List of Figures

3.1 Basic experimental setup for particle image velocimetry 23

4.1 'Fibresheet' light sheet delivery unit. 34
4.2 PIV enclosure 36
4.3 PIV Synchronisation setup 38
4.4 PIV timing diagram 39
4.5 PIV apparatus 40
4.6 JBL 2446H loudspeaker and cylindrical tube adaptor 41
4.7 Frequency response of tube/termination/loudspeaker system. 42
4.8 Tube terminations 42
4.9 PCB pressure transducer adaptor 44
4.10 Experimental setup for probe microphone calibration 47
4.11 Phase difference between probe and reference microphones 49

5.1 Schematic diagram showing the four acoustically generated flow regions observed by Ingard and Labate 52
5.2 PIV measurement of potential flow at low sound levels: R=1mm termination at 136.6dB. 55
5.3 PIV velocity vector map at peak outflow for the R=1mm termination at 136.6dB with radial and axial velocity profiles. 56
5.4 Potential flow above an idealised piston located in the plane of the open end. 57
5.5 Idealised Potential flow velocity vector map at peak outflow above a piston located at the open end with radial and axial velocity profiles. . . 58
5.6 Normalised axial velocity magnitude as a function of axial distance for both the PIV measurement of the R = 1mm termination at 136.6dB and the pistonic model of potential flow. 59
5.7 PIV results for the the sharp (unflanged) termination at an SPL of 148dB. 61
5.8 PIV results for the the sharp (unflanged) termination at an SPL of 157.2dB. 72
5.9 Normalised velocity and pressure signals measured at the open end open end of the tube for the sharp edged termination at 168dB 82
5.10 PIV results for the the sharp (unflanged) termination at an SPL of 168dB. 83
5.11 PIV velocity magnitude contour maps for the R=0mm termination at 146.9dB with streamlines. 93
5.12 PIV results for the the R=0mm termination at an SPL of 158.2dB. . . . 95

5.13 Normalised velocity and pressure signals measured at the open end open end of the tube for the sharp edged termination at 158.2dB. 105
5.14 PIV results for the the R=0mm termination at an SPL of 162.3dB. . . . 106
5.15 Normalised velocity and pressure signals measured at the open end open end of the tube for the sharp edged termination at 162.3dB. 116
5.16 PIV results for the the R=0.3mm termination at an SPL of 157.1dB. . . 118
5.17 PIV velocity magnitude contours with streamlines for the the R=4mm termination at an SPL of 168dB. 122

6.1 Two microphone technique experimental setup used by Atig [Atig 04] . 128
6.2 Two types of pipe termination geometry studied both in this study and by Atig 128
6.3 Real part of the termination impedance as a function of the amplitude of the acoustic velocity at the open end for the five different terminations. From Atig [Atig 04]. 129
6.4 Left: microphone positioning setup. Right: photograph showing silhouette of probe microphone positioned above the tube termination. . 131
6.5 Least Squares fit of PCB signal at 136.7dB for the R = 0mm termination. 132
6.6 Normalised PCB transducer and Probe microphone signals at 168dB for the R = 0mm termination 133
6.7 (a) Original PCB transducer signal at 168dB for the R = 0mm termination. (b) Corrected signal and non-linear least squares fit of corrected PCB signal 134
6.8 Pressure amplitude as a percentage of the maximum amplitude as a function of distance from the open for a standing wave in a 46cm tube open at both ends with zero impedance at the open ends. 135
6.9 Volume velocity calculations for axially symmetric flows 137
6.10 Volume velocity data and least-square fit results for sharp ended termination. 140
6.11 Volume velocity data and least-square fit results for R = 0mm termination. 142
6.12 Volume velocity data and least-square fit results for R = 0.3mm termination. 144
6.13 Volume velocity data and least-square fit results for R = 1mm termination. 145
6.14 Volume velocity data and least-square fit results for R = 4mm termination. 147
6.15 Reduced chi-square values for non-linear least squares volume velocity fit as a function of the acoustic velocity amplitude $|u_{ac}|$. 148
6.16 Real part of the normalised termination impedance for five termination geometries as a function of the acoustic velocity amplitude $|u_{ac}|$. 151
6.17 Comparison of the real part of the termination impedance as a function of acoustic velocity amplitude $|u_{ac}|$ calculated using two methods for the sharp termination. 153
6.18 Comparison of the real part of the termination impedance as a function of acoustic velocity amplitude $|u_{ac}|$ calculated using two methods for the R=0mm termination. 154

6.19 Comparison of the real part of the termination impedance as a function of acoustic velocity amplitude $|u_{ac}|$ calculated using two methods for the R=0.3mm termination. 154
6.20 Comparison of the real part of the termination impedance as a function of acoustic velocity amplitude $|u_{ac}|$ calculated using two methods for the R=1mm termination. 155
6.21 Comparison of the real part of the termination impedance as a function of acoustic velocity amplitude $|u_{ac}|$ calculated using two methods for the R=4mm termination. 155
6.22 Comparison of the acoustic particle velocity measured with PIV with the acoustic velocity amplitude $|u_{ac}|$ measured with the PCB transducer using the linear approximation. 156
6.23 Phase Measurements: (a) Phase difference between the pressure and volume velocity signals. (b) Phase angle of the pressure signal relative to reference signal. (c) Phase angle of the volume velocity signal relative to reference signal. 157
6.24 Flow regime 1. Averaged velocity magnitude contour maps with streamlines: (a) R = 0mm termination at $|u_{ac}| = 2.75ms^{-1}$. (b) R = 0.3mm termination at $|u_{ac}| = 4.89ms^{-1}$. (c) R = 1mm termination at $|u_{ac}| = 2.76ms^{-1}$. 158
6.25 Flow regime 2. Averaged velocity magnitude contour maps with streamlines: (a) R = 0mm termination at $|u_{ac}| = 6.97ms^{-1}$. (b) R = 0.3mm termination at $|u_{ac}| = 11.47ms^{-1}$. (c) R = 1mm termination at $|u_{ac}| = 14.64ms^{-1}$. 159
6.26 Flow regime 3. Averaged velocity magnitude contour maps with streamlines: (a) R = 0mm termination at $|u_{ac}| = 7.87ms^{-1}$. (b) R = 0.3mm termination at $|u_{ac}| = 14.80ms^{-1}$. (c) R = 1mm termination at $|u_{ac}| = 19.33ms^{-1}$. 160
6.27 Effect of edge roundness on flow separation 161

7.1 Schematic showing the orientation of reference planes used in the pistonic modelling procedure. 169
7.2 Vortex sound measurement areas. 171
7.3 Acoustic resistance as a function of the acoustic velocity amplitude $|u_{ac}|$ - Area 1. The results of the vortex sound calculation using two determinations of the potential field. 172
7.4 Acoustic resistance as a function of the acoustic velocity amplitude $|u_{ac}|$ - Area 2. The results of the vortex sound calculation using two determinations of the potential field. 173
7.5 Acoustic resistance as a function of the acoustic velocity amplitude $|u_{ac}|$ - Area 3. The results of the vortex sound calculation using two determinations of the potential field. 175
7.6 Acoustic resistance as a function of time - Area 1. The results of the vortex sound calculation using two determinations of the potential field for the R = 0mm termination. 176

7.7 Acoustic resistance as a function of time - Area 2. The results of the vortex sound calculation using two determinations of the potential field for the R = 0mm termination. 177
7.8 Acoustic resistance as a function of time - Area 3. The results of the vortex sound calculation using two determinations of the potential field for the R = 0mm termination. 178
7.9 Vortex sound power contours for the the R=0mm termination at an SPL of 162.3dB. 179
7.10 Schematic representation showing a vortex in a potential flow u. 183

A.1 Image array showing interrogation areas and pixels 190
A.2 Particle Displacement 191
A.3 Image separation time and sound pressure level 194
A.4 Particle displacement and its first and second order approximations . . . 195
A.5 First order error in particle displacement due to small angle approximation 195

List of Tables

4.1 Pulse generator settings for PIV measurements of the acoustic particle velocity field 39

A.1 Field of view sizes for several resolutions and frame rates of the Phantom v5.0 high speed camera. 192

A.2 Time intervals between frames and image capture rates at various image resolutions for different sized fields of view and maximum velocity . . . 193

Chapter 1

Introduction

1.1 Context

The acoustic velocity field at the open ends and side holes of woodwind musical instruments is well understood at low sound levels in terms of linear acoustics. As long as the sound level is low enough non-linear effects remain negligible and the velocity field can be modelled as a potential flow. At the sound levels observed under playing conditions in woodwind instruments, however, this is not the case and non-linear flow phenomena are well known to affect the acoustical behaviour. This can significantly alter the timbre and playability of an instrument. The shape of the open end or side hole plays an important role in determining the strength and importance of the non-linearities.

Particle Image Velocimetry (PIV) is a non-intrusive optical technique for the measurement of whole-field instantaneous velocity data. The technique does not disturb the flow and offers the benefit of allowing both qualitative and quantitative descriptions of a flow field to be made. A fluid is seeded with tiny particles which faithfully follow the motion of the flow and is illuminated in a plane by a pulsed light source. The scattered light is recorded by a camera and the resultant images are analysed to produce a mesh of vectors that describe the local flow direction and speed.

Advances in digital camera technology and increased computer processor speeds mean that PIV is becoming a more commonly used tool in both research and industry. It has previously been shown to be suitable for the measurement of acoustic velocity fields in a number of recent studies [Rockliff 02a, Sharpe 89, Bamberger 01, Hann 95].

1.2 Aims

The work in this thesis is primarily concerned with the measurement of acoustic particle velocity fields at the open ends of tubes, in which high amplitude sound fields are generated by a loudspeaker, using the PIV technique. The main objectives are:

1. to investigate the presence of non-linear effects in high amplitude acoustically

generated flows at the open ends of tubes and to examine the effect of varying the termination geometry.

2. to obtain termination impedance measurements at high acoustic amplitudes using velocity information provided by the PIV technique, in conjunction with pressure measurements, and to compare these with results obtained in a separate study using a two-microphone method.

3. to evaluate the losses associated with acoustically generated vortex structures using vortex sound theory.

1.3 Content

The background to the work in this thesis is given in chapters 2, 3 and 4. This includes a discussion of some basic acoustical and fluid dynamical concepts, an overview of the PIV technique and details of the experimental apparatus and procedures used in the following chapters. Chapters 5, 6 and 7 then focus on the experimental methods and results.

Chapter 2 contains an introduction to some basic equations and theories used in the description of acoustic fields in pipes. The main parameters to be obtained experimentally in subsequent chapters are presented.

Chapter 3 describes the PIV technique, including an outline of its basic principle, and discusses some of the major experimental parameters to be optimised. Details of the experimental methods and analysis procedures relevant to this study are given.

A description of the apparatus and methods used for the PIV measurements made in this study is given in chapter 4. This includes a discussion of the design of a PIV enclosure, synchronisation with the acoustic field and a section on microphone calibration.

In chapter 5 the results of PIV measurements of the acoustic particle velocity field at the open end of a tube in which an acoustic field has been established at a range of sound levels are presented. The chapter begins with a review of existing experimental studies using flow visualisation and PIV. The effect of changing the geometry of the termination is examined. A detailed discussion of the observed acoustically generated non-linear flow phenomena is then given. PIV velocity vector maps are presented along with velocity magnitude and vorticity contour maps.

Chapter 6 starts with a discussion of the linear theory of radiation impedance and goes on to review the non-linear case. A recent experimental study of the termination impedance of tubes with different termination geometries at high acoustic amplitudes using a two-microphone technique is outlined and the results presented. A method for

measuring the termination impedance using the volume velocity measured from the PIV velocity data obtained in chapter 5 in association with pressure measurements is discussed. The error evaluation process is reviewed. The termination impedance results are presented and compared with the results obtained elsewhere using the two-microphone technique. A comparison with the PIV results obtained in chapter 5 is made by examination of time-averaged PIV velocity data.

Chapter 7 outlines a method of evaluating the acoustical losses, in terms of a termination resistance, associated with vortex generation and vortex shedding by the application of vortex sound theory to the PIV data obtained in chapter 5. A pistonic potential flow model is developed for comparison with PIV measurements and its validity is discussed. The variation of the observed losses with acoustic velocity amplitude and with time are examined. The spatial distribution of vortex sound power is discussed.

In chapter 8 a summary of the main conclusions of this work are presented. Suggested extensions to this work are then given.

Chapter 2

Background Acoustics

2.1 Introduction

In this chapter some of the basic equations and theories used to describe acoustic fields, both generally and in specific relation to the acoustic fields associated with musical flue instruments are given. Definitions of the acoustical parameters measured experimentally in later chapters are introduced. This is followed by a review of some important fluid dynamical concepts relevant to the description of acoustic fields in pipes. The background and principles of vortex sound theory are explained and a derivation of the Powell-Howe analogy is given.

2.1.1 Acoustic Intensity

The acoustic intensity, I, of a sound field is defined as the rate of energy transmission per unit area through a plane normal to the direction of propagation, time-averaged over the period of an acoustic cycle, T:

$$I =< pu >_T = \frac{1}{T}\int_0^T pu dt \tag{2.1}$$

where p and u are the acoustic pressure and velocity, respectively.

For a plane harmonic wave travelling through air in the positive x direction, the acoustic pressure and velocity are related by $p = \rho_0 cu$, where $\rho_0 = 1.21$ kgm^3 is the density of air and $c = 343\text{ms}^{-1}$ is the speed of sound in air at standard temperature and pressure (STP). For a harmonic wave the RMS pressure and velocity (commonly known as the *effective* pressure p_e and velocity u_e) are given by:

$$p_e = \frac{|p|}{\sqrt{2}} \tag{2.2}$$

$$u_e = \frac{|u|}{\sqrt{2}} \tag{2.3}$$

where $|p|$ and $|u|$ are the acoustic pressure and velocity amplitudes.

The acoustic intensity, measured in watts per square metre (Wm^{-2}), is then:

$$I = \frac{p_e^2}{\rho_0 c} \tag{2.4}$$

Due to the wide dynamic range encountered in acoustic signals it is convenient to express intensity measurements logarithmically in terms of an intensity level, IL, measured in decibels (dB), in relation to a standard reference signal, I_0:

$$IL = 10 \log_{10} \left(\frac{I}{I_0} \right) \tag{2.5}$$

Conventionally, the standard reference intensity I_0 for air is chosen as $10^{-12}\mathrm{Wm}^{-2}$. This value corresponds to an intensity slightly below the threshold of human hearing at a frequency of 1000Hz. Using equations 2.4 and 2.5 we can thus define the sound pressure level, SPL, as:

$$SPL = 10 \log_{10} \left(\frac{p_e^2}{p_0^2} \right) = 20 \log_{10} \left(\frac{p_e}{p_0} \right) \tag{2.6}$$

where $p_0 = 2 \times 10^{-5}\mathrm{Pa}$ is the effective pressure measured at the standard reference intensity, I_0.

2.1.2 Impedance

Specific Acoustic Impedance

It is often useful to describe the characteristics of the medium through which an acoustic wave propagates in terms of its specific acoustic impedance, z, as a function of angular frequency, ω. The specific acoustic impedance is defined as the ratio of the acoustic pressure to the associated acoustic particle velocity at a point in space:

$$z(\omega) = \frac{p(\omega)}{u(\omega)} \tag{2.7}$$

This is in general a complex quantity. For a plane wave the pressure and velocity are in phase and the specific acoustic impedance is real and independent of angular frequency:

$$z = \pm \rho_0 c \tag{2.8}$$

where the choice of sign depends on whether the plane wave is propagating in the positive or negative x-direction, and $\rho_0 c$ is called the characteristic impedance of the

medium. For air at STP, ρ_0 =1.21kgm^{-3} and c =343ms^{-1}, giving:

$$\rho_0 c = 415\text{kgm}^{-3} \quad \text{(air at STP)} \tag{2.9}$$

Acoustic Impedance

When discussing the transmission of sound waves between vibrating surfaces of dissimilar media or between volumes of different size it is useful to define the acoustic impedance Z. This is especially helpful when considering acoustic transmission through pipes and through systems of lumped acoustic elements. The acoustic impedance is defined as the ratio of the acoustic pressure at a surface of cross sectional area S and the volume velocity U through the surface, where $U = uS$. It is related to the specific acoustic impedance at a surface as such:

$$Z(\omega) = \frac{z(\omega)}{S} = \frac{p(\omega)}{U(\omega)} \tag{2.10}$$

The acoustic impedance can also be expressed as

$$Z(\omega) = |Z(\omega)| \exp^{i\phi(\omega)} \tag{2.11}$$

where $|Z(\omega)|$ is the magnitude of acoustic impedance and $\phi(\omega)$ is the phase difference between the pressure and acoustic velocity. It should be noted that the acoustic impedance is only strictly valid in linear acoustical systems.

Radiation Impedance

The acoustic impedance in the plane of the open end of a tube is called the radiation impedance. In the linear approximation (for low frequencies such that $ka \ll 1$) the radiation impedance for an unflanged tube is given [Levine 48] as:

$$Z_r = \left\{ \frac{(ka)^2}{4} + jk\delta_0 \right\} Z_c \quad \text{(Unflanged)} \tag{2.12}$$

where $\delta_0 = 0.6133a$ is the unflanged tube end correction, with a the tube radius, $k = \frac{2\pi}{\lambda}$ is the wavenumber and $Z_c = \frac{\rho_0 c}{S}$ is the characteristic impedance of air. For an infinite flange at the open end the radiation impedance is [Nomura 60]:

$$Z_r = \left\{ \frac{(ka)^2}{2} + jk\delta_\infty \right\} Z_c \quad \text{(Infinite Flange)} \tag{2.13}$$

where the flanged tube end correction is $\delta_\infty = 0.8216a$. The radiation impedance for the open ends of most musical instruments will realistically fall somewhere between the unflanged and flanged values [Nederveen 98] since tube walls have a finite thickness and cannot be considered truly unflanged or infinitely flanged.

2.1.3 Acoustic velocity and pressure

Using equations 2.3,2.6, 2.7 and 2.8 it is possible to calculate the sound pressure level for a plane wave travelling in air with a given acoustic particle velocity amplitude:

$$SPL = 20\log_{10}\left(\frac{\rho_0 c|u|}{\sqrt{2}p_0}\right) \tag{2.14}$$

and vice-versa:

$$|u| = \frac{\sqrt{2}p_0}{\rho_0 c}10^{\frac{SPL}{20}} = 0.0682 \times 10^{(0.05SPL-6)} \tag{2.15}$$

2.2 Resonance in an open ended cylindrical tube

Consider a sinusoidal disturbance at a point within an air filled cylindrical tube of internal radius a and length L. The wavelength of the sinusoidal disturbance is such that $ka = \frac{2\pi a}{\lambda} \ll 1$. The disturbance initiates a travelling wave which propagates in both positive and negative x-directions. When the wave reaches the open ends at $x = 0$ and $x = L$ it experiences an abrupt change in acoustic impedance resulting in part of the wave being reflected back down the tube in the opposite direction and part of it being transmitted as sound. The positive and negative going reflected waves interfere within the tube and result in the formation of a standing wave.

The pressure at each open end is approximately equal to atmospheric pressure. In the ideal case the acoustic impedances Z_0 and Z_L at the open ends will be zero and so there will be pressure nodes at $x = 0$ and $x = L$ and all of the sound wave will be reflected back into the tube, with none of it being externally radiated. These positions will also correspond to the locations of displacement anti-nodes as the air here is free to move into and out of the tube. It is clear that only certain wavelengths of sound will be permitted within these boundary conditions and standing waves will only be established for these wavelengths. These wavelengths correspond to the natural modes, or resonant frequencies, of the tube. These natural modes must have an integer n number of half-wavelengths of the sound equal to the length of the tube:

$$L = \frac{n\lambda_n}{2} \quad \text{n=1,2,3,...} \tag{2.16}$$

where λ_n is the wavelength of the nth natural mode. Using the relation $\nu = \frac{c}{\lambda}$, the nth natural frequency ν_n is given by;

$$\nu_n = \frac{c}{\lambda_n} = \frac{nc}{2L} \quad \text{n=1,2,3,...} \tag{2.17}$$

In reality the acoustic impedance of each of the open ends will have a finite value since some if the incident wave is radiated as sound from the open ends into the surrounding air. The acoustic impedance at the open ends is equal to the radiation impedance Z_r as described in section 2.1.2. The outcome of this is that the effective length L_e of the tube is increased by a small end correction:

$$L_e = \begin{cases} L + \delta_0 a = L + 0.6133a & \text{(Unflanged)} \\ L + \delta_\infty a = L + 0.8216a & \text{(Infinite Flange)} \end{cases} \tag{2.18}$$

A simple alteration to the calculated natural modes of the tube is then necessary with L replaced by the effective length L_e in equation 2.17.

2.3 Useful dimensionless parameters

In the field of fluid dynamics it is often important to be able to compare measurements of flows with different length or velocity scales. A number of non-dimensional parameters have been developed for this purpose. A few of the parameters relevant to this study are detailed in this section.

Strouhal number

The Strouhal number is commonly used in the study of unsteady or oscillatory fluid flow dynamics. It is the ratio of unsteady inertial forces to convection and gives a measure of the non-linearity of a flow. It is defined as:

$$St = \frac{fL}{U} \quad \text{(Strouhal Number)} \tag{2.19}$$

where f is the oscillation frequency, L is a characteristic length scale of the flow (for the purposes of this study $L = 2a$, where a is the tube radius) and U is a characteristic velocity of the flow (for the purposes of this study $U = u_{ac}$ where u_{ac} is the acoustic velocity amplitude and the Strouhal number $Sr = Sr_{ac}$ is the acoustic Strouhal number). A small Strouhal number ($St < 1$) indicates the presence of significant non-linearity. A flow can be characterised as linear if the Strouhal number is large ($St > 1$). For high Strouhal numbers (low acoustic velocities) the acoustic flow in a resonant tube can be considered as a potential flow (see section 2.4) during inflow and

outflow [Rockliff 02a].

Reynolds number

The Reynolds number is used to determine whether a fluid flow is laminar or turbulent and to determine the dynamical similarity between flows with different speeds and/or geometries. It is defined as the ratio of inertial forces (those which force the fluid through a pipe, for example fluid momentum, gravity, pressure gradients) to viscous forces (frictional forces which increase the drag on the fluid):

$$Re = \frac{\rho UL}{\mu} \quad \text{(Reynolds Number)} \tag{2.20}$$

where U and L are as defined above, and μ is the dynamic viscosity of the fluid. For air at STP the density $\rho = \rho_{air} = 1.21\text{kgm}^{-3}$ and $\mu = \mu_{air} = 1.81 \times 10^{-5}\text{Pa·s}$. It is generally accepted that for flow within a pipe, a laminar flow regime can be expected for $Re < 2000$. In this case viscous forces dominate the flow. Above a critical Reynolds number Re_{crit} there is a transition to a turbulent flow regime. The exact value of Re_{crit} depends on the flow configuration and has to be determined experimentally but is usually taken as being somewhere between 2000 and 4000. Close to the critical Reynolds number is an unstable transition period where the flow can contain both laminar and turbulent regimes or chaotic fluctuations between the two. A turbulent flow regime can be expected for $Re > 4000$ with inertial forces dominating the flow.

Mach number

The Mach number gives a measure of the ratio of inertial to elastic (compressibility) forces within a flow. It is defined as:

$$M = \frac{U}{c_0} \quad \text{(Mach Number)} \tag{2.21}$$

where U is as previously defined and c_0 is the speed of sound in the fluid. For $M \ll 1$ the compressibility of the fluid can be ignored. This is the case for the work in this study.

Helmholtz number

The Helmholtz number is defined as:

$$He = \frac{L}{\lambda} \quad \text{(Helmholtz Number)} \tag{2.22}$$

where L is a characteristic length scale of the flow (for the purposes of this study it is the diameter of the pipe) and λ is the acoustic wavelength. For $He \ll 1$ the wavelength is much larger than the source dimensions and the flow region is described as compact. A plane wave description of acoustic propagation in a straight pipe can then be used. This assumption can be made for all of the work in this study.

2.4 Potential Flow

Under normal playing conditions, the Reynolds number of the bulk flow in most musical instruments is high ($Re \gg 1$) and the flow can be considered to be largely free from viscous (frictional) forces. Although these frictional forces play an extremely important role in real flows, they are generally concentrated in thin regions close to walls of the instrument called boundary layers or in localised turbulent shear layers and jets. It can often, therefore, be useful to approximate the bulk flow within a musical instrument by ignoring any boundary layer effects and to consider only flows in the frictionless limit (inviscid flows).

In general a velocity field $\vec{v}$ can be considered to consist of an irrotational and a solenoidal (rotational) part:

$$\vec{v} = \nabla\phi + \nabla \times \vec{\psi} \tag{2.23}$$

where ϕ is the scalar potential, $\vec{\psi}$ is the stream function vector and $\nabla = \frac{\delta}{\delta x}\vec{i} + \frac{\delta}{\delta y}\vec{j} + \frac{\delta}{\delta z}\vec{k}$ is the grad operator and $\vec{i}$, $\vec{j}$ and $\vec{k}$ are unit vectors in the x, y and z directions, respectively. Additionally, a velocity field can be thought of as consisting of a time-invariant mean flow $\vec{v}_0$ superposed with a fluctuating, time-dependent, part $\vec{v}'$:

$$\vec{v} = \vec{v}_0 + \vec{v}' \tag{2.24}$$

The flow of an inviscid fluid that is both irrotational and divergence-free (incompressible) is described as a potential flow. A potential flow field is then just the irrotational part of the velocity field:

$$\vec{v} = \nabla\phi \tag{2.25}$$

which must therefore satisfy the following equations:

$$\vec{\omega} = \nabla \times \vec{v} = 0 \quad \text{(Irrotational)} \tag{2.26}$$

$$\nabla \cdot \vec{v} = 0 \quad \text{(Incompressible)} \tag{2.27}$$

where $\vec{\omega}$ is the vorticity field.

As previously stated, potential flows are non-physical in that they do not include all of the characteristics of real fluid flows. Turbulent flows and flows in which boundary layers are present cannot be accounted for. The concept of a potential flow can however be used in the solution of many practical fluid dynamical and acoustical problems.

2.5 Non-linearity

At high acoustic amplitudes non-linear flow effects can significantly influence the flow at the open end of a tube and a linear approach can no longer be used. If the acoustic velocity amplitude is high enough, flow separation will occur at the tube exit and result in vortex shedding and subsequent jet formation. Vortex shedding occurs when vorticity within the boundary layer becomes saturated and is consequently transferred to the bulk flow. This transfer of rotational energy to the main flow results in the gradual dissipation of energy by frictional interactions. The work in this thesis is concerned with the investigation of velocity field at the open end of a tube at sound levels high enough to generate such non-linear effects. A description of what is meant by the terms boundary layer and flow separation is given in this section. A full discussion can be found in a number of standard fluid dynamics texts [Bachelor 02, Tritton 99].

2.5.1 Boundary layers

The assumption of irrotationality over the entire flow field can lead to quite unrealistic results [Hirschberg 95]. The potential flow approximation assumes an inviscid flow and neglects the effect of the boundary layer allowing a tangential slip velocity at solid walls. In reality the fluids' viscosity causes it to 'stick' to the walls (This is known as the no slip boundary condition, $v_{wall} = 0$). At high Reynolds numbers there is a thin transition layer close to the wall in which viscous forces are important where the velocity changes rapidly from the velocity in the bulk of the flow to a velocity equal to zero at the wall [Tritton 99]. This transition region is called the boundary layer. The flow is solenoidal (i.e. the fluid has rotational motion: $\vec{\omega} \neq 0$) in this region [Hirschberg 95] and energy dissipation occurs due to the presence of significant frictional forces.

The thickness of the viscous boundary layer in the presence of an acoustic field (sometimes called the acoustic boundary layer) δ_{ac} within a duct is given by [Rockliff 02a, Peters 93a, Thompson 05]:

$$\delta_{ac} = \sqrt{\frac{\mu}{\omega\rho}} \tag{2.28}$$

where μ is the coefficient of dynamic viscosity of the fluid, ρ is the fluid density and $\omega = 2\pi f$ is the radian frequency of an acoustic oscillation with frequency f. The

significance of the boundary layer effects within a duct depends on the ratio δ_v/r of the boundary layer thickness to the tube radius. From equation 2.28 it can be seen that the boundary layer thickness is frequency dependent and is greatest at low frequencies. For this study a pipe of radius 8mm is used and a typical oscillation frequency is 380Hz, so at STP the acoustic boundary layer thickness is 0.08mm. The spatial extent of the boundary layer is then only 1% of the pipe radius and so attenuation of the sound field due to viscous effects within the acoustic boundary layer can be considered negligible for the purposes of this study.

There are two main boundary layer regimes: laminar and turbulent [Bachelor 02]. In both regimes fluid at the wall remains stationary while fluid near the wall moves in the direction of the main flow. In the laminar case the fluid particles at the smooth outer-most surface of the boundary layer experience a viscous drag due to the particles in the main flow. There is a then a steady transition from the velocity at this outer-most surface to that of zero velocity at the wall. In the turbulent case the outer-most surface of the boundary layer is uneven and mixing between the boundary layer and the main flow results in more efficient transfer of fluid particles in the stream-wise direction within the boundary layer [van Lier 01]. For this reason turbulent boundary layers are much more stable than laminar boundary layers and are less likely to separate from walls.

Hirschberg [Hirschberg 97] found that the acoustic boundary layer becomes turbulent for a Reynolds number based on the acoustic boundary layer thickness $Re_{\delta_{ac}}$ exceeding 400. This Reynolds number is defined as:

$$Re_{\delta_{ac}} = \frac{u_{ac}\delta_{ac}}{\nu} \tag{2.29}$$

where $\nu = \mu/\rho$ is the kinematic fluid viscosity (equal to $1.5 \times 10^{-5}\text{m}^2\text{s}^{-}1$ for air at STP) and u_{ac} is the acoustic velocity amplitude. In this study, with acoustic velocity amplitudes between 1ms^{-1} and 15ms^{-1}, this Reynolds number is between 5 and 80. The boundary layer within the pipes used for the experiments in this work are thus expected to remain laminar over the range of acoustic velocities studied.

2.5.2 Flow Separation

As previously stated, the viscous effect of the boundary layer can be considered to have little effect on the bulk (inviscid) flow within a duct at high Reynolds numbers since the effects are limited to a thin region close to the walls. At an open end, however, flow separation can occur even at low Reynolds numbers. Flow separation occurs when there is a deceleration of the main flow [Hoffmans 99, Smith 03], due to a sudden expansion

in pipe diameter or at an open end, for example, which results in flow reversal close to the wall. The flow is then unable to follow the contour of the wall and the boundary layer separates from the wall introducing vorticity into the main flow. The point of separation depends on the geometry of the wall and on the exact nature of the flow.

At high Reynolds numbers the separated boundary layer remains spatially distinct from the surrounding flow for a short time and forms a so called shear layer. This is a transition layer between the the main (high velocity) flow and the reversed flow region close to the wall. Shear layers are unstable and tend to roll-up into discrete structures with concentrated vorticity called vortices. Free jets (unstable high velocity regions bounded by shear layers) often accompany boundary separation in cylindrical ducts and tend to produce vortex rings which are gradually broken down into smaller and smaller structures by the action of turbulence until viscous forces dominate and the remaining kinetic energy is dissipated as heat.

2.5.3 Vorticity

The vorticity $\vec{\omega}$ of a fluid is related to its local angular rate of rotation and is given by the curl of the velocity field $\vec{v}$:

$$\vec{\omega} = \nabla \times \vec{v} \tag{2.30}$$

In a two-dimensional flow in the x-y plane the vorticity is perpendicular to the flow and is given by:

$$\omega_z = \frac{\delta v_y}{\delta x} - \frac{\delta v_x}{\delta y} \tag{2.31}$$

where v_x and v_y are the x and y components of the velocity field, and ω_z is the z component of the vorticity field.

2.6 Vortex Sound Theory

A turbulent flow in the presence of an acoustic field will add to or remove energy from the acoustic field resulting in generation or attenuation of sound. Vortex sound theory is a generalisation of Lighthill's theory [Lighthill 52] and can be used to predict the generation or absorption of sound by vorticity within a turbulent flow. It has been successfully used to identify and describe the sound production mechanisms in flute embouchures [Howe 75, Bamberger 02, Bamberger 04, Bamberger 05] and clarinet reeds [Hirschberg 95] among others. The principle has also been applied to noise reduction in ventilation systems and gas transport systems. The inclusion of small apertures in ducts and jet pipes is known to attenuate unwanted acoustic fields [Howe 80]. The sound field causes flow separation at the aperture edges and acoustical

energy is dissipated by the resultant vortex shedding and jet production.

In 1952, Lighthill [Lighthill 52] used the fundamental equations of fluid dynamics to develop the idea of an aero-acoustic analogy. By considering a flow field as being composed of a source flow region superposed with a reference flow, aero-acoustic sound sources could be identified by comparison between physical (real) and idealised flows. Specifically, Lighthill considered a listener immersed in a static, quiescent reference fluid at some distance from a source flow region. Sound sources were then recognised as the difference between the actual flow within the source region and an extrapolation of the idealised reference flow to the source region.

Powell's formulation of Lighthill's analogy [Powell 64] made explicit that in free field conditions (low Mach number ($M \ll 1$), high Reynolds number ($Re \ll 1$) and compact source regions ($He \ll 1$)) sound production in a flow was determined by the kinematics of the vorticity distribution. The associated Coriolis force $\vec{f}_c = -\rho_0(\vec{\omega} \times \vec{v})$, experienced by a fluid particle, produces a force which acts on an otherwise irrotational flow. The divergence of this Coriolis force was then recognised as the source of sound. Howe [Howe 80] generalised the approach further by replacing the quiescent reference flow with an acoustic potential flow. Howe proposed that the irrotational, time-dependent part of the scalar potential velocity field (equation 2.58) should be defined as the reference flow.

2.6.1 The Powell-Howe analogy

In the what follows the inhomogeneous wave equation for an inviscid, homoentropic flow is derived and some simplifications for the special case of compact flows with low Mach and low Strouhal numbers are made. This approach reveals the vorticity field as the main source of aerodynamically generated sound under conditions comparable with those found under playing conditions in real musical instruments.

Conservation of momentum

The momentum conservation equation for a non-viscous fluid is given by Euler's equation:

$$\rho \frac{D\vec{v}}{Dt} = -\vec{\nabla} p + \vec{f} \tag{2.32}$$

where $\rho \equiv \rho(\vec{x}, t)$ is the (scalar) fluid density field, $\vec{v} \equiv \vec{v}(\vec{x}, t)$ is the velocity vector field, p is the pressure and $\vec{f}$ represents external forces acting on the body of the fluid. The convective derivative (also known as the Lagrangian operator) is defined as:

$$\frac{D}{Dt} = \frac{\delta}{\delta t} + \vec{v} \cdot \vec{\nabla} \tag{2.33}$$

and the gradient operator, $\vec{\nabla}$ is given by:

$$\vec{\nabla} \equiv \frac{\delta}{\delta x}\vec{i} + \frac{\delta}{\delta y}\vec{j} + \frac{\delta}{\delta z}\vec{k} \tag{2.34}$$

where $\vec{i}$,$\vec{j}$ and $\vec{k}$ are cartesian unit vectors in the x, y, and z directions, respectively. Using the vector identity:

$$(\vec{v}\cdot\vec{\nabla})\vec{v} = \frac{1}{2}\vec{\nabla}v^2 + (\vec{\nabla}\times\vec{v})\times\vec{v} \tag{2.35}$$

$$= \frac{1}{2}\vec{\nabla}v^2 + \vec{\omega}\times\vec{v} \tag{2.36}$$

where the vorticity $\vec{\omega} = \vec{\nabla}\times\vec{v}$ and $v = |\vec{v}|$ is the velocity magnitude, it is possible to rewrite Euler's equation in the absence of external body forces as:

$$\rho\frac{\delta\vec{v}}{\delta t} + \frac{1}{2}\rho\vec{\nabla}v^2 + \rho(\vec{\omega}\times\vec{v}) + \vec{\nabla}p = 0 \tag{2.37}$$

Conservation of mass

The equation describing the conservation of mass for flows in which there are no volume sources is:

$$\frac{\delta\rho}{\delta t} + \vec{\nabla}\cdot(\rho\vec{v}) = \frac{\delta\rho}{\delta t} + \rho\vec{\nabla}\cdot\vec{v} + \vec{v}\cdot\vec{\nabla}\rho = 0 \tag{2.38}$$

where the following vector identity has been used:

$$\vec{\nabla}\cdot(\rho\vec{v}) = \rho\vec{\nabla}\cdot\vec{v} + \vec{v}\cdot\vec{\nabla}\rho \tag{2.39}$$

Taking the time derivative of the conservation of mass equation (equation 2.38) we get:

$$\frac{\delta}{\delta t}\left\{\frac{\delta\rho}{\delta t} + \rho\vec{\nabla}\cdot\vec{v} + \vec{v}\cdot\vec{\nabla}\rho\right\} = 0 \tag{2.40}$$

$$\frac{\delta^2\rho}{\delta^2 t} + \frac{\delta}{\delta t}(\rho\vec{\nabla}\cdot\vec{v}) + \frac{\delta}{\delta t}(\vec{v}\cdot\vec{\nabla}\rho) = 0 \tag{2.41}$$

Using the product rule for differentiation on the second term of equation 2.41 we get:

$$\frac{\delta}{\delta t}(\rho\vec{\nabla}\cdot\vec{v}) = \frac{\delta\rho}{\delta t}(\vec{\nabla}\cdot\vec{v}) + \rho\left(\vec{\nabla}\cdot\frac{\delta\vec{v}}{\delta t}\right) \tag{2.42}$$

and for the third term:

$$\frac{\delta}{\delta t}(\vec{v}\cdot\vec{\nabla}\rho) = \frac{\delta\vec{v}}{\delta t}\cdot\vec{\nabla}\rho + \vec{v}\cdot\left(\vec{\nabla}\frac{\delta\rho}{\delta t}\right) \tag{2.43}$$

giving for the time derivative of the conservation of mass equation:

$$\frac{\delta^2\rho}{\delta^2 t} + \frac{\delta\rho}{\delta t}(\vec{\nabla}\cdot\vec{v}) + \rho\left(\vec{\nabla}\cdot\frac{\delta\vec{v}}{\delta t}\right) + \frac{\delta\vec{v}}{\delta t}\cdot\vec{\nabla}\rho + \vec{v}\cdot\left(\vec{\nabla}\frac{\delta\rho}{\delta t}\right) = 0 \tag{2.44}$$

This can be further simplified using the vector identity (equation 2.39) to combine terms including the time rate of change of density:

$$\frac{\delta^2\rho}{\delta^2 t} + \vec{\nabla}\cdot\left(\frac{\delta\rho}{\delta t}\vec{v}\right) + \rho\left(\vec{\nabla}\cdot\frac{\delta\vec{v}}{\delta t}\right) + \frac{\delta\vec{v}}{\delta t}\cdot\vec{\nabla}\rho = 0 \tag{2.45}$$

Next, taking the divergence of the Euler equation in the absence of body forces (equation 2.37) we get:

$$\vec{\nabla}\cdot\rho\frac{\delta\vec{v}}{\delta t} + \vec{\nabla}\cdot\frac{1}{2}\rho\vec{\nabla}v^2 + \vec{\nabla}\cdot\rho(\vec{\omega}\times\vec{v}) + \vec{\nabla}^2 p = 0 \tag{2.46}$$

Once more, using the product rule for differentiation for the first and second terms on the left hand side we get:

$$\vec{\nabla}\cdot\rho\frac{\delta\vec{v}}{\delta t} = \frac{\delta\vec{v}}{\delta t}\cdot\vec{\nabla}\rho + \rho\left(\vec{\nabla}\cdot\frac{\delta\vec{v}}{\delta t}\right) \tag{2.47}$$

and

$$\begin{aligned}
\vec{\nabla}\cdot\frac{1}{2}\rho\vec{\nabla}v^2 &= \frac{1}{2}(\vec{\nabla}\rho)\cdot(\vec{\nabla}v^2) + \frac{1}{2}\rho\vec{\nabla}^2 v^2 && (2.48)\\
&= \vec{\nabla}\cdot\left(\frac{1}{2}\rho\vec{\nabla}v^2\right) && (2.49)\\
&= \vec{\nabla}\cdot\left[\vec{\nabla}\left(\frac{1}{2}\rho v^2\right) - \frac{1}{2}v^2\vec{\nabla}\rho\right] && (2.50)
\end{aligned}$$

where the vector identity given in equation 2.39 has been used in the second line and the standard result from vector calculus has been applied in the third line:

$$\vec{\nabla}(ab) = a\vec{\nabla}b + b\vec{\nabla}a \tag{2.51}$$

Here a and b are scalar fields and have been replaced by $\frac{\rho}{2}$ and v^2, respectively, in the above equation. This gives for the divergence of equation 2.37:

$$\frac{\delta\vec{v}}{\delta t}\cdot\vec{\nabla}\rho + \rho\left(\vec{\nabla}\cdot\frac{\delta\vec{v}}{\delta t}\right) + \vec{\nabla}\cdot\left[\vec{\nabla}\left(\frac{1}{2}\rho v^2\right) - \frac{1}{2}v^2\vec{\nabla}\rho\right] + \vec{\nabla}\cdot\rho(\vec{\omega}\times\vec{v}) + \vec{\nabla}^2 p = 0 \tag{2.52}$$

Subtracting equation 2.52 from equation 2.45 we see that the third and fourth terms

in equation 2.45 cancel with the first and second terms in equation 2.52, giving:

$$\frac{\delta^2\rho}{\delta^2 t} + \vec{\nabla}\cdot\left(\frac{\delta\rho}{\delta t}\vec{v}\right) - \vec{\nabla}\cdot\left[\vec{\nabla}\left(\frac{1}{2}\rho v^2\right) + \frac{1}{2}v^2\vec{\nabla}\rho\right] - \vec{\nabla}\cdot\rho(\vec{\omega}\times\vec{v}) - \vec{\nabla}^2 p = 0 \qquad (2.53)$$

which rearranges as:

$$\vec{\nabla}^2 p - \frac{\delta^2\rho}{\delta^2 t} = -\vec{\nabla}\cdot\left[\rho(\vec{\omega}\times\vec{v}) + \vec{\nabla}\left(\frac{1}{2}\rho v^2\right) - \left(\frac{\delta\rho}{\delta t}\vec{v}\right) - \frac{1}{2}v^2\vec{\nabla}\rho\right] \qquad (2.54)$$

Inhomogeneous wave equation

For a homoentropic flow (constant and uniform entropy) we have:

$$\frac{D\rho}{Dt} = \frac{1}{c_0^2}\frac{Dp}{Dt} \qquad (2.55)$$

which allows equation 2.54 to be expressed in the form of an inhomogeneous wave equation for the pressure, p:

$$\vec{\nabla}^2 p - \frac{1}{c_0^2}\frac{\delta^2 p}{\delta t^2} = -\vec{\nabla}\cdot\left[\rho(\vec{\omega}\times\vec{v}) + \vec{\nabla}\left(\frac{1}{2}\rho v^2\right) - \left(\frac{\delta\rho}{\delta t}\vec{v}\right) - \frac{1}{2}v^2\vec{\nabla}\rho\right] \qquad (2.56)$$

For the special case of small Mach numbers ($M \ll 1$) and small Strouhal numbers ($St \ll 1$) the last two terms on the right hand are of order $St \cdot M^2$ and M^2 respectively and can be neglected. Also, for a compact source region ($He \ll 1$) at low Mach numbers the second term can be neglected [Atig 04]. If we further assume that density fluctuations are negligible ($\rho \simeq \rho_0$) we get:

$$\vec{\nabla}^2 p - \frac{1}{c_0^2}\frac{\delta^2 p}{\delta t^2} = -\vec{\nabla}\cdot[\rho_0(\vec{\omega}\times\vec{v})] \qquad (2.57)$$

This can be recognised as the wave equation for an inhomogeneous flow where the divergence of the Coriolis force density $\vec{f_c} = -\rho_0(\vec{\omega}\times\vec{v})$ due to the rotational motion of the fluid is identified as the sole source (or drain) of sound. In the case where the velocity field is a potential flow the source term is zero since the curl of a potential field is zero.

2.6.2 Howe's energy corollary

Definition of the acoustic velocity

Howe [Howe 80] proposed that in the presence of a mean flow the acoustic velocity field $\vec{u}_{ac}$ can be defined as the time-dependent part of the irrotational component of the

flow:

$$\vec{u}_{ac} = \nabla\phi' \tag{2.58}$$

where ϕ' is the time-dependent part of the scalar potential field (section 2.4).

Energy conservation

At low Mach numbers the conservation of instantaneous acoustical energy is given by Kirchoff's energy equation:

$$\frac{\delta E}{\delta t} + \vec{\nabla} \cdot \vec{I} = \vec{f} \cdot \vec{u}_{ac} \tag{2.59}$$

where the instantaneous Energy density E is:

$$E = \frac{1}{2}\rho_0 u_{ac}^2 + \frac{1}{2}\frac{p^2}{\rho_0 c_0^2} \tag{2.60}$$

and $\vec{I} = p\vec{u}_{ac}$ is the instantaneous acoustic intensity. For a periodic acoustic field the time-average of equation 2.59 gives the power transferred to (or removed from) the acoustic field within a volume V by an external force $\vec{f}$:

$$< P >= \oint_S < \vec{I} \cdot \vec{n} > ds = \oint_V < \vec{f} \cdot \vec{u}_{ac} > dV \tag{2.61}$$

where the triangular brackets represent the time-average: $< P >= \frac{1}{T}\int_0^T P dt$. Howe's energy corollary identifies the external force $\vec{f}$ as the Coriolis force density $\vec{f}_c = -\rho_0(\vec{\omega} \times \vec{v})$:

$$P_s = -\rho_0 \oint_V (\vec{\omega} \times \vec{v}) \cdot \vec{u}_{ac} dV \tag{2.62}$$

It is therefore possible to make an estimate of the acoustic power transferred P_s from a source region within a solenoidal flow to the acoustic field if the total velocity, the acoustic velocity and the vorticity fields are known. In the case where the solenoidal flow is generated by an acoustic field, acoustical power is dissipated by conversion into the rotational energy of the vorticity field. The rate of energy absorption is $P = -P_s$. The power dissipated can be related to the real part of the non-dimensionalised termination impedance Z_t/Z_c of a tube as [Atig 04]:

$$Re\left(\frac{Z_t}{Z_c}\right) = -\frac{2 < P_s >}{S Z_c u_{ac}^2} \tag{2.63}$$

Chapter 3

Particle Image Velocimetry

3.1 Introduction

Particle Image Velocimetry (PIV) is an optical measuring technique that allows the velocity of small, neutrally buoyant, tracer particles suspended in a fluid to be simultaneously determined at a number of points in a region of space illuminated by a two-dimensional light sheet. The technique has been applied in a wide range of scientific and engineering fields in which fine spatial structures in complex flows are important. These include flows in the fields of aerodynamics, ventilation systems, medical imaging, boundary layer turbulence and most recently in acoustics and the measurement of sound fields.

PIV holds a number of major benefits over other velocity measurement and flow visualisation techniques. Velocity measurements made using techniques such as Hot-Wire Anemometry (HWA) [Pratt 77, Brunn 95] or using a 'Microflown' [van der Eerden 98, de Bree 03a, de Bree *et al* 96, de Bree 03b] give highly accurate velocity measurements but have the significant disadvantages of measuring at a single point in the flow and of disturbing the flow by the intrusion of a probe. Another single measurement point method is Laser Doppler Anemometry (LDA) [Durst 80, Adrian (Editor) 93, Tropea 95] which, being an optical technique, has the added benefit of non-intrusivity. LDA can be used to scan across a region of space to build up a quantitative picture of a region of the flow, but this is a time consuming process and is only suited to steady state flows. Particle tracking velocimetry (PTV) [Agüi 87, Dracos (Editor) 96] and laser speckle velocimetry (LSV) [Barker 77, Maynart 83] are techniques which, like PIV, make use of small tracer particles to visualise the flow but provide a mainly qualitative description of the motion. The Schlieren [Holder 63, Settles 01] method also provides an excellent means of flow visualisation. Quantitative information is limited but can be extracted through image processing [Vergez 05].

PIV offers a balance between the need for a qualitative description and the need to be able to quantify certain aspects of the flow. It is a non-intrusive whole field

technique, measuring the velocity simultaneously at a number of points in a planar region of space, allowing both a full numerical description of the flow as well as a general physical description. It can be used to make accurate velocity measurements even in high speed flows with shocks or in boundary layers without affecting the flow. This is extremely useful in the study of unsteady flows and in flows where both large and small scale spatial structures are present. Previous studies in the field of acoustics have used PIV to successfully measure both steady and oscillating velocity fields in air [Rockliff 02a, Dufford 02, Hann 95, Hann 97a, Hann 97b, Sharpe 89, Skulina 03]. Technological developments mean that it is now possible to take a snapshot of an acoustic field, and 'see' the sound.

The main principles of PIV are discussed in this chapter, focusing on those that are specifically relevant to the work in this study. Wider overviews of the PIV technique, including the extension to three-dimensions, can be found a number of dedicated publications and journal papers [Westerweel 93, Grant (editor) 94, Raffel 98, Lauterborn 84, Grant 97, Adrian 91, Stanislas 97].

3.2 PIV Principle

The principle of PIV is very simple. Unless the fluid of interest already contains impurities of a suitable size, the flow is 'seeded' with tracer particles. The particles within the flow are illuminated (at least) twice, in a plane containing the region of interest, by a thin pulsed light sheet. The light scattered by the particles and hence the positions of the particles at the time of each pulsed illumination is recorded photographically by a camera. By measuring the displacement of the particles between the two (or more) recordings the fluid velocity can be then determined if the time between illuminations is known.

A typical PIV experimental arrangement is shown in figure 3.1 (page 23). The flow is seeded with small tracer particles and is illuminated at times t and t' in a plane of interest by a narrow light sheet, usually generated by a laser. The choice of time between the illuminations depends on the mean flow velocity and the magnification of the images. The scattered light from each illumination is recorded separately onto two frames of a special digital cross correlation CCD camera [1]. These digital images are then stored in the memory of a computer for future analysis. It should be noted that it is also possible to use the PIV technique by recording two illuminations onto a single frame [Raffel 98], but as this technique is generally redundant with modern digital cameras and was not used in this study, it will not be discussed further. The

[1] Early PIV experiments used traditional wet-film photography and took a considerably longer time to analyse.[Grant (editor) 94]

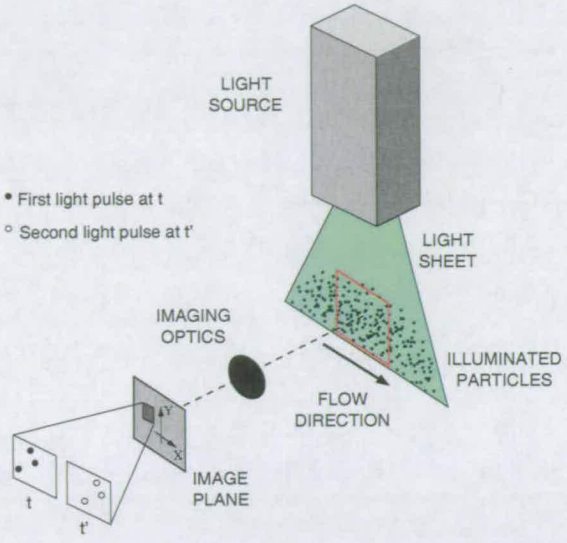


Figure 3.1: Basic experimental setup for particle image velocimetry

remainder of this chapter will concentrate solely on the multi-frame, single exposure method.

The analysis of the digital PIV images is performed by first dividing each image into a grid of smaller sub-areas called *interrogation areas*. Using the cross-correlation statistical method, a displacement vector for the tracer particles is made for each interrogation area, with the assumption that the particles have moved homogeneously between the two illuminations. This process is repeated for each interrogation area in the image. A two-dimensional map of two-component velocity vectors is then obtained by considering the time delay between the illuminations and the magnification of the image.

In what follows a more detailed description of the image acquisition and analysis stages of the PIV procedure will be given.

3.3 Image acquisition

Acquiring high quality images is of primary importance in the PIV process. Optimisation of a number of experimental parameters including particle size, illumination duration, time delay between illuminations and image magnification is necessary to ensure accurate results.

3.3.1 Flow illumination

The choice of illumination method used for PIV mainly depends on the range of velocities to be measured and the size of the region of interest. To accurately determine the location of a tracer particle within an image the duration of the illuminating light pulse must be short enough that the particle does not move appreciably during the pulse exposure to avoid blurring or streaking of the image. It is also essential that during this short time the particle should be able to scatter enough light to be detected by the imaging optics which requires that a large amount of light energy must be available in a short space of time. Pulsed lasers immediately fulfil this requirement (although other light sources can be used for PIV [Raffel 98]) and also benefit by the ease with which the beam can be manipulated. The type of laser used depends on the range of fluid velocities to be measured. Continuous wave lasers with an in-line mechanical shutter can be used for low velocity measurements. For high velocity flows and for acoustic flows in air, however, a pulsed laser is typically needed. For the experiments carried out with acoustic flows in this thesis involving particle velocities up to around 20ms^{-1} a copper vapour laser was used.

Copper vapour lasers are inherently pulsed in nature and are characterised by a high average power (1-30W), pulse durations of the order of 10ns, and pulse repetition rates within the kHz range. The short exposure time effectively freezes the motion of the particles and the high output power ensures good light scattering if a suitable choice of seeding particles is made. The high repetition rate of the laser used (50kHz) allows acoustic velocity amplitudes of up to around 19ms^{-1} to be measured (for an area under investigation of approximately 3cm by 2cm and a frequency of 380Hz - see appendix A, equation A.9).

A number of optical configurations can be used for the generation of a light sheet. Depending on the type and quality of the laser used the lens configuration may require anything from a single cylindrical lens to a combination of cylindrical and spherical lenses to condition the light sheet to the correct thickness with high intensity. Details of lenses and light sheet generating optics can be found in any standard optics textbook. An number of tried and tested lens configurations used in PIV are given by Raffel *et al* [Raffel 98].

Details of the laser and optical system used in this study are given in section 4.2.1. An optical fibre was used to deliver the light to the experimental arrangement. This offers a high level of safety when working with high powered pulsed lasers, although some slight attenuation in light intensity is always associated with the use of optical fibres. A specially designed Oxford Lasers 'Fibresheet' light sheet generating unit was also used to generate a high quality light sheet.

3.3.2 Seeding Particles

PIV is an indirect method, measuring the velocity of a fluid element by measurement of the velocity of tracer (or seeding) particles. The fluid motion is assumed to determine the velocity of these particles. Careful choice of tracer particle is therefore necessary to ensure that the particles faithfully follow the motion of the fluid. Particles are chosen to be small enough to be as close to neutrally buoyant as possible but large enough to scatter light efficiently.

Fluid mechanical properties

Any difference between the density of the tracer particle and that of the surrounding fluid can result in an impeded response due to the inertia of the particle to any fluid acceleration. In air this difference in density is unavoidable and it is therefore essential that the resulting velocity lag is minimised. The velocity lag in the presence of a constantly accelerating fluid is given in several references [Raffel 98, Schlicke 01].

For the case of a spherical particle with diameter d_p and density ρ_p suspended in an acoustic field with frequency f (i.e. for a fluid under oscillatory acceleration) Vignola *et al* [Vignola 92] derived a model that incorporated both viscous drag and pressure gradient forces. They found that below a threshold frequency $f^* = 1/(2\pi\tau_p)$ the pressure gradient force was negligible and that the particles followed the flow very closely. The relaxation time of the particle, τ_p, is a measure of the ability of the particle to achieve velocity equilibrium with the fluid:

$$\tau_p = \frac{d_p^2 \rho_p}{18\mu} \tag{3.1}$$

where μ is the dynamic viscosity of the fluid.

Below the threshold frequency, Melling [Melling 97] showed that the acoustic particle velocity amplitude $|u_a|$ could be related to the amplitude of the seeding particle $|u_p|$ by:

$$|u_a| = |u_p|\sqrt{1 + 2\pi f \tau_p} \tag{3.2}$$

The corresponding phase relationship was shown to be:

$$\angle u_a = \angle u_p + \tan^{-1}(2\pi f \tau_p) \tag{3.3}$$

These equations show that smaller particle diameters respond more faithfully to the oscillatory fluid motion. Smaller particles, however, scatter light less efficiently. Typical particles used in gas flows are smoke particles or atomised oil particles which range between 0.5 and 10μm. It is easier to match particle density to fluid density in flows

in liquids. This allows the use of larger particles (40-1000μm), which have better light scattering properties.

Experiments carried out in this study were made with seeding particles from a SAFEX 2004 fog generator with a mean diameter given by the manufacturer of 1μm [Dantec 98]. The dynamic viscosity of air is $\mu = 1.82 \times 10^{-5}$Nsm^{-2}. The fluid used by the fog generator is a mixture of water with a trace amount of alcohol and so the particle density can be considered to be approximately the same as water (ρ_p =1000kgm^{-3}) [Dantec 05]. These values give a transition frequency $f^* = 45711$Hz. The frequency used in this study was well below this limit so it can be assumed that the particles will follow the flow accurately. At a frequency of acoustic excitation of 380Hz (as used in all of the PIV experiments in this study) the discrepancy between the acoustic particle velocity and the tracer particle velocity is 0.4%, and the phase lag is 0.48 degrees.

Light scattering properties

The intensity of scattered light from a particle increases with increasing particle diameter and varies with the observation angle. For particles larger than the wavelength of light, Mie's scattering theory can be used. This states that the intensity of scattered light is proportional to square of the particle diameter [van de Hulst 92].

It is possible to increase the detected light by increasing the particle size, but as already discussed this is in conflict with the need for a good particle response to the fluid motion. The particle concentration can also be increased to increase the brightness, but this reduces the signal to noise ratio due to the effect of multiple scattering. It is therefore necessary to make a trade off between these two size constraints.

Tracer particle distribution and concentration

For optimal evaluation, no structures should be visible in the PIV images. The tracer particles should be homogeneously distributed with a medium density. This may be difficult to achieve in some practical experimental situations, for example those in which boundary layer separation occurs, where tracer particles can tend to become entrained into specific regions of the flow. Careful positioning of seeding nozzles may be required to achieve homogeneity in some situations.

If the density of tracer particle images on the PIV recording is too high it is not possible to pick out individual particles as they can overlap each other and produce a speckle pattern requiring statistical analysis. This is the basis of laser speckle velocimetry (LSV). The drawback of the LSV technique is that the high particle concentration can affect the fluid motion.

On the other hand, if there is a low seeding density the individual particle images

can easily be visually identified and tracked between each of the different illuminations. This is the basis of a technique called particle tracking velocimetry (PTV). The problem with this technique is that the low density of particles can lead to loss of information in areas where there are no particles. The ideal particle concentration for PIV lies in the medium density region between these two extremes.

Tracer particle imaging

The minimum practical size of particle to use for PIV is restricted by the diffraction limit of the imaging optics. For an aberration free lens at low magnifications the diffraction limited particle diameter is given by the diameter d_{Airy} of an Airy disk [Raffel 98]:

$$d_{Airy} = 2.44 f^{\#}(M+1)\lambda \tag{3.4}$$

where $f^{\#}$ is the f-number of the lens, defined as the ratio of the focal length to aperture diameter, M is the magnification of the image and λ is the wavelength of the light source. This is normally of the order of a few microns for a standard camera lens. Smaller particles than this can be used and will appear with a diameter d_{Airy} in the image but will be dimmer due to the poorer scattering ability.

3.3.3 Image capture

As mentioned in section 3.2 there are two main methods of recording PIV images. Multiple exposures can be recorded on a single frame (single frame/multi-exposure or SFME method), or single exposures can be recorded onto multiple frames (multi-frame/single exposure or MFSE method). The SFME method was mainly used with wet-film photography and will not be discussed here for reasons already given.

Technological advances in digital cross-correlation CCD (charge coupled device) cameras and high speed computer processors have led to the standard use of the MFSE method in most PIV laboratories. The inter-frame times between image acquisitions for current double exposure cameras can be of the order of a few nanoseconds for an image resolution of 1280 $\times$ 1024 pixels. Continuous running high speed digital cameras currently have frame rates of typically 21kHz at a resolution of 512 $\times$ 256 pixels up to 190kHz at resolutions too small to be useful for PIV.

The spatial resolution of CCD arrays is much lower than that of photographic images. This is not a serious problem, however, since the aim of PIV is to sample the motion at a sufficient number of points for statistical analysis, and not to reproduce the scene precisely. Some technical details and an overview of the operation of CCD sensors is given in [Raffel 98].

3.4 Image analysis

The image analysis stage of the PIV process involves dividing the recorded image into a grid of sub-areas (interrogation areas), typically 32 × 32 pixels. Each interrogation area is then statistically analysed using a correlation method. There are two main correlation methods used for PIV analysis. The SFME method uses an auto-correlation technique to extract velocity data from a single, double exposed, frame. The MFSE method uses the cross-correlation technique to analyse a pair of single exposure frames. As the SFME method will not be discussed in this thesis, the following discussion will be restricted to the cross-correlation technique.

The software ('TedPIV') used for the PIV analysis in this thesis was developed by Schlicke [Schlicke 01] at the University of Edinburgh.

3.4.1 Cross-correlation

The cross-correlation is a measure of the similarity of two functions and is used in PIV analysis as a pattern matching method. The method essentially looks at an interrogation area on each of the two images and determines the shift in pixels needed to achieve the best overlap between the two areas. By multiplying this shift by the magnification in metres per pixel of the image and dividing by the time delay between images the average velocity within each interrogation area is determined. The process is then repeated for each interrogation area in the image and a velocity vector map of the flow is obtained.

If we describe the pixel grey-scale values corresponding to an interrogation area at position (i,j) in image 1 as $f(i,j)$ and similarly in image 2 as $g(i,j)$,where i and j are the horizontal and vertical pixel coordinates of the digital image then the cross-correlation function $R_{fg}(i,j)$ in the digital domain is:

$$R_{fg}(i,j) = \sum_{x=0}^{M} \sum_{y=0}^{N} f(i,j)g(x-i, y-j) \tag{3.5}$$

with interrogation areas of dimensions $M \times N$ pixels.

It is computationally very expensive to calculate the cross-correlation using the above equation. The calculation can be performed much more efficiently using correlation theorem: a correlation in real space is equivalent to a complex conjugate multiplication in Fourier space. This gives for the cross-correlation (represented by $\otimes$);

$$R_{fg}(i,j) = f(i,j) \otimes g(i,j) \Longleftrightarrow \mathcal{F}\{R_{fg}(x,y)\} = F(u,v)G^*(u,v) \tag{3.6}$$

where $F(u,v)$ and $G(u,v)$ are the Fourier transforms of $f(i,j)$ and $g(i,j)$, * denotes

a complex conjugate and $\mathcal{F}$ represents a Fourier transform. It is therefore possible to compute the cross-correlation by taking the inverse Fourier transform of the product of the Fourier transforms of each of the interrogation areas.This process is significantly simpler and computationally less expensive to calculate.

The resulting $M \times N$ cross-correlation function (or *correlation plane*, as it is sometimes known) generally consists of contributions from two types of correlation. The first of these is the desired particle-pair correlation between identical particles in the first and second interrogation areas. The second is an undesirable random correlation between particle images in the first interrogation area with different particle images in the second. If the shift of each particle between interrogation areas is constant then the contribution from particle-pairs will add together to produce a peak that is significantly higher than the noise peaks produced by the random correlations. The location of the principle peak relative to the centre of the interrogation plane corresponds to the constant shift described earlier. The height of the main peak relates to the number of particle pair correlations and hence to the signal to noise ratio. Accurate determination of the location of the principle peak is therefore the key to measuring accurate displacements.

Spurious vectors or *outliers* will result if there is a low rate of particle pair detection. If this occurs the signal to noise ratio will be too low and the main peak will fall below the background noise level. Outliers will occur if, for example, the seeding is not satisfactorily homogeneous. Outlier detection is an important part of the post-processing of PIV vector maps and is discussed in more detail in section 3.4.4.

3.4.2 Peak detection

In order to ensure an optimal determination of the mean particle displacement the location of the peak in the correlation plane should be detected as accurately as possible. Since the digital image data is discrete the correlation values are determined only for integral displacements. The accuracy of this displacement is then $\pm\frac{1}{2}$ pixel. This accuracy is acceptable for displacements approaching half the width of the interrogation area, but this error will be significant for smaller displacements.

A number of peak-fitting functions can be used to estimate the location of the correlation peak to sub-pixel accuracy. The method of *three-point estimators* is most commonly used. Using this method a suitable function is fitted to the correlation data at the location of the peak by consideration of each of the two nearest neighbours in both the x and y directions. The Gaussian function is most frequently used for this purpose. This is because the particle images have an approximately Gaussian profile and, since the correlation of two Gaussian functions results in another Gaussian function, it is

assumed that the peak in the correlation plane should also be Gaussian in form. The three-point estimator method works best for narrow correlation peaks (small particle images). The optimum particle image diameter for cross-correlation using the MFSE method is around 1.5 pixels [Raffel 98].

The analysis software used in this study uses the three-point estimator method assuming a Gaussian particle image profile. The peaks in the correlation plane are determined using this method to within an error of between ± 0.05 and ± 0.1pixels [Raffel 98].

3.4.3 Sources of error

The signal to noise ratio of the correlation plane should be maximised to ensure accurate velocity determination. This can achieved by either increasing the number of valid particle-pair correlations or by reducing the number of random correlations. A number of factors will affect the quality of the correlation. These include out-of-plane motion, the density of seeding particles, the size of the particle image and the interrogation area size. More details on error sources and optimisation techniques can be found in [Rockliff 02a, Raffel 98].

3.4.4 Post processing - vector validation

Outliers are vectors which are obviously incorrect and which differ significantly in magnitude and direction from their nearest neighbours. They are caused by random correlations due to, for example, high velocity gradients, low seeding density or reflections and glare from surfaces. It is important to remove outliers from the vector field to ensure that algorithms for the calculation of vector operators (differentials, for example) will work correctly. Incorrect data or data drop-outs will give spurious results so a method of vector replacement is needed to ensure a complete data field.

The PIV analysis software used in this study used a *local median filtering* technique to validate the PIV vector maps. The velocity of each vector is compared with the median value from its eight nearest neighbours. If the original vector differs from this median value by a critical amount it is removed and replaced by a more suitable vector. The replacement vector is calculated by interpolation between the nearest neighbours.

3.5 Summary

In this chapter the basic principles of PIV have been introduced. Considerations regarding the choice of experimental parameters have been outlined and an overview of

the image analysis post-processing techniques given. The following chapter describes the PIV system and experimental practices used in this study.

Chapter 4

PIV Apparatus and Experimental Procedures

4.1 Introduction

This chapter describes the apparatus and methods used for the PIV measurements made in this study. An initial description of the basic PIV system used for the acoustic velocity field measurements in chapter 5 is given in section 4.2. This includes details of the design of a purpose made PIV enclosure which was built to enhance the safety and simplicity of the PIV experimental work.

The focus of this study is to make PIV measurements of the velocity field at the open end of a tube in which a high amplitude sound field has been established. The following section (4.3) describes the general experimental setup including acoustical apparatus, the subjects of the study and the methods used in the set up and execution of the PIV experimental procedure. Section 4.4 then goes on to describe the calibration of probe microphone used to make pressure measurements at the open end of a tube for the termination impedance calculation described in chapter 6.

4.2 PIV System Apparatus

4.2.1 Copper Vapour Laser

An Oxford Lasers LS20-50 copper vapour laser was used as the light source for the PIV experiments in this study. Copper vapour lasers are inherently pulsed in nature and are suitable for a wide range of PIV applications from the acquisition of a continuous series of images for the study of transient flow behaviour, to the output of pairs of light pulses with very short time separation for imaging the acoustic velocity field. Limitations of the applicability of the system to the measurement of acoustic fields are described in appendix A.

The LS20-50 is a pulsed laser with a pulse repetition frequency of up to 50kHz. The average power of the laser is 20W and each light pulse has a duration of 25 - 30ns at

a wavelength of 510.6nm (green). It is a class IV laser and several precautions have to be taken for its safe use. Specifically, eye and skin exposure to direct or reflected laser light should be avoided.

The light is delivered to the flow region under study through a single high power transmission optical fibre (diameter approximately 1mm) via an Oxford Lasers 'Fibresheet' light sheet delivery unit. The use of an optical fibre offers an element of safety in that the light is delivered straight to the experiment without use of mirrors; the beam is thus enclosed and as such requires much less time to align. The optical fibre delivery also allows a simple means of transferring the beam between different experimental setups with a minimum of disruption.

The Oxford Lasers 'Fibresheet' unit is shown in figure 4.1. A laser beam with a Gaussian intensity profile and a diameter of approximately 1mm enters the unit in the upper right hand corner. This meets a semi-silvered mirror which partially transmits a small portion of the laser beam. The remaining light is internally reflected and continues until it meets a fully silvered mirror (parallel to the semi-silvered mirror) which returns the beam back to the semi-silvered mirror for partial transmission and reflection. The process repeats and produces a narrow light sheet which is comprised of a series of overlapping Gaussian beams. It is essential that the mirror surfaces are perfectly aligned to ensure that the overlap of the Gaussian profiles produces a clean light sheet with no visible stripes or bright patches. The mirrors can be seen in the figure and a schematic overlay shows the path of the laser beam. Two cylindrical lenses used to condition the light sheet. The resulting light sheet is 50mm wide and 1mm thick at its narrowest part.

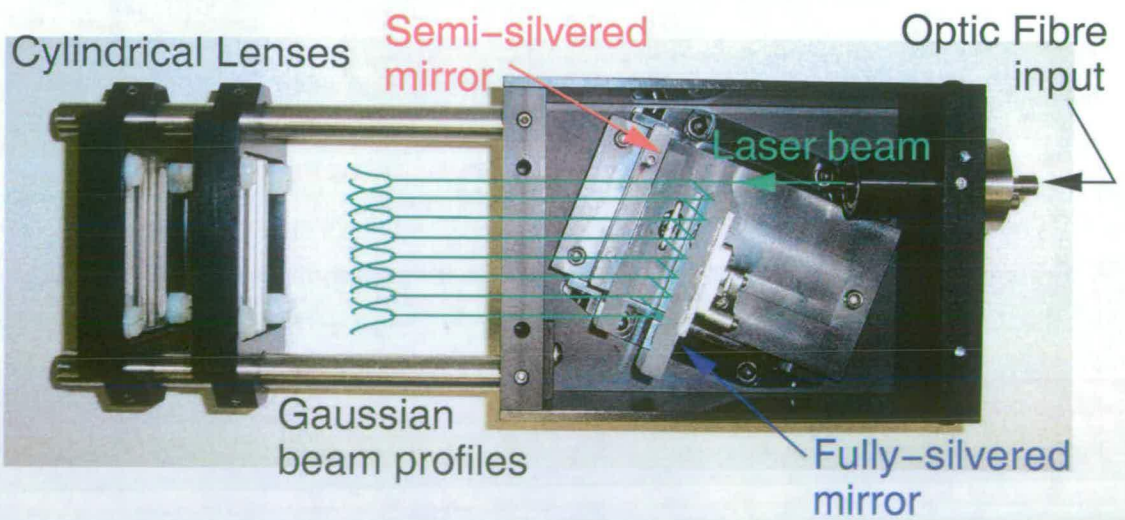


Figure 4.1: 'Fibresheet' light sheet delivery unit.

Problems were encountered with the light sheet quality on a number of occasions in the course of the experimental work. Bright and dark stripes running parallel with the sheet were observed. The 'Fibresheet' was returned to the manufacturer for re-alignment of the mirrors and although improvements were made the problem always remained to some lesser extent. This was possibly due to further misalignment during transit. The problem was, however, easily overcome by careful alignment of the light sheet with the subject such that the dark patches either did not appear in the image at all or were visible only in areas of the image where the affect on the correlation was less important.

4.2.2 Digital Camera - PCO Sensicam

A PCO Sensicam 'Double Shutter' CCD camera was used to acquire raw PIV images for this study. This camera can take two separate images at a resolution of 1280×1024 pixels with a minimum of 200ns between images. It is possible to programme the delay, relative to an input trigger signal, and the exposure time of the first image. There is a choice of two operating modes that determine the delay between the end of the first exposure of the start of the second exposure: short mode (200ns) and long mode (1μs). For the purpose of this work long mode was used. The choice of operating mode made no difference in this study since the time between exposures was determined only by the times of the laser light pulses. The second exposure continues for a time (called the *readout time*) depending on how long the computer takes to process the first image. The user therefore has no direct control over the duration of the second exposure. In this study the readout time taken from a window in the camera control software was 243ms.

4.2.3 PIV Enclosure Design

A special PIV enclosure was designed and built for the purposes of all of the PIV experimental work carried out for this thesis. The reasons for doing so are multiple and include safety and practical requirements.

Primarily the function of the enclosure was to prevent extraneous laser light from escaping and causing potentially very serious and permanent damage to the eyes and skin of the experimentalist. In addition the enclosure was to provide a level of sound insulation, reducing the sound level within the lab to a more acceptable working level, although ear protectors and plugs were worn at all times during experiments carried out at high sound levels.

The solution arrived at was a cubic aluminium box of side length 1.2m, containing a steel scaffold on which sliding optical rails were mounted to hold the laser optics

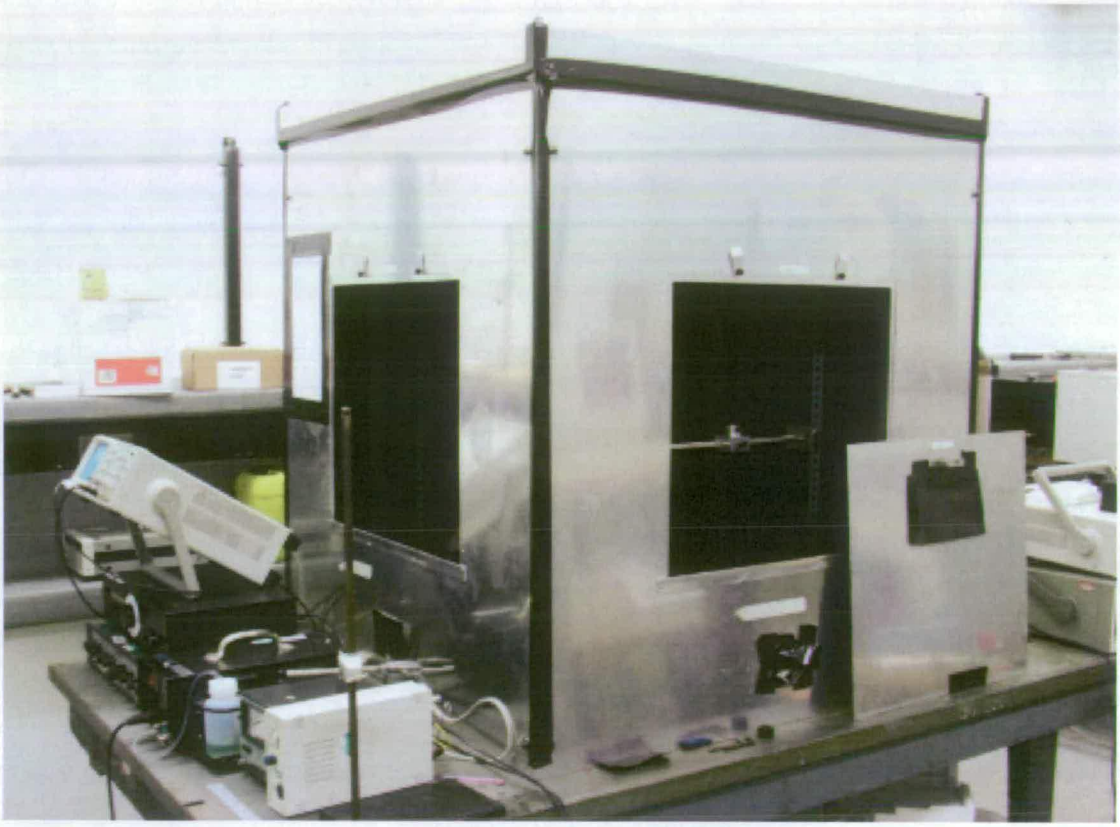


Figure 4.2: PIV enclosure

and digital camera (Figure 4.2). This met the requirement for the minimisation of extraneous laser radiation as well as providing a sealed volume in which to contain the PIV seeding particles. Access hatches were located on four sides to allow easy repositioning of the optical rails and access to the experimental apparatus.

A single viewing window was placed on one of the hatches to help with laser alignment at low light output levels. Small multi purpose openings were also made to allow access for electrical and optical cables and to let particles from the fog generator into the enclosure. All openings or gaps in the enclosure were closed and sealed with duct tape before commencing any experimental work.

Several practical difficulties were overcome in the design of the enclosure. Previous PIV studies of musical wind instruments [Rockliff 02a] have made use of small perspex boxes surrounding the subject of the study to contain the seeding particles. The digital camera was located outside the box, viewing through the perspex. This caused a reduction in image quality due to glare and discolouration caused by smoke residue. Additionally, the relatively small dimensions of the box posed problems with flow

obstruction.

By locating both the laser optics and the digital camera inside the enclosure the glare and discolouration problems were greatly reduced. The relatively large dimensions of the enclosure removed the problems with flow obstruction.

To improve the contrast of the recorded images and to further improve safety by reducing unwanted reflected light the inside of the enclosure was painted matt black.

Optical rails were used so that it was possible to quickly align the digital camera and laser optics consistently between experimental setups. These were designed to allow both horizontal and vertical alignment: the camera and optics could be easily repositioned vertically up or down on the supporting steel frame, depending on the needs of the experiment.

X-Y translation stages were fitted to allow fine adjustments to the positions of the digital camera and laser optics. These were extremely useful in several ways. The digital camera translation stage helped to ensure that the location of the subject in the PIV raw image was consistent between different experiments. It also provided a simple means of adjusting the focus of the camera by moving the translation stage in the forward and backward directions without inadvertently nudging the setup and misaligning the field of view. The translation stage attached to the laser optics allowed quick and safe fine tuning of the alignment of the light sheet with the flow field to be measured.

A lab jack was used to make adjustments to the vertical position of the experimental apparatus within the field of view of the camera.

4.2.4 PIV Timing and Synchronisation

A Berkley Nucleonics model 500A pulse generator was used in conjunction with Labview to provide a semi-automated system for the collection of PIV images at pre-specified phase angles of acoustic flows generated by a loudspeaker. In order to gather information about the repeatability of the PIV experiments, multiple measurements (usually between 25 and 30) were made at each phase angle over several acoustic cycles so that averaging and error analysis could be carried out during post-processing.

A schematic diagram showing the PIV synchronisation setup is shown in figure 4.3. A reference sine wave signal at a frequency relevant to the experiment being carried out (the fundamental resonant frequency of the tube being studied) and sampled at 1MHz was generated by Labview and output to the JBL 2446H loudspeaker via a Pioneer A-107 audio amplifier to set up the acoustic field to be measured. Simultaneously, a 3V square wave, also sampled at 1MHz, with +3V DC offset was used to generate a 6V pulse at a frequency of 2Hz (in the case where, as in this study, the fundamental

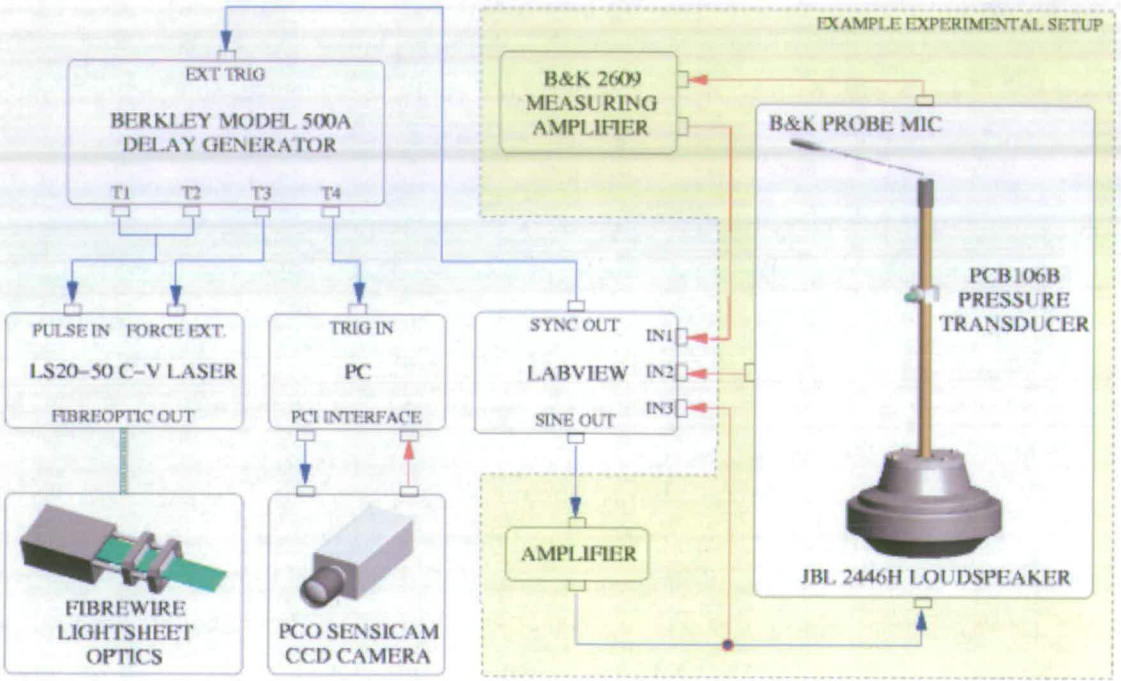


Figure 4.3: PIV Synchronisation setup

frequency was a multiple of two) with which to trigger the pulse generator. The leading edge or positive-going part of this triggering pulse was initially synchronised with the positive-going zero-crossing of the reference sinusoid. A timing delay could be introduced between the positive-going parts of the triggering and reference signals to step through the acoustic cycle at any chosen sample rate. For the purposes of the work in this study it was decided that measurements at 10 equally spaced phase steps through the acoustic cycle were adequate to give a good description of the flow behaviour.

Upon receipt of a positive going trigger pulse, a sequence of timing pulses was output by the Berkley pulse generator to synchronise the output of laser light pulses with the exposures of the digital camera. By adjusting the #PULSES control on the pulse generator it was possible to set the number of input trigger pulses that were responded to. In this way a number of images could be acquired at each phase angle, at intervals of 0.5s, before increasing the timing delay and repeating the process to capture images at the chosen number of phase steps through the acoustic cycle. The main advantage of this technique was that it allowed a large number of PIV measurements of the acoustic particle velocity to be made much more quickly than previous experiments with manual triggering of single PIV measurements [Rockliff 02a, Skulina 03].

Four output signals were sent from the pulse generator on channels T1 to T4 after

	Channel	Delay(ms)	Width(ms)	Polarity
Laser Pulse 1	T1	2.6316	0.0004	+
Laser Pulse 2	T2	2.6516	0.0004	+
Force External	T3	0	300	-
PCO camera	T4	2.5416	0.1	+

Table 4.1: Berkley 500A pulse generator settings for PIV measurements of the acoustic particle velocity with a sinusoidal acoustic input signal at 380Hz.

triggering. Channel T3 was used to output a negative-going pulse to the 'FORCE EXTERNAL' input of the laser. This was to instruct the laser to bypass its internal clock and await external timing signals from its 'PULSE IN' input channel. The duration of this signal had to be long enough to ensure that the laser's internal clock did not restart triggering light pulses before the digital camera had finished its second exposure (see 4.2.2), as this would invalidate the second PIV image. Channel T4 sent the signal to trigger the first exposure of the digital camera. Channels T1 and T2 sent the positive-going pulses to the 'PULSE IN' input of the laser to trigger the individual light pulses. Table 4.1 gives details of the timing setting of these pulses as used in the PIV experiments described in chapter 5 with an acoustic signal at 380Hz.

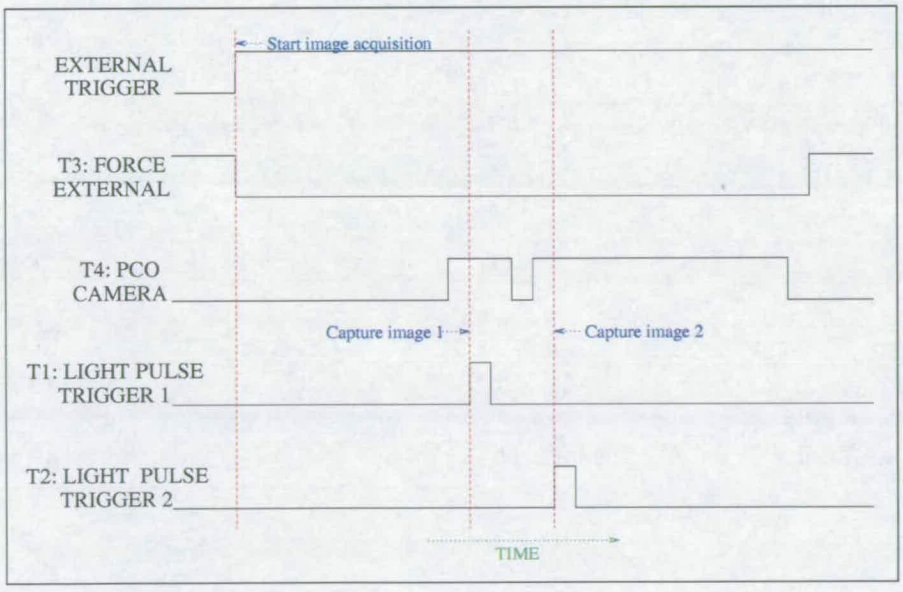


Figure 4.4: PIV timing diagram (not to scale)

A generic timing diagram of the system used illustrating the sequence of timing events is shown in figure 4.4. A positive-going pulse triggers the timing sequence and the laser is immediately forced to await signals from an external source with which to

trigger individual light pulses. The first exposure of the camera is then initiated and a short time afterwards the first light pulse is triggered. The first exposure then ends and the camera automatically begins the second exposure a short time later. The second light pulse is then triggered. This process is carried out in light secure boxes so that a minimum of extraneous light enters the camera during exposure.

4.3 Experimental method

The main features of the PIV apparatus used are shown in figure 4.5 and are described in the previous section 4.2. A 20W Oxford Lasers LS20-50 copper vapour pulsed laser capable of repetition rates up to 50kHz is connected via an optical fibre to the 'Fibresheet' light sheet delivery optics, producing a light sheet 50mm wide and 1mm thick at its narrowest point. The high repetition rate of the laser allows accurate measurement of acoustic velocity amplitudes up to about $20ms^{-1}$ (see appendix A). The light sheet is aligned with the tube axis and a PCO Sensicam CCD camera positioned to view an area of interest around the open end of the tube, perpendicular to the light sheet.

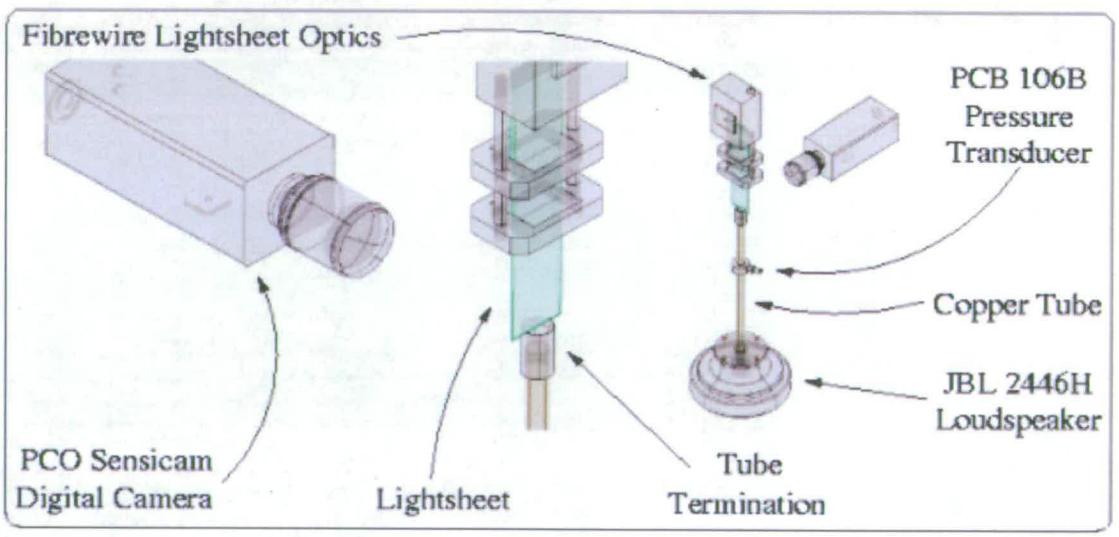


Figure 4.5: PIV apparatus

4.3.1 Loudspeaker

The focus of the work described in chapter 5 is to take PIV measurements of high amplitude acoustic fields in and around the open ends of a cylindrical tube. A JBL 2446H 8Ω compression driver, driven by the Labview sine wave output and an external amplifier, was used to generate the acoustic fields within the tube. An adaptor was

constructed to attach the tube securely to the loudspeaker orifice. The adaptor used to attach the 18mm OD cylindrical copper tube to the loudspeaker is shown in figure 4.6. This device was precision machined by colleagues in Le Mans and fits very snugly into the opening of the loudspeaker, allowing the tube to be mounted securely to the sound source. Vacuum grease was applied between all contacting surfaces and at all joints to ensure that a good seal was made. The copper tube opens into a small cavity at the loudspeaker end an can be considered to be approximately open at both ends.

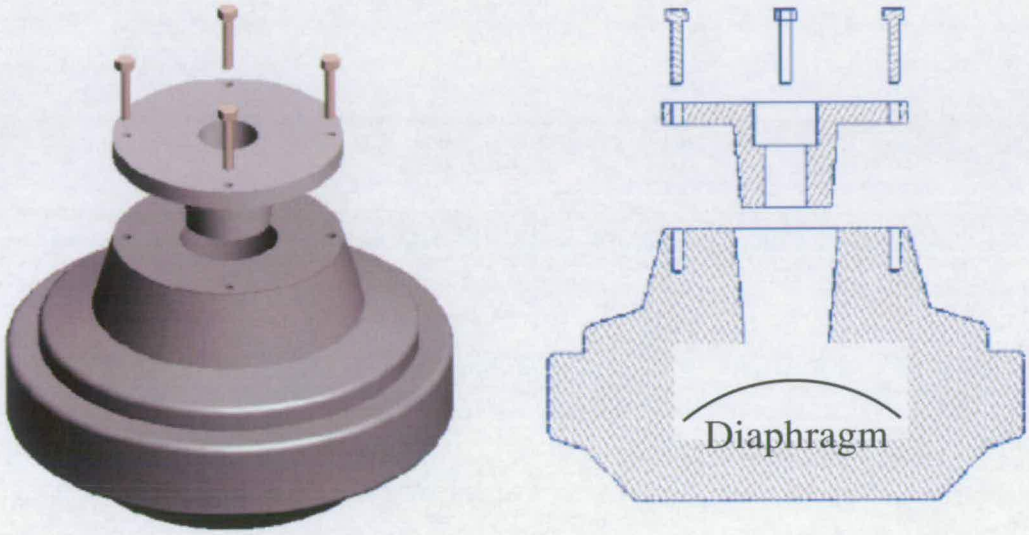


Figure 4.6: JBL 2446H loudspeaker and cylindrical tube adaptor

4.3.2 Copper tube and terminations

A copper tube of internal radius 8mm and wall thickness 1mm with one of five carefully machined terminations, each with a different geometry, fitted to the open end was used in this study. A good seal is obtained by the application of vacuum grease to all necessary surfaces and joints. The length L of the tube from the loudspeaker cavity to the open end of the termination was 460mm. The resonant frequency was found to be 380Hz by locating a probe microphone on-axis at the open end of the termination and finding a pressure maximum by scanning through a range of frequencies close to an estimated value calculated using $f_0 = c_0/2L$, where c_0 is the speed of sound. Figure 4.7 shows a plot of the frequency response of the tube/termination/loudspeaker system confirming this value.

The five tube terminations used are shown in figure 4.8. All have a wall thickness

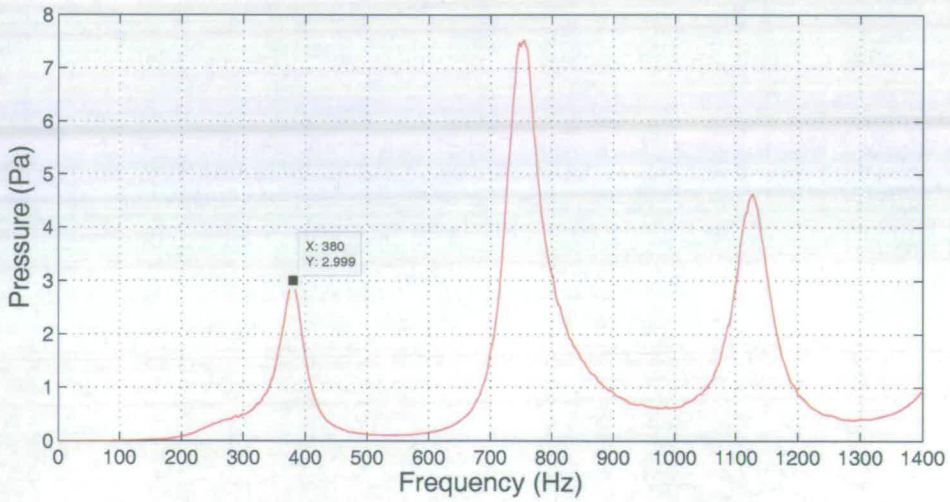


Figure 4.7: Frequency response of tube/termination/loudspeaker system.

of 4.5mm and as such do not fully represent either a flanged or unflanged tube terminations, but are somewhere in between. Each termination has an internal radius of 8mm and is designed to slot onto the end of the copper tube described above with as smooth a join on the internal surface as possible. The sharp edged tube termination has a 20° external taper at its open end to approximate an unflanged tube. The four other terminations have carefully machined radii of curvature on the internal edges. The radii of curvature, R were chosen to match those used by Atig [Atig 03]. These were: 0mm (square edges), 0.3mm, 1mm and 4mm. The terminations were constructed in aluminium and then anodised black to minimise reflective surfaces for use in PIV experiments.

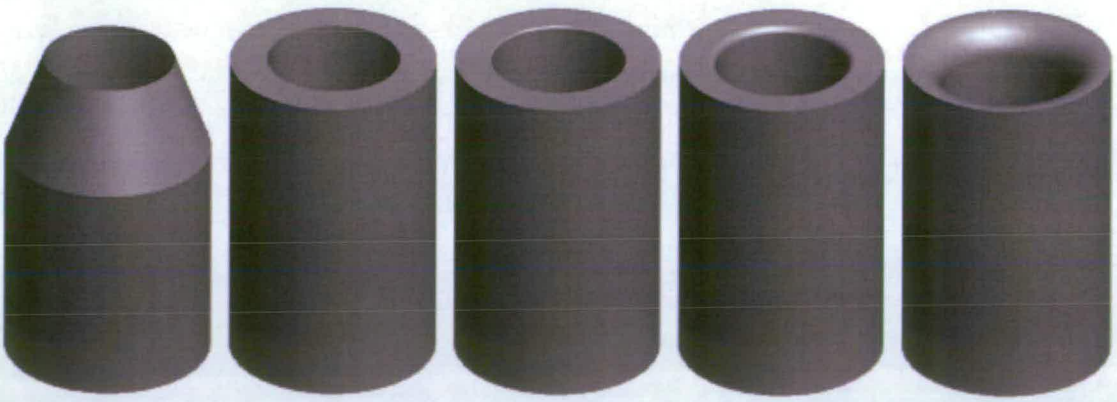


Figure 4.8: Five tube terminations used. Left to right: Sharp edge, R=0mm, R=0.3mm, R=1mm, R=4mm

4.3.3 Monitoring the acoustic field within the tube

A PCB Piezotronics model 106B pressure transducer (from here onward referred to as the PCB transducer) is mounted onto the copper tube 160mm from the open end using the adaptor shown in figure 4.9. This distance was chosen to be the same as used in the two microphone method experiments of Atig [Atig 03] to allow easy comparison between results. It should be noted that a threaded retaining bolt was used to securely mount the PCB transducer into the adaptor, although this is not shown on the diagram. The PCB transducer was used to monitor the sound pressure amplitude within the tube and to ensure that it was set consistently between experiments with different terminations. The output signal was also recorded to enable a calculation of the pressure and linear acoustic velocity amplitude (section 6.3.1).

To mount the PCB transducer a 1mm diameter hole was drilled into the copper tube at a distance of 160mm from the open end of the termination. Another small hole in the PCB adaptor was aligned with this hole using a 1mm allen key and the device was secured into place using a small grub screw on the rear of the adaptor. Again, vacuum grease was used to ensure that a good seal was made.

The sensitivity s of the PCB transducer stated by the manufacturer was 4.48×10^{-5}V/Pa. In order to set the acoustic amplitude within the tube it was necessary to be able to calculate the sound pressure level from the peak-to-peak voltage output, V_{pp}, measured in Volts, from the PCB transducer and vice-versa. The sound pressure level, SPL, at the position of the PCB transducer is given by:

$$SPL = 20\log\left(\frac{p_e}{p_0}\right) \tag{4.1}$$

where p_e is the effective (rms) pressure and $p_0 = 2 \times 10^{-5}$Pa is the reference pressure. The pressure amplitude $|p|$ is given by

$$|p| = \frac{V_{pp}}{2s} \tag{4.2}$$

The effective pressure for a sine wave is

$$p_e = \frac{|p|}{\sqrt{2}} \tag{4.3}$$

and so:

$$SPL = 20\log\left(3.942 \times 10^{8} V_{pp}\right) \tag{4.4}$$

It is then an easy step to calculate the required peak-to-peak voltage level for a given

sound pressure level:

$$V_{pp} = 2.537 \times 10^{\left(\frac{SPL}{20} - 9\right)} \tag{4.5}$$

A look-up chart was made using equation 4.5 and placed in the laboratory to allow the sound pressure level at the position of the PCB sensor to be conveniently set to the required level by monitoring the PCB transducer output voltage signal on an oscilloscope trace.

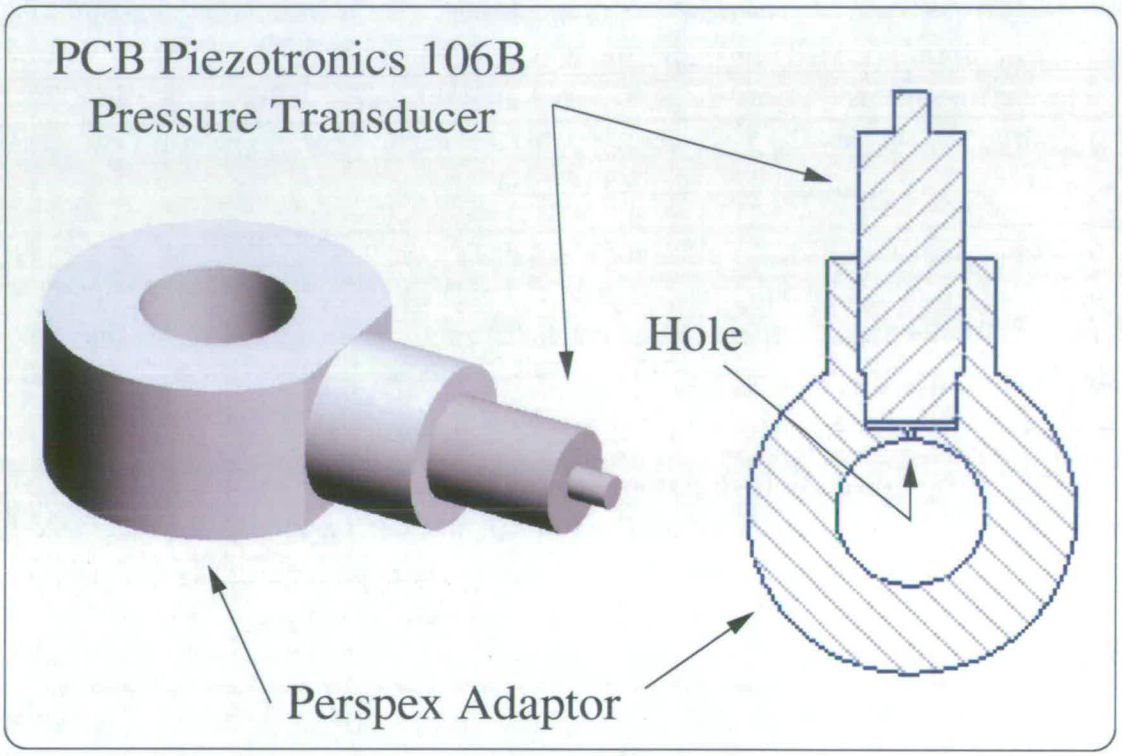


Figure 4.9: PCB pressure transducer adaptor

4.3.4 Optical alignment

The laser optics, digital camera and loudspeaker-tube-termination configuration were located in the sealed PIV enclosure as described in section 4.2.3. This enclosure served two main purposes. The first of these was to prevent extraneous laser light from escaping and causing a possible safety hazard and the second was to provide a sealed volume in which to contain the PIV seeding particles.

Alignment of the laser optics and camera with the tube terminations were then carried out. Careful adjustment of the angle between the optical axis of the camera and the plane of the open end of the termination was important. To prevent unwanted reflections from the rear internal edge of the termination (an increasing problem

with larger radii of curvature terminations) this angle should be as small as possible. However, as the aperture control of the lens was broken and set fully open, this led to a narrow depth of field. This caused a problem since if the optical axis of the lens was in the plane of the open end of the termination, the front edge of the termination was out of focus, causing a slight blurring in the recorded image. Both problems lead to a number of invalid vectors close to the centre of the region of interest. A compromise position was found somewhere between the two extremes to minimise the effect. The adjustment was made by trial and error by carefully inserting wedges of cardboard under the loudspeaker and checking the image using the PCO image capture software.

Once the optical axis of the digital camera was aligned with the tube termination it was a simple operation to align the laser light sheet. In order to ensure minimum detection of out of plane particle motions the narrowest part of the light sheet was used. This is located approximately 100mm from the output lens. The 'Fibresheet' unit was roughly located at the correct vertical position on the scaffold in the PIV enclosure. An X-Y translation stage attached to the laser optics was then used to fine tune the position of the light sheet. The laser was turned on and an attenuator used to reduce the light output to a safe level for viewing. The laser optics were vertically adjusted until the narrowest part of the light sheet was observed on the surface at the open end of the tube termination. The horizontal position and angle from vertical were adjusted so that the plane of the light sheet coincided with the tube axis.

The focal plane of the camera lens was set prior to taking any measurements by injecting some seeding particles into the enclosure and using the real time image capture facility of the PCO camera software to determine when seeding particles illuminated by low output laser light were brought into focus. Once set, the tube termination was centred horizontally in the image using a translation stage and the pixel positions of the corners of tube termination noted. The focus of the camera was not adjusted further during a set of measurements to avoid accidentally misaligning it. If any focal adjustment was necessary it was done by moving the camera forward or back carefully on its translation stage.

4.3.5 Seeding particles

Seeding particles with a mean diameter of 1μm were generated using a Safex Nebelgerät F2004 fog generator using standard fog fluid. A single short burst of particles were added to the PIV enclosure through a small sealable aperture on the side and allowed to homogenise for five to ten minutes. This amount of fog would generally be sufficient and remain in a stable suspension for about 45 minutes - enough time for a set of 6-8 experimental measurements with one termination. Regular visual checks were made on

the number of particles using images recorded with the PCO camera software so that more particles could be added between experiments if necessary.

4.3.6 PIV measurement procedure

Before commencing a set of measurements on a newly fitted termination a verification system was used to check that the loudspeaker/tube/termination system was properly sealed and working correctly. This was a simple procedure of checking that for a 5V amplitude sine wave input to the loudspeaker (as read form the oscilloscope trace) the sound pressure level within the duct was in the region of 161.2-162.3dB (corresponding to a peak-to-peak PCB transducer output of between 284mV and 319mV. A sound pressure level lower than this indicated a problem. All electrical connections were checked and the verification system repeated. If the sound pressure level still remained too low then the implication was that air leaks were present and the tube was removed, resealed with vacuum grease and the verification procedure repeated.

Once the all apparatus was prepared and the optics aligned, the access hatches on the PIV enclosure were sealed. Seeding particles from the SAFEX Nebelgerät F2004 fog generator were then introduced into the enclosure and allowed to homogenise for a few minutes before Labview was initiated to set up the acoustic field and the laser light turned on.

The sound pressure level within the tube was monitored by viewing the output signal from the PCB transducer, after passing through a PCB Piezotronics ICP sensor signal conditioner type 482A22, on an oscilloscope. The peak-to-peak voltage output from the PCB transducer was adjusted by varying the volume control on the amplifier. Once the sound pressure level within the tube was set to the required level the measurement sequence described in section 4.2.4 was then initiated and repeated for each of 10 phase angles through the acoustic cycle with between 25 and 30 PIV image pairs recorded at each phase angle. Measurements were made at a number of internal sound pressure levels ranging between 136.3dB and 169.1dB for each of the five tube terminations. It was expected that at the lowest levels the particle velocity would be low enough that non-linear effects would be negligible and the velocity field would represent a close approximation to potential flow.

The quality and usefulness of a set of images or particular experimental setup were evaluated prior to, and occasionally during, the acquisition of a set of measurements using a trial version of some PIV software called 'PIVView' produced by PIVtec. This was an extremely useful tool for the quick evaluation of PIV images within the laboratory and saved a lot of time that would have otherwise been spent inconveniently transferring large data files to the office computer for analysis and inspection.

4.4 Microphone Calibration

A Brüel and Kjær half-inch microphone (cartridge type 4192, with preamplifier and probe attachment) was used for pressure measurements near the tube termination. The reference microphone used for calibration was another Brüel and Kjær half-inch microphone with cartridge type 4134.

The Brüel and Kjær Pulse System with a type 3109 input/output module and LAN interface module type 7533 with Pulse Labshop version 6.1 software were used to calibrate the Brüel and Kjær Microphones used in the all of the experiments presented in this thesis. The Pulse system is a PC based data acquisition system and has in-built functions and procedures to allow the accurate calibration of microphones. It has stored frequency response data for all Brüel and Kjær microphones and allows precision measurements of pressure and phase.

4.4.1 Experimental Method

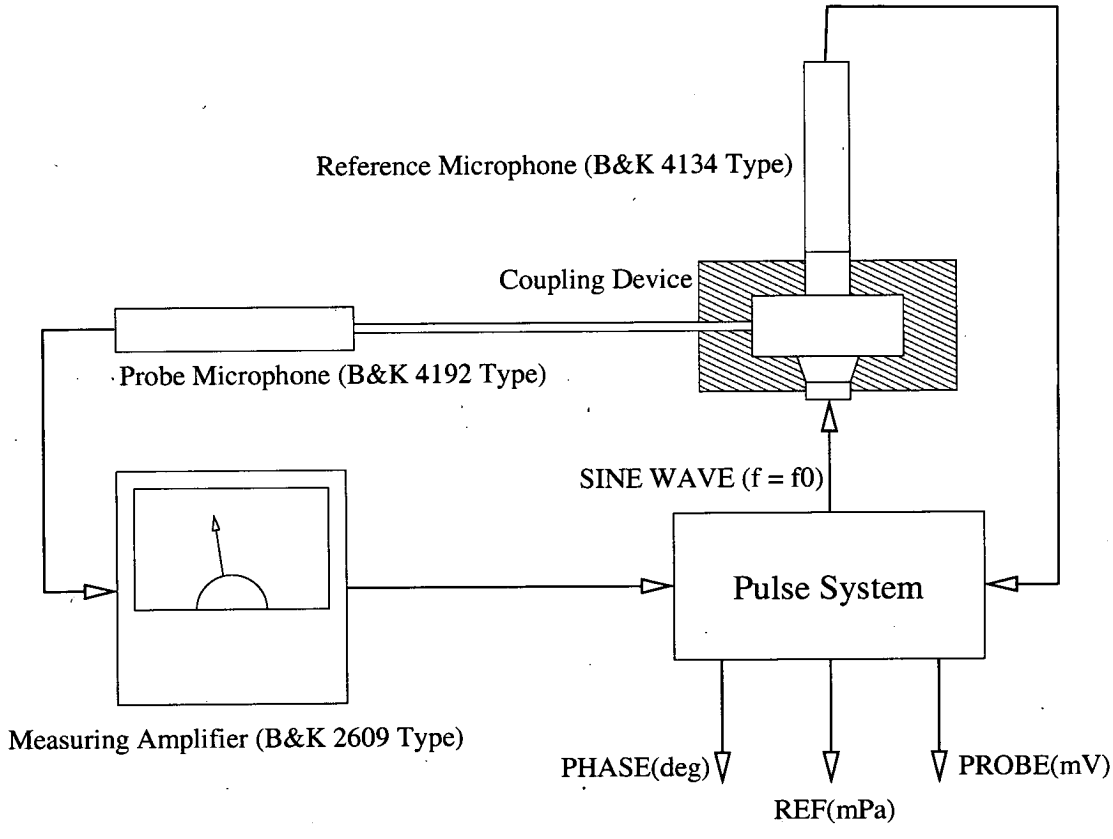


Figure 4.10: Experimental setup for probe microphone calibration

The system used for the probe microphone calibration is shown in Figure 4.10. A sealed coupling device provided by Brüel and Kjær specifically for calibration purposes (UA0040 probe microphone kit) was used.

The Brüel and Kjær type 4192 half-inch microphone with a 235mm long, 2mm diameter probe attachment (to be calibrated) was inserted into a 2mm hole in the side of the coupling device and sealed using putty. A Brüel and Kjær type 4134 half-inch microphone, providing the reference signal, was screwed into the top of the coupling device ensuring a good seal. A small loudspeaker located in the base of the coupling device acted as the sound source for the calibration procedure.

The Probe microphone preamp was not fitted with a modern Brüel and Kjær plug and was not compatible with the input socket of the Pulse hardware. For this reason the output voltage signal from the probe microphone had to be passed through a Brüel and Kjær type 2609 analogue measuring amplifier before connection to the Pulse hardware using a standard BNC connector. The measuring amplifier allows the acoustic pressure level to be read from a dial on the front panel and the gain level to be adjusted. The gain level (in dB) is set and noted once the signal to the loudspeaker is started by choosing a level at which the needle on the analogue dial remains above 0dB and below full scale deflection.

The rms output voltage at full scale deflection (i.e. when the needle on the dial reads maximum of 10V) is $\sqrt{10}$V. A 0dB gain reading from the dial corresponds to a voltage reading (also from the dial) of 1V. To calculate the nominal sound pressure level (in dB) measured by the probe microphone given the output voltage V_{out} from the Brüel and Kjær type 2609 analogue measuring amplifier the following equation is used:

$$\text{Nominal Probe dB reading} = SPL_{nominal} = 20\log(\sqrt{10}V_{out}) + \text{Gain Setting} \quad (4.6)$$

The Pulse System simultaneously measures the pressure from the Brüel and Kjær type 4314 reference microphone and uses the stored frequency response data for this microphone to provide a flat response. The magnitude of the correction $SPL_{correction}$ to the probe microphone is therefore:

$$SPL_{correction} = SPL_{ref} - SPL_{nominal} \quad (4.7)$$

where SPL_{ref} is the sound pressure level measured by the reference microphone. The Pulse software is initialised and a random noise signal in the frequency range of 0-1.6kHz is generated and sent via an amplifier to the small loudspeaker in the coupling device. The gain setting on the Brüel and Kjær type 2609 measuring amplifier is set to

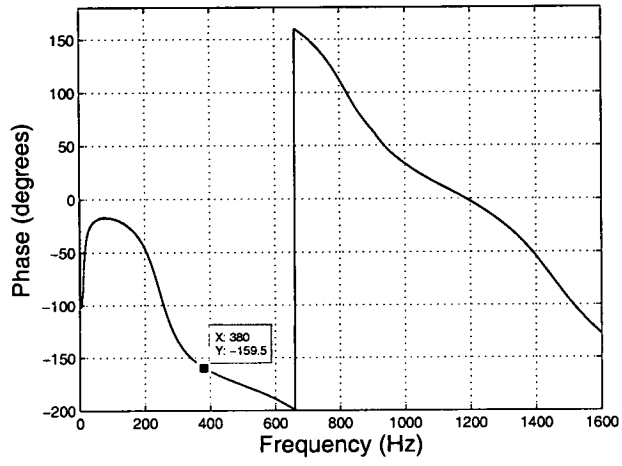


Figure 4.11: Phase difference between probe and reference microphones

110dB and the sound pressure level adjusted to read 10dB on the dial, giving a total sound pressure level reading of 120dB. The Pulse system is then initiated and samples the data from each of the microphone channels. An autospectrum of data from each channel is displayed on screen from which the amplitude of the two signals is read at a frequency of 380Hz as used in the PIV experiments in chapter 5. The signal from the probe microphone is given in volts, and the signal from the reference microphone in dB (re 20μPa) . In addition, the cross-correlation between the two signals gives the nominal phase difference between the two microphones. This is displayed as a function of frequency in figure 4.11. The signal from the probe microphone is reverse biased, so to obtain the phase correction $\phi_{correction}$ for the probe microphone the value read from the cross correlation at 380Hz is corrected by the addition of 180°.

The following values are given for the amplitudes of the signals: V_{out} = 34.2mV; SPL_{ref} = 88.3dB (re 20μPa). The procedure described above gives $SPL_{correction} = -2.3dB$ and $\phi_{correction} = -20.5°$.

Chapter 5

PIV Measurements of the Acoustic Behaviour of Open Ended Pipes

5.1 Introduction

Flow visualisation techniques can provide valuable insight into complicated flow phenomena and can offer a deeper physical understanding of what is going on. This is extremely useful in the often abstract field of fluid dynamics where it can be difficult to draw physical meaning from the complicated mathematical formulations. The major benefit of using PIV rather than other flow visualisation techniques is that it allows both general qualitative observations and quantitative analysis of the entire flow field.

Several authors [Sivian 35, Ingard 50, Rockliff 02a, Keefe 83] have observed non-linear flow behaviour at apertures and open ends of woodwind musical instruments and noted that the shape of the opening plays an important role in the type of behaviour observed. To investigate the effect on the local acoustical flow behaviour of changing the geometry of the open end of a musical instrument at sound levels comparable to those measured in real instruments, this work presents a set of experiments that have been carried out using the PIV technique to investigate one of the simplest possible representations of a woodwind instrument. A length of copper tubing with five interchangeable terminations, each with a differing level of roundness, has been used for this purpose. A high amplitude sound field has been generated within the tube by a loudspeaker and measurements have been made of the acoustic particle velocity field just outside the open end using PIV.

The previous chapter has already detailed the apparatus and procedures used for the measurements made in this study. This chapter begins with a brief description of the background to this work. The PIV results will then be presented in the contexts of both velocity and vorticity fields to enable a detailed qualitative description of the measured flow fields.

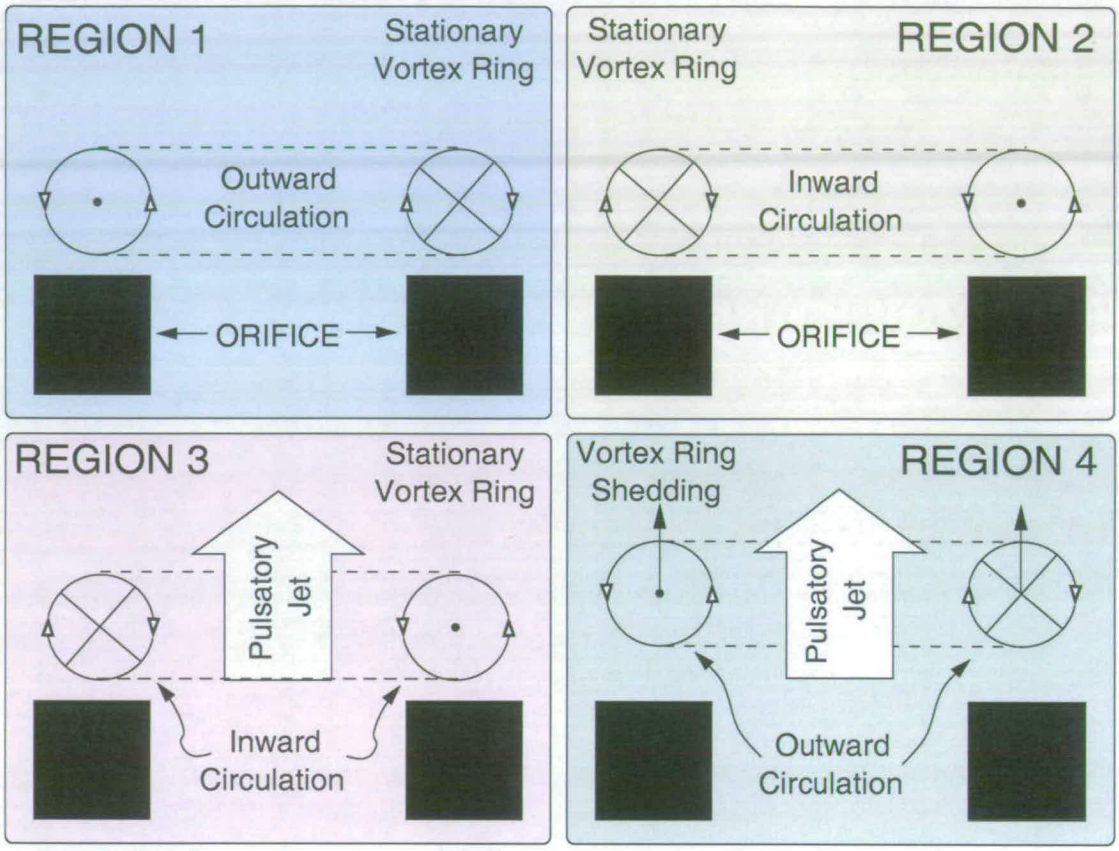


Figure 5.1: Schematic diagram showing the four acoustically generated flow regions observed by Ingard and Labate [Ingard 50] and discussed in section 5.2.1.

5.2 Background

5.2.1 Non-linear acoustic flows

Non-linear acoustical behaviour at orifices was noted by Sivian in 1935 [Sivian 35]. The amplitude of the sound field was shown to affect the acoustic resistance of a circular orifice in a plate placed at the end of a tube. In 1950 Ingard and Labate [Ingard 50] used used smoke particles to visualise the flow outside a number of orifices of different size at a range of acoustic amplitudes to investigate the link between the non-linear acoustic impedance and the formation of vortices and jets. The flow visualisation identified four flow regions for the range of orifice diameters studied which vary with frequency and acoustic amplitude (see figure 5.1). Region 1 occurs at low amplitudes and has stationary vortices just outside the orifice edges with outward circulation (mean flow directed out of the orifice along the axis, symmetrically on either side of the orifice). The size of these vortices increases with acoustic amplitude. At slightly higher acoustic

amplitudes region 2 occurs with stationary vortices circulating in the opposite direction (inward circulation) to those in region 1. In region 3, at medium acoustic amplitudes, turbulent effects begin and a pulsatory jet is superposed with vortices circulating as in region 2. A 'break-through' to region 4 occurs at high amplitudes is described in which pulsatory jets are produced and vortex rings are shed periodically. Air is periodically drawn in diffusely on one side of the orifice and expelled along the axis on the other. There is an average outflow along the axis and inflow near the sides of the orifice. The acoustic amplitude at which region 4 is attained is reported to be well defined for most of the orifices tested. This work showed that the non-linear effects observed are dependent on the acoustic velocity amplitude, frequency and on the geometry of the orifice.

Measurements of the non-linear acoustic resistance of an orifice were made by Ingard and Ising [Ingard 67] using the first harmonic components of the velocity, measured using hot-wire anemometry in the orifice, and pressure. It was found that the acoustic resistance was proportional to the orifice flow velocity at high sound levels. Later studies by Disselhorst and van Wijngaarden [Disselhorst 80], and by Peters *et al* [Peters *et al* 93], showed that the constant of proportionality between the acoustic amplitude and acoustic resistance was dependent on the sharpness of the edge of a tube termination.

A number of experimental and theoretical studies into these non-linear effects have been carried out by several authors. Boundary layer separation is well known to occur due to frictional forces at edges at the open end of a tube. The consequent vortex formation and shedding results in additional energy dissipation. Acoustical energy is converted into rotational energy and is gradually dissipated as heat by frictional forces. The geometry of the termination affects the strength of this non-linear behaviour and the associated acoustical energy loss. For a sharp edged tube flow separation occurs on both inflow and outflow. For a rounded termination vortex shedding is expected to be a much less significant loss mechanism [Rockliff 02a].

Several authors have presented flow visualisations of jet formation and vortex shedding at sharp and square edged nozzles [Disselhorst 80, Hoffmans 99]. Flow visualisations and PIV measurements have been made of the sound produced by the coalescence of acoustically generated vortex rings produced at a sharp edged nozzle at high velocity amplitudes by Schram [Schram 03].

5.2.2 Recent use of PIV in the field of musical acoustics

Recent work by Rockliff [Rockliff 02a, Rockliff 01] has used PIV to measure the velocity field at the open end of a cylindrical tube. The termination impedance

was calculated using velocity data obtained using PIV and the pressure measured with a probe microphone. Some difficulties were found in accurately determining the phase of the velocity signal. Comparison with impedance measurements made with a two microphone method [Atig 01] show that the results gained using the PIV technique are consistently higher but follow the same trend. A similar procedure is presented by Skulina in [Skulina 03]. Measurements have been made using PIV of acoustic streaming velocity fields at high amplitudes in a standing wave tube [Rockliff 02a, Campbell 00, Sharpe 89]. Studies of acoustic particle velocity fields and acoustic streaming velocity fields outside tone holes using PIV have revealed the presence of jet structures which vary in direction with frequency and acoustic amplitude [Rockliff 02a, Rockliff 02b, Skulina 02, Skulina 05].

PIV has been applied to the measurement of the acoustic velocity field in the head joint of a flute [Bamberger 01, Bamberger 02, Bamberger 04, Bamberger 05]. Studies of the acoustic velocity field at the exit of a bass reflex port on a loudspeaker [Moreau 05, Esposito 03], in acoustic wave guides [Boucheron 04], and in a mechanical vocal fold model [Bruecker 04] have also been made.

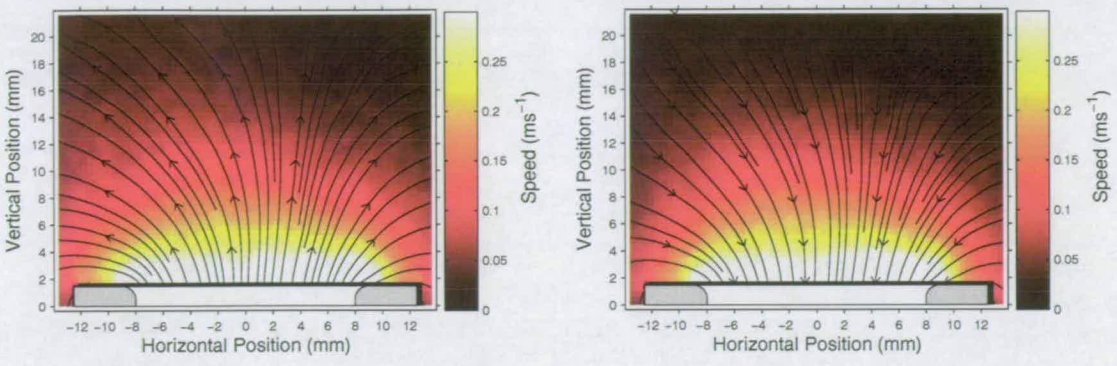
5.3 PIV Results

In the following section a review of the measurements made using PIV is given. A large amount of PIV data was generated in this study, and many interesting effects were observed. A select few of these results are presented here in an attempt to present only the most interesting.

5.3.1 Low amplitude measurements

At the lowest sound pressure levels examined in this work it was verified that the flow field can be considered a good representation of potential flow. At low acoustic particle velocity amplitudes (0.5 - 1ms^{-1}) the corresponding acoustic Strouhal numbers are larger than 1 (Sr_{ac} between 12 and 6) and the flow is expected to be free from any non-linear phenomena and should be irrotational. This is in agreement with observations. Depending on the geometry of the tube termination the flow retained potential-like behaviour for sound pressure levels measured within the tube at the position of the PCB sensor of 136.8dB for the sharp edged termination up to 146.9dB for the most rounded termination.

As expected, the rounded tube terminations exhibited the closest similarity to potential flow over a wider dynamic range. The tube terminations with sharper inner edge showed a departure from linear behaviour at lower sound pressure amplitudes.



(a) Peak outflow

(b) Peak inflow

Figure 5.2: PIV measurement of potential flow at low sound levels. Velocity magnitude contours with streamlines for the R=1mm termination at 136.6dB. Grey areas represent the termination wall locations.

At the lowest levels measured (approximately 136.5dB) the velocity fields for all tube terminations were essentially free from any non-linear behaviour. Any deviation from perfectly symmetrical flow was due to the fact that convection current velocities within the PIV enclosure were comparable with the acoustic particle velocity and were difficult to eliminate completely from measurements at these low amplitudes. At higher sound amplitudes the convection velocities were negligible compared with the acoustic velocity and so this was not a problem. At low amplitudes this problem was minimised by allowing the air within the enclosure to settle before any measurements were made.

Figure 5.2 shows a pair of velocity magnitude contour plots with streamlines at points in the acoustic cycle corresponding to maximum inflow and outflow for a rounded tube termination with a radius of curvature R=1mm at 136.6dB. As can be seen the inflow and outflow are symmetrical and diffuse at this sound level. The wave-fronts in front of the centre close to the open end are approximately plane waves. The streamlines have been calculated in Matlab using the 'streamslice' command. These describe the paths followed by imaginary massless particles placed in the flow.

Figure 5.3 shows the vector map at maximum outflow for the R=1mm termination at 136.6dB. Velocity profiles of the vertical velocity components in the radial and axial directions are shown above and to the right of the vector map. The planes from which the velocity profiles are taken are indicated by the red dashed lines on the velocity vector map. As can be seen there is a slight asymmetry between the left and right hand sides of the radial velocity profile plot, but the flow can be considered to be very nearly axisymmetric. The shape of the velocity profiles on outflow are a mirror image of the velocity profiles on inflow in both the radial and axial plots.

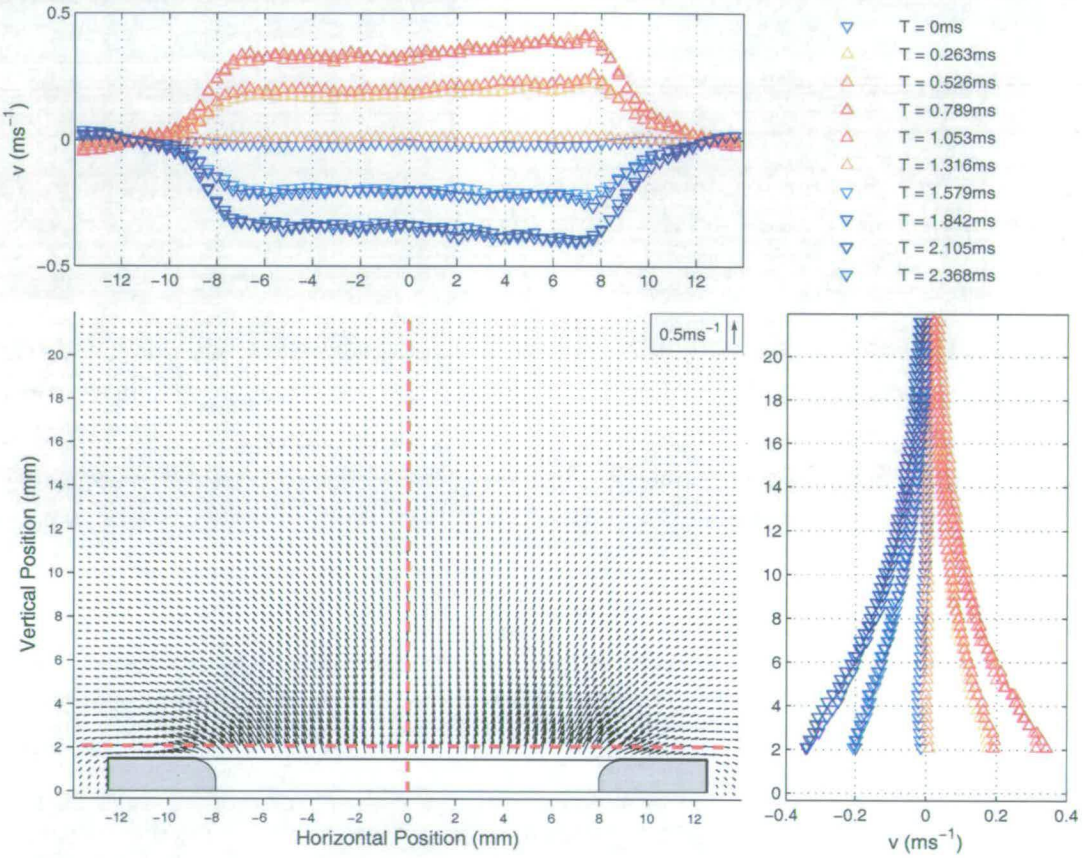
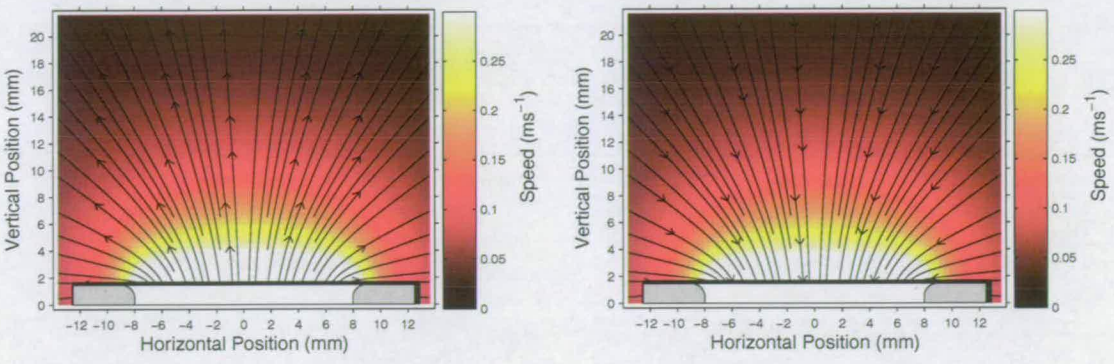


Figure 5.3: PIV velocity vector map at peak outflow for the R=1mm termination at 136.6dB. Radial (top) and axial(right) velocity profiles at a series of times through the acoustic cycle are also shown. Grey areas represent the termination wall locations. Red dashed lines represent planes in which velocity profiles are measured.



(a) Peak outflow

(b) Peak inflow

Figure 5.4: Potential flow above an idealised piston located in the plane of the open end. Velocity magnitude contours with streamlines for a sound level and open end location corresponding to the R=1mm termination at 136.6dB measured using PIV. Grey areas represent the (imaginary) tube wall locations corresponding to the PIV data.

For comparison the potential acoustic velocity field above a piston located in the plane of the open end has been calculated numerically, as described in section 7.2.3. Contour plots showing the magnitude of the velocity field at maximum outflow and inflow above the idealised case of a plane piston are shown in figure 5.4. Streamlines are added to indicate the flow direction. Again, the flow is symmetrical and diffuse on inflow and outflow. The streamlines show slightly less curvature than in the experimental case, and since the tube walls and edges are not taken into account in the model the flow in these areas is not ideal. However, the overall agreement between the modelled and the experimentally determined potential flows is good.

Figure 5.5 shows the corresponding velocity vector map at peak outflow for the modelled case with the radial and axial velocity profiles. The amplitude of the oscillation has been adjusted so that the velocity in the plane just above the piston is the same as the velocity measured from the PIV measurement. The flows in both the PIV measurements and in the idealised case above a piston are in good agreement. There are some subtle differences in the flow direction which are most likely to be due to convection currents within the PIV enclosure and the non-ideal modelling of the tube edges. The radial velocity profiles also appear to be qualitatively similar with axial and temporal symmetry. There is a striking similarity in the rate of change of axial velocity amplitude with distance in the axial direction.

The axial velocity profiles are examined further using a normalisation procedure. Firstly, the magnitudes of the axial velocity profiles from the PIV data at each of the phase steps (except the two phase steps with near-zero amplitudes which were rejected

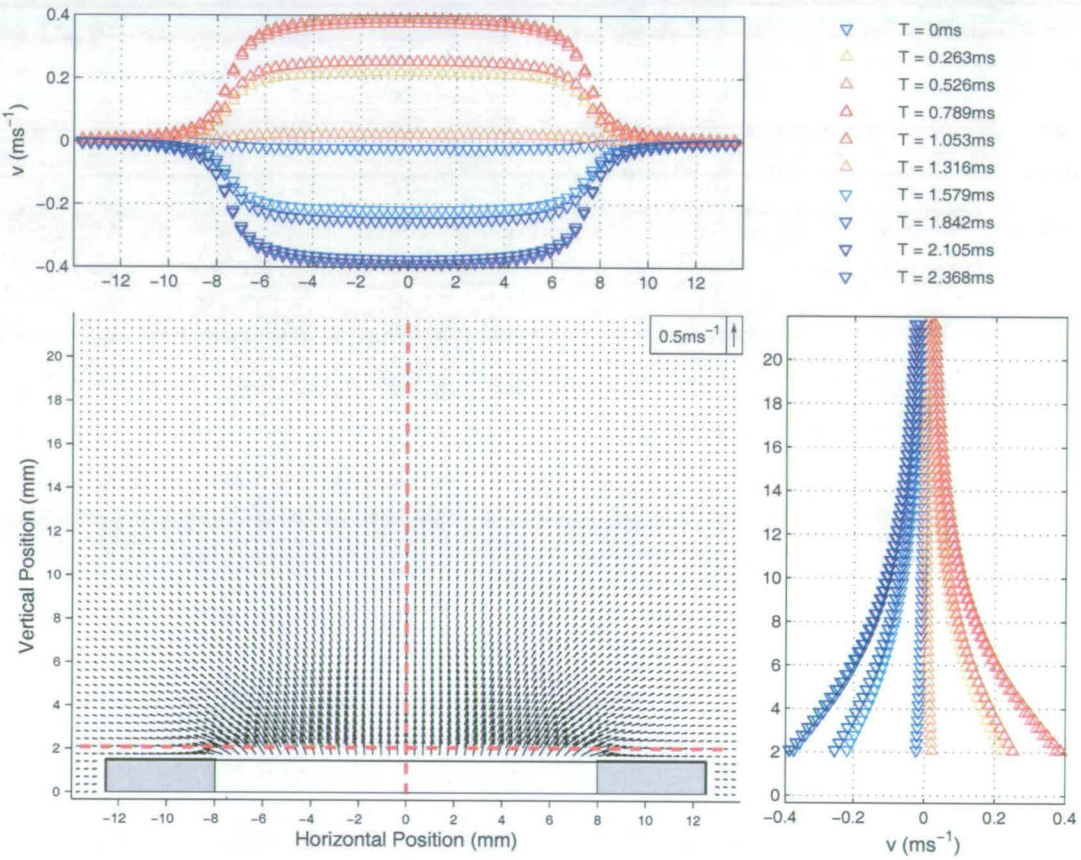


Figure 5.5: Idealised Potential flow velocity vector map at peak outflow above a piston located at the open end. Radial(top) and Axial(right) velocity profiles at a series of times through acoustic cycle. The sound level is equivalent to the PIV measurement of the R=1mm termination at 136.6dB Grey areas represent the tube wall locations corresponding to the PIV data. Red dashed lines represent planes in which velocity profiles are measured.

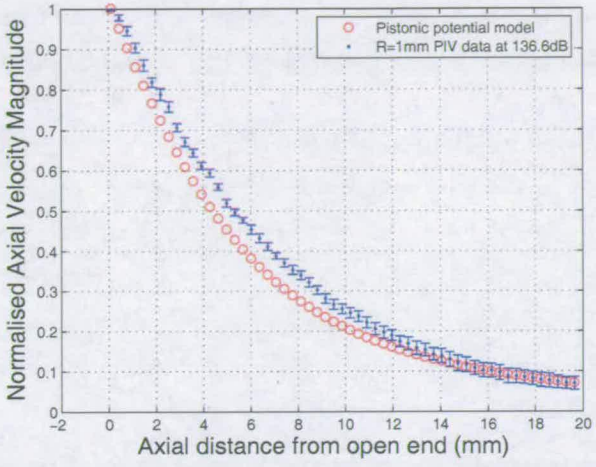


Figure 5.6: Normalised axial velocity magnitude as a function of axial distance for both the PIV measurement of the R = 1mm termination at 136.6dB and the pistonic model of potential flow.

from this calculation) were normalised by dividing by the maximum axial velocity at that phase. This produced a series of velocity profiles with amplitudes between zero and one. A mean value and associated standard error of the normalised axial velocity at each axial position was calculated in Matlab. This was then plotted as a function of axial distance from the open end along with a normalised axial velocity data from the modelled data (no averaging was necessary since the profile at all phase steps is identical). The result of this procedure for the PIV and modelled data corresponding to the R = 1mm termination at 136.6dB is shown in figure 5.6. As can be seen there is an excellent agreement with between the experimental and theoretical results.

Modelling the flow at the open end as that above a piston located directly at the open is an over-simplification and the exact details of two results cannot be expected to agree completely. However, the results suggest that the velocity field measured for the R = 1mm termination at 136.6dB with PIV is a good approximation to potential flow. Modelling the potential flow at the open end of a tube as that above a piston appears to be justified in both a qualitative and quantitative sense. The calculation and use of the pistonic potential flow model in the estimation of energy losses using vortex sound theory is described in chapter 7.

In the following sections (5.3.2 - 5.3.5) a number of PIV vector maps are displayed. For clarity a brief description of some of the features is now made. In each vector map a waveform is shown in the upper left corner. This shows the temporal form of the acoustic particle velocity and a red marker is used to indicate the point in the acoustic

cycle where the measurement is made. The waveform is generated by calculating at each step the acoustic volume velocity averaged over a plane just outside the open end of the tube as described in section 6.3.2. The result of the calculation is interpolated to give the curve shown. Additionally, a reference acoustic particle velocity vector is shown in the upper right corner of each vector map as a visual aid. The locations of the tube terminations are shown in grey and the opening in the tube is shown in white. Two contour maps are also shown to allow the distributions of velocity and vorticity to be easily observed.

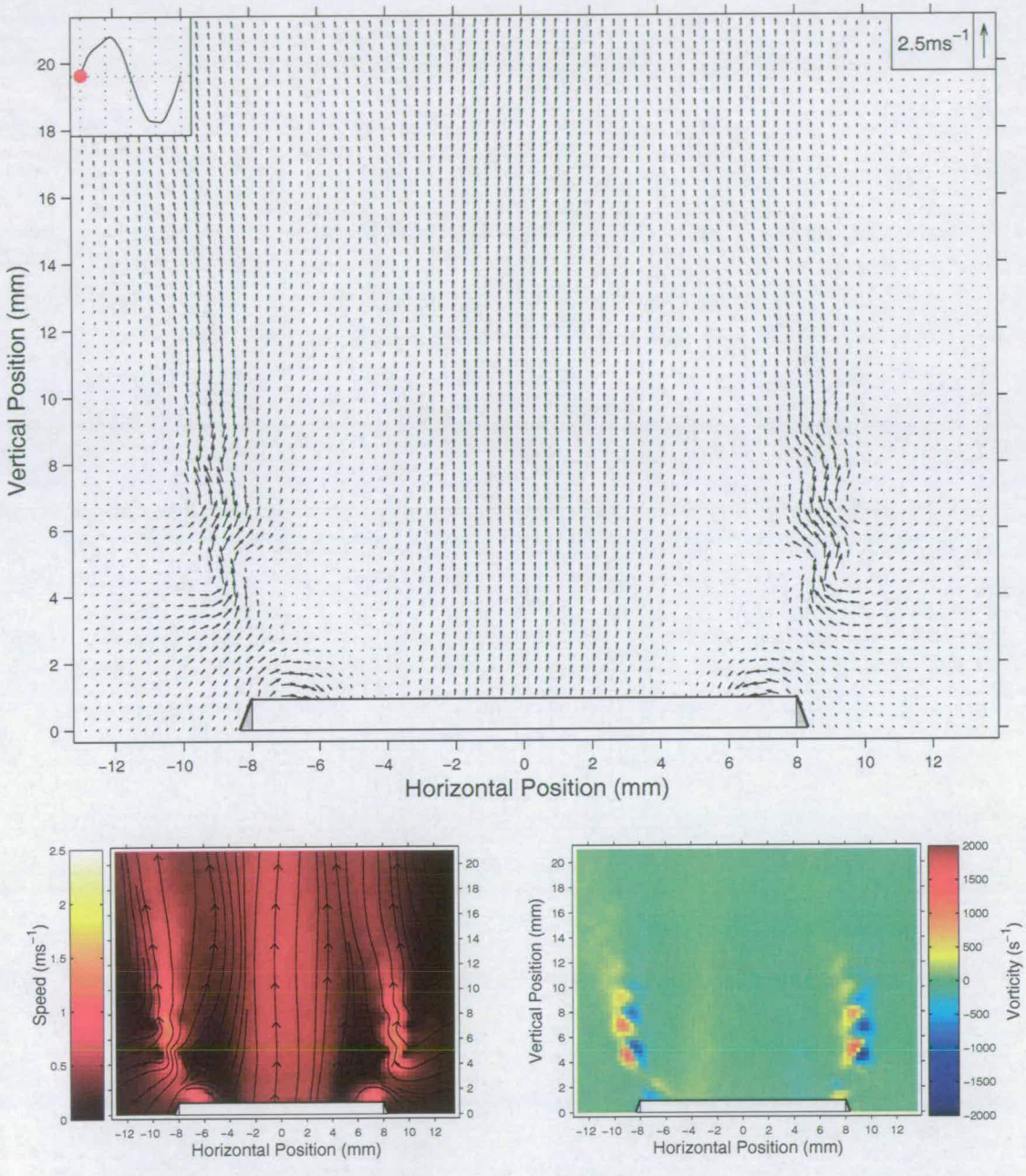
5.3.2 Sharp (Unflanged) termination

The sharp edged termination was designed to mimic an unflanged tube with thin walls (Figure 4.8) as studied experimentally by Disselhorst and van Wijngaarden [Disselhorst 80] and Peters *et al* [Peters *et al* 93]. Because of the special geometry of this termination flow separation at the tube edges was expected to occur at relatively low velocity amplitudes both on inflow and outflow, hastening the onset of non-linearities. As expected, this special case showed departure from linear behaviour at sound pressure levels, measured within the tube at the position of the PCB transducer, as low as 141.9dB with localised vortex structures generated outside the termination on outflow and drawn into the tube on inflow. By 143.8dB the first signs of jet driven streaming are observed with a pulsatile jet on outflow and strong inflow close to the open end leading to the presence of a mean outward jet flow a short distance from the open end. The onset of such non-linear phenomena was most rapid and striking with the sharp edged termination.

Vortex shedding regime 1

Between 145.8dB and 148dB a transition to an unusual flow regime was observed that was not reproduced with any of the other terminations. The PIV results showing this flow regime are in figure 5.7. This regime is characterised by periodic vortex shedding, the presence of a strong outward jet on outflow from the centre of the open end and inflow concentrated to a region close to the tube walls resulting in jet driven streaming. The acoustic particle velocity amplitude is 1.7ms^{-1}. A rough estimation of the mean speed of propagation of the vortices, made by dividing the distance between vortices by the period of the acoustic cycle, yields a value of about 1.15ms^{-1} for a vortex at a distance of 2mm from the tube exit slowing to 0.75ms^{-1} at a distance of 6mm. It should be noted that the curve in the upper left corner of the velocity vector map, showing the temporal form of the acoustic velocity, appears to be essentially sinusoidal.

In this situation it appears that the acoustic particle velocity amplitude is high



(a) Phase step 1. Time = 0.000ms

Figure 5.7: PIV results for the the sharp (unflanged) termination at an SPL of 148dB ($|u_{ac}| = 1.70ms^{-1}$). (Top) PIV velocity vector maps. The upper left hand velocity waveform indicates at which stage of the acoustic cycle the vector map is taken. (Bottom left) Velocity magnitude contours with streamlines. (Bottom right) Vorticity contours. Time is with respect to the trigger point. Grey areas represent the termination wall locations.

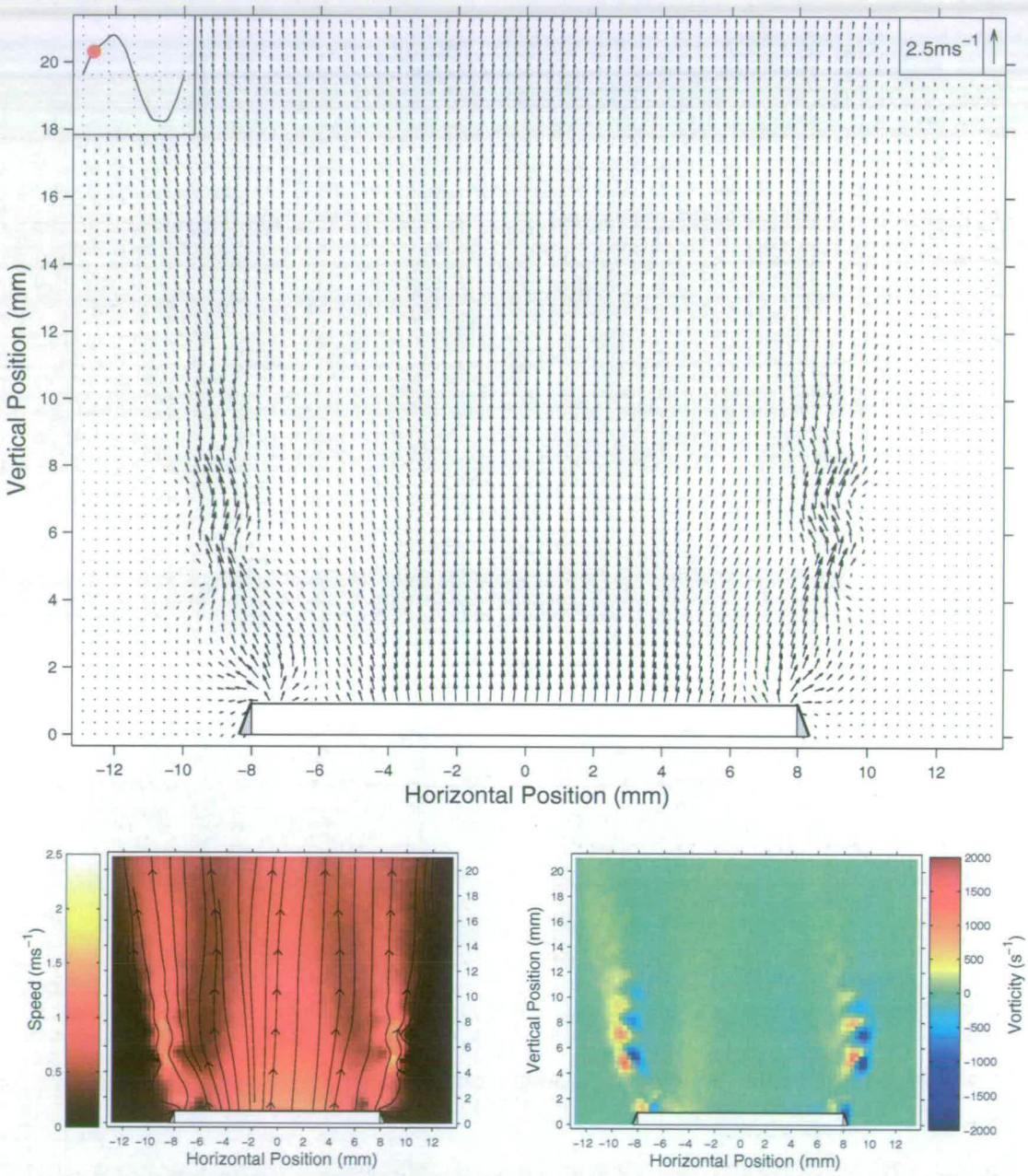


Figure 5.7 continued. (b) Phase step 2. Time = 0.263ms.

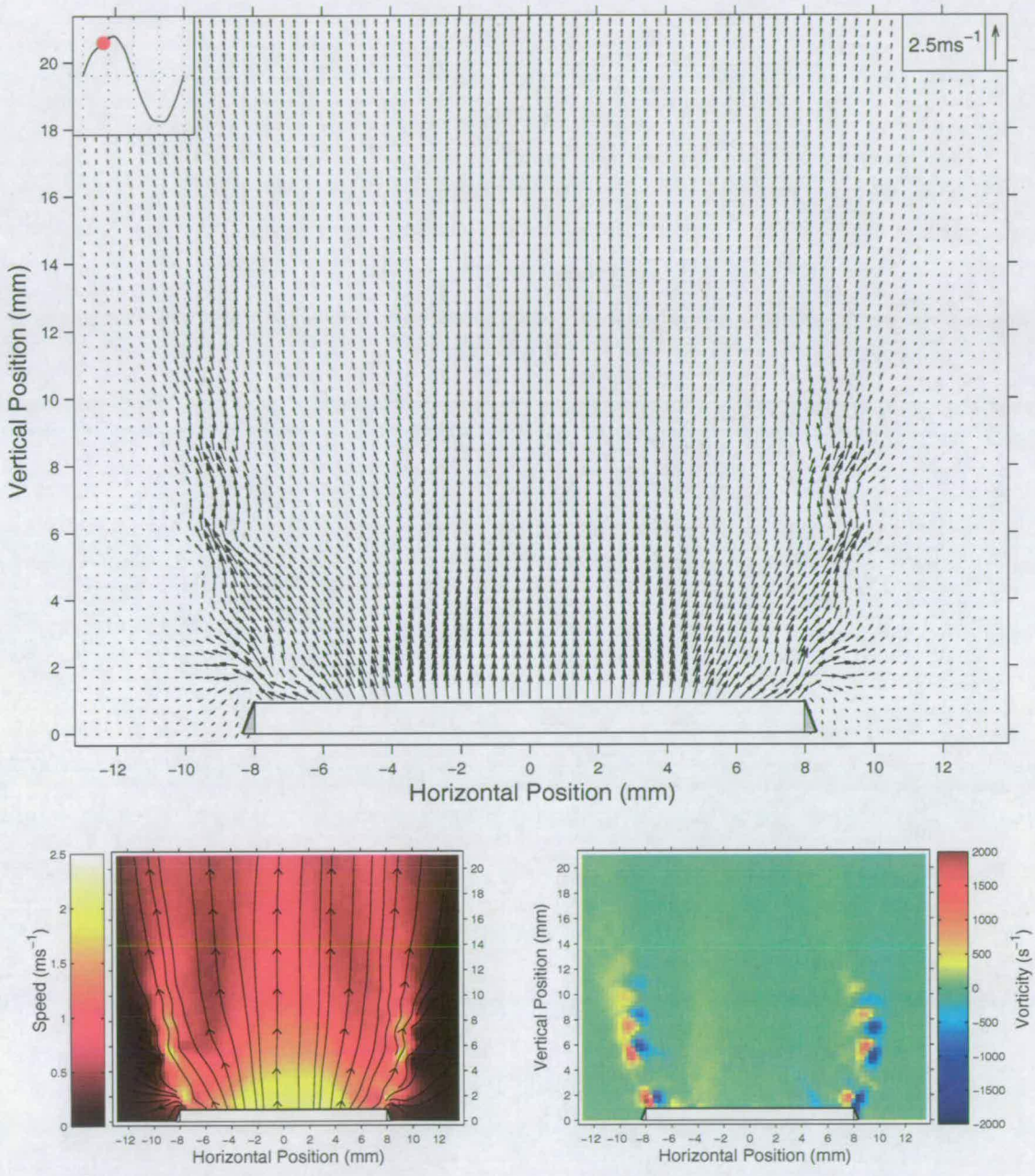


Figure 5.7 continued. (c) Phase step 3. Time = 0.526ms

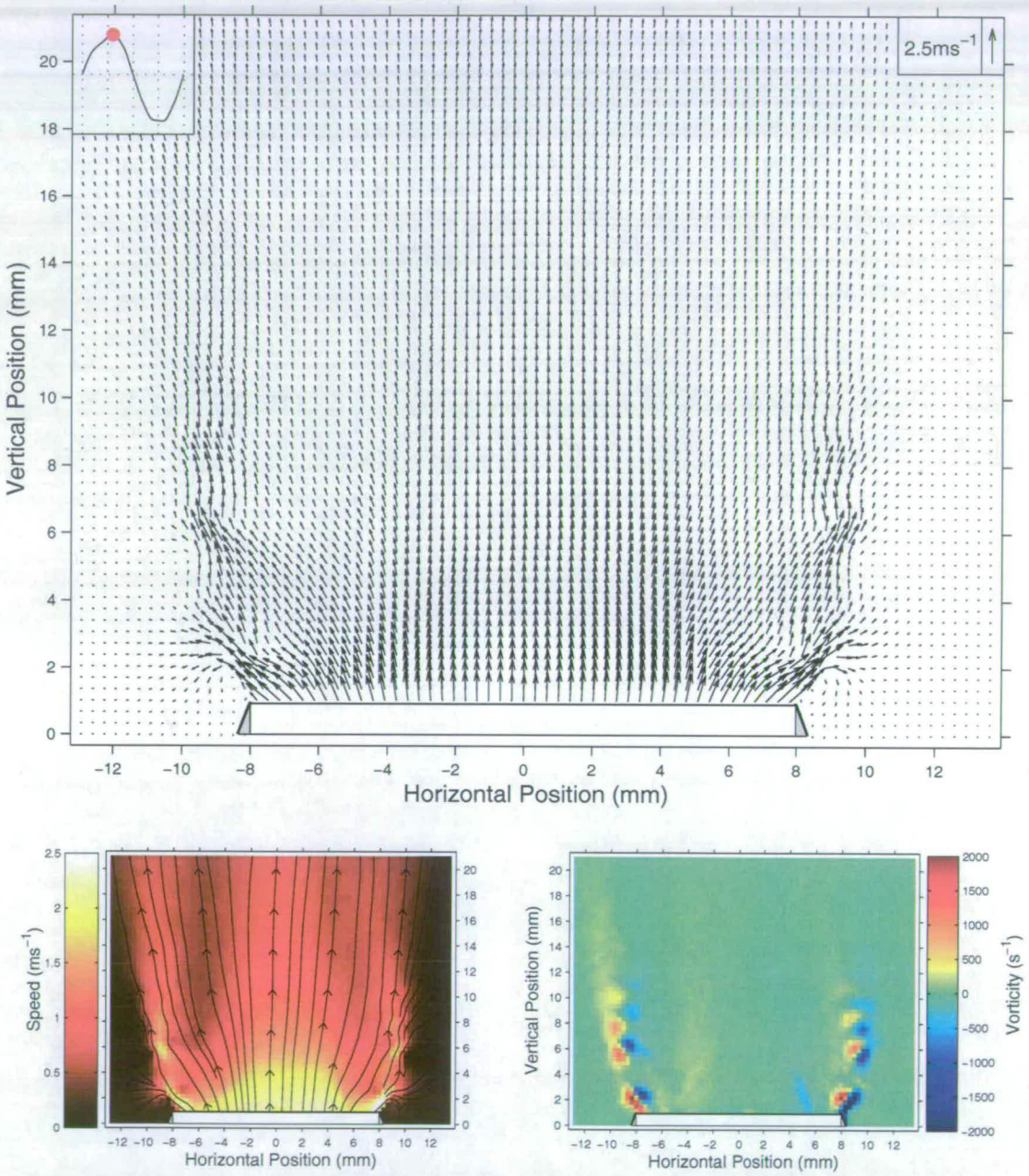


Figure 5.7 continued. (d) Phase step 4. Time = 0.789ms

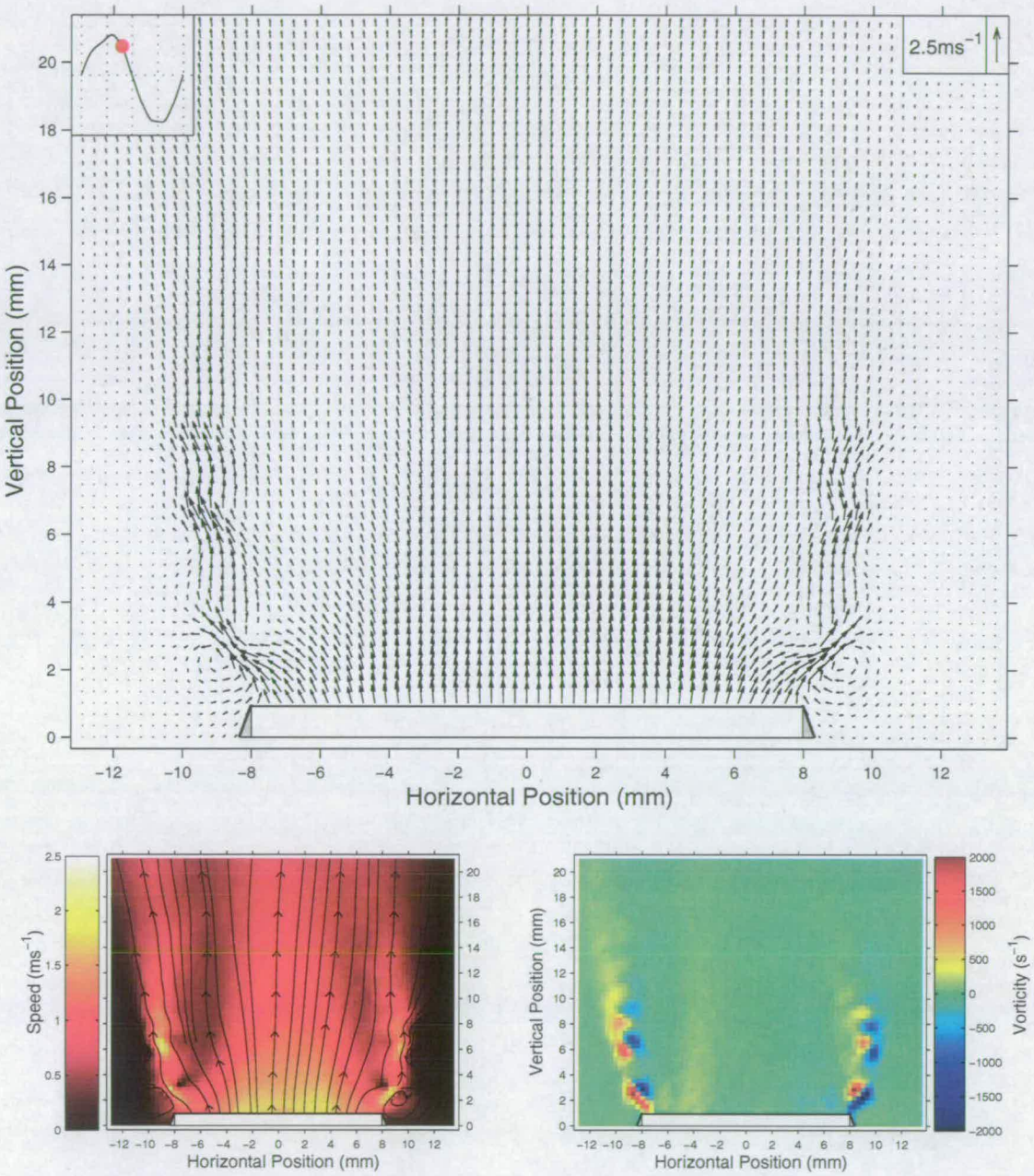


Figure 5.7 continued. (e) Phase step 5. Time = 1.053ms

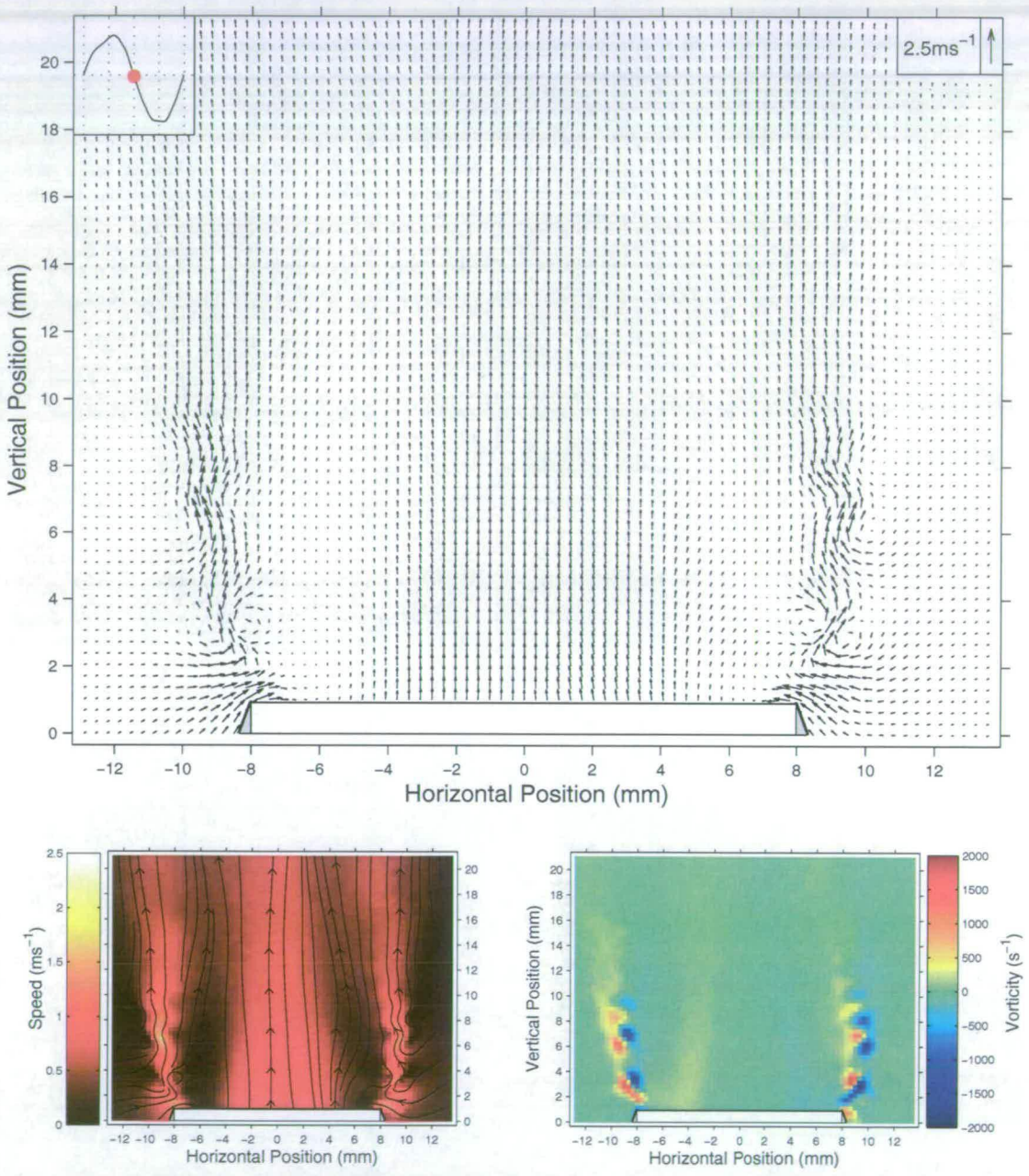


Figure 5.7 continued. (f) Phase step 6. Time = 1.316ms

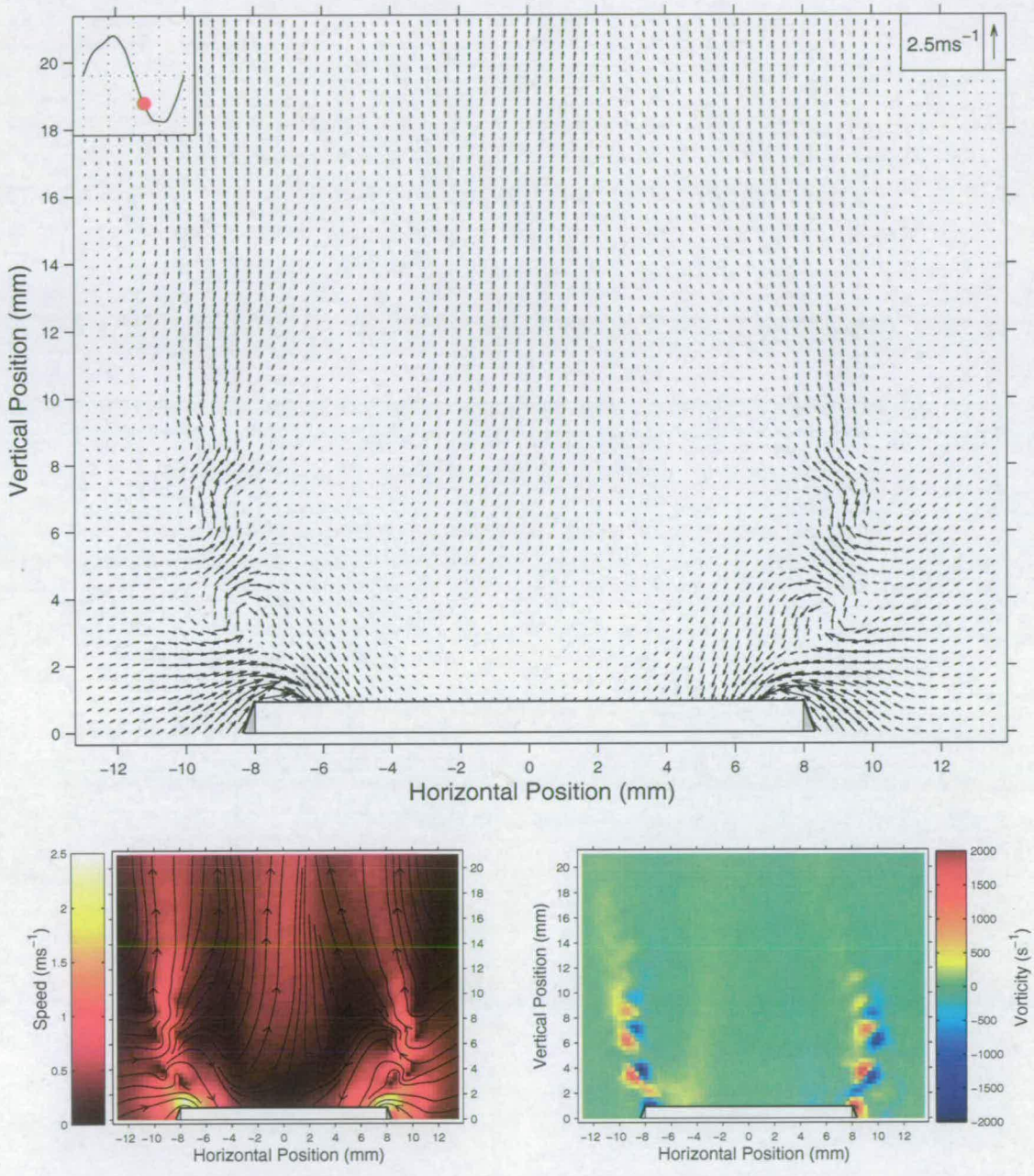


Figure 5.7 continued. (g) Phase step 7. Time = 1.579ms

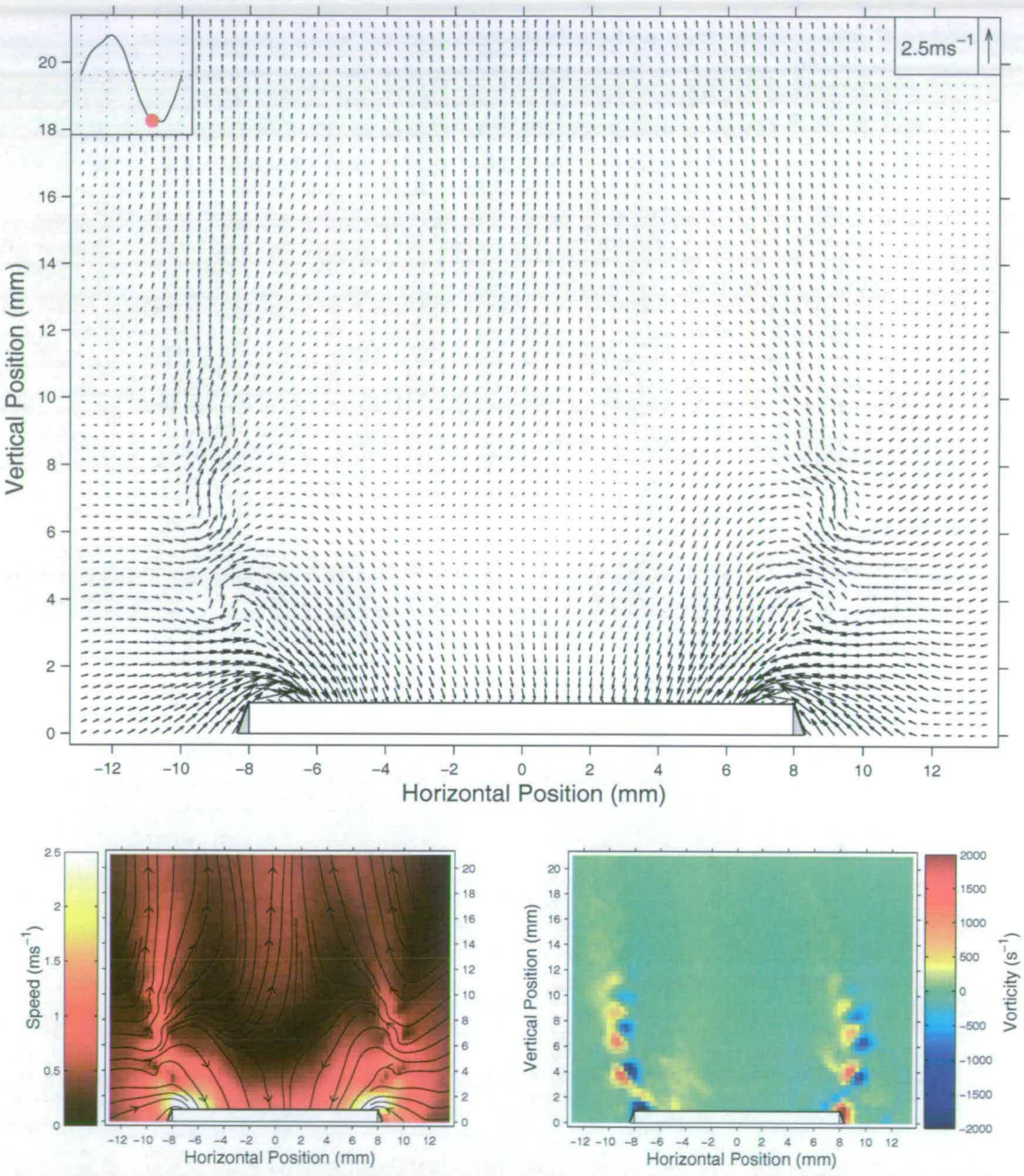


Figure 5.7 continued. (h) Phase step 8. Time = 1.842ms

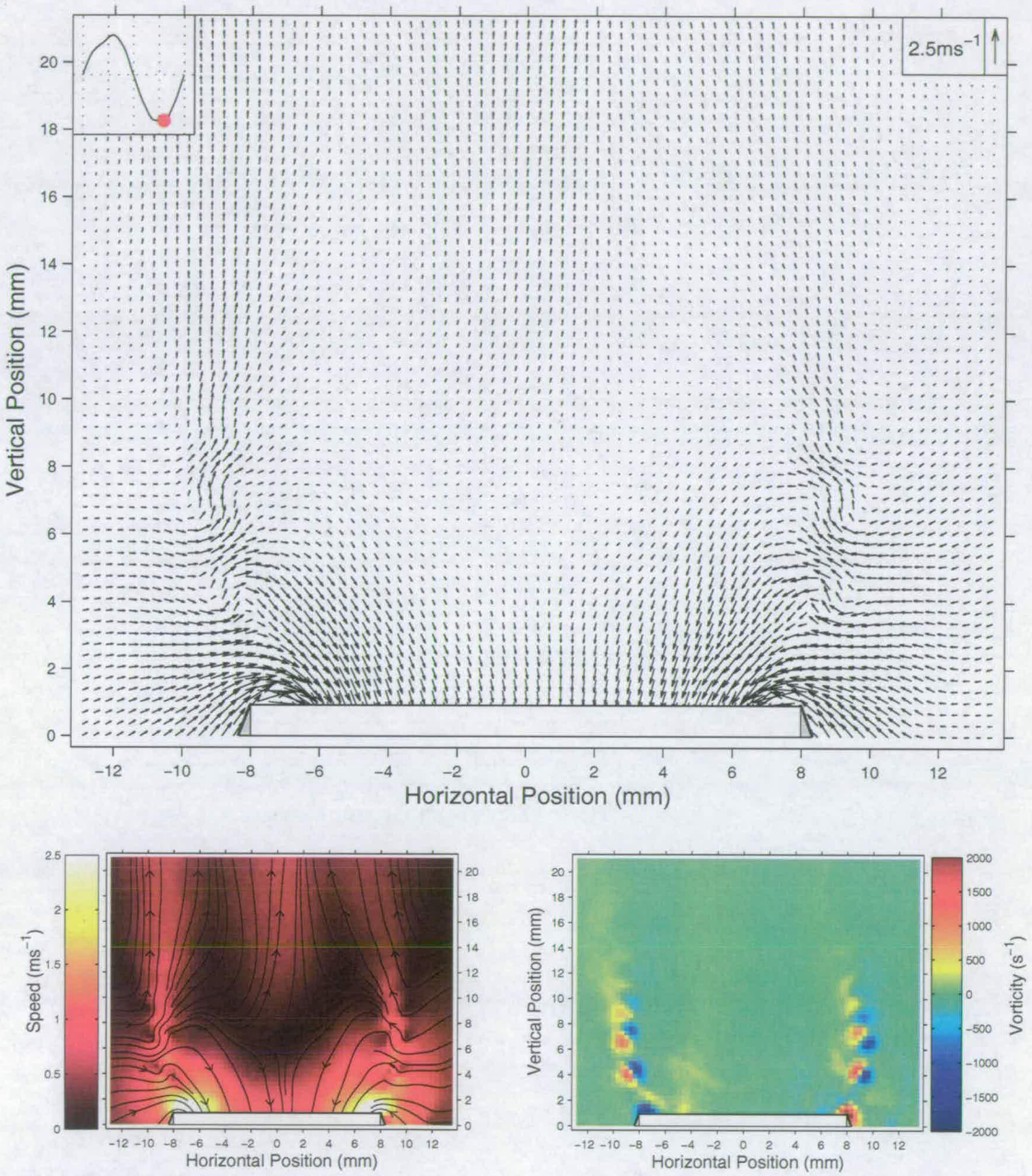


Figure 5.7 continued. (i) Phase step 9. Time = 2.105ms

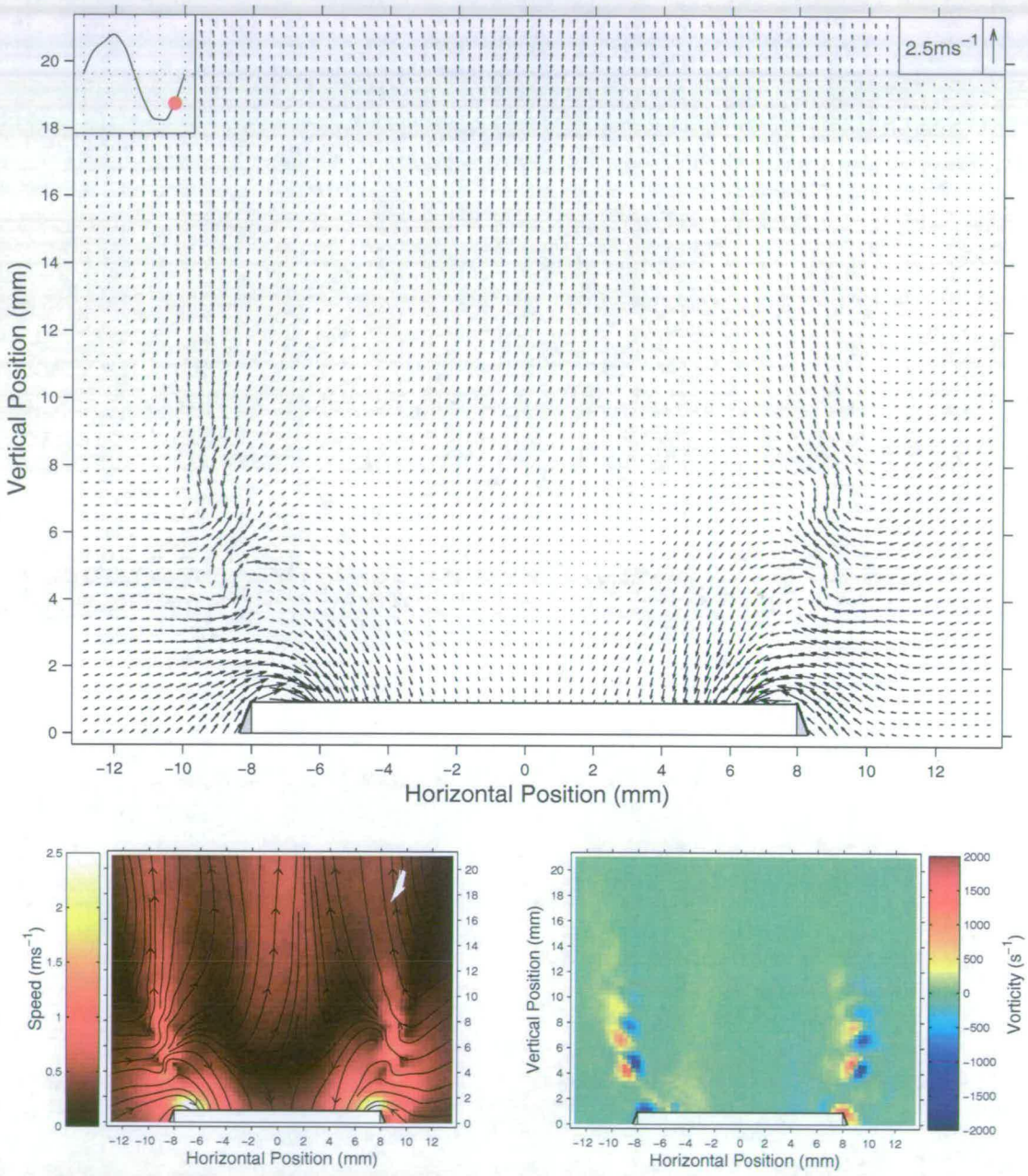


Figure 5.7 continued. (j) Phase step 10. Time = 2.368ms

enough to cause the boundary layer to periodically separate on inflow and then on outflow. This results in the observed shedding of vortex rings (remembering the axisymmetric nature of the flow) with the vortices initially travelling with a velocity comparable to the acoustic particle velocity amplitude and slowing gradually and diffusing as they move downstream. The most striking feature of this flow regime is that, unlike in any of the other measurements made, the vortices shed over as many as four previous periods of the acoustic cycle are discernible. This phenomenon can be explained by considering the previously mentioned fact that only with this termination is boundary layer separation expected to occur at such a low acoustic amplitude that the vortices generated propagate with a low enough speed to remain within the field of view. The low propagation speed also has the effect of reducing the rate of dissipation of vorticity, allowing the vortex structures to remain intact for longer.

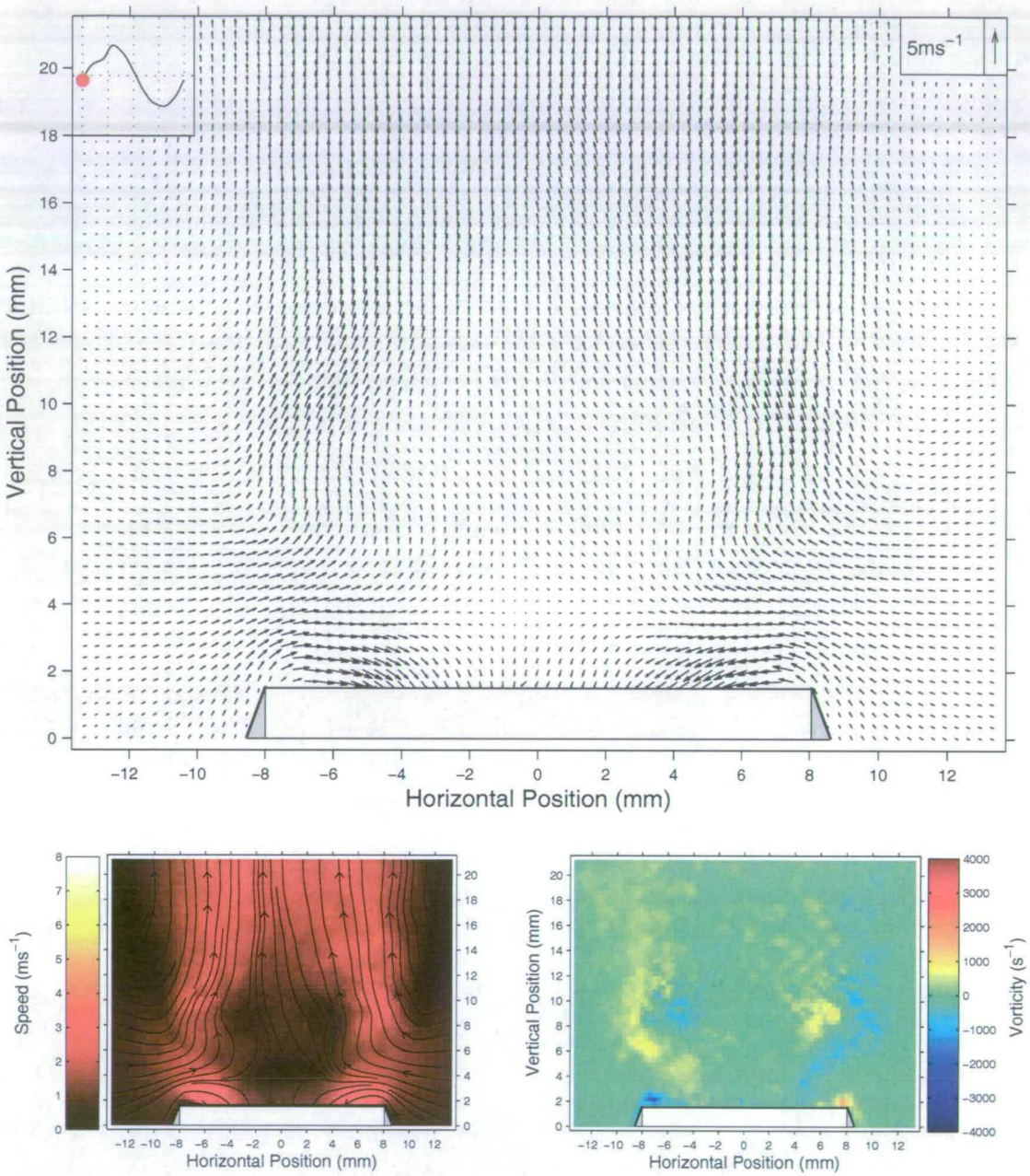
Vortex shedding regime 2

Above 148dB a second flow regime is observed in which vortex rings from previous acoustic cycles are rapidly diffused by the action of jet streaming. One such regime is shown in figure 5.8 at a sound pressure level of 157.2dB. Pairs of vortex ring structures are shed on the outflow part of the cycle. Flow separation occurs at the sharp edge on inflow and a vortex ring with circulation directed into the open end is generated just inside the termination [1]. On outflow the high velocity close to the tube edges causes further flow separation and a vortex ring with circulation directed out of the tube is generated. The vortex ring generated on inflow is expelled as the counter-rotating vortex ring is shed. The vortex ring pairs propagate only a short distance away from the open end with a self induced velocity before being rapidly diffused. By the time the next acoustic cycle begins, only a remnant of the original vortex structures can be discerned in the field of view of the vorticity contour maps.

The velocity magnitude contours clearly show the presence of a localised pulsed synthetic (zero net mass flux) jet in the narrow region between the counter rotating vortex rings as they are shed from the sharp edges in phase steps 3 to 5 (figures 5.8(c)-(e)). This feature can also be seen in the corresponding velocity vector maps. The combined effect of the two counter rotating vortex rings appears to be to create this pulsed jet which momentarily propels the vortex ring pair away from the tube edge, after which the vortices slow down and diffuse as the inflow part of the cycle begins.

There is a slight distortion of the waveform in the upper left corner of the PIV velocity vector maps just prior to maximum outflow. This may be due to an additional

[1] It should be noted that although what happens inside the tube is not directly observable in these experiments, the presence of vortices inside the tube can be inferred by what is subsequently observed on outflow.



(a) Phase step 1. Time = 0.000ms

Figure 5.8: PIV results for the the sharp (unflanged) termination at an SPL of 157.2dB ($|u_{ac}| = 4.95ms^{-1}$). (Top) PIV velocity vector maps. The upper left hand velocity waveform indicates at which stage of the acoustic cycle the vector map is taken. (Bottom left) Velocity magnitude contours with streamlines. (Bottom right) Vorticity contours. Time is with respect to the trigger point. Grey areas represent the termination wall locations.

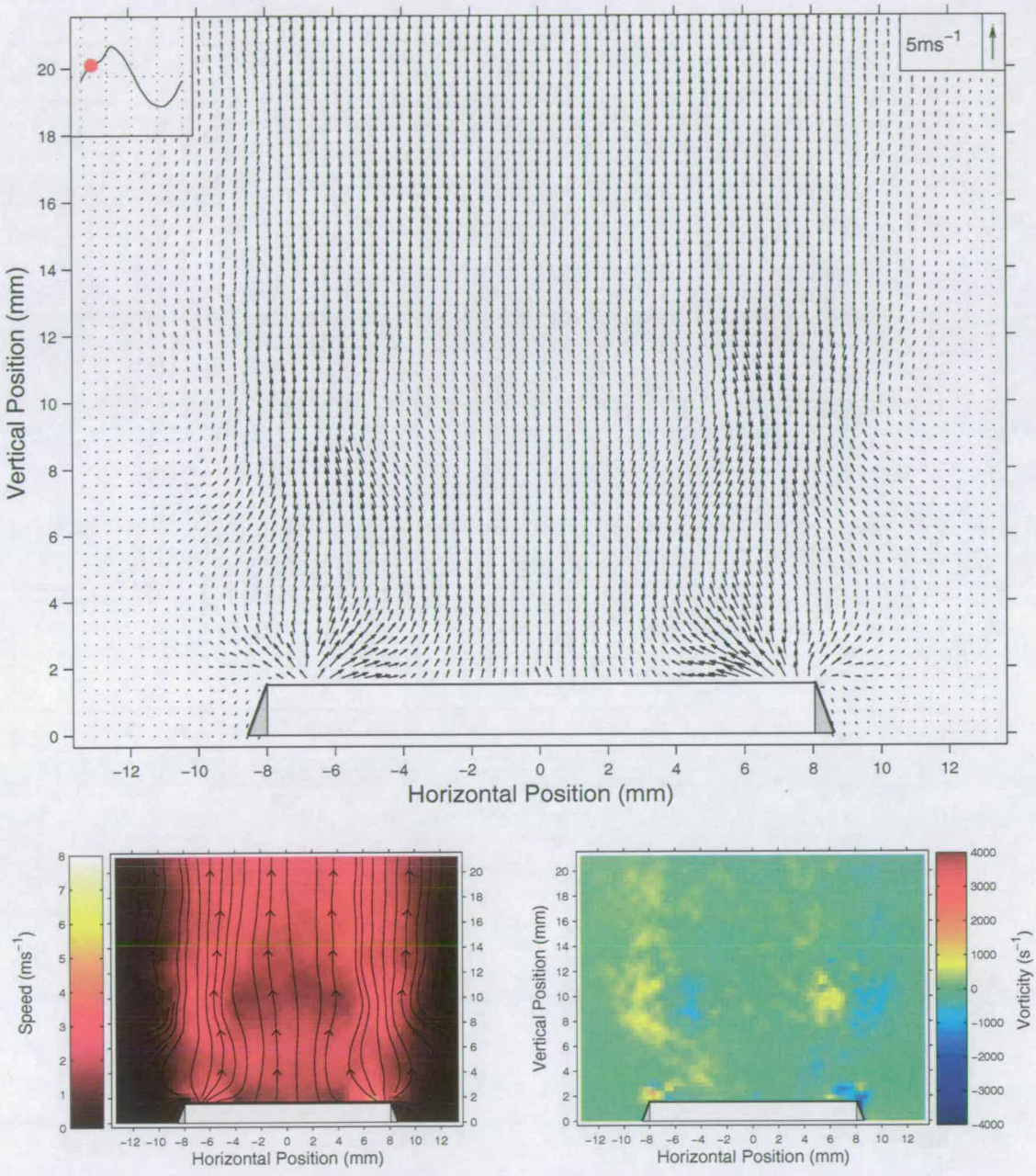


Figure 5.8 continued. (b) Phase step 2. Time = 0.263ms.

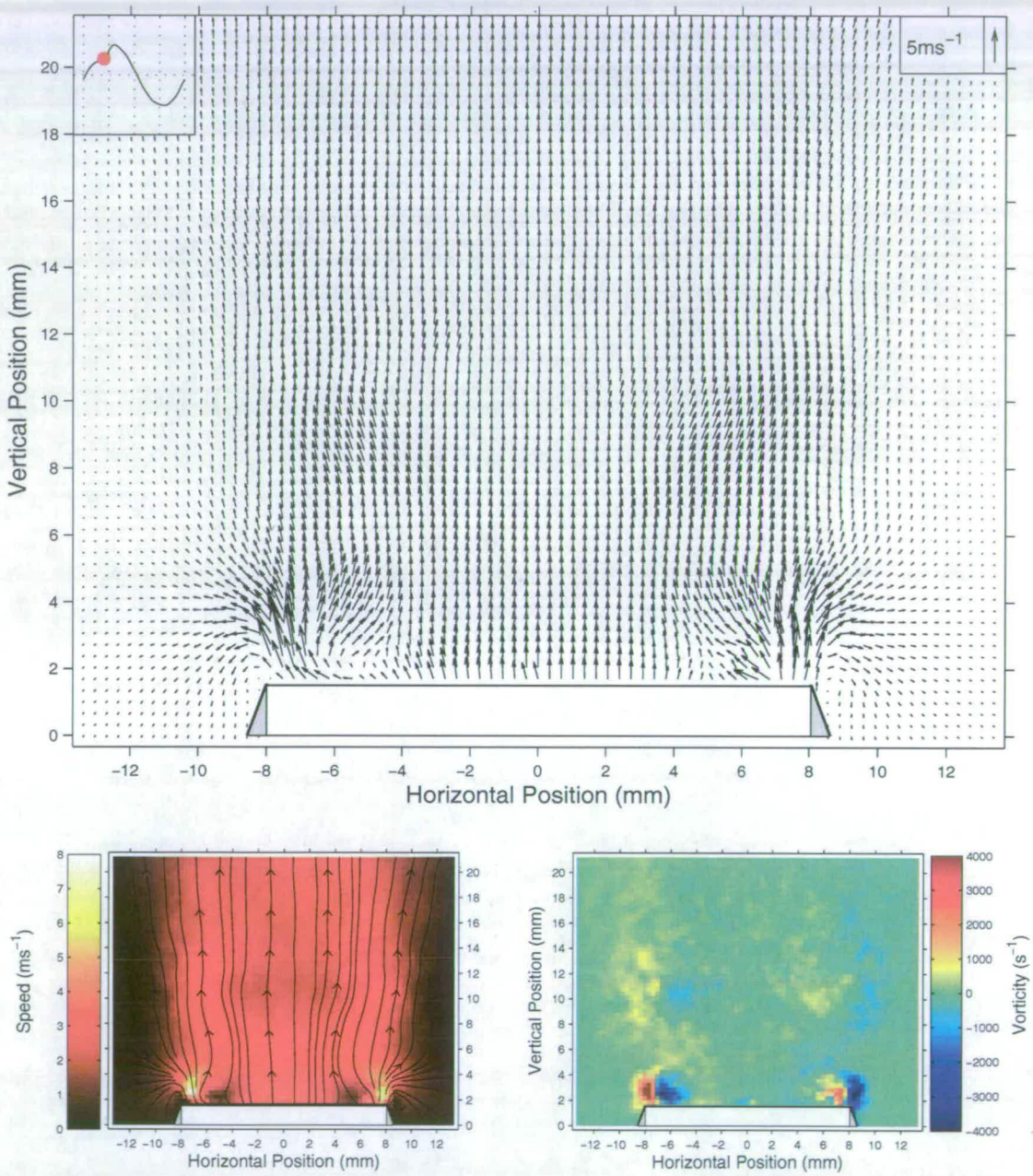


Figure 5.8 continued. (c) Phase step 3. Time = 0.526ms

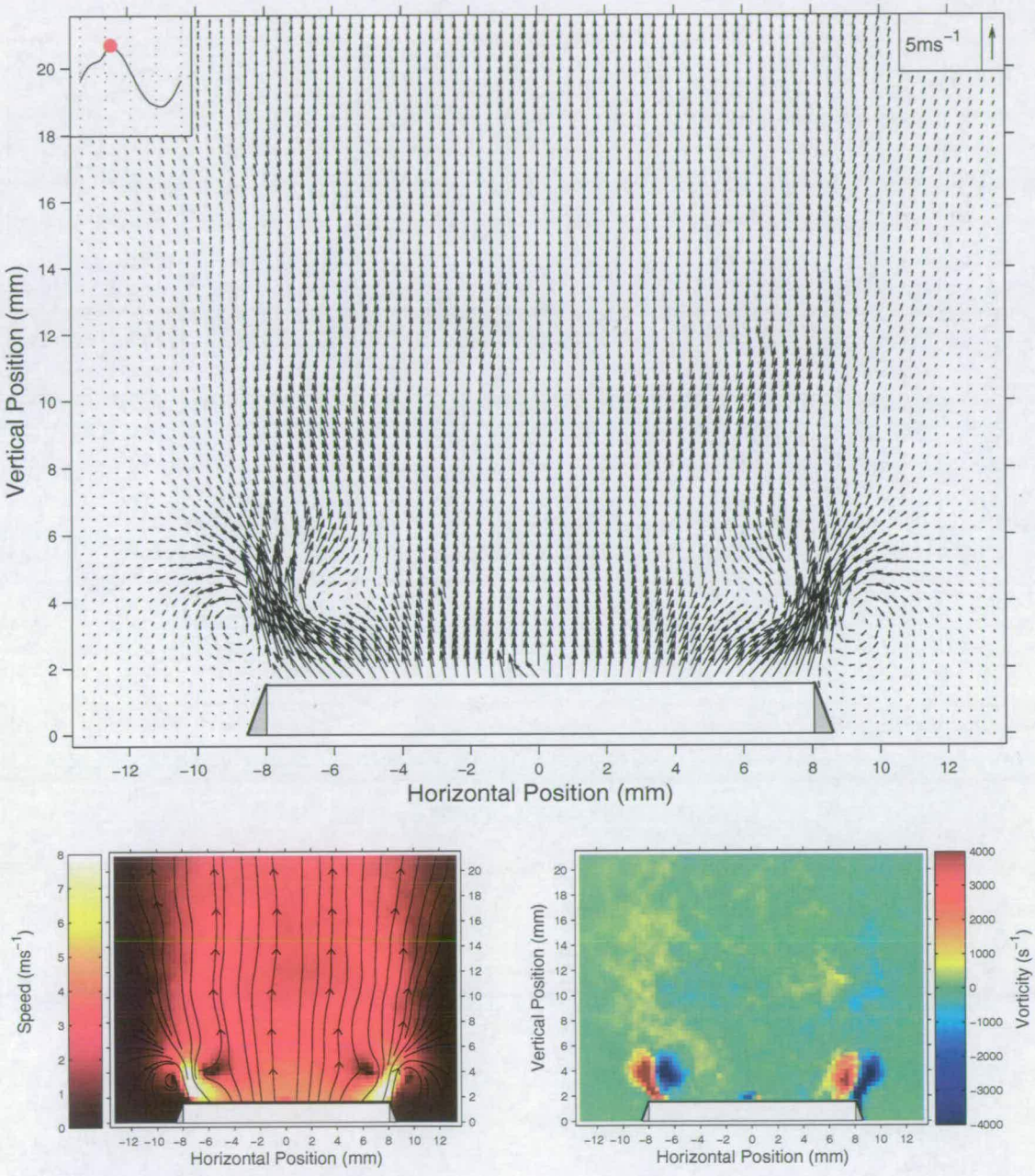


Figure 5.8 continued. (d) Phase step 4. Time = 0.789ms

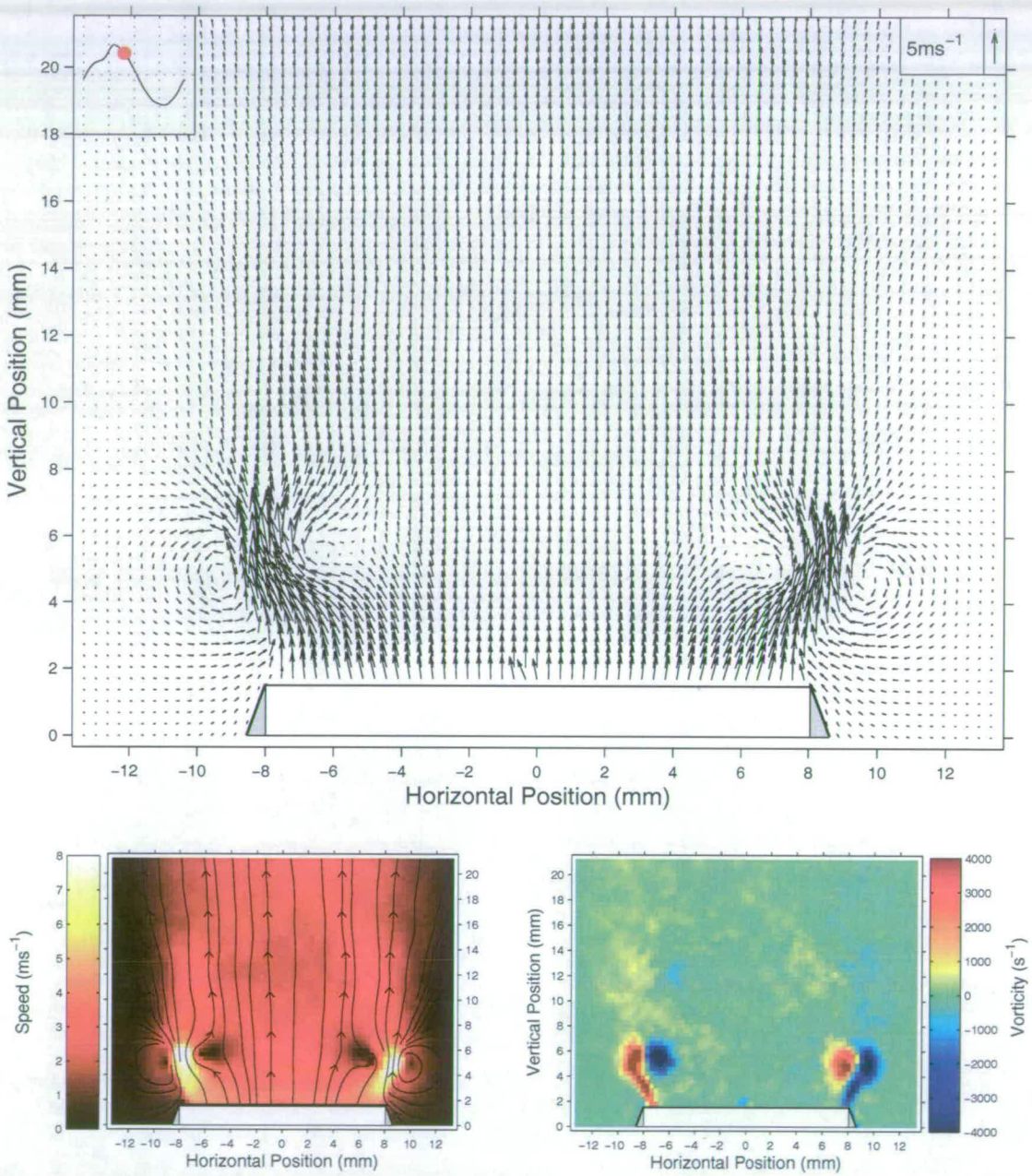


Figure 5.8 continued. (e) Phase step 5. Time = 1.053ms

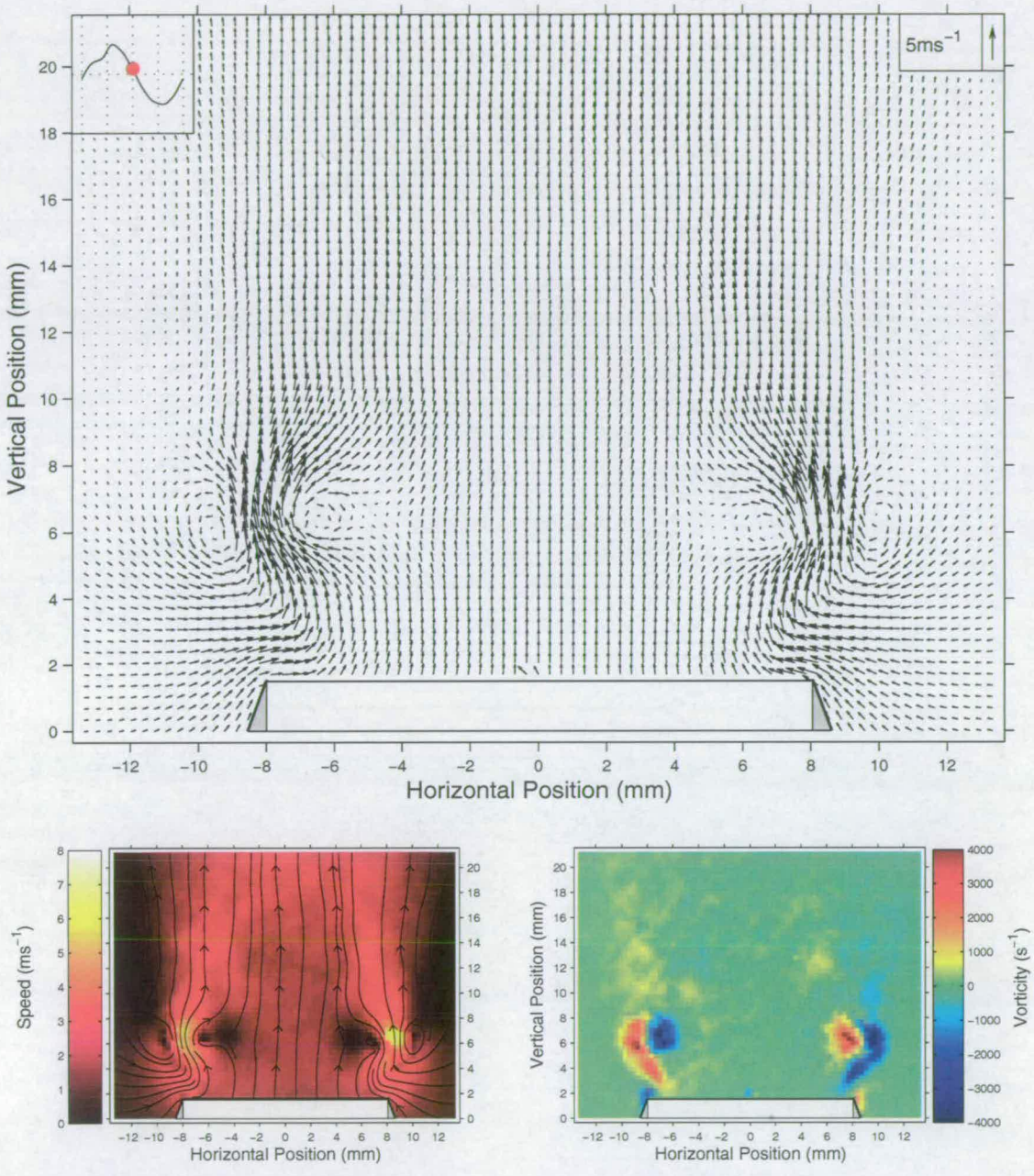


Figure 5.8 continued. (f) Phase step 6. Time = 1.316ms

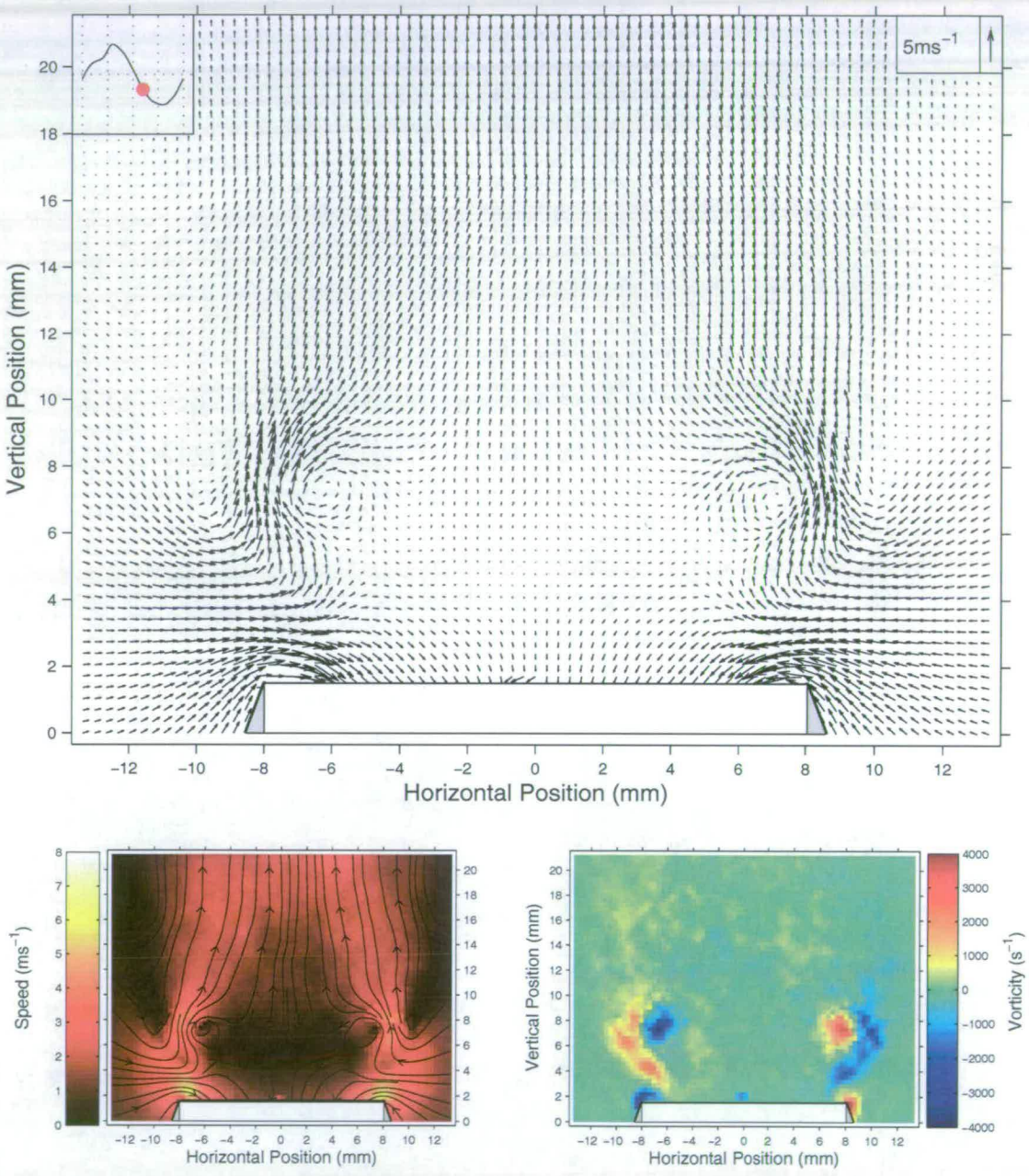


Figure 5.8 continued. (g) Phase step 7. Time = 1.579ms

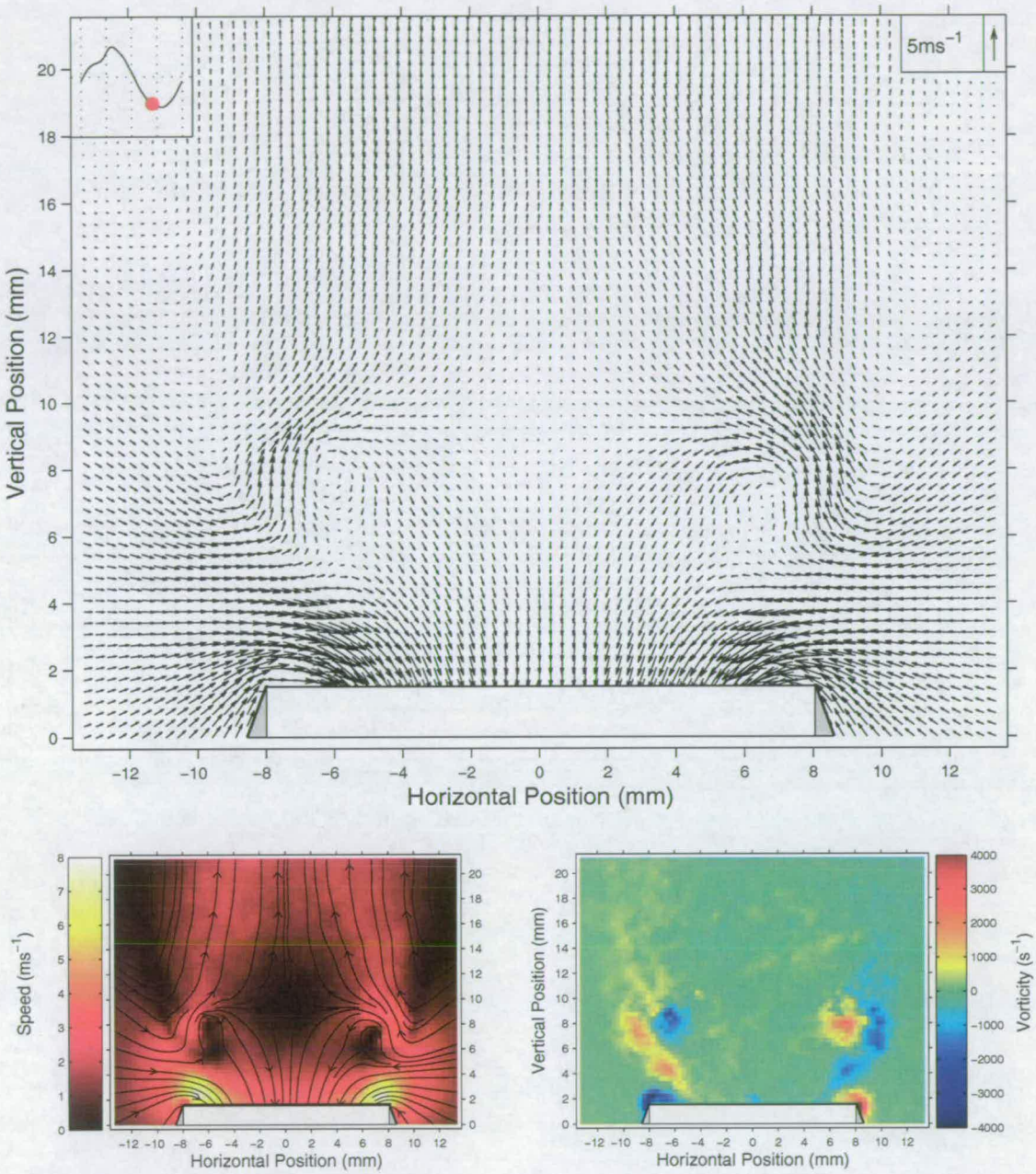


Figure 5.8 continued. (h) Phase step 8. Time = 1.842ms

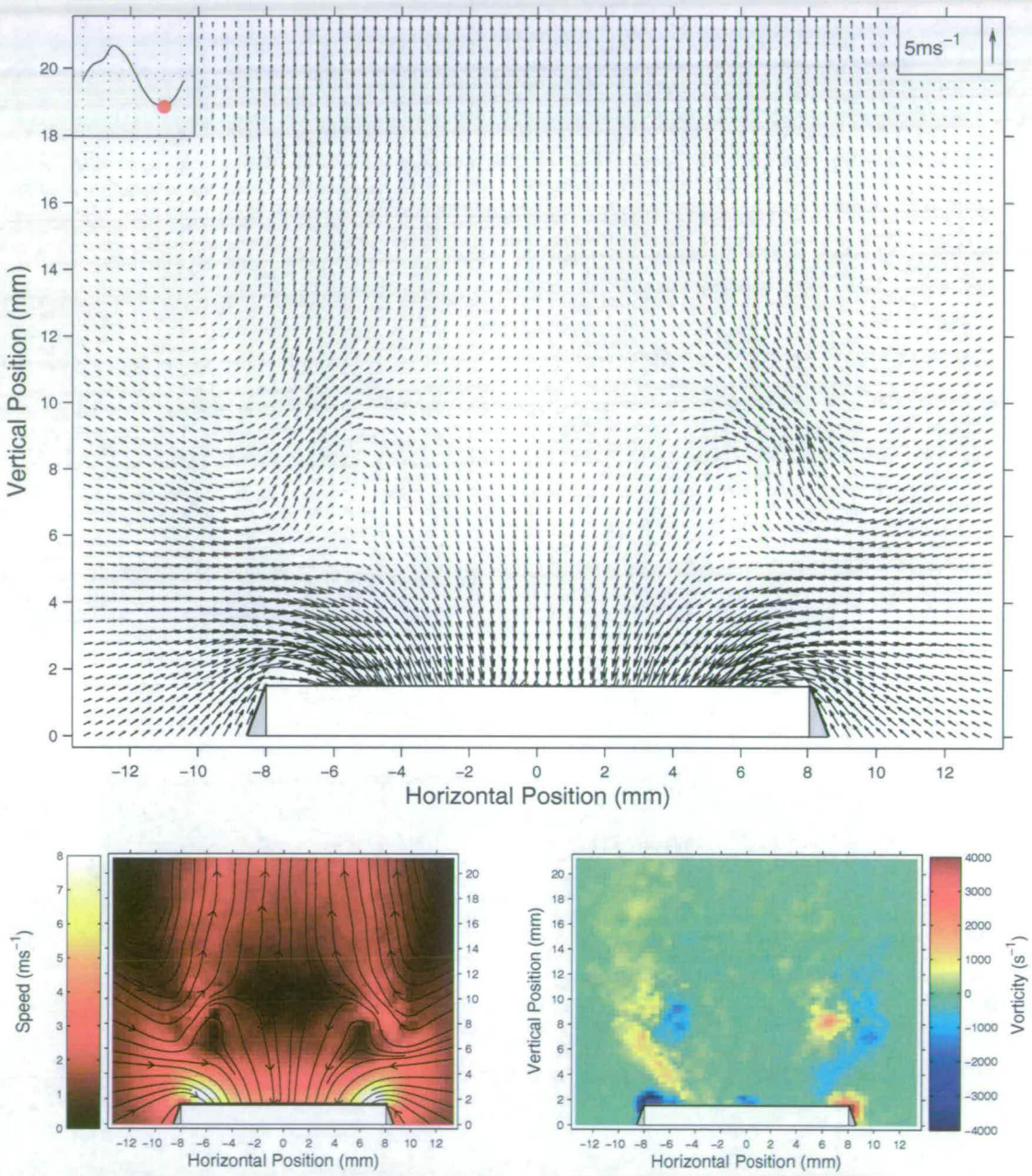


Figure 5.8 continued. (i) Phase step 9. Time = 2.105ms

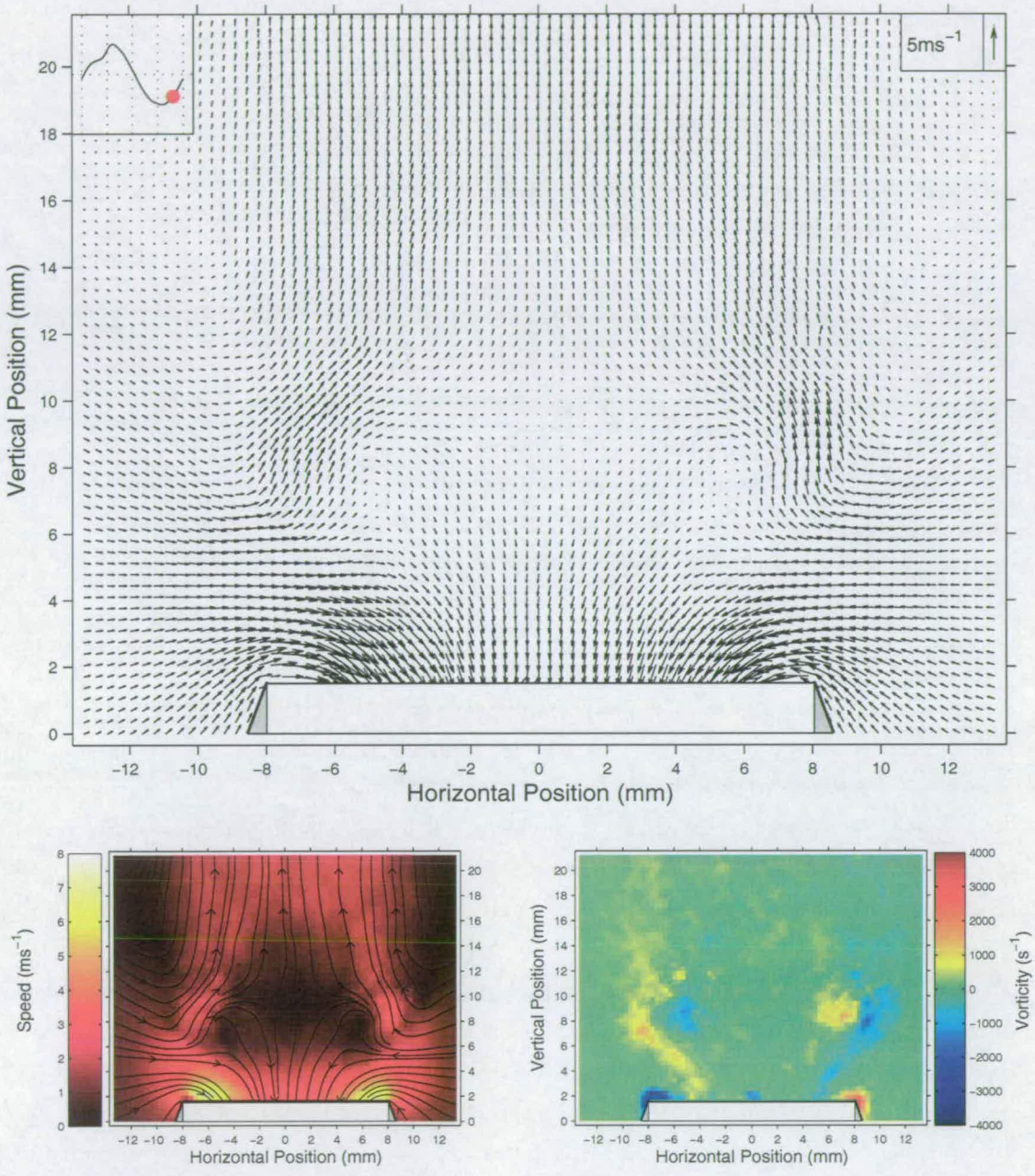


Figure 5.8 continued. (j) Phase step 10. Time = 2.368ms

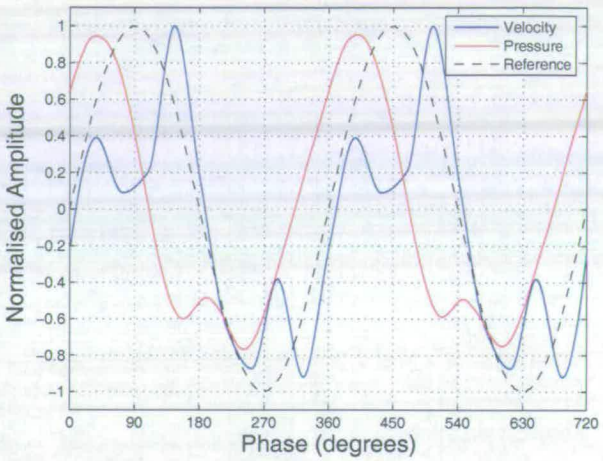


Figure 5.9: Normalised velocity (blue) and pressure signals (red) measured at the open end open end of the tube for the sharp edged termination at 168dB. Also shown for comparison is the reference signal (- - -) synchronised with the trigger source

drag force caused by the inward circulating vortex ring generated on inflow.

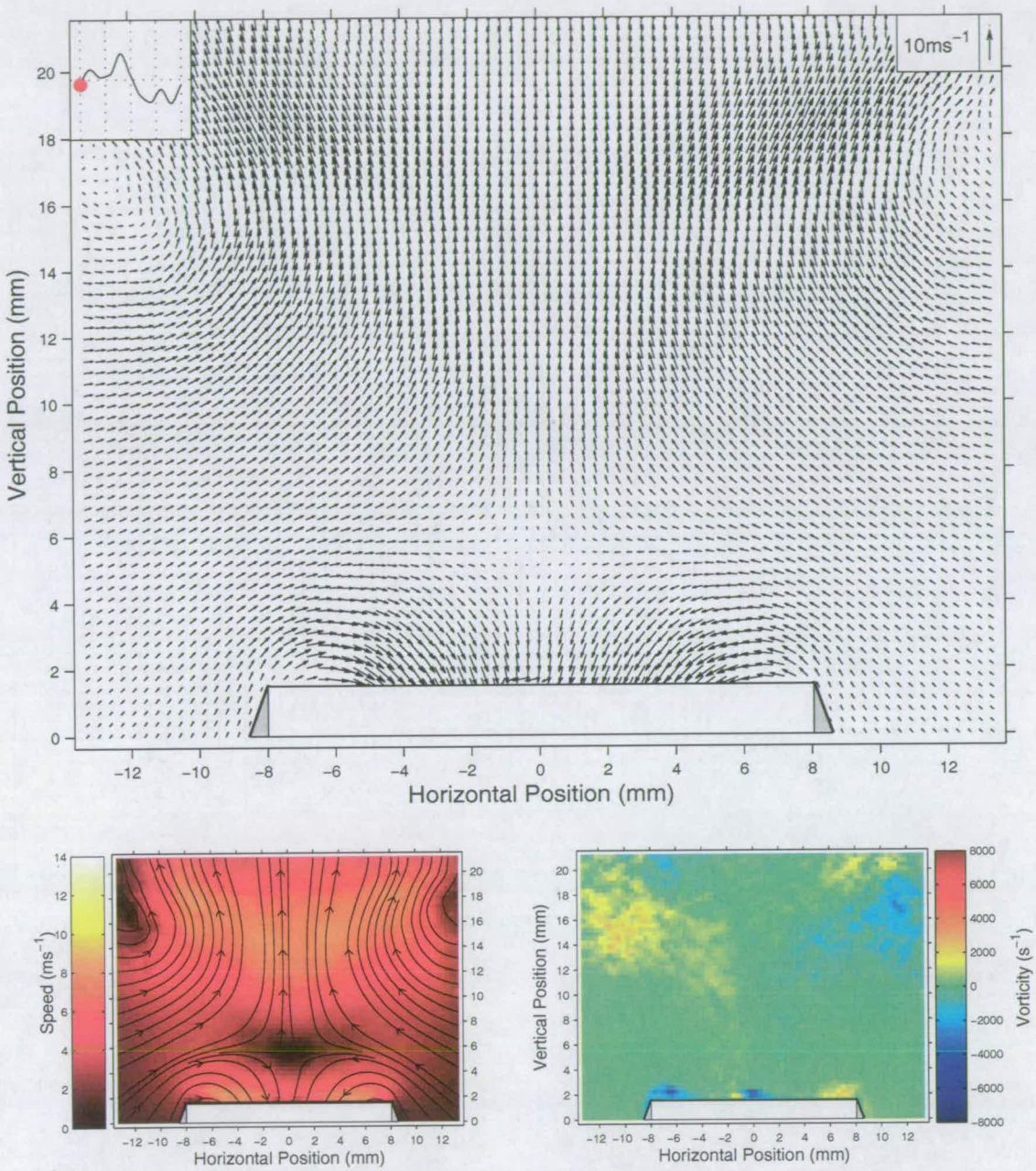
Vortex shedding regime 3

A third flow regime is observed for the sharp edged termination at 168dB, the highest sound pressure level measured, and can be seen in figure 5.10. It may be that this is just an extreme, high amplitude extension of the second vortex shedding regime already discussed, but there are some notable features of the flow that seem to require a separate categorisation.

Firstly the presence of a free-jet (an area of high velocity bounded by a separated shear layer) is observed close to the open end. This can be seen especially clearly at phase step 5 (figure 5.10(e)). A separated shear layer is indicated by the linear regions of high vorticity at the open end in the vorticity contour map. The enclosed free-jet is seen in both the velocity vector map and the velocity magnitude contour map.

The second notable feature is that at this high sound level the shed vortex rings are no longer in stable counter-rotating pairs. There is some initial weak vorticity just as the flow turns outward. The shear layer then separates from the tube edges, as already discussed, and begins to roll up as the inflow part of the cycle commences. As the shear layer rolls up, there is only very weak counter-rotation to this outward circulating vorticity. This results in a single strong outward synthetic jet along the tube axis. Vorticity is diffused very quickly by the presence of this jet.

The velocity waveform for the sharp edged termination at 168dB is shown in blue



(a) Phase step 1. Time = 0.000ms

Figure 5.10: PIV results for the the sharp (unflanged) termination at an SPL of 168dB ($|u_{ac}| = 17.2ms^{-1}$). (Top) PIV velocity vector maps. The upper left hand velocity waveform indicates at which stage of the acoustic cycle the vector map is taken. (Bottom left) Velocity magnitude contours with streamlines. (Bottom right) Vorticity contours. Time is with respect to the trigger point. Grey areas represent the termination wall locations.

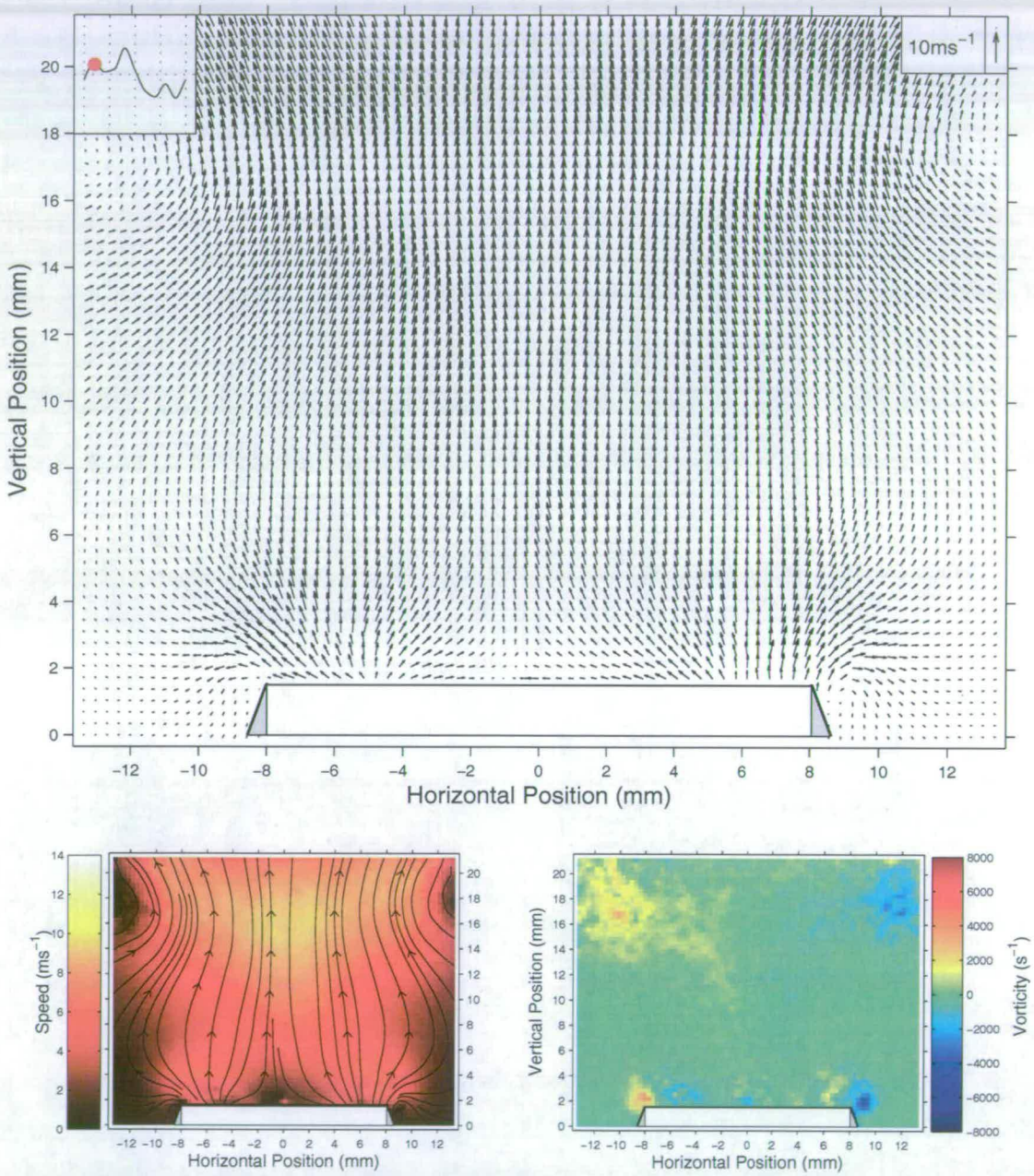


Figure 5.10 continued. (b) Phase step 2. Time = 0.263ms.

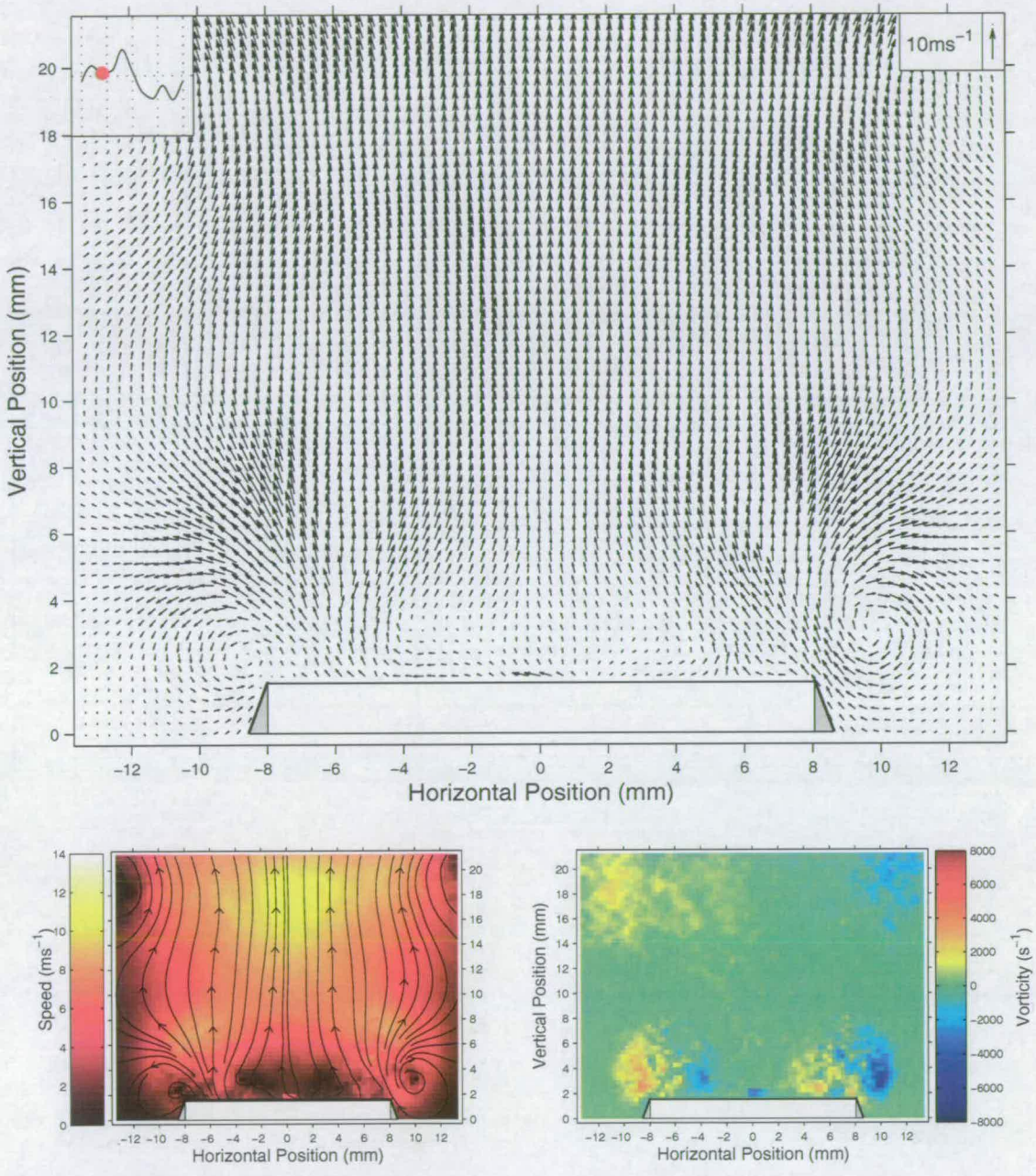


Figure 5.10 continued. (c) Phase step 3. Time = 0.526ms

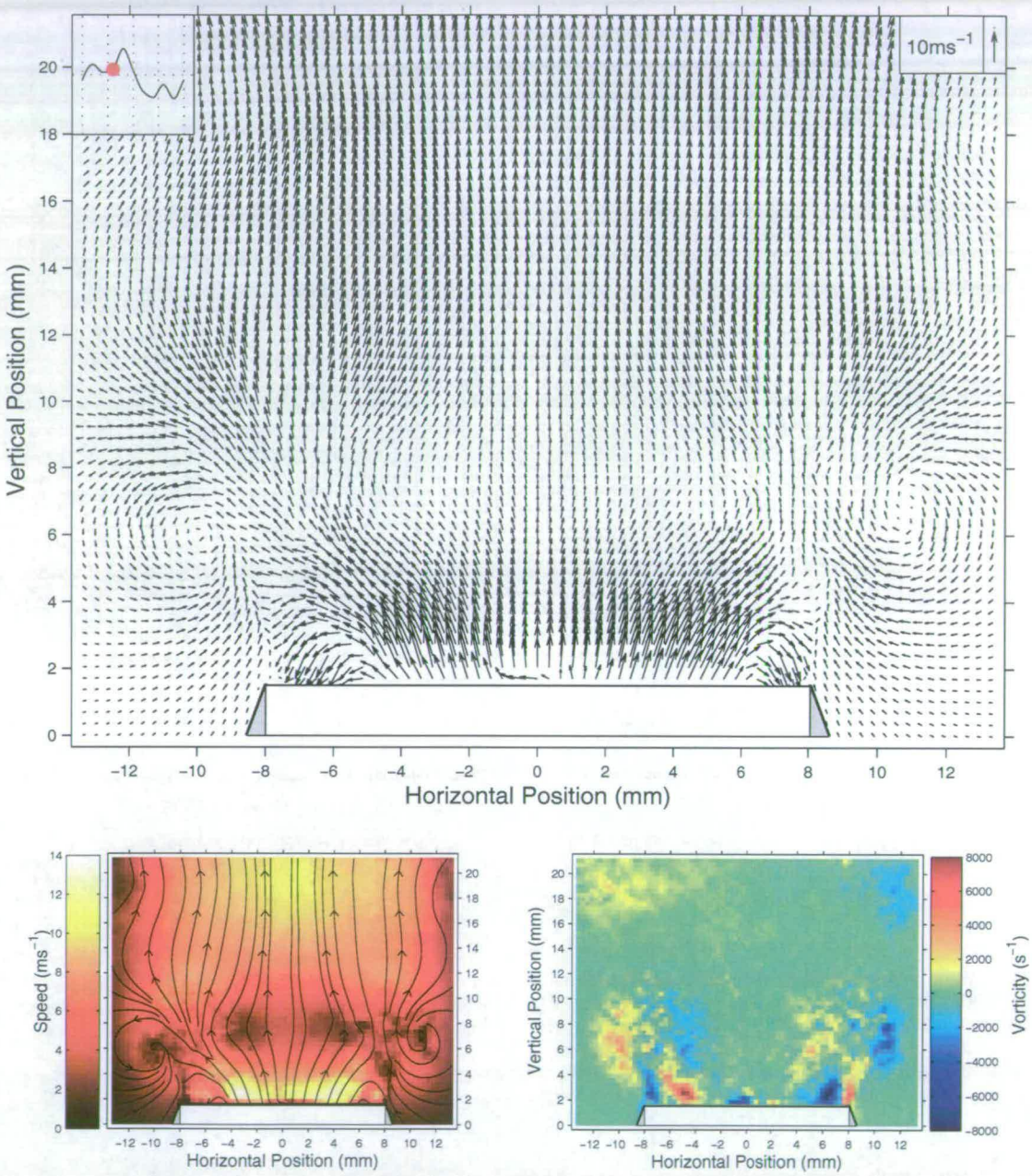


Figure 5.10 continued. (d) Phase step 4. Time = 0.789ms

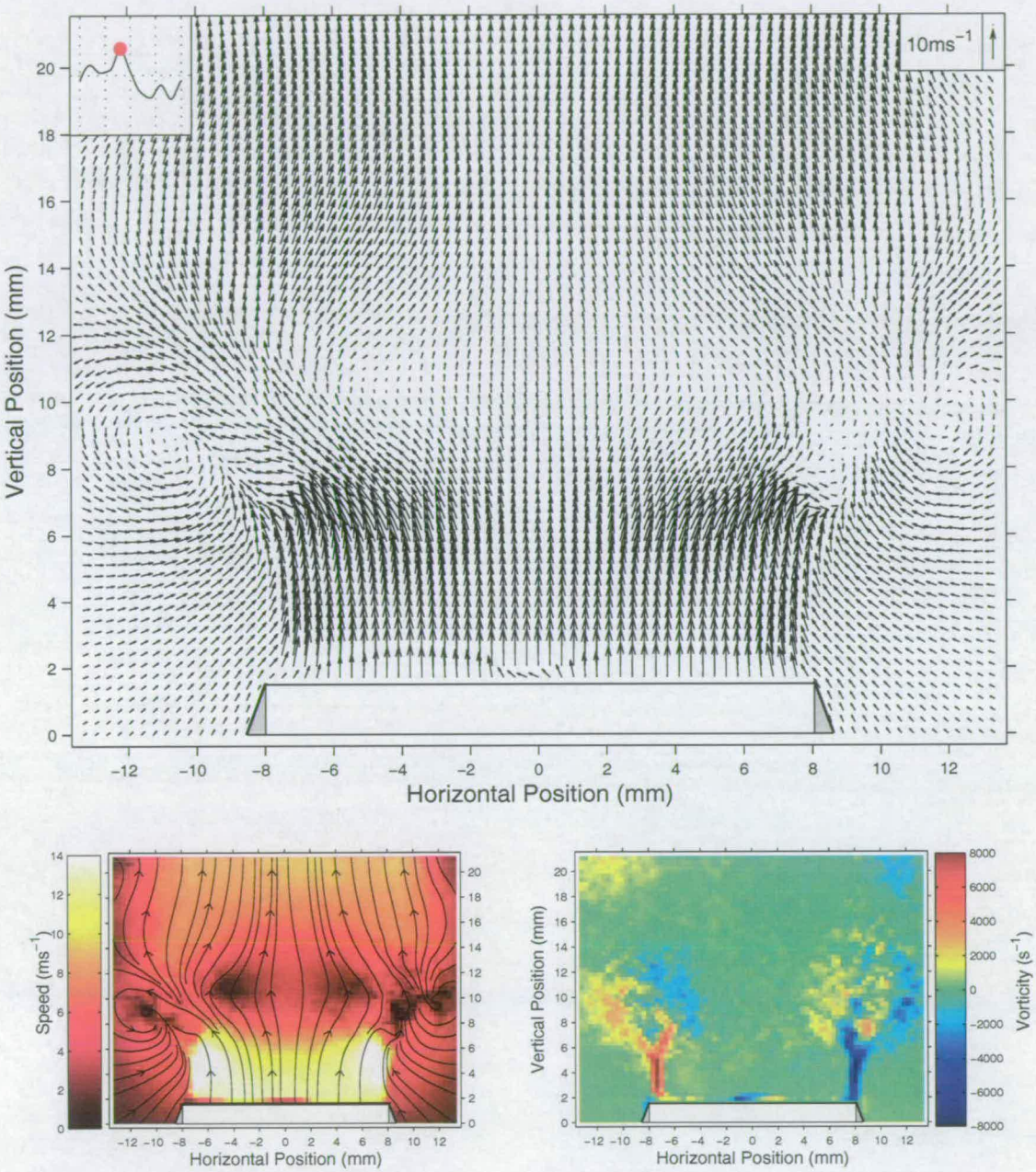


Figure 5.10 continued. (e) Phase step 5. Time = 1.053ms

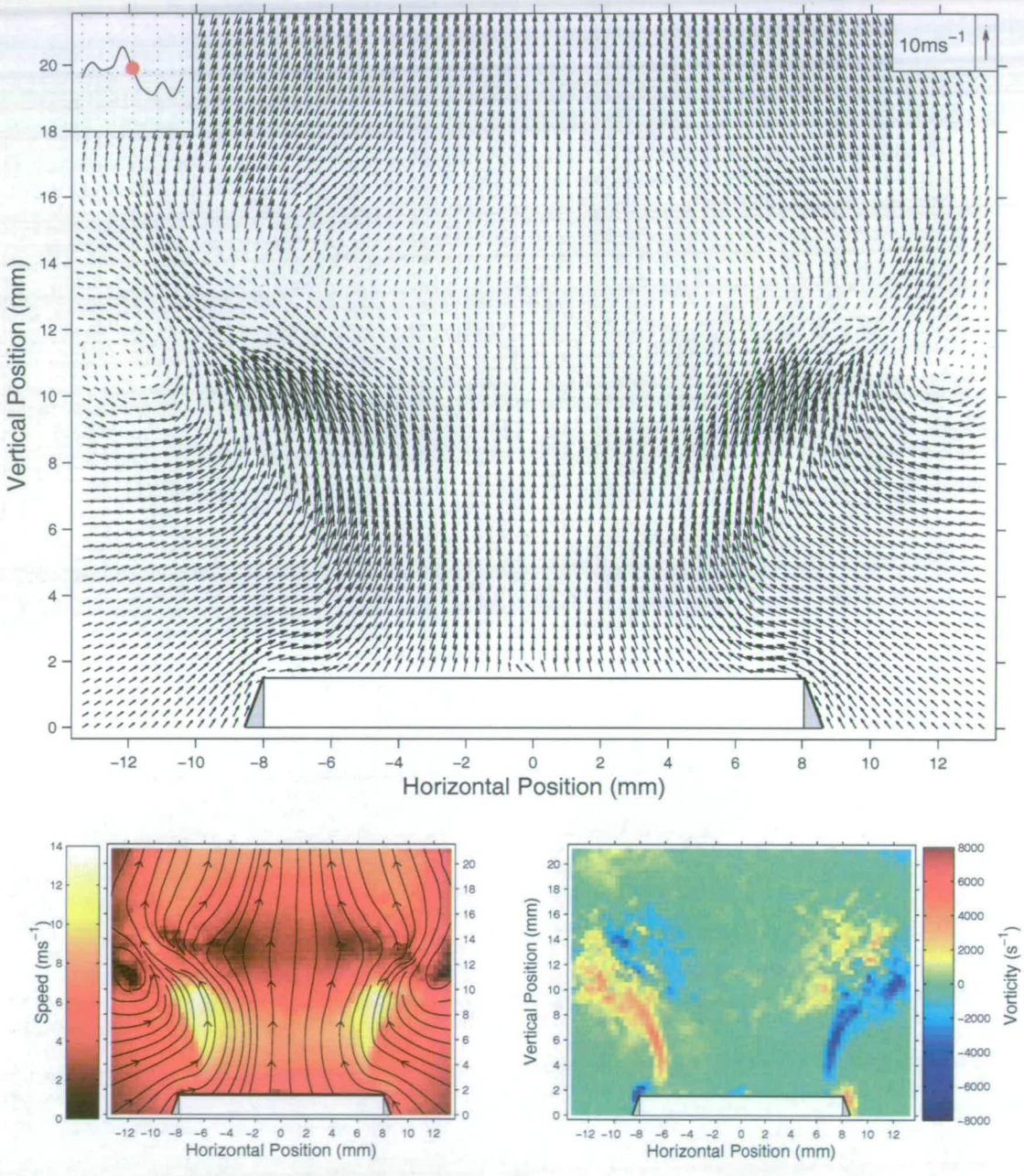


Figure 5.10 continued. (f) Phase step 6. Time = 1.316ms

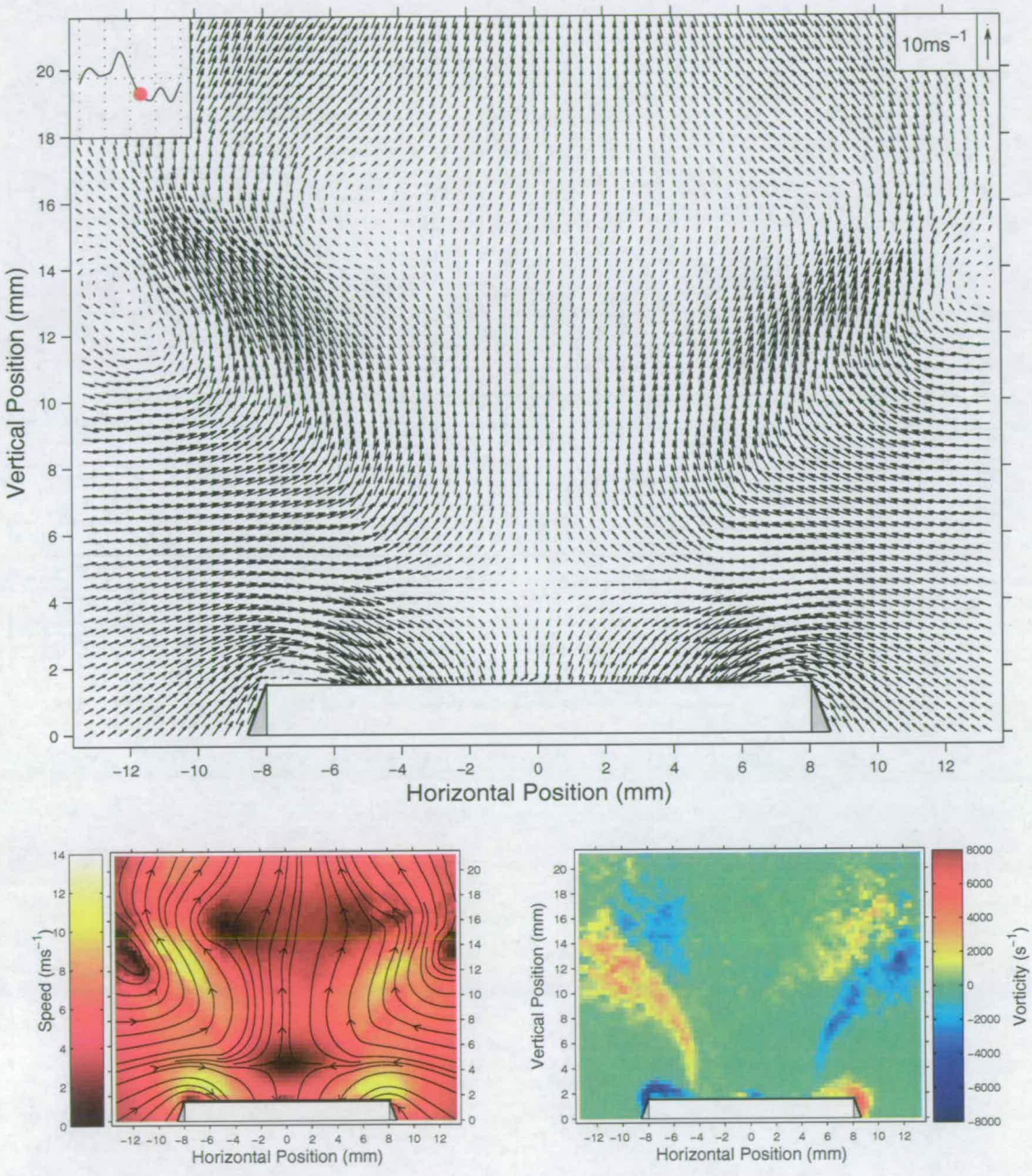


Figure 5.10 continued. (g) Phase step 7. Time = 1.579ms

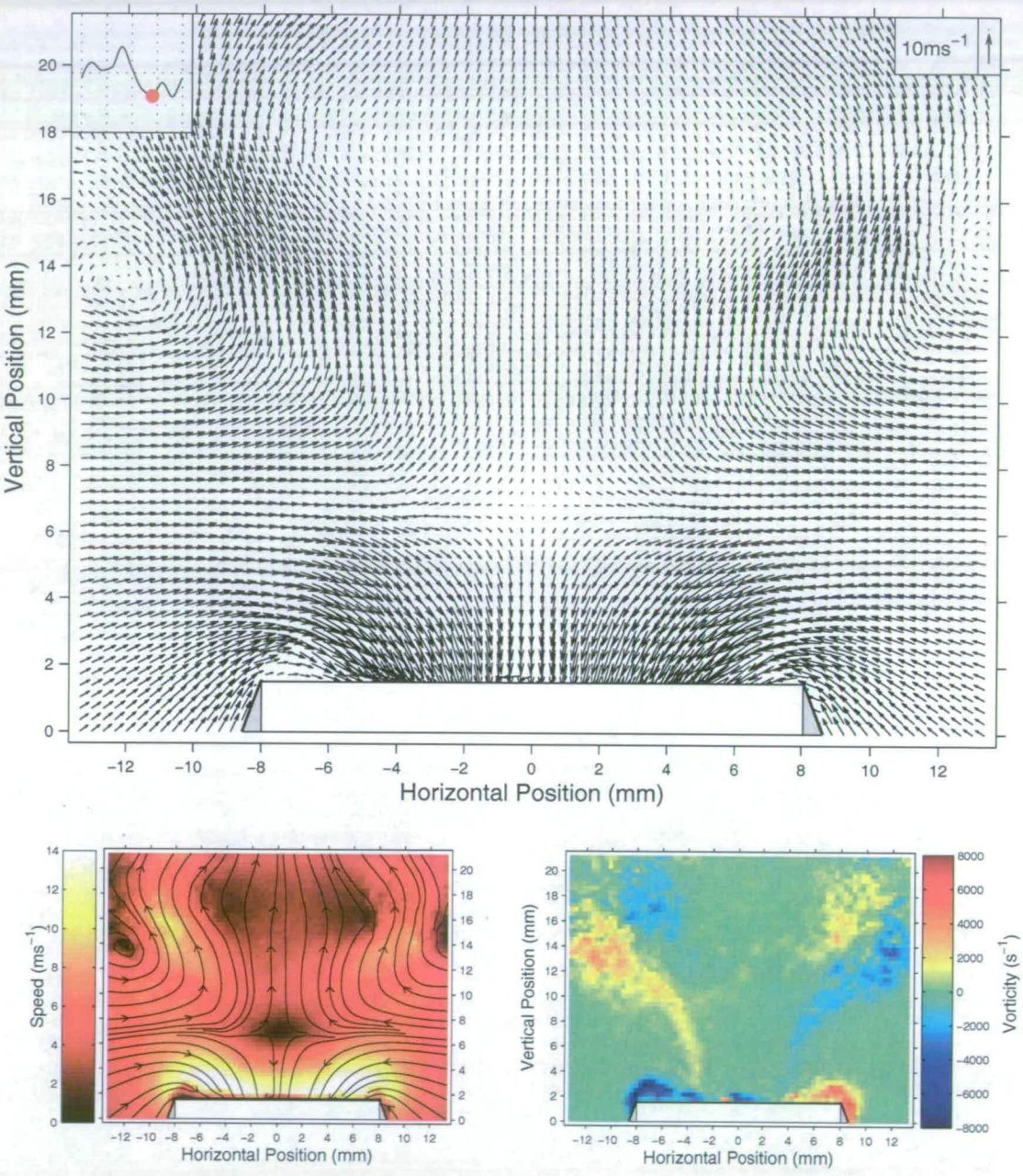


Figure 5.10 continued. (h) Phase step 8. Time = 1.842ms

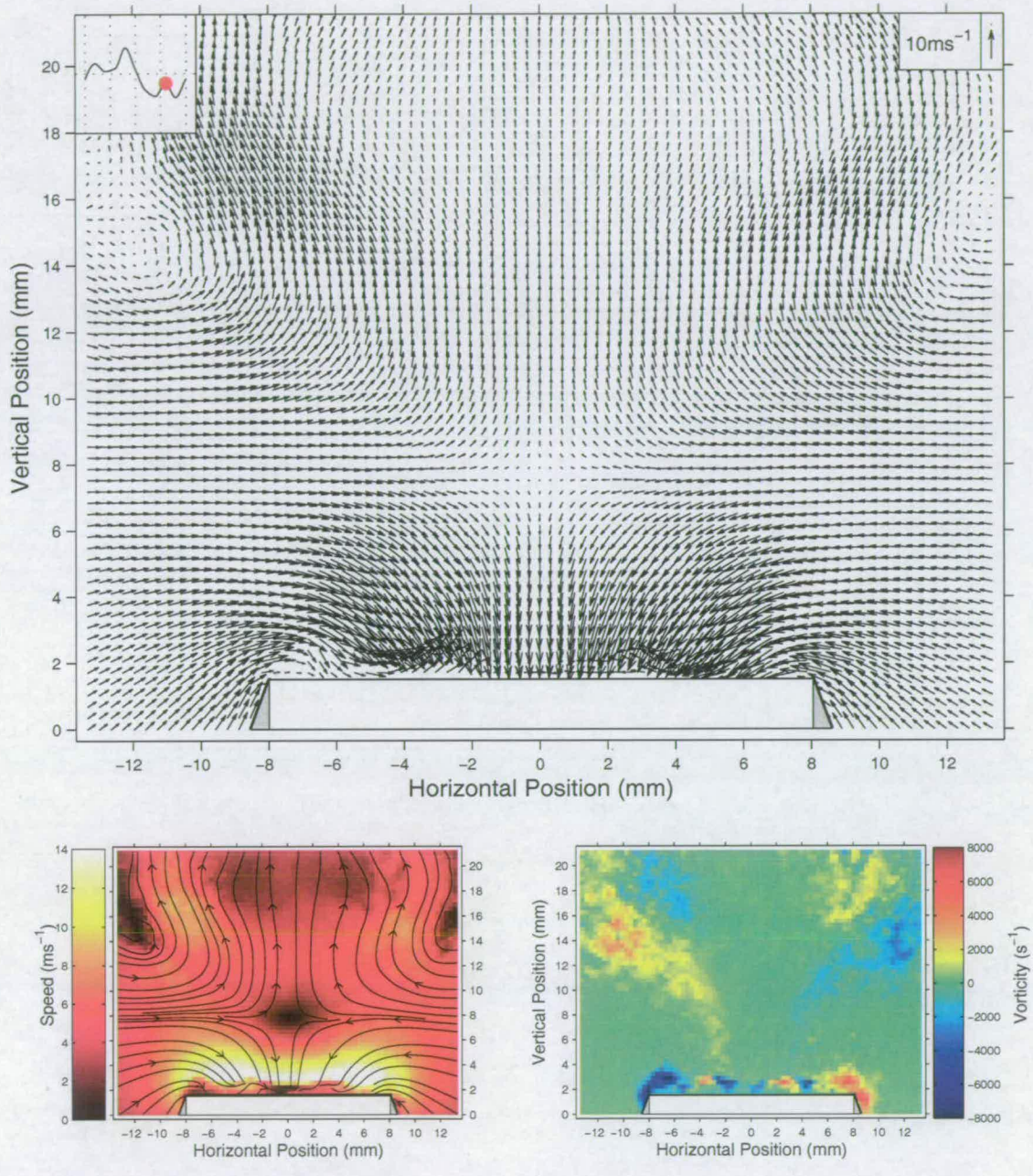


Figure 5.10 continued. (i) Phase step 9. Time = 2.105ms

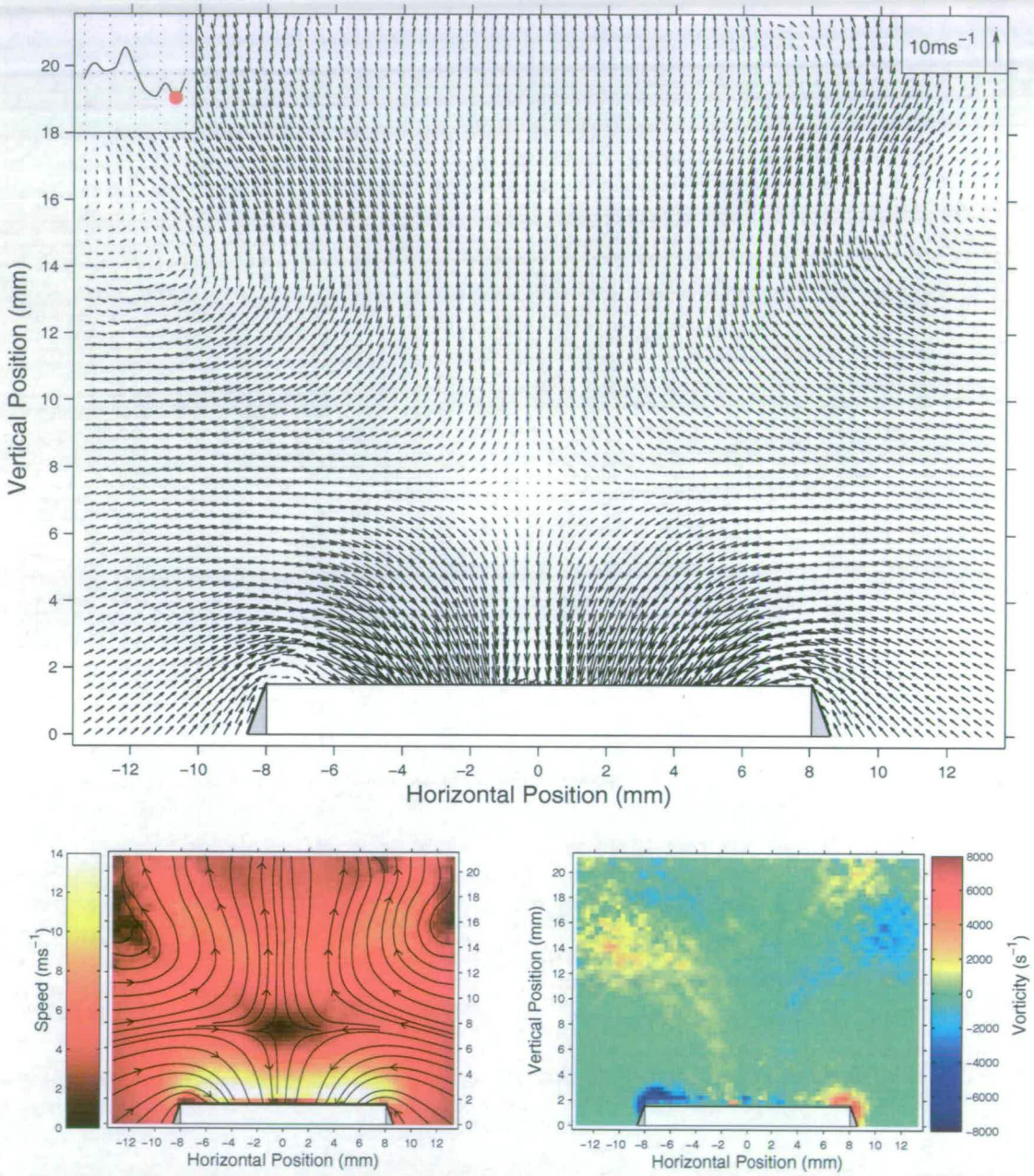
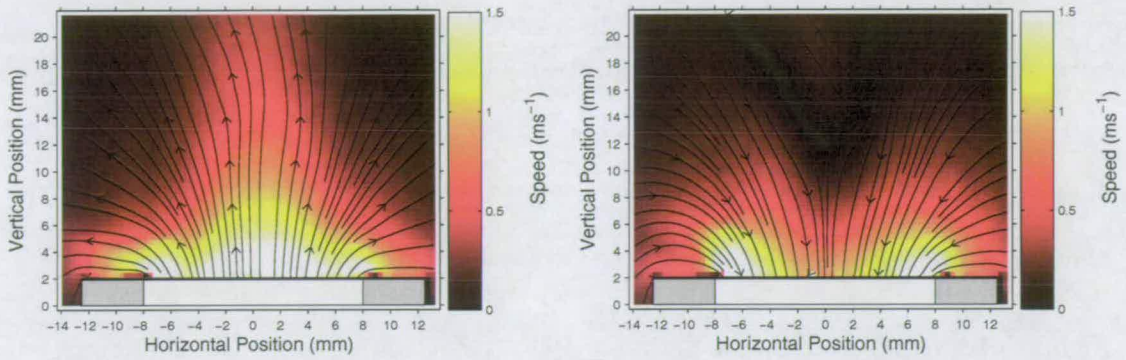


Figure 5.10 continued. (j) Phase step 10. Time = 2.368ms



(a) Peak outflow

(b) Peak inflow

Figure 5.11: Asymmetric flow develops as the velocity amplitude increases. PIV velocity magnitude contour maps for the R=0mm termination at 146.9dB with streamlines. Grey areas represent the termination wall locations.

in figure 5.9. The velocity field at the open end is clearly no longer sinusoidal at this sound level. The corresponding pressure waveform measured using a probe microphone at the open end is also shown in red. This shows essentially sinusoidal behaviour on outflow and a slightly distorted wave shape on inflow. This suggests the presence of some higher harmonics in the pressure and velocity fields. This may be due to the observed vorticity and free jet affecting the velocity and pressure fields in the near field of the open end.

5.3.3 R=0mm termination

As discussed in section 5.3.1, at 136.7dB the flow field at the open end of the R=0mm termination is potential-like in nature with symmetrical inflow and outflow. As the sound pressure level within the tube increases the velocity field becomes less symmetrical with the flow fields on inflow and outflow becoming more distinct. On outflow the velocity in the central region strengthens. On inflow the fluid velocity becomes stronger closer to the tube walls with the combined result of creating an outward jet which can be observed over the entire acoustic cycle. Example PIV images of inflow and outflow for this type of flow are shown in figure 5.11 for the R=0mm termination at a sound pressure level within the tube, measured at the position of the PCB transducer, of 146.9dB and a particle velocity amplitude $|u_{ac}| = 1.51\text{ms}^{-1}$.

The asymmetry develops further as the velocity amplitude increases. The outflow velocity close to the wall increases and boundary layer separation begins to affect the flow behaviour. Inflow becomes concentrated to regions of strong flow close to the walls

of the tube opening. Vortex structures begin to be generated on outflow and are drawn back into the tube on inflow. The strength and size of these vortex structures increases as the sound pressure level increases.

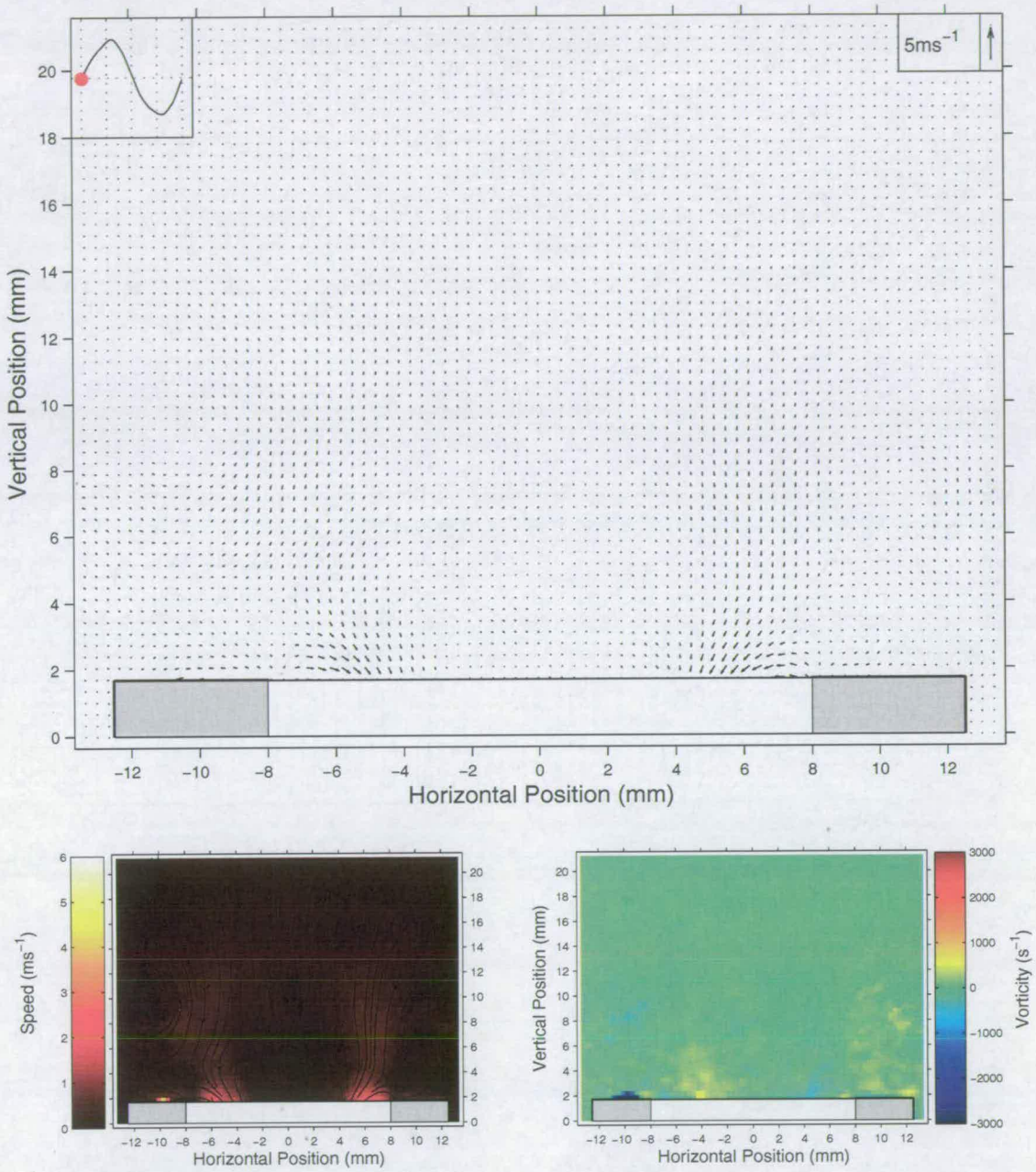
Vortex generation regime

Figure 5.12 shows a complete series of PIV vector and contour maps showing the acoustic particle velocity field for the R=0mm tube termination at 158.2dB (measured at the PCB transducer). The acoustic particle velocity amplitude is $5.56 ms^{-1}$. The normalised pressure and velocity waveforms for this measurement are shown in figure 5.13. As can be seen the pressure and velocity fields are still essentially sinusoidal at this sound level.

During the outflow stage of the acoustic cycle (phase steps 2-6) the flow is observed to be strongest near the centre and close to the inner wall of the tube termination. During the inflow stage of the acoustic cycle (phase steps 7-10, 1) air is initially drawn into the tube most strongly close to the inside wall of the tube termination (figure 5.12(g))and then diffusely from all directions.

On outflow the air within the boundary layer exits the open end at a relatively high velocity it encounters a region of stationary air just outside the termination. Boundary layer separation occurs at the right angled inside edge of the termination. The high spatial velocity gradient present at the location of the tube edge as the separated high velocity boundary layer impinges on this stagnant air results in the generation of localised vorticity. Unlike in the situation with the sharp termination, where the vortices are generated and shed periodically, reattachment occurs on the outer flange and a vortex ring is generated which clings to the outside edges of the termination. The development of this vortex structure is most strikingly displayed in phase steps 4-6. Once the inflow part of the acoustic cycle has begun this vortex ring is drawn back into the tube

Vortex structures are thus generated on outflow, with increasing size and strength as the acoustic velocity amplitude increases, which cling to the tube walls at the end of the termination due to reattachment of the boundary layer. On inflow air is drawn diffusely into the tube from all directions causing the vortex structures to be sucked back inside. As the acoustic particle velocity amplitude increases the inflow becomes concentrated to regions of strong flow close to the walls of the tube opening. This is expected to cause vortices to be generated inside the tube on inflow but this cannot be confirmed experimentally in this study.



(a) Phase step 1. Time = 0.000ms

Figure 5.12: PIV results for the the R=0mm termination at an SPL of 158.2dB ($|u_{ac}| = 5.56ms^{-1}$). (Top) PIV velocity vector maps. The upper left hand velocity waveform indicates at which stage of the acoustic cycle the vector map is taken. (Bottom left) Velocity magnitude contours with streamlines. (Bottom right) Vorticity contours. Time is with respect to the trigger point. Grey areas represent the termination wall locations.

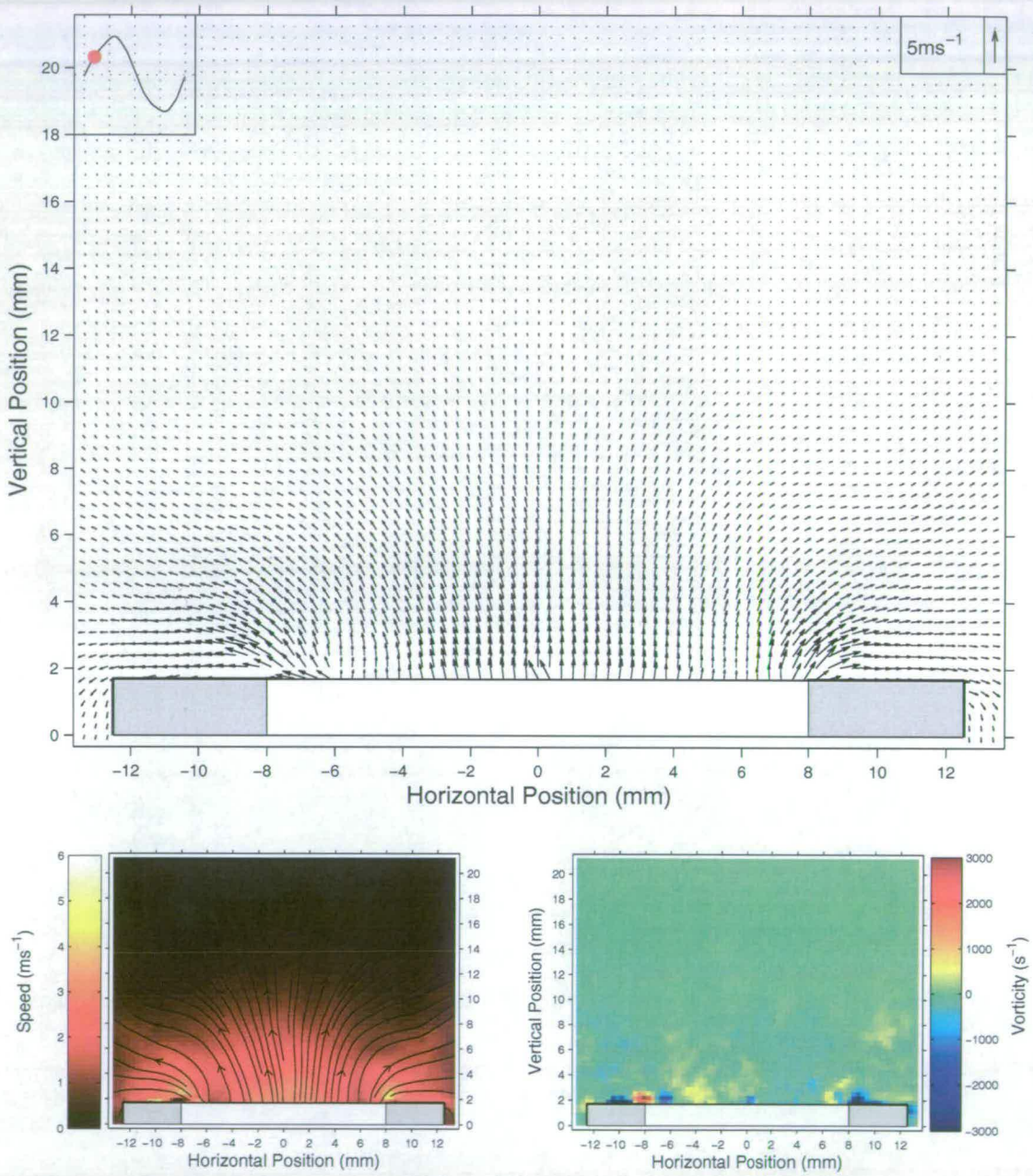


Figure 5.12 continued. (b) Phase step 2. Time = 0.263ms.

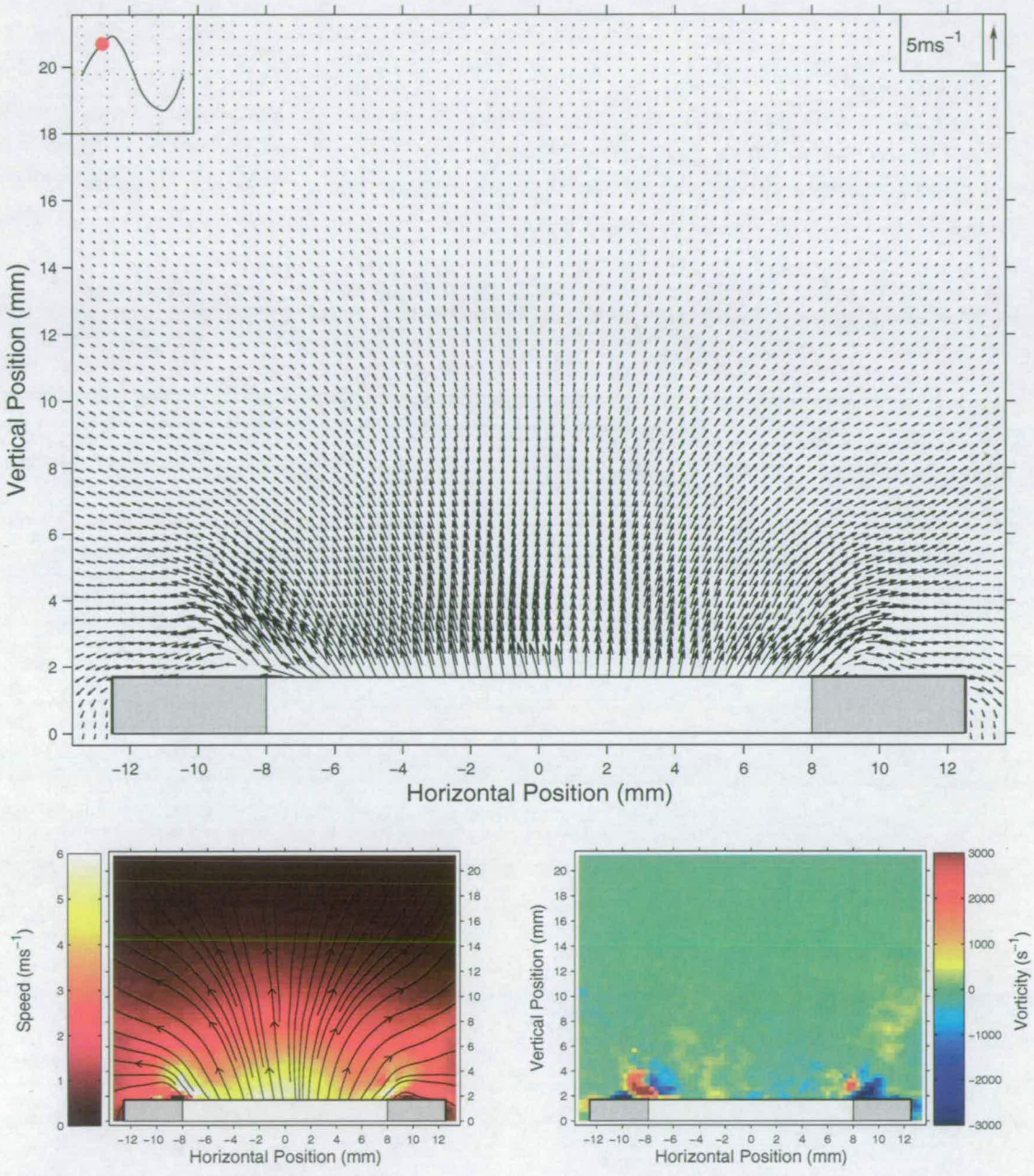


Figure 5.12 continued. (c) Phase step 3. Time = 0.526ms

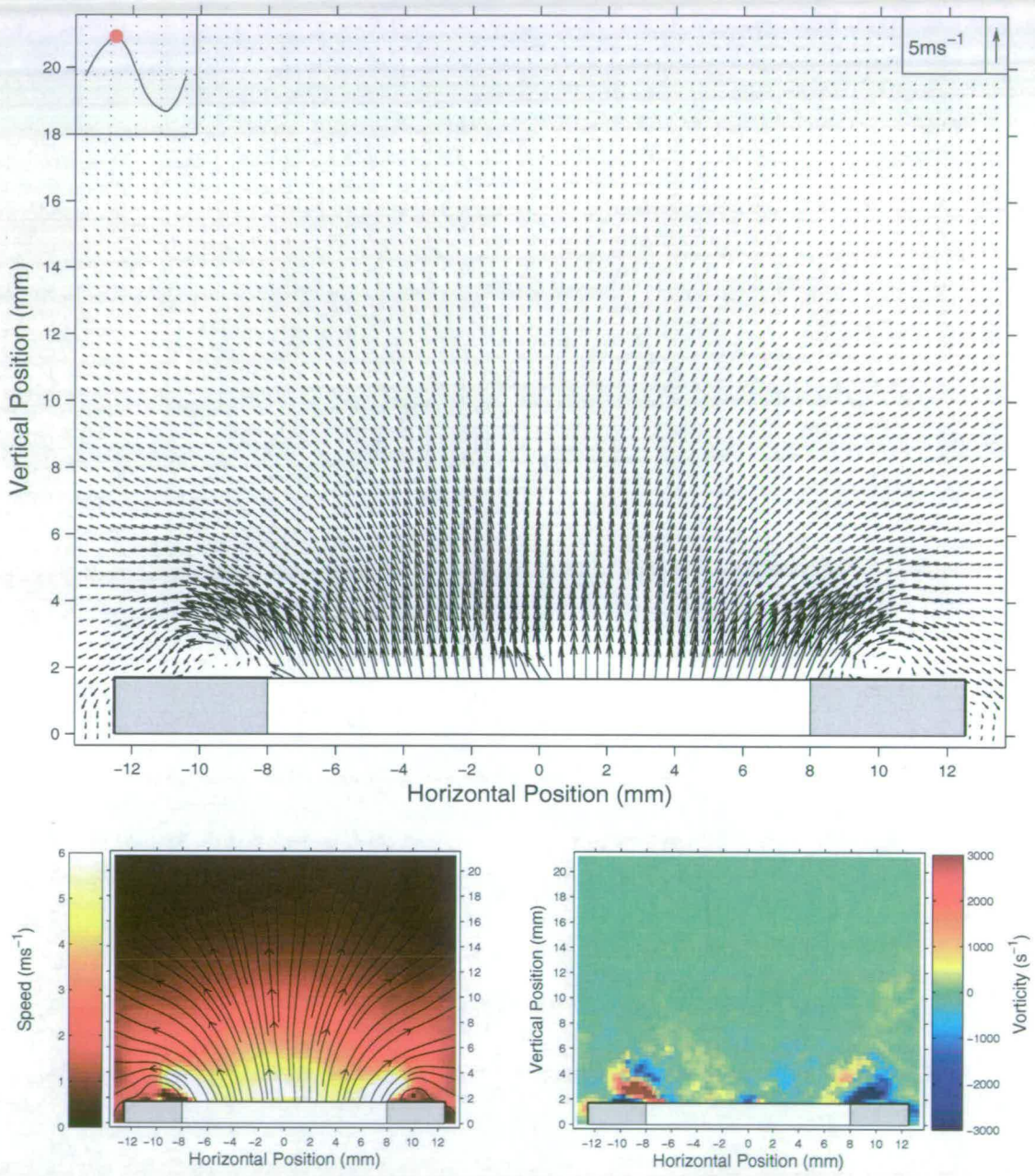


Figure 5.12 continued. (d) Phase step 4. Time = 0.789ms

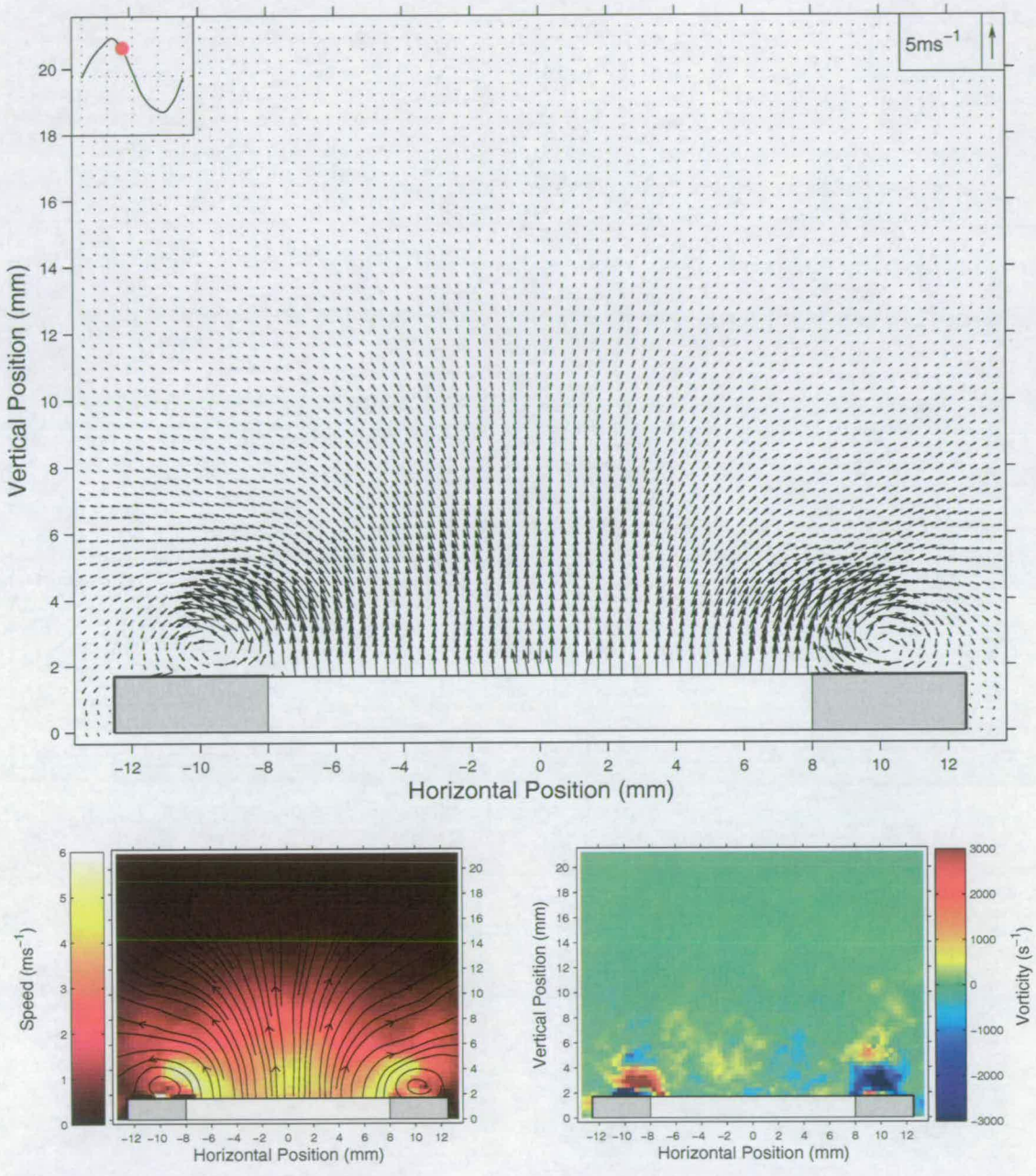


Figure 5.12 continued. (e) Phase step 5. Time = 1.053ms

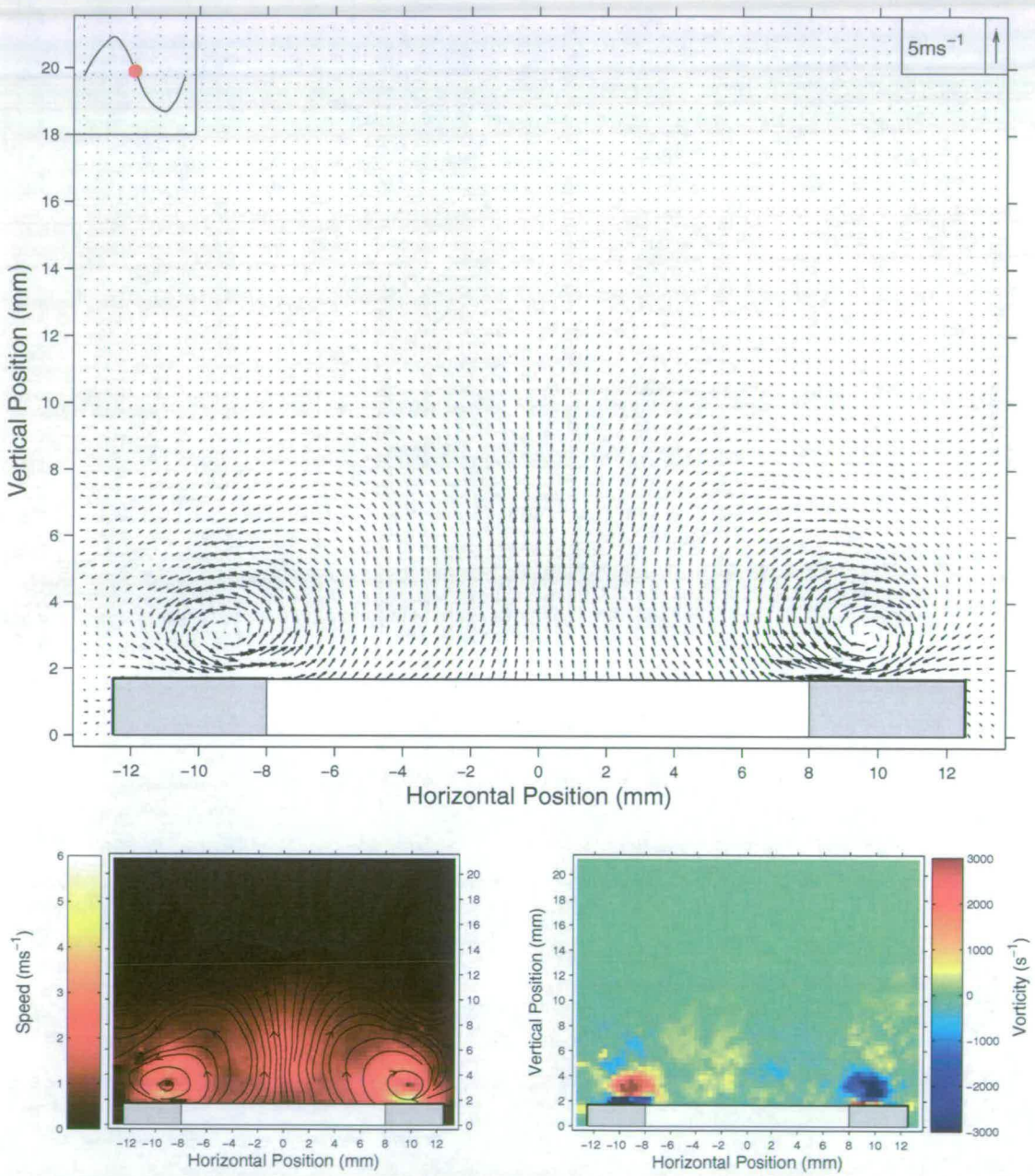


Figure 5.12 continued. (f) Phase step 6. Time = 1.316ms

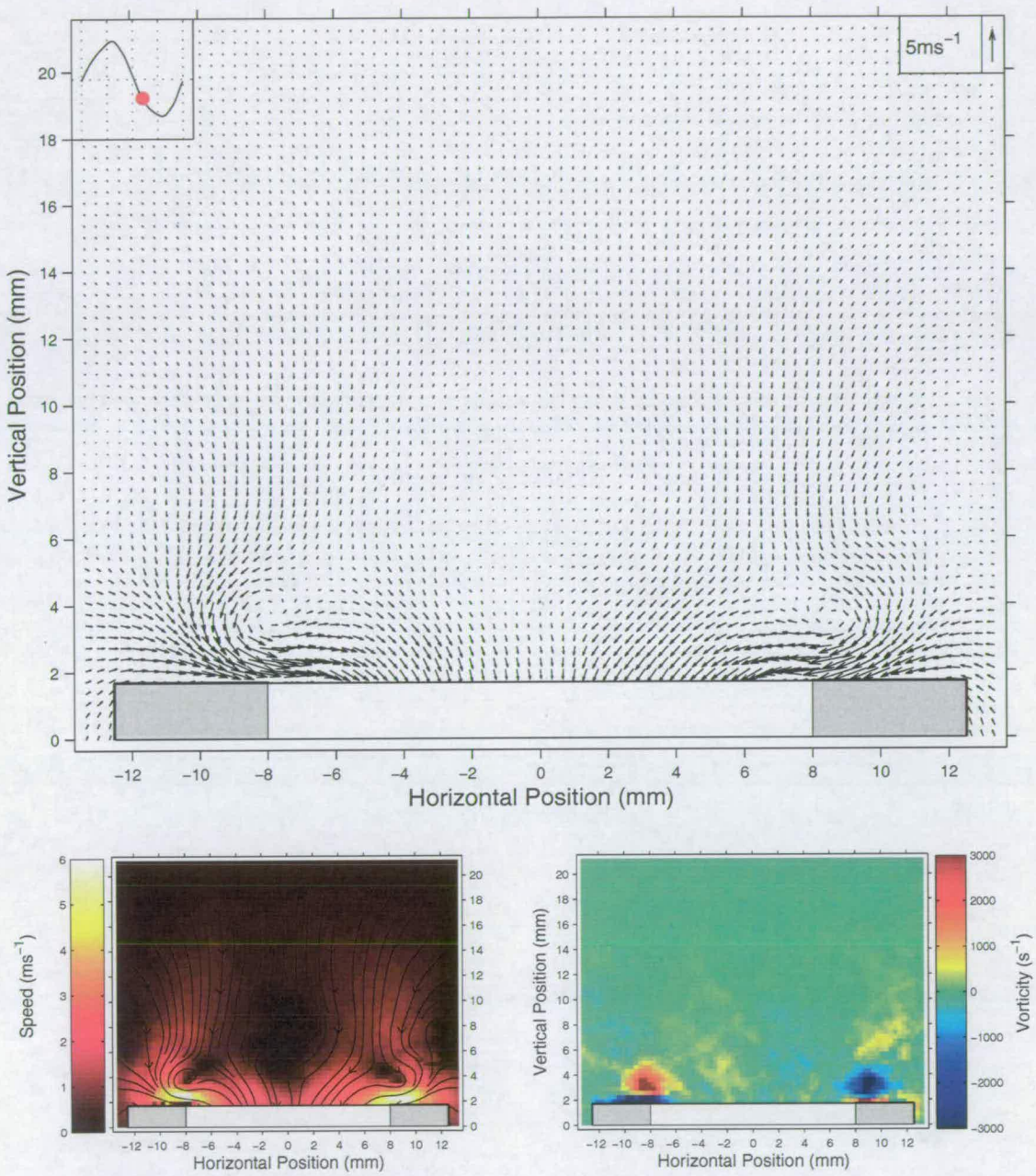


Figure 5.12 continued. (g) Phase step 7. Time = 1.579ms

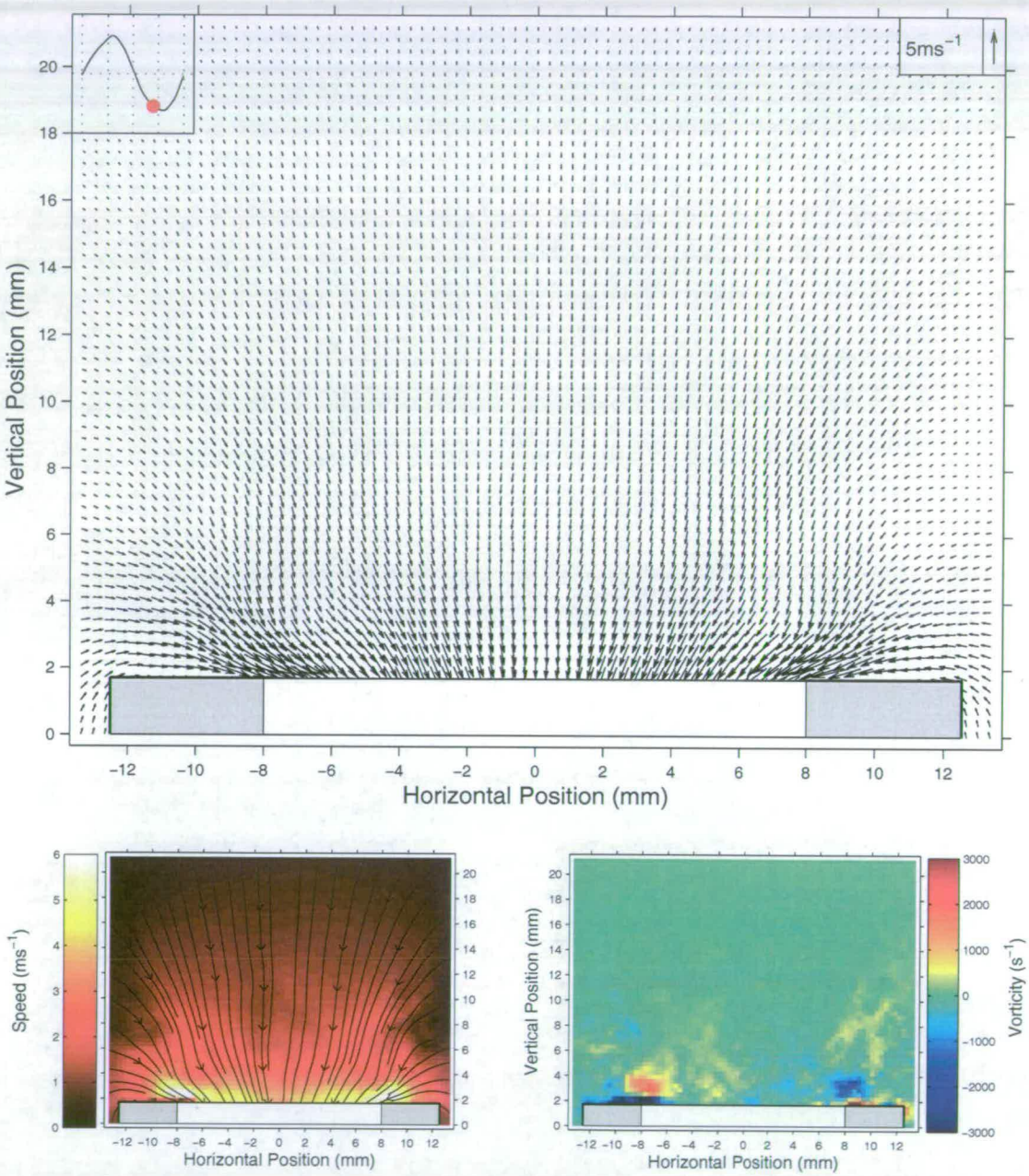


Figure 5.12 continued. (h) Phase step 8. Time = 1.842ms

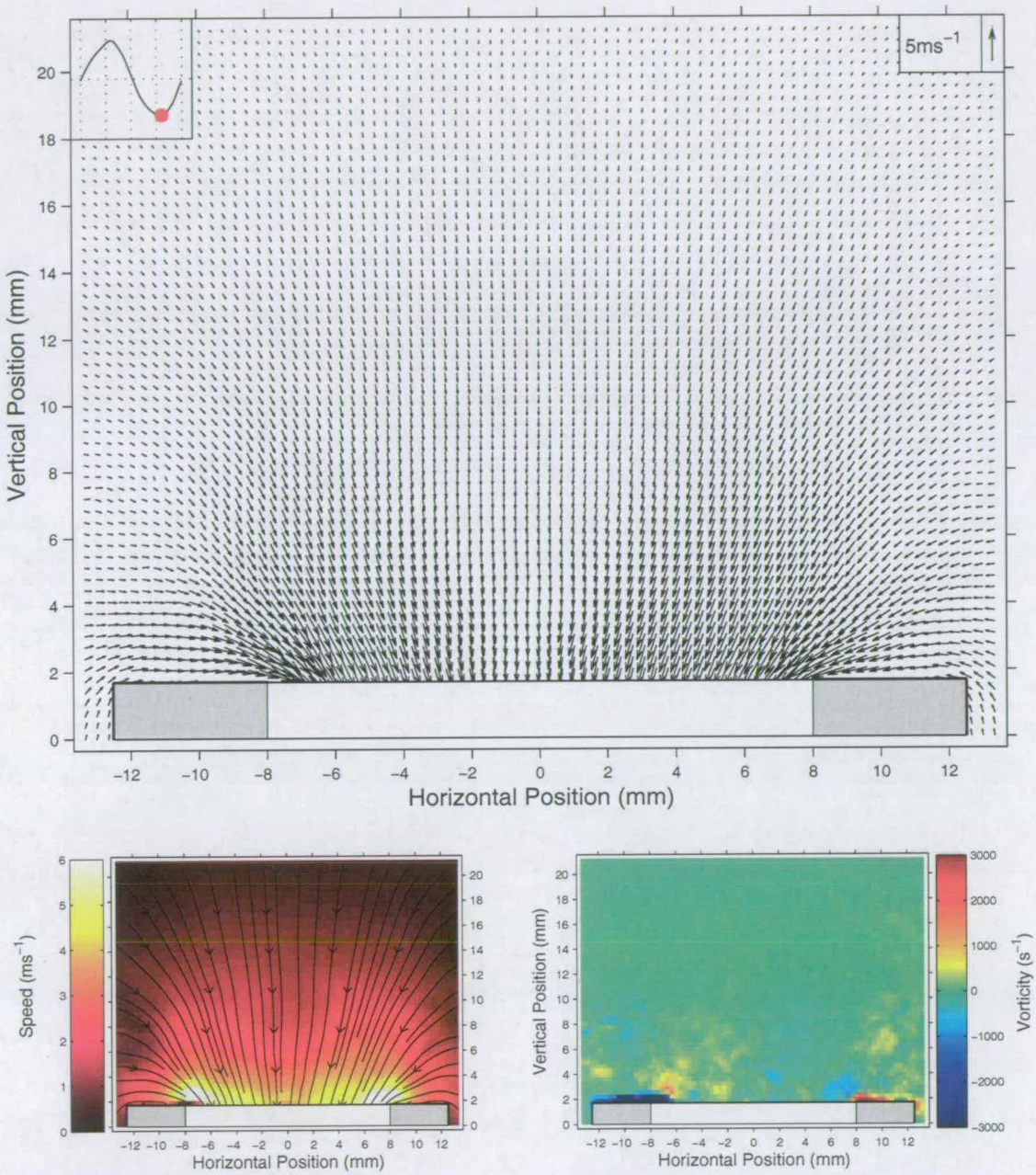


Figure 5.12 continued. (i) Phase step 9. Time = 2.105ms

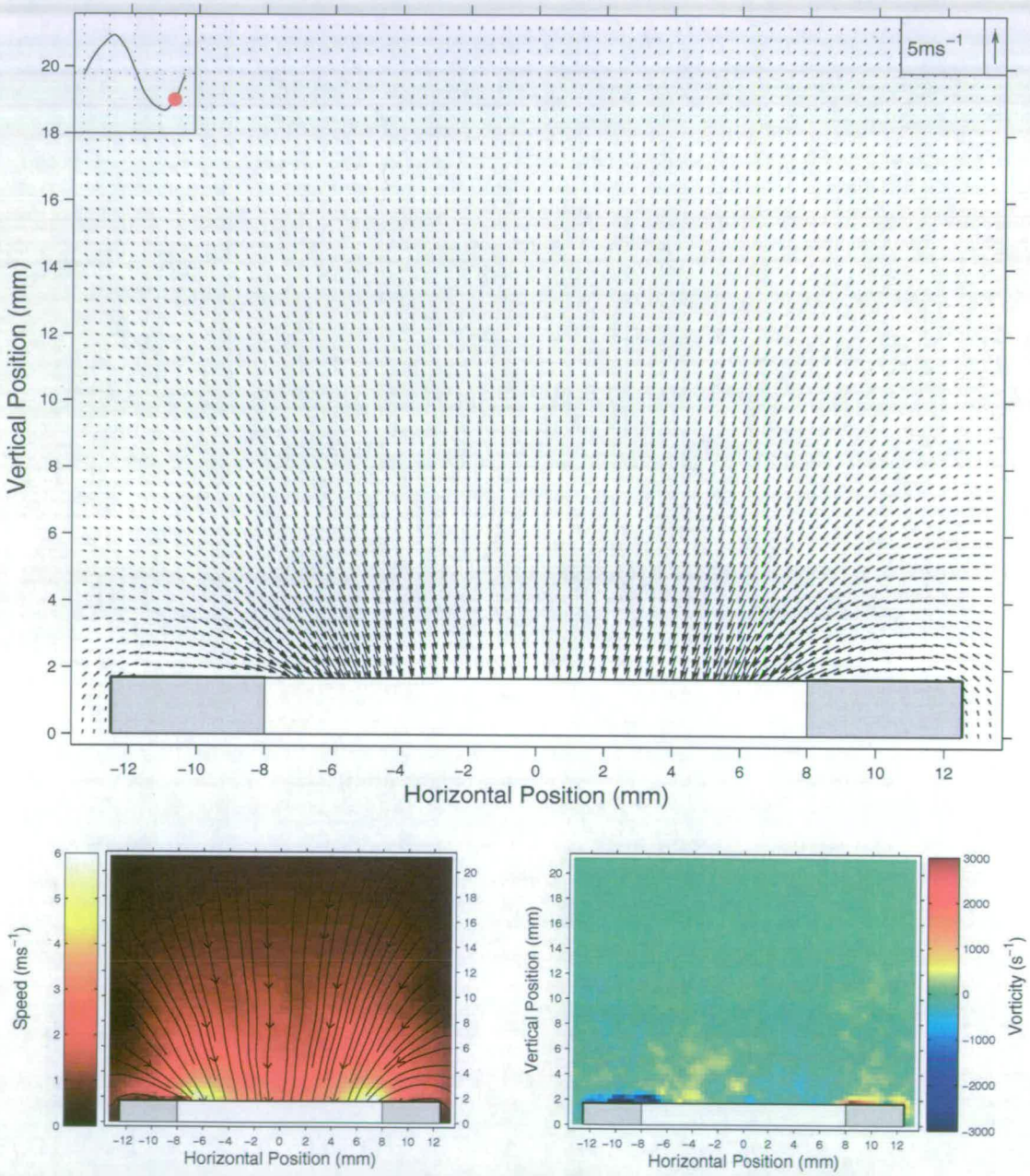


Figure 5.12 continued. (j) Phase step 10. Time = 2.368ms

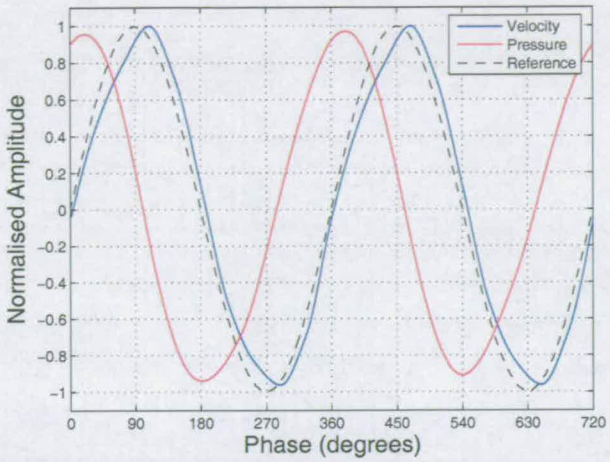
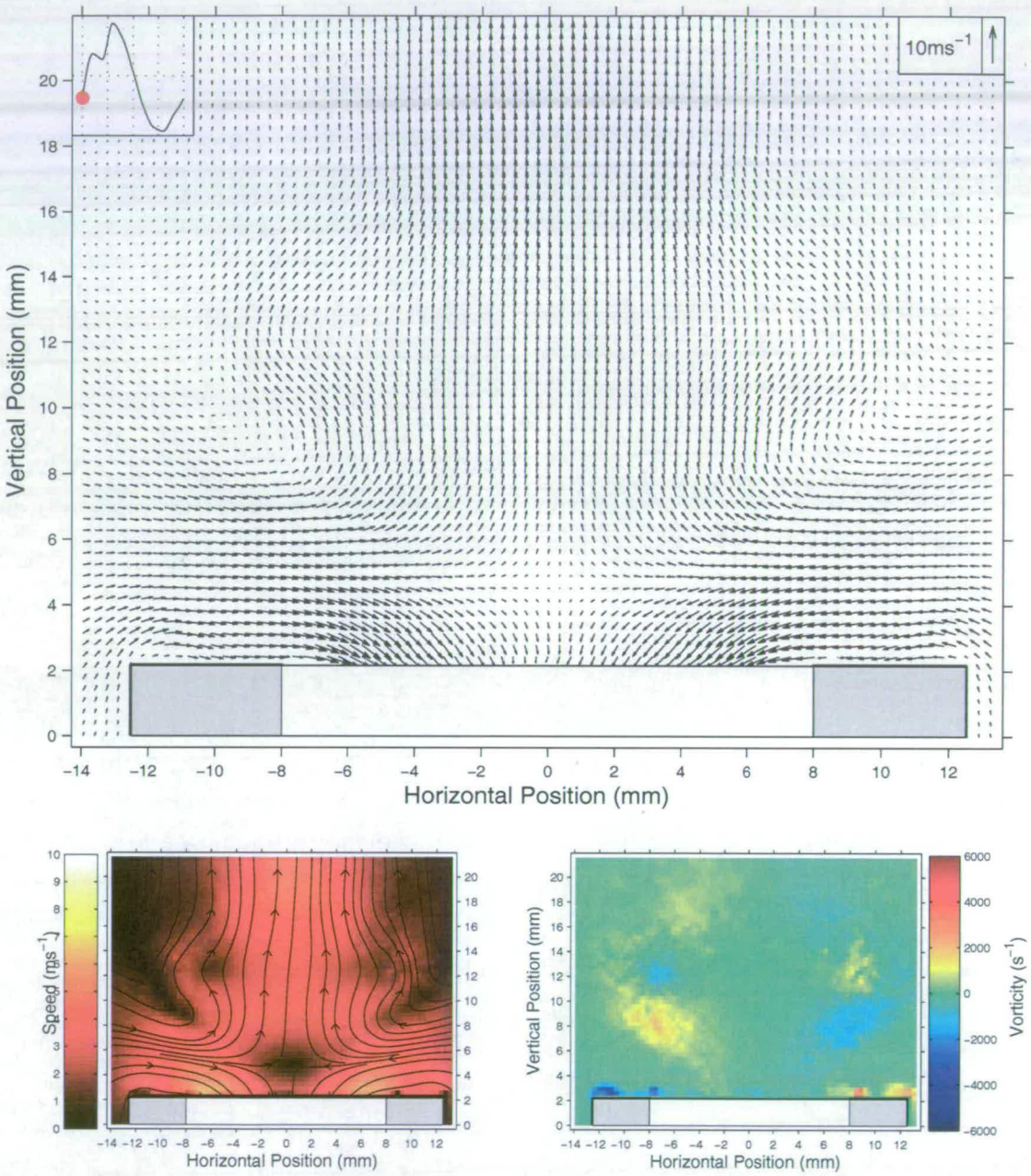


Figure 5.13: Normalised velocity (blue) and pressure signals (red) measured at the open end open end of the tube for the sharp edged termination at 158.2dB. Also shown for comparison is the reference signal (- - -) synchronised with the trigger source.

Vortex shedding regime

As the sound pressure level is increased further the velocity field in the vicinity of the tube termination undergoes a dramatic transition to a new flow regime. For the R=0mm termination this transition occurs at a sound pressure level within the tube of 161.2dB corresponding to a linear acoustic particle velocity amplitude of 7.87ms^{-1}. The vortex structures which previously clung to the tube termination are now shed with the same frequency as the acoustic cycle. An outward jet with a speed equal to approximately one half of the acoustic particle velocity amplitude is observed a short distance from the open end. As the acoustic amplitude increases past this vortex shedding threshold the size and strength of the shed vortices is amplified and the associated synthetic jet strongly affects the flow. This flow regime appears to be equivalent to the flow region 4 described by Ingard and Labate [Ingard 50].

A series of PIV vector maps showing the evolution of the velocity field through the acoustic cycle above the vortex shedding transition for the R=0mm termination at a sound pressure level of 162.3dB is shown in figure 5.14. As the ejection stage of the acoustic cycle begins an initial pulsed jet can be seen leaving the centre of the tube (phase step 2). This jet strengthens as the acoustic cycle progresses and is followed a short time later, at the peak of the acoustic cycle, by high velocity outflow in the boundary layer region close to the tube walls (phase step 4) and the formation of pairs of counter-rotating vortex ring pairs which continue to propagate downstream.



(a) Phase step 1. Time = 0.000ms

Figure 5.14: PIV results for the the R=0mm termination at an SPL of 162.3dB ($|u_{ac}| = 8.88ms^{-1}$). (Top) PIV velocity vector maps. The upper left hand velocity waveform indicates at which stage of the acoustic cycle the vector map is taken. (Bottom left) Velocity magnitude contours with streamlines. (Bottom right) Vorticity contours. Time is with respect to the trigger point. Grey areas represent the termination wall locations.

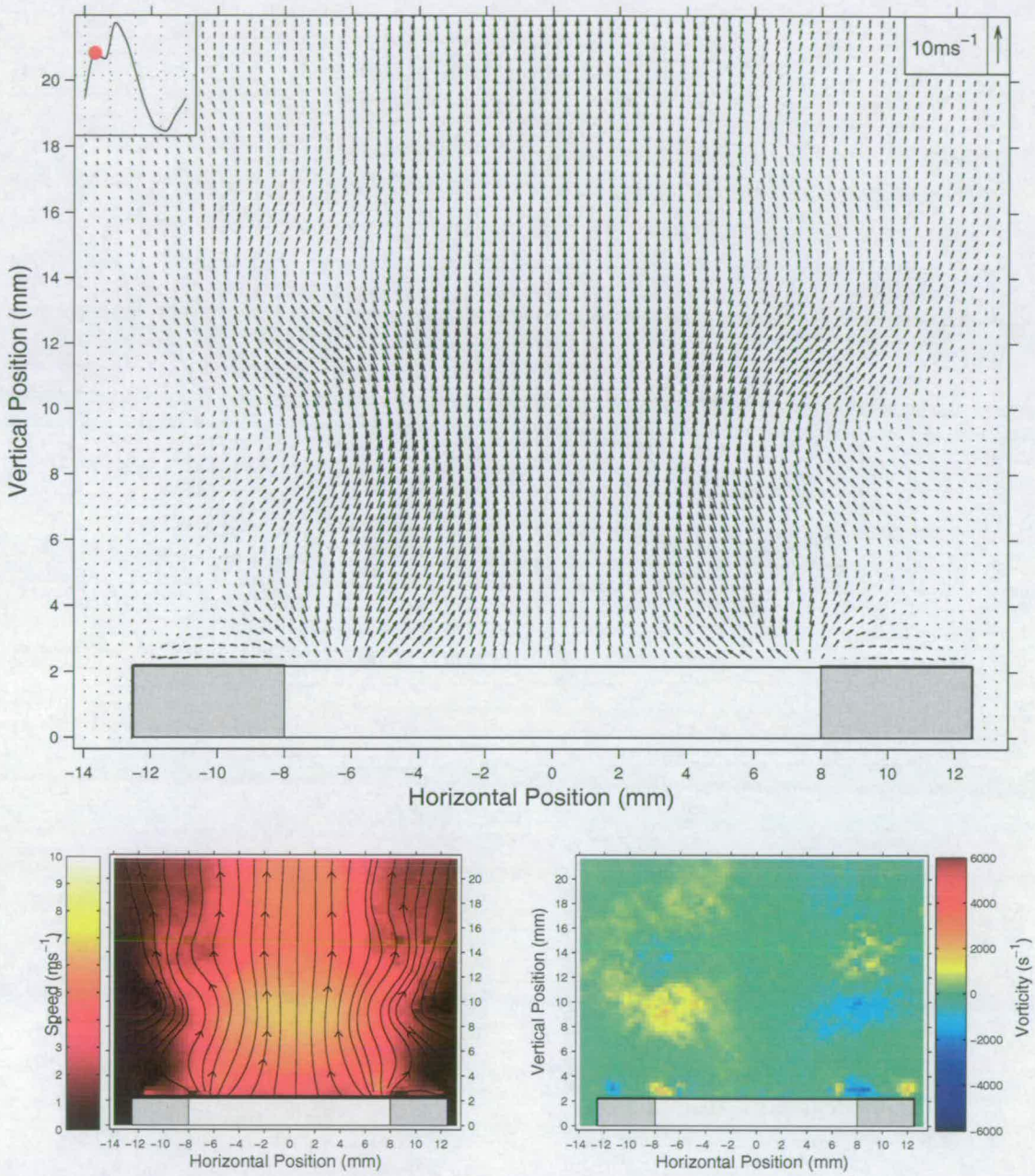


Figure 5.14 continued. (b) Phase step 2. Time = 0.263ms.

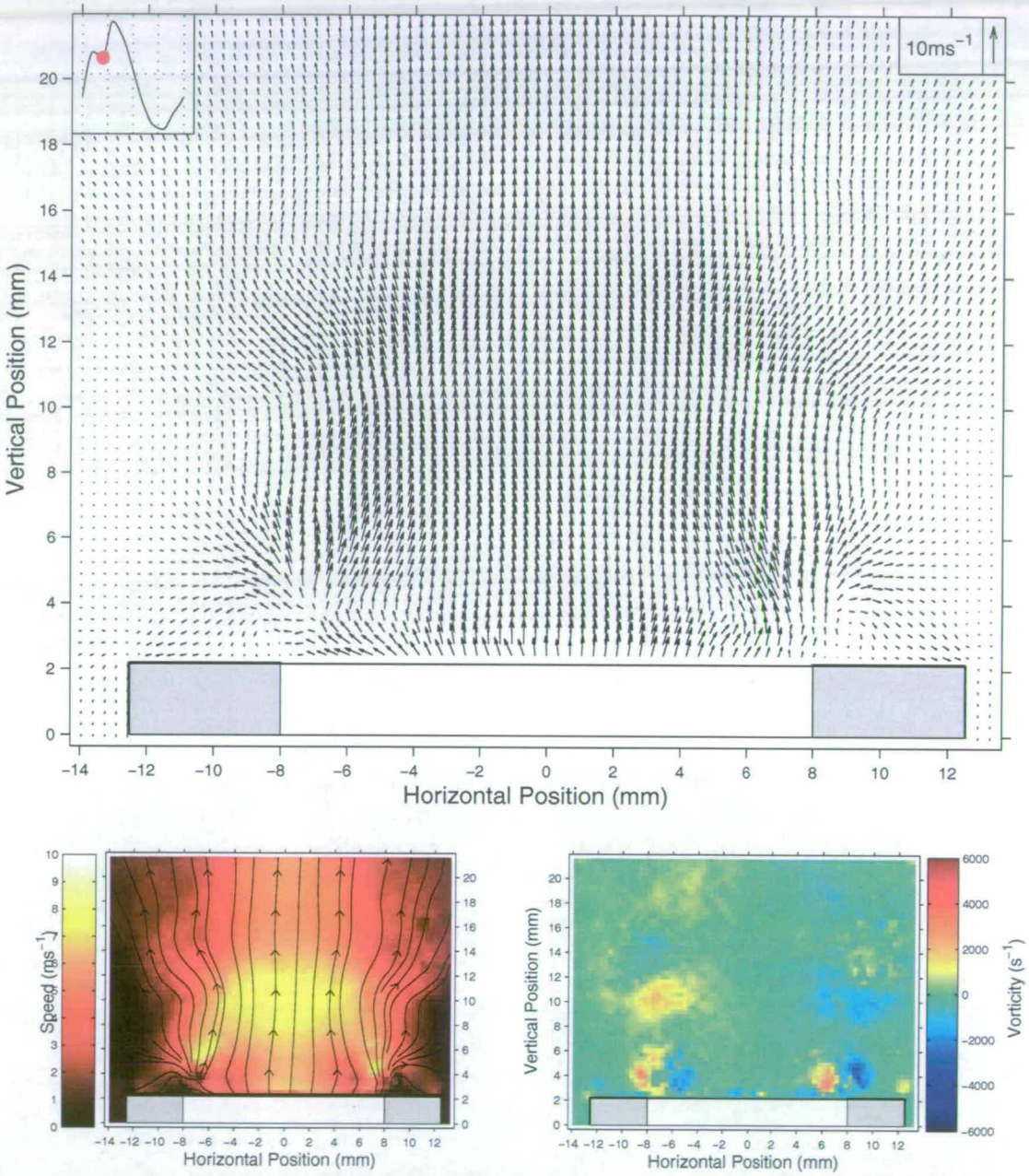


Figure 5.14 continued. (c) Phase step 3. Time = 0.526ms

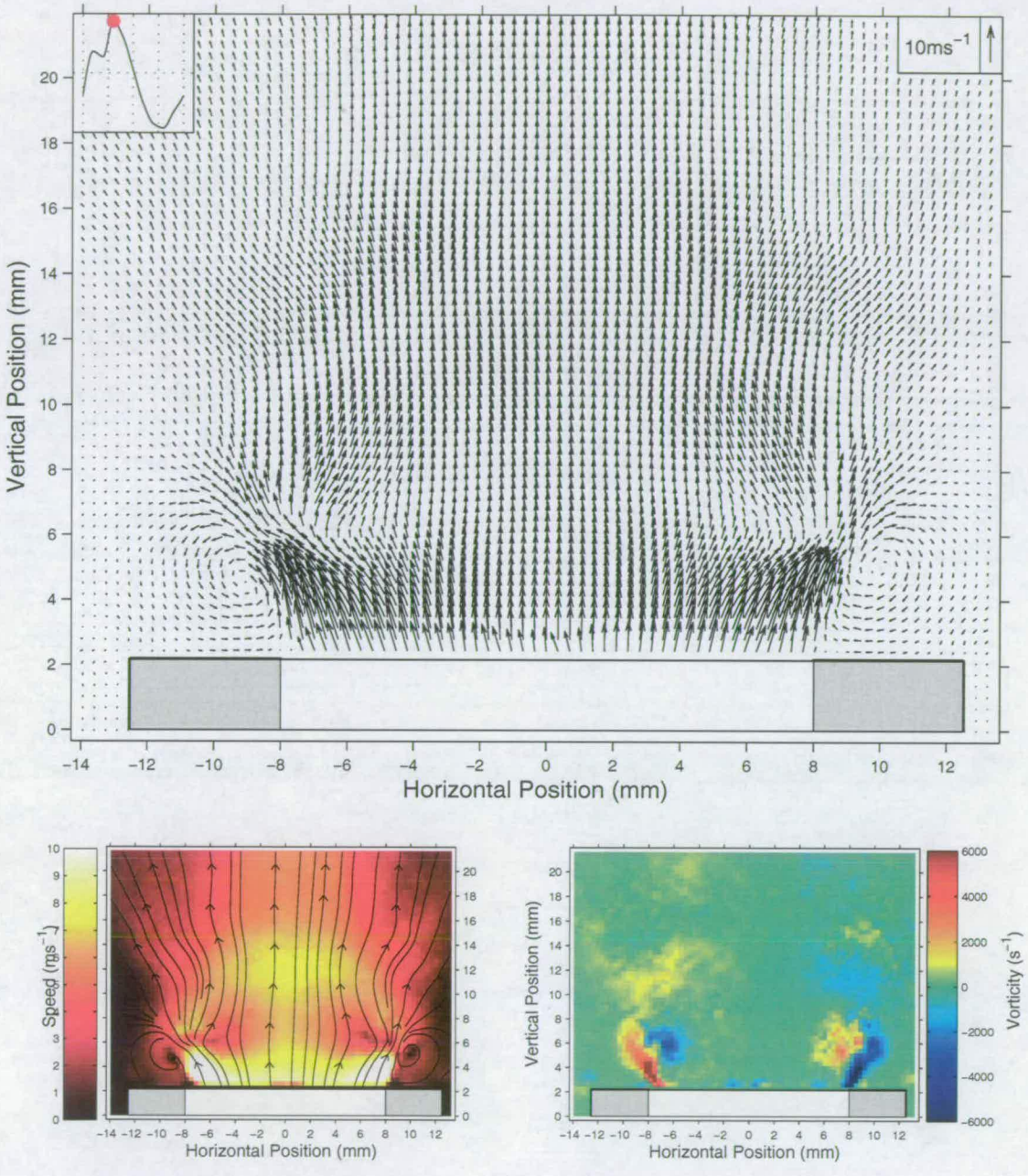


Figure 5.14 continued. (d) Phase step 4. Time = 0.789ms

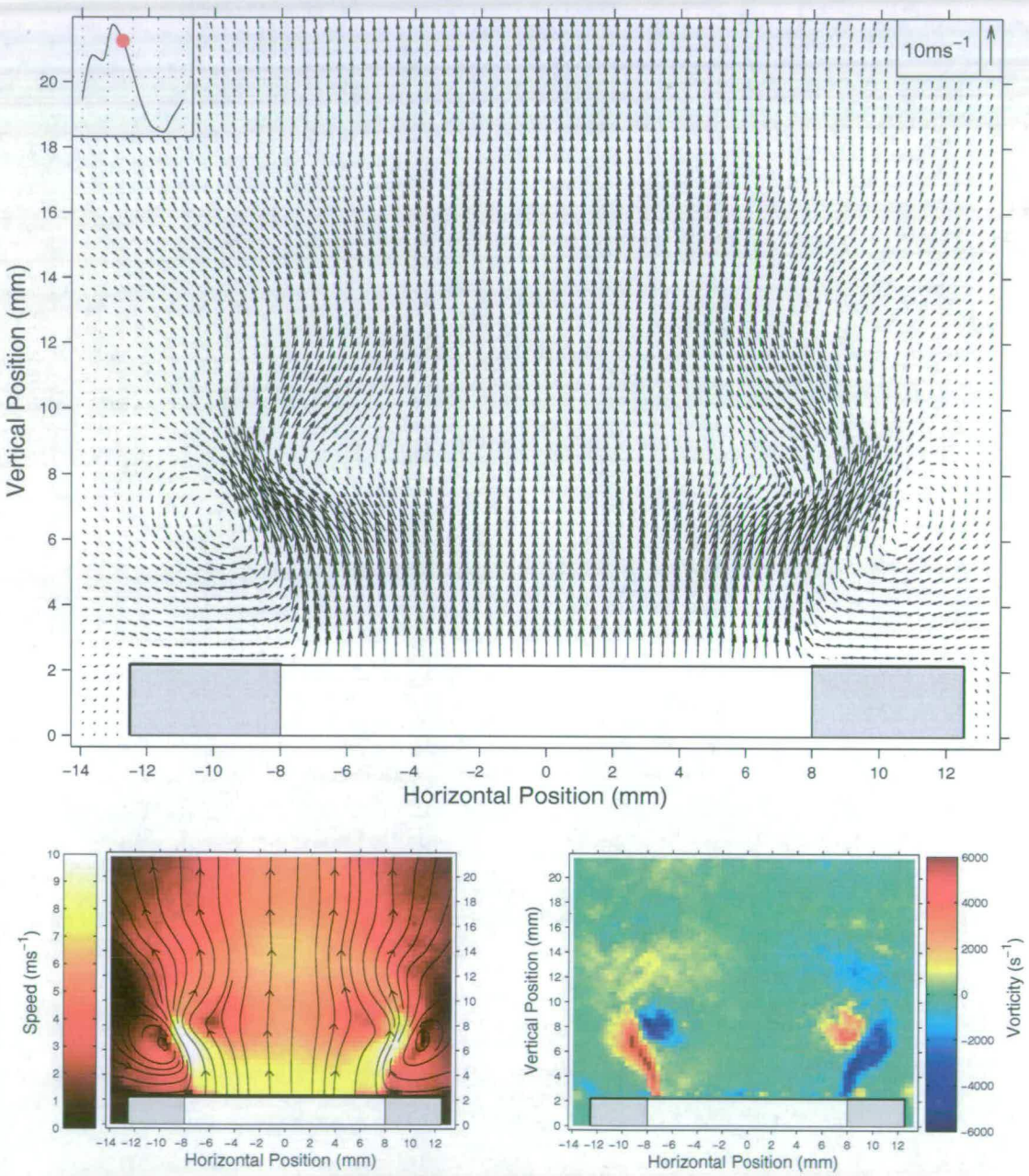


Figure 5.14 continued. (e) Phase step 5. Time = 1.053ms

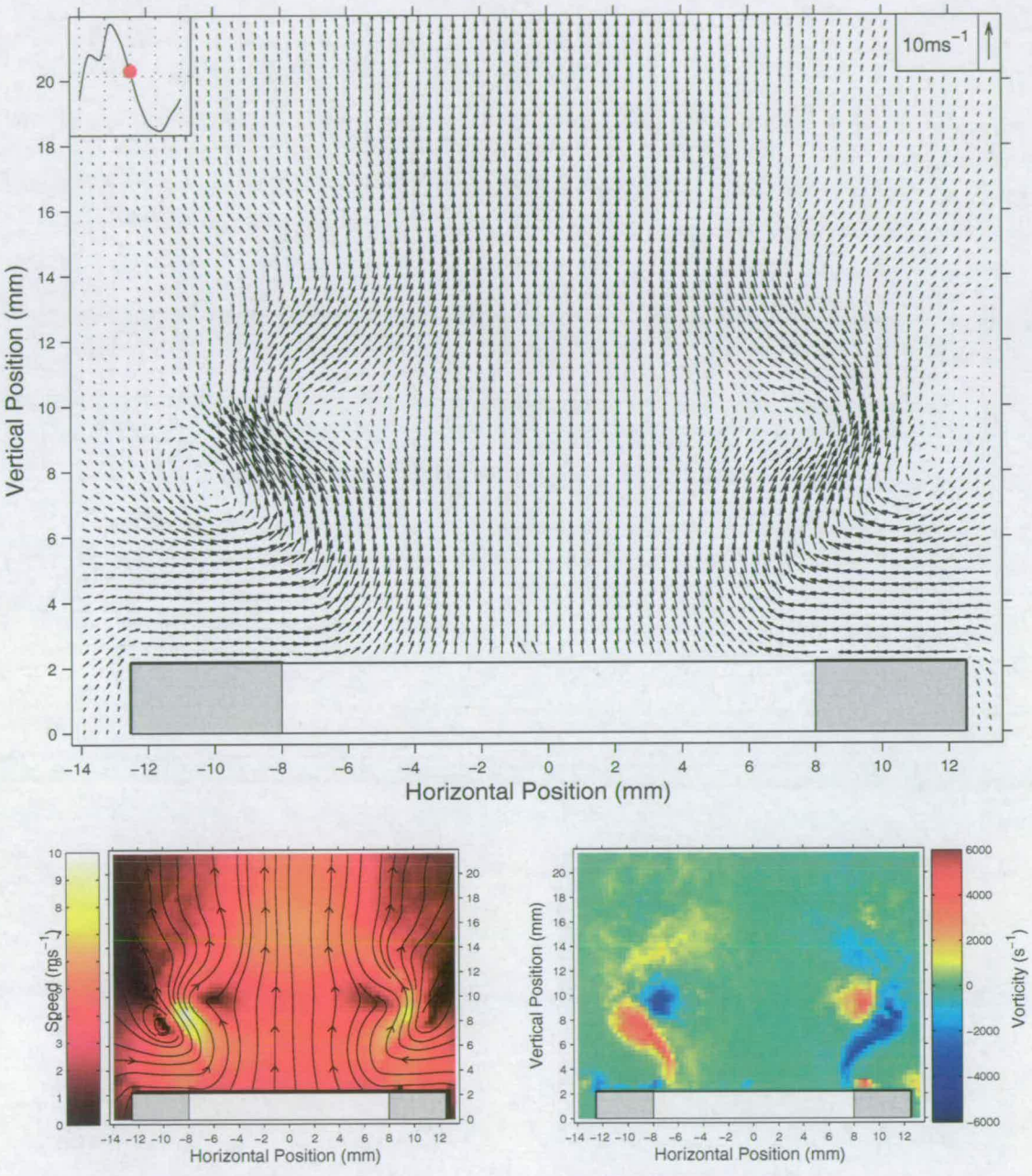


Figure 5.14 continued. (f) Phase step 6. Time = 1.316ms

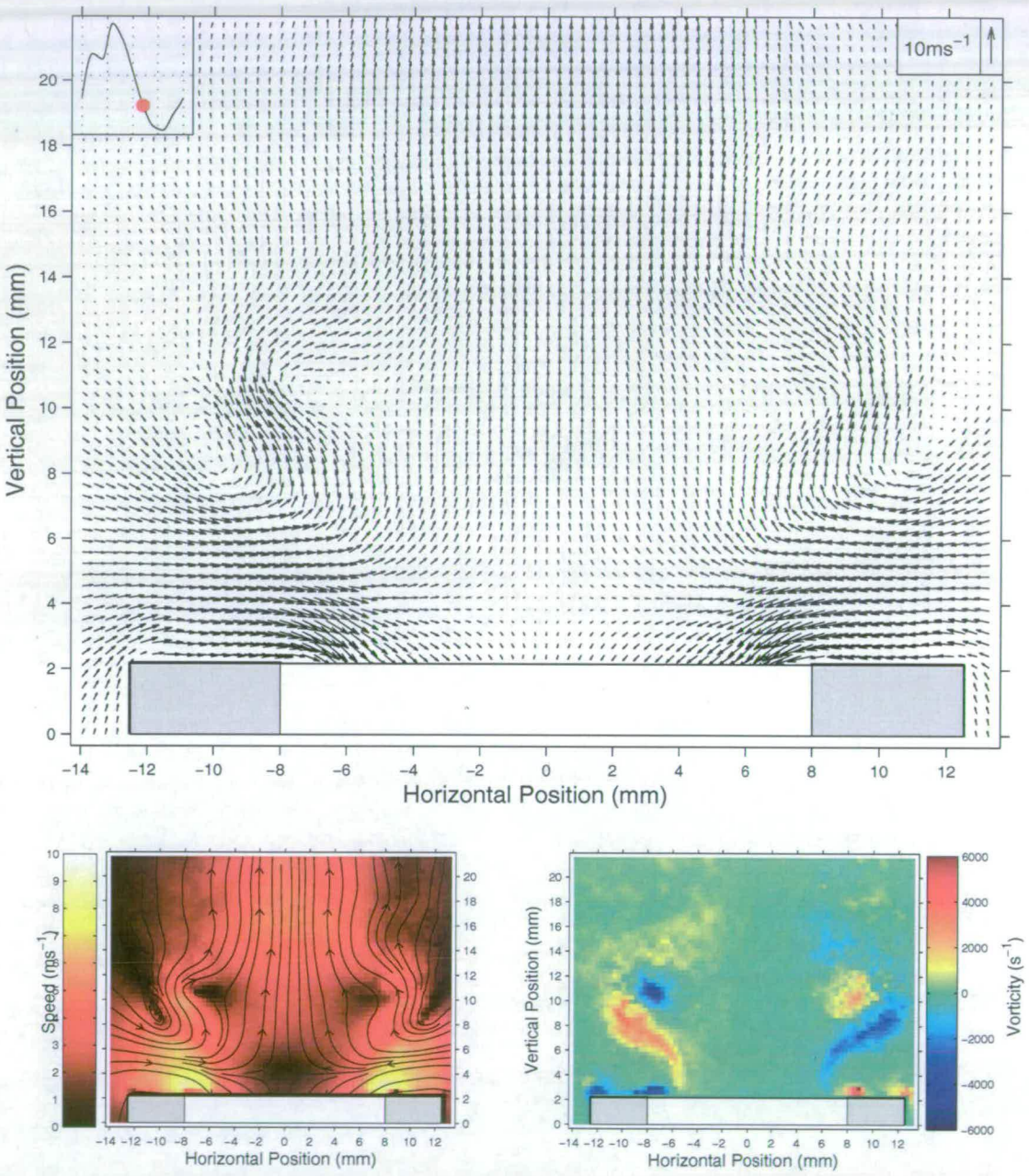


Figure 5.14 continued. (g) Phase step 7. Time = 1.579ms

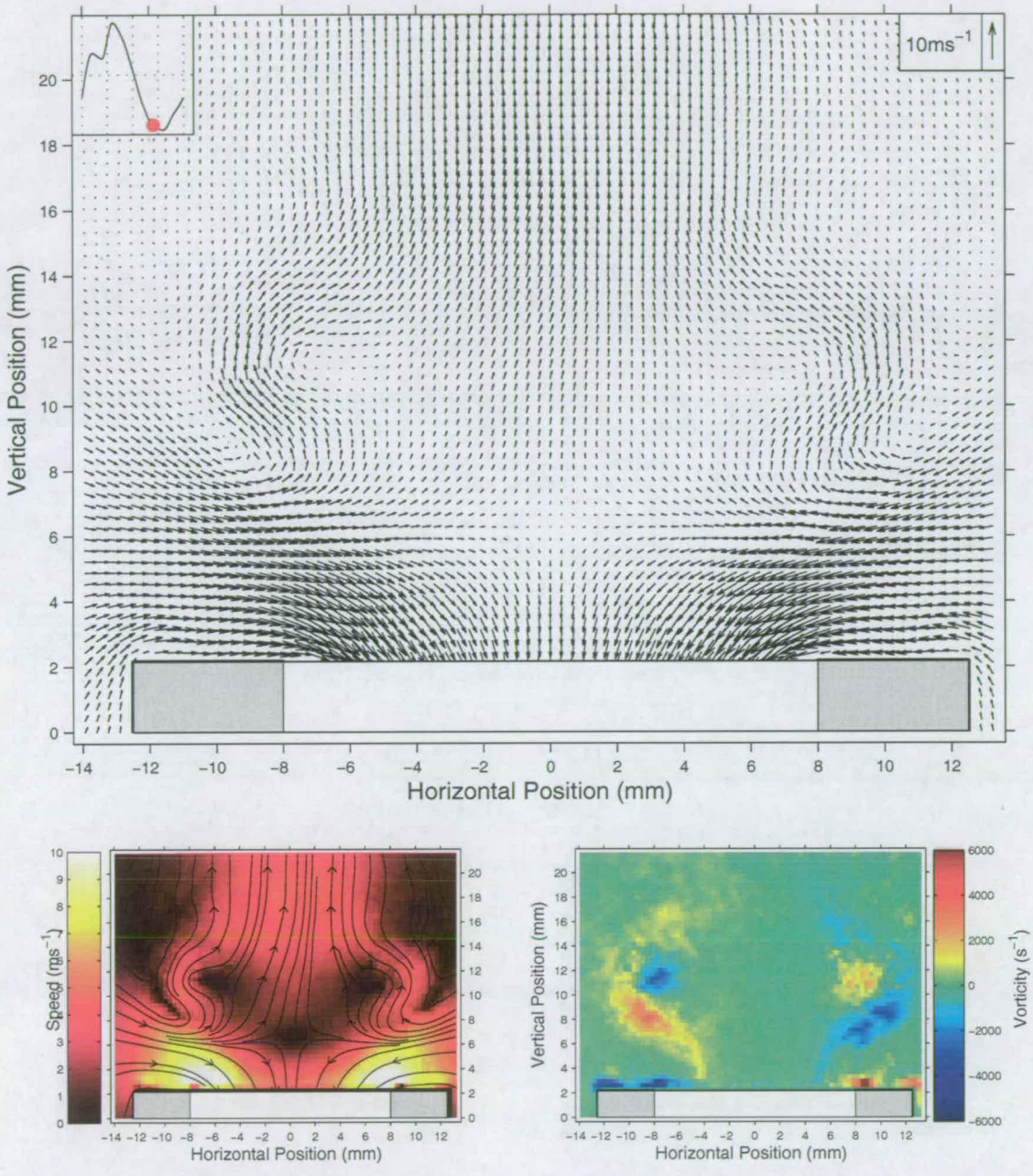


Figure 5.14 continued. (h) Phase step 8. Time = 1.842ms

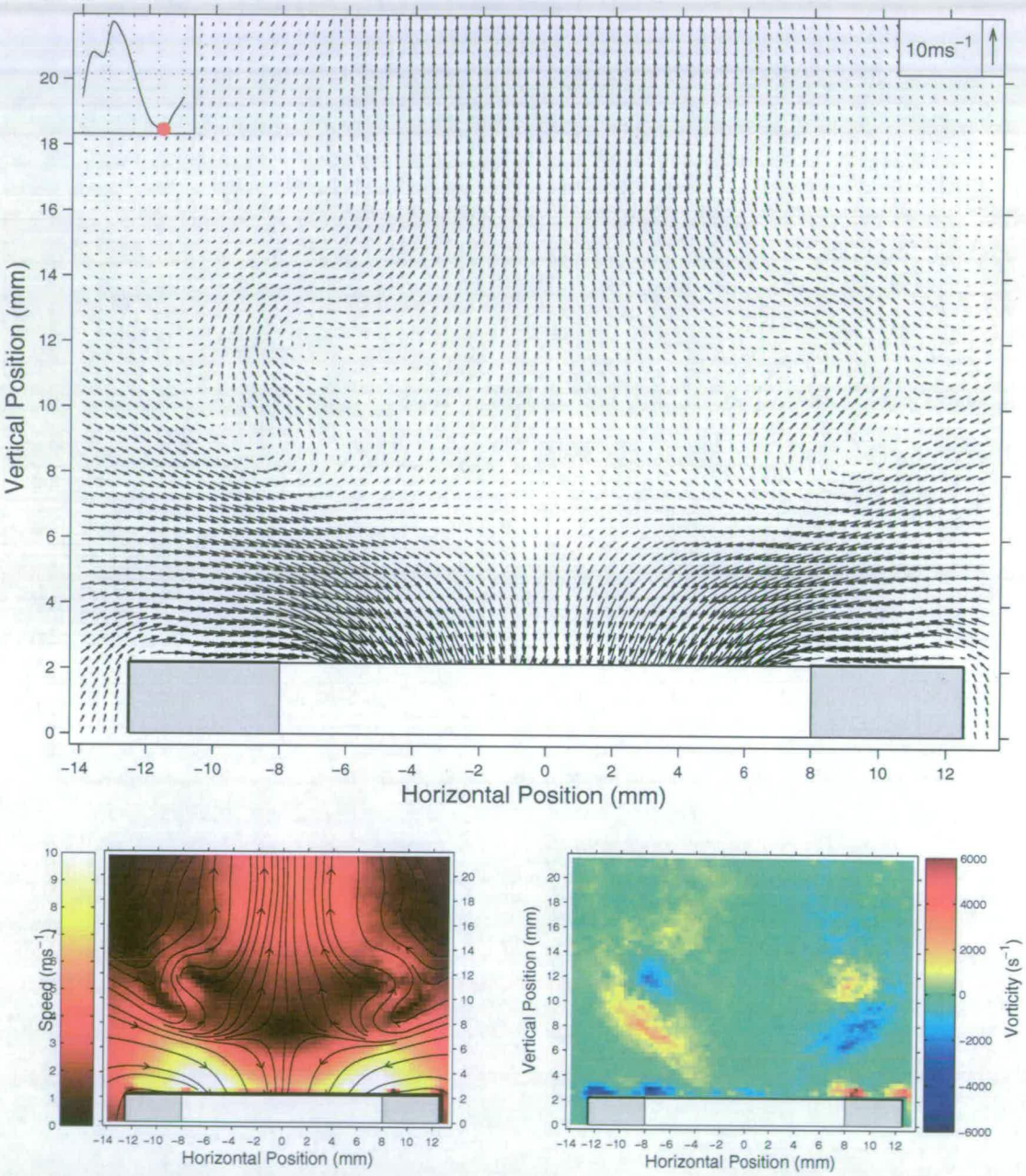


Figure 5.14 continued. (i) Phase step 9. Time = 2.105ms

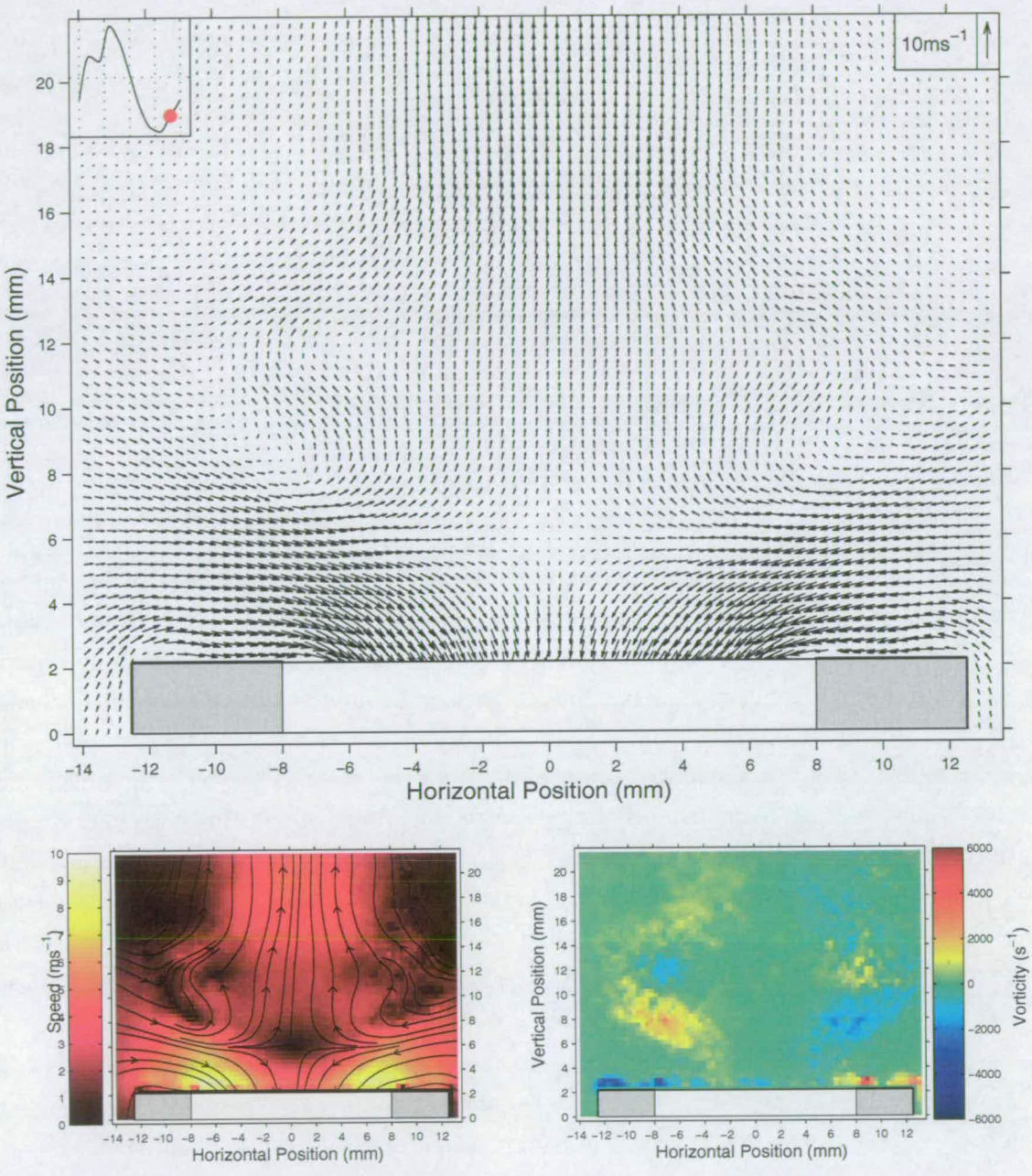


Figure 5.14 continued. (j) Phase step 10. Time = 2.368ms

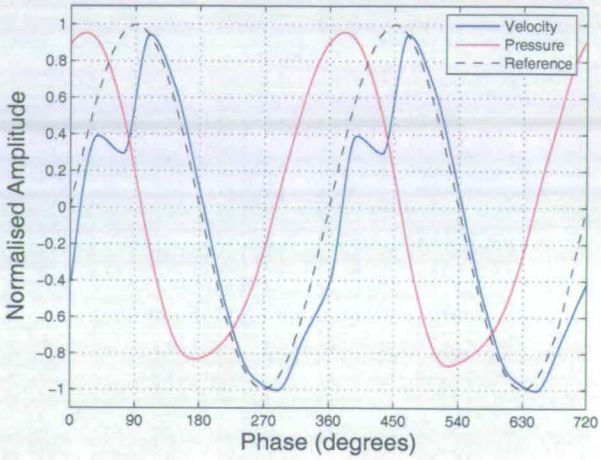


Figure 5.15: Normalised velocity (blue) and pressure signals (red) measured at the open end open end of the tube for the sharp edged termination at 162.3dB. Also shown for comparison is the reference signal (- - -) synchronised with the trigger source.

The mechanism by which this vortex ring pair is generated appears to be similar to that for the flow observed with the sharp edged termination at 157.2dB. On inflow strong flow close to the wall causes boundary layer separation at the inner right angled edge and inward circulating vortex ring generation inside the tube. On outflow strong flow in the opposite direction causes flow separation and vortex generation outside the tube. Additionally, the inflow generated vortices are expelled. The strength of the outward circulating vortex ring is stronger than the inward circulating vortex, unlike in the case of the sharp edge where the two vortex rings are comparable in strength. This unbalance explains why the vortex ring pair observed for the R = 0mm termination at 162.3dB travels on a much more curved trajectory and rotates through about 90 degrees, while in the sharp edged case at 157.2dB the vortex pair travels in an almost straight line away from the tube edge with no global rotation.

As they move further from the open end the outward circulating vortex ring entrains the surrounding air and begins to draw air in from the sides, feeding air into the central (synthetic) jet (phase step 6). The suction stage of the acoustic cycle then begins. Throughout this stage air is drawn into the tube most strongly close to the tube walls and a remnant of the outward jet can still be seen. A stagnation point is observed just outside the open end during inflow. The stagnation point can be seen throughout inflow and moves from a coordinate of (0,4) through (0,6), (0,7), (0,6) to (0,5) in phase steps 7,8,9,10 and 1.

The velocity and pressure waveforms for this measurement is shown in figure 5.15.

The velocity is non-sinusoidal at this sound level, showing a dip corresponding with the PIV measurement at phase step 3 (figure 5.14), just prior to the ejection of the vortex structure. As with the case of the sharp termination at 157.2dB this may be due to an additional drag force caused by the inward circulating vortex ring generated on inflow. The pressure signal is still sinusoidal in nature, confirming that the observed distortion in the velocity is due to non-linear flow phenomena rather than harmonic distortion of the loudspeaker.

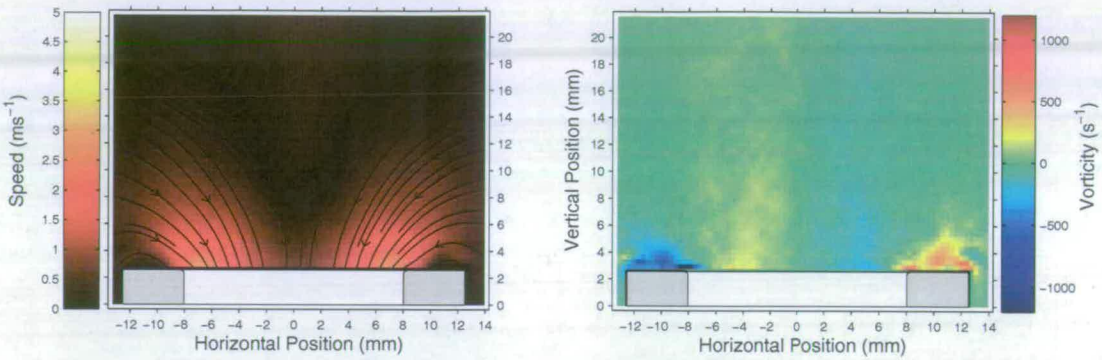
5.3.4 R=0.3mm and R = 1mm terminations

The R = 0mm and 1mm terminations show a number of similarities to the range of flow behaviour observed for the R=0mm termination. There is a flow regime in which vortices are generated on outflow and drawn back in to the tube on inflow for each of these terminations. The sound level at which this occurs is different for each of the terminations. For the R = 0.3mm and R = 1mm termination, external vortex generation begins at sound pressure levels of around 164.5dB and 166.7dB respectively, compared to 158.2dB for the R = 0mm termination. The corresponding acoustic velocity amplitudes are approximately 11.47ms^{-1} and 14.64ms^{-1}.

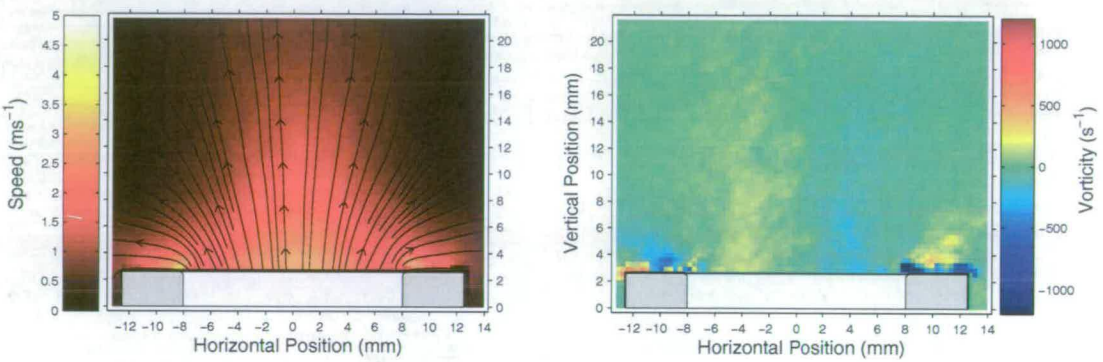
Similarly, a transition to vortex shedding is observed for each of these terminations, again at a higher sound pressure level for each termination as the radius of curvature of the inner edge increases. For the R = 0.3mm termination the vortex shedding transition occurs at 166.7dB ($|u_{ac}|$ = 14.8ms^{-1}). For the R = 1mm termination the threshold is at 169.1dB ($|u_{ac}|$ = 19.33ms^{-1}) and occurs at a velocity amplitude close to the upper measurement limit.

These two flow regimes are very similar in appearance for each of the R = 0mm, 0.3mm and 1mm terminations and have already been shown for the case of the square edged termination. Below the vortex generation regime another flow regime is observed for each of these terminations, but is most clearly seen in the R=0.3mm termination at 157.1dB, and is shown in figure 5.16. This flow regime is characterised by jet flow directly outward from the centre of the open end on outflow and air drawn in most strongly from the sides on inflow. This is an example of jet streaming. On average there is a region of outward flow in front of the open end, and a region of inward flow near the edges of the tube.

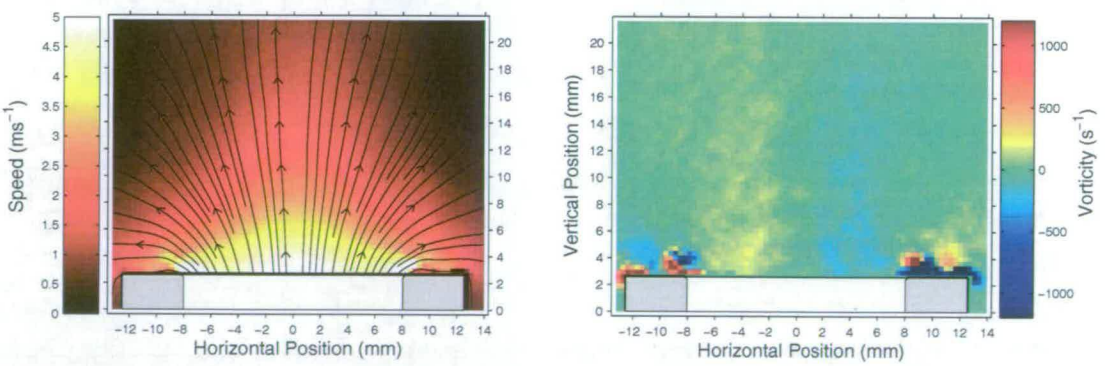
The vorticity maps also show another distinguishing feature of this flow regime. There are areas of vorticity above the tube termination walls that seem to rotate in the wrong direction (inward circulation) and are present over most of the acoustic cycle. At first glance it appears that these may be due to flow separation at the outer right angled edge on inflow. However, careful examination of the vorticity maps reveal what



(a) Phase step 1. Time = 0.000ms

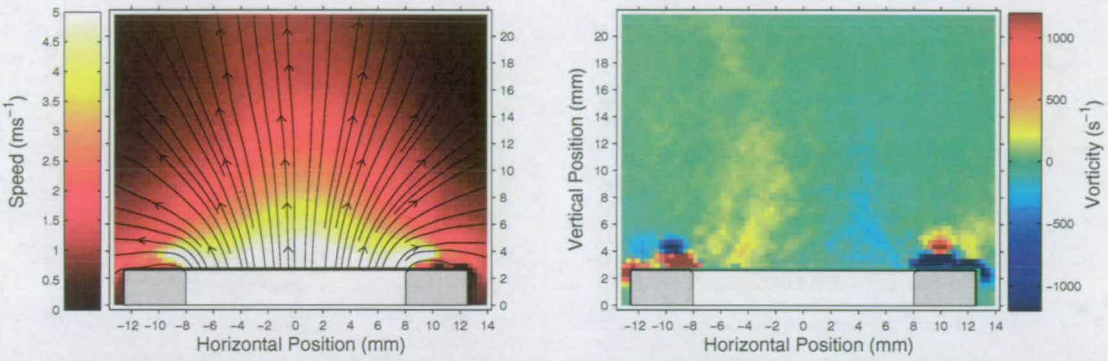


(b) Phase step 2. Time = 0.263ms.

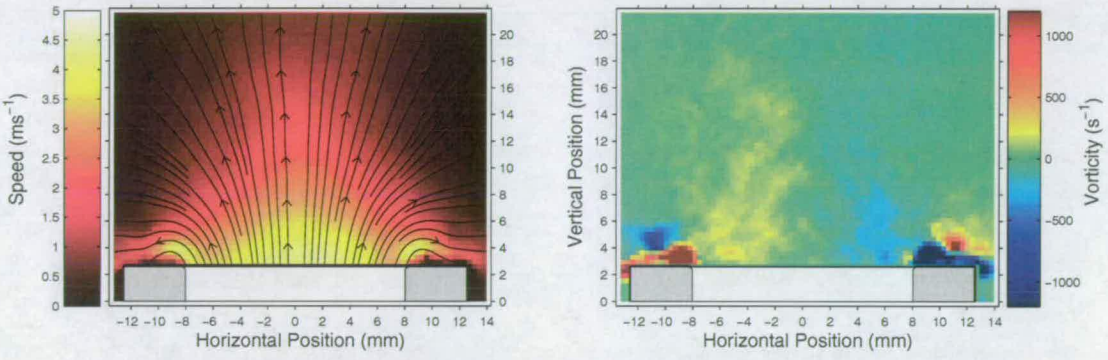


(c) Phase step 3. Time = 0.526ms

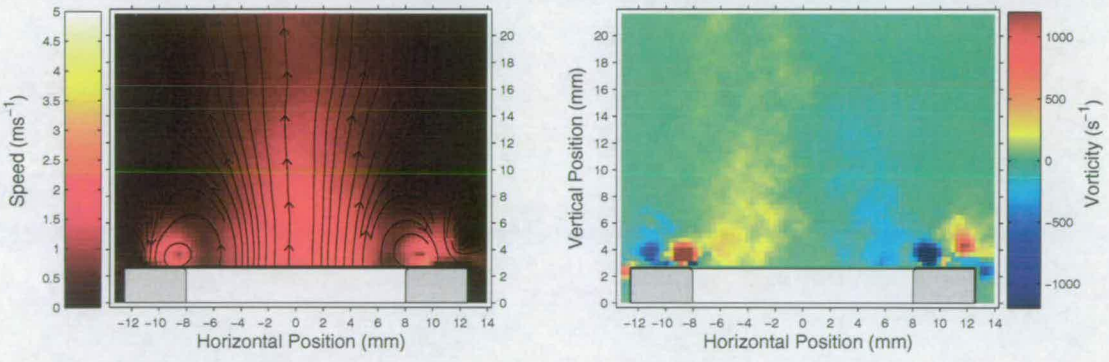
Figure 5.16: PIV results for the the R=0.3mm termination at an SPL of 157.1dB ($|u_{ac}| = 4.89ms^{-1}$). (Left) Velocity magnitude contours with streamlines. (Right) Vorticity contours. Time is with respect to the trigger point. Grey areas represent the termination wall locations.



(d) Phase step 4. Time = 0.789ms

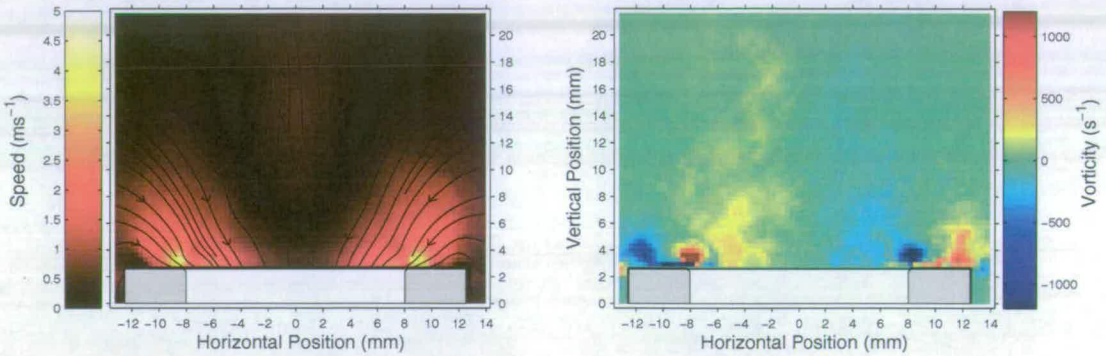


(e) Phase step 5. Time = 1.053ms

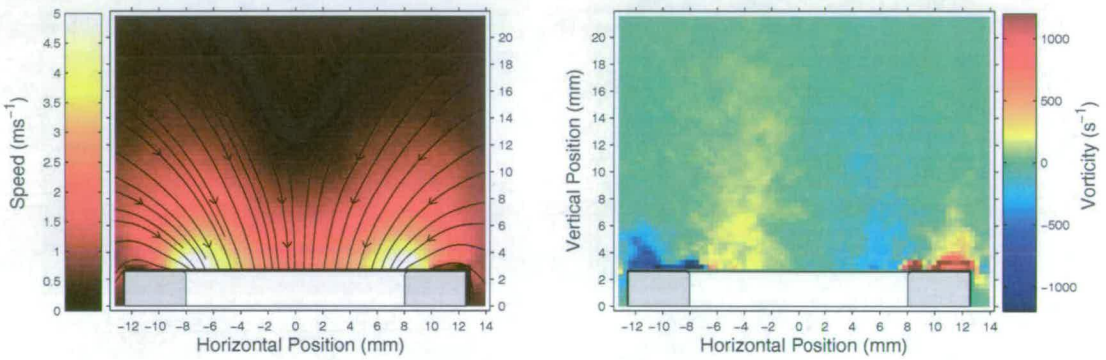


(f) Phase step 6. Time = 1.316ms

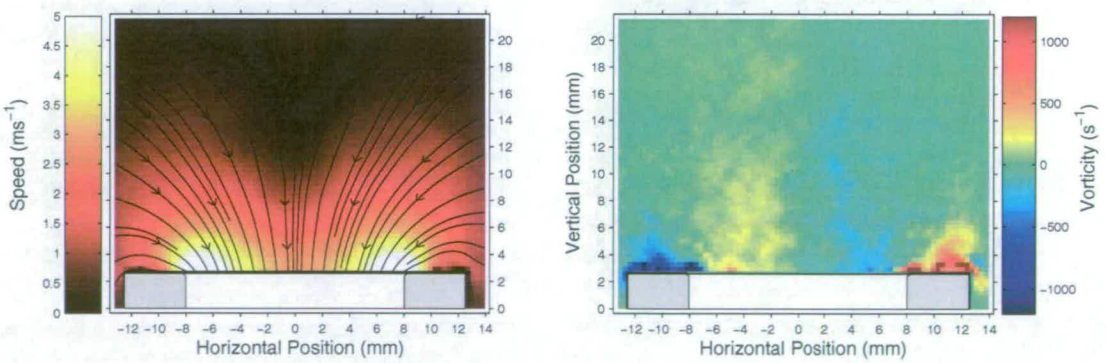
Figure 5.16 continued.



(g) Phase step 7. Time = 1.579ms

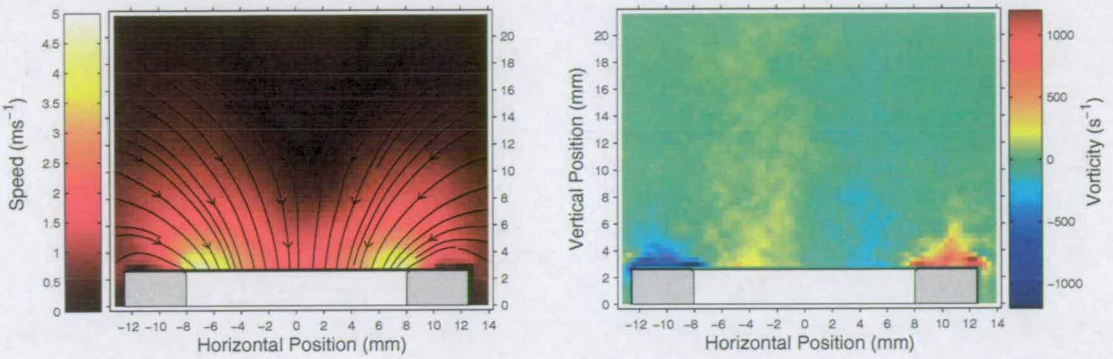


(h) Phase step 8. Time = 1.842ms



(i) Phase step 9. Time = 2.105ms

Figure 5.16 continued.



(j) Phase step 10. Time = 2.368ms

Figure 5.16 continued.

is actually happening.

As previously discussed with the sharp edged and R = 0mm terminations, boundary layer separation on inflow can cause the generation of a vortex ring with inward circulation just inside the open end. On inflow flow separation occurs at the same edge with a flow velocity in the opposite direction resulting in an outward circulating vortex ring just outside the open end. At sound levels above the vortex generation threshold, as discussed above, generally only the outward circulating vortex ring is observed outside the tube for the R = 0mm, 0,3mm and 1mm terminations. Above this level vortex shedding occurs and both inward and outward vortex rings can be seen externally, as they propagate away from the open end.

In this case, however, the story is slightly different. It appears that weak vortex rings with inward and outward circulation are still generated on inflow and outflow respectively. The vortex ring generated on outflow appears to exert a torque on the inward circulating vortex ring which causes it to 'leapfrog' the outward circulating vortex over the remainder of the outward part of the acoustic cycle. The inward circulating vortex can be seen emerging in phase step 3 (figure 5.16(c)) and moving around the outside of the outward circulating vortex through an angle of about 180 degrees by the time phase step 6 is reached (just prior to inflow). Inflow then begins and the remaining inward rotating vorticity is diffused and drawn gradually back towards the boundary layer at the surface of the open end. It is possible that this vorticity is drawn back into the tube and is recirculated on the next acoustic cycle. PIV measurements of the internal flow are necessary to confirm this behaviour.

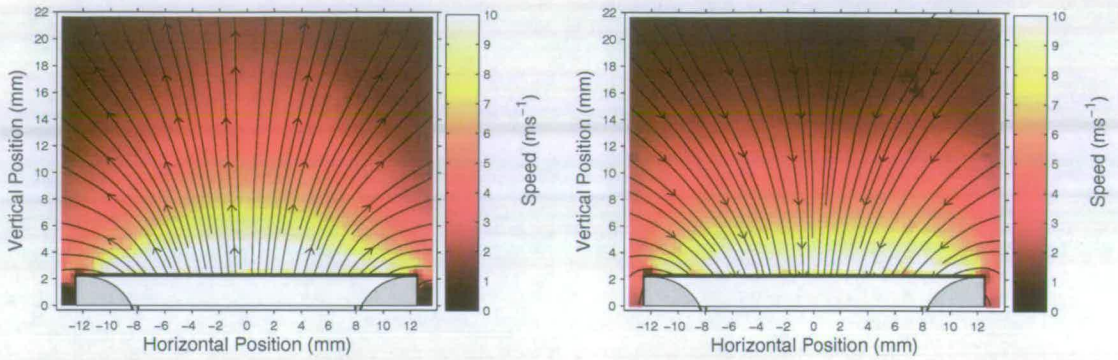


Figure 5.17: PIV velocity magnitude contours with streamlines for the the R=4mm termination at an SPL of 168dB ($|u_{ac}| = 16.84ms^{-1}$). (Left) Maximum outflow (Right) Maximum inflow. Grey areas represent the termination wall locations.

5.3.5 R=4mm termination

The flow above the R = 4mm termination remained potential-like and diffuse for the entire range of measurements made. Figure 5.17 shows velocity magnitude contour plots at maximum outflow and inflow for this termination at a sound pressure level of 168dB. The acoustic velocity amplitude is 16.84ms^{-1}. No vortex shedding was observed for this termination at any of the sound levels measured. Vorticity was noted at the outside edge of the termination on inflow and outflow. Larger vortex structures may have been present to the sides of the termination but were not observable in the field of view used in this study.

5.4 Conclusions

The results of the PIV measurements have revealed that each of the tube terminations can be classified in terms of a limited number of distinct flow regimes. At low acoustic velocity amplitudes non-linear effects are negligible and the velocity field can be described to a good approximation as a potential flow. As the acoustic velocity amplitude increases the sharp edged termination goes through a series of distinct vortex shedding regimes. The R = 0mm, 0.3mm and 1mm terminations show the closest similarity to one another in their observed flow behaviour. There is a distinct transition to a flow regime in which vortex shedding and jet formation become important loss mechanisms. The acoustic amplitude at which this transition occurs clearly depends strongly on the geometry of the termination.

It has been shown in this chapter that PIV measurements of the acoustic particle

velocity provides an invaluable insight into acoustically generated non-linear flow phenomena. The development of interactions between vortex structures and the acoustic field can be observed over the course of an acoustic cycle. This affords a better understanding than is offered by acoustic streaming measurements alone or by other flow visualisation techniques.

Chapter 6

Termination impedance measurements of open ended pipes with PIV

6.1 Introduction

At low acoustic amplitudes, the behaviour of the acoustic field near the open end of a resonant tube is well understood in terms of linear acoustics and the local flow well described by a potential flow model. As the sound pressure within the tube increases, however, localised non-linear effects such as acoustic streaming and vortex shedding increasingly affect the flow behaviour at the open end of the tube. These effects additionally result in an increase in the real part of the terminating impedance of the tube and have implications in the study and construction of woodwind musical instruments.

The detailed geometry of the termination of the open end of a tube plays an important role in the strength of the effects described above. In this chapter an experimental technique based on PIV measurements of the acoustic particle velocity field at the open end of a tube in which a high amplitude sound field has been generated by a loudspeaker will be described. This work will aim to obtain the acoustic volume flow from the PIV velocity maps in order to allow the terminating impedance to be calculated at a number of sound levels using sound pressure level measurements made using a probe microphone. The additional effect of the outcome of changing the termination profile of the open end of a tube and how this affects the real part of the termination impedance will be investigated. A qualitative evaluation of the physical flow mechanisms contributing to the observed losses will be made by comparison of the termination impedance results with PIV vector maps.

6.2 Background

6.2.1 Linear radiation impedance

As described in section 2.2, in order for a standing wave to establish within a tube sufficient sound wave energy must be reflected back into the tube from its ends to maintain the stationary sound field. In the case of an open ended tube, as a sound wave reaches the open end it encounters an abrupt change in acoustical conditions resulting in a sudden change in acoustic impedance. This results in part of the sound wave being reflected back into the tube and the remainder being transmitted as sound. The acoustic impedance at the open end of a tube, often called the radiation impedance Z_r, is a complex quantity that can be split into real and imaginary parts and is defined as the ratio of the acoustic pressure p and the volume flow rate U:

$$Z_r = R + jX = \frac{p}{U} \tag{6.1}$$

where the real part of the radiation impedance, R, is the radiation resistance corresponding to the dissipation of energy from the open end. The radiation reactance, X, is the imaginary part of the radiation impedance and relates to the fluid inertia around the end of the tube.

The geometry of the open end of a tube plays an important role in determining the values of both the radiation resistance and reactance. For an unflanged tube Levine & Schwinger [Levine 48] showed that in the linear regime (i.e. for low acoustic amplitudes at the open end of the tube) the radiation impedance Z_{rlin} is given for low frequencies (i.e such that $ka \ll 1$) by:

$$Z_{rlin} = \left\{ \frac{(ka)^2}{4} + jk\delta_0 \right\} Z_c \tag{6.2}$$

where k is the wavenumber, a the tube radius, $\delta_0 = 0.6133a$ is the unflanged tube end correction and $Z_c = \rho_0 c/S$ is the characteristic impedance of a tube of cross sectional area S in air.

For the same tube but with the addition of an infinite flange at the open end, Nomura *et al.* [Nomura 60] found the linear radiation impedance to be:

$$Z_{rlin} = \left\{ \frac{(ka)^2}{2} + jk\delta_\infty \right\} Z_c \tag{6.3}$$

with the flanged tube end correction $\delta_\infty = 0.8216a$.

Dalmont *et al* [Dalmont 01] found the radiation impedance for tubes with a number of different flanges by numerical simulation and by experiments with an impedance

sensor. Reflections from the edges of circular flanges were shown to have a significant effect.

At high acoustic amplitudes non-linear effects begin to affect the flow behaviour both inside and outside the tube. Effects such as acoustic streaming (steady non-zero time-averaged fluid motions), shock wave formation (deformation of the of the acoustic wave as it propagates along the tube) and vortex formation (a localised effect at the open end of the tube) have been observed. At such high sound levels the linear equations 6.2 and 6.3 are no longer valid [Ingard 67].

6.2.2 Non-linear radiation impedance

Once non-linear effects begin to appear at the open end of a pipe it is often useful to characterise the flow phenomena in terms of the acoustic Strouhal number St (equation 2.19) based on the pipe radius, and the Mach number M (equation 2.21) based on the acoustic velocity amplitude at the open end. The non-linear behaviour of an open ended pipe has previously been modelled by Disselhorst and van Wijngaarden [Disselhorst 80] and by Peters *et al* [Peters *et al* 93, Peters 93b]. For high Strouhal number acoustic flows (high frequency or low acoustic velocity amplitude) the results of Disselhorst and van Wijngaarden for a sharp edged tube suggest an additional non-linear contribution to the termination impedance given by:

$$\frac{Z_{nl}}{Z_c} = \beta.M.St^{\frac{1}{3}}. \tag{6.4}$$

where the parameter β was found by numerical simulation to be between 0.6 and 1 [Disselhorst 80].

6.2.3 Recent work with tube terminations

Recent work by Atig [Atig 03, Atig 04] using a two microphone technique has shown that the radius of curvature of the inner edge of a tube termination is linked to and has a significant effect on the behaviour of the real part of the terminating impedance of an open ended tube at high acoustic amplitudes. The experimental setup used by Atig is shown in figure 6.1.

The two microphone technique is based on the plane wave hypothesis, so that a linear relationship between the pressure and velocity amplitudes is assumed (i.e. $p = \rho_0 cu$). Using this method it is possible to measure the pressure and velocity at any cross section of a tube. The acoustic velocity at the open end of the tube is given by:

$$u = j\frac{p_1}{Z_c}\frac{H_{12}\cos(kL_1) - \cos(kL_2)}{\sin k(L_1 - L_2)} \tag{6.5}$$

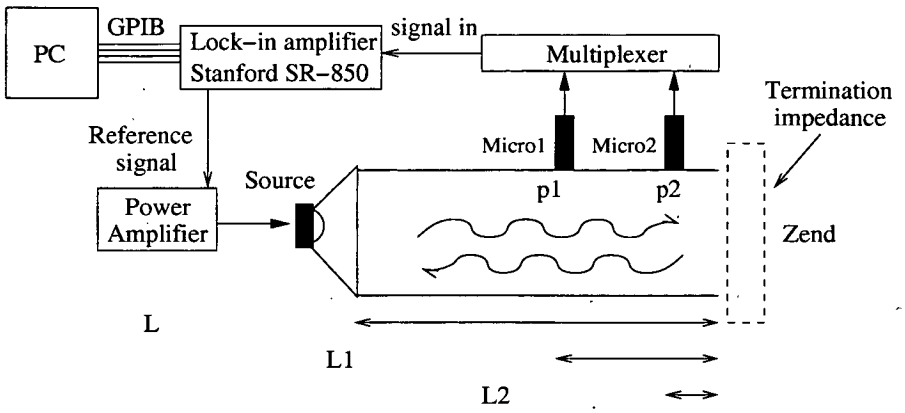


Figure 6.1: Two microphone technique experimental setup used by Atig [Atig 04]

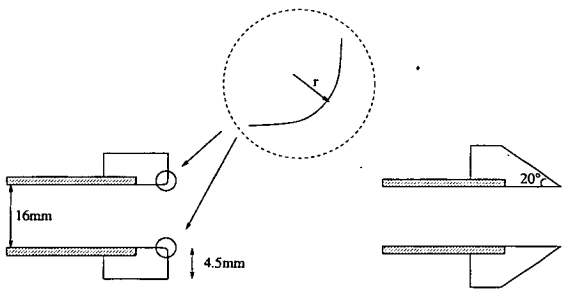


Figure 6.2: Two types of pipe termination geometry studied both in this study and by Atig [Atig 04]) Left: Rounded tube edges with radius of curvature r = 0, 0.3,1 and 4mm. Right: Sharp edged tube with bevel angle of 20°.

where the transfer function $H_{12} = \frac{p_2}{p_1}$ is the ratio of pressures measured at the positions of the two microphones and L_1, L_2 are the distances of the two microphones from the open end. The normalised termination impedance is then calculated using:

$$\frac{Z_{end}}{Z_c} = j\frac{H_{12}\sin(kL_1) - \sin(kL_2)}{\cos(kL_2) - H_{12}\cos(kL_1)} \tag{6.6}$$

The experimental measurements of the real part of the normalised termination impedance (acoustic resistance) produced by Atig are shown in figure 6.3. As can be seen the rate of increase of energy loss depends on the radius of curvature of the inner edge of the termination. Also noted was a discontinuity in the magnitude of the acoustic resistance for certain termination geometries at specific acoustic amplitudes.

The major components and operating conditions used in the present work were deliberately kept the same as those used by Atig [Atig 03, Atig 04] to ensure comparability between results. The tube terminations used in this study were identical

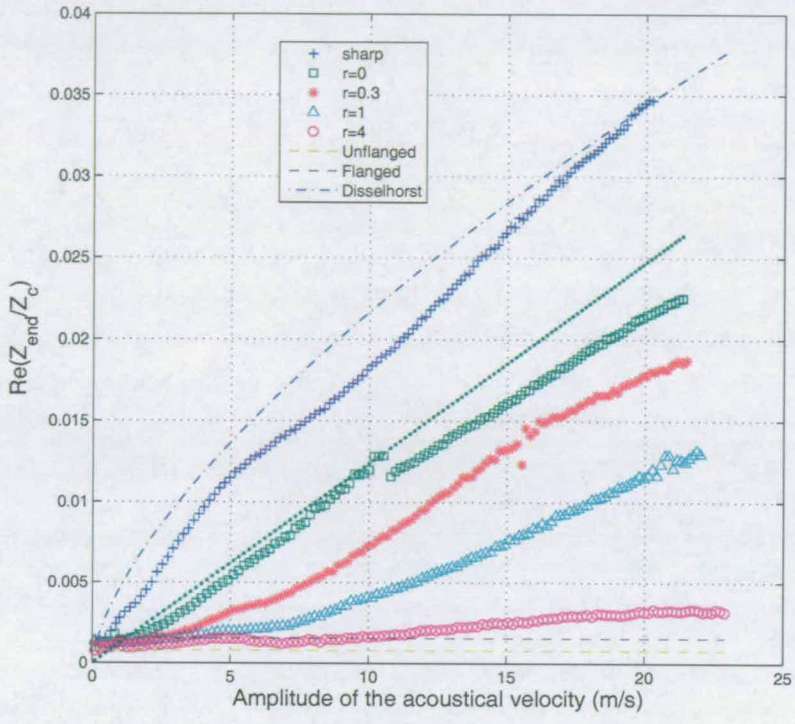


Figure 6.3: Real part of the termination impedance as a function of the amplitude of the acoustic velocity at the open end for the five different terminations shown in figure 4.8. (+) Sharp edge; (Square) R = 0mm; (*) R = 0.3mm; (△) R = 1mm; (○) R = 4mm; (- · -) Equation 6.4 with $\beta = 0.6$; (· · ·) $Z/Z_c = 4M/3\pi$ (from Peters *et al* [Peters *et al* 93]); (- - -) equations 6.2 (lower) and 6.3(upper). From Atig [Atig 04].

to those used by Atig and were manufactured by the same technician in the same workshop in LAUM at the Université du Maine, Le Mans. The compression drivers used in both studies were the same (JBL model 2446H) and the coupling device for mounting the copper tube onto the sound source was also identical to the one used by Atig. The copper tube was the same length, diameter and thickness. The same model of PCB transducer was used to measure the pressure within the tube at the same distance from the open end in both studies.

6.3 Termination impedance measurement technique

An estimate of the non-linear energy loss at the open end of the tube can be made by a calculation of the real part of the termination impedance at the open end of a tube. This section describes the use of PIV data in conjunction with pressure measurements made

with a probe microphone to calculate the real part of the termination impedance. The term 'termination impedance' is used here, rather than 'radiation impedance' (which is used to describe energy losses at an open end solely due to the sudden change in cross sectional area) since the method used here also measures contributions to the impedance due to non-linear loss mechanisms.

At high sound pressure levels non-linear propagation effects can lead to upper harmonic generation within a tube [Hirschberg 96]. Since the concept of impedance within a tube is only valid for a mono-frequency wave an approximation was introduced to allow the termination impedance to be estimated for each of the tube terminations at a range of sound pressure levels. By considering only the first harmonic components of the pressure and volume velocity signals the idea of a termination impedance remains useful [Ingard 67].

The termination impedance Z_t is given by:

$$Z_t = \frac{|p|}{|U|} e^{j(\phi_p - \phi_u)} \tag{6.7}$$

where $|p|$ and $|U|$ are the magnitudes of the first harmonic components of the pressure and volume velocity amplitudes and ϕ_p and ϕ_u are the relative phases of pressure and velocity respectively. With knowledge of the phase difference between pressure and velocity at the open end of the tube it is therefore possible to calculate the termination impedance if the pressure and volume velocity are known.

Assuming cylindrical symmetry, the volume velocity at the open end is calculated by splitting the tube cross section into annular regions each with an associated velocity measured from the PIV maps (see section 6.3.2). It should be noted that in this study it has been chosen to estimate the amplitude and phase of the first harmonic component of the volume velocity by performing a non-linear least squares fit with a sine wave at the fundamental frequency of the tube (380Hz).

The normalised acoustic resistance R_n can then be established by taking the real part of the measured termination impedance Z_t and dividing by the characteristic impedance Z_c:

$$R_n = \Re\left(\frac{Z_t}{Z_c}\right) \tag{6.8}$$

The flows measured in this study are highly non-linear, therefore the definition of impedance is not strictly valid. However, the work in this chapter is based on a simplification and attempts to evaluate what is happening to a linearised version of the acoustic field at non-linear amplitudes.

6.3.1 Pressure measurements

After completion of a series of PIV measurements a separate set of simultaneous recordings of the major acoustical signals was made to allow phase differences and amplitudes to be measured. Signals measured (in Volts) were: the source (reference) sinusoid, the PCB transducer output and the output from a Brüel and Kjær microphone with a 25mm long and 2mm diameter probe attachment placed a short (known) distance from the open end of the tube. Since the PIV measurements were synchronised with the source sinusoid, as described in section 4.2.4, these acoustical measurements ensured that the phase difference between the first harmonic components of the pressure and velocity fields could be calculated at a point in the acoustic field. The probe microphone

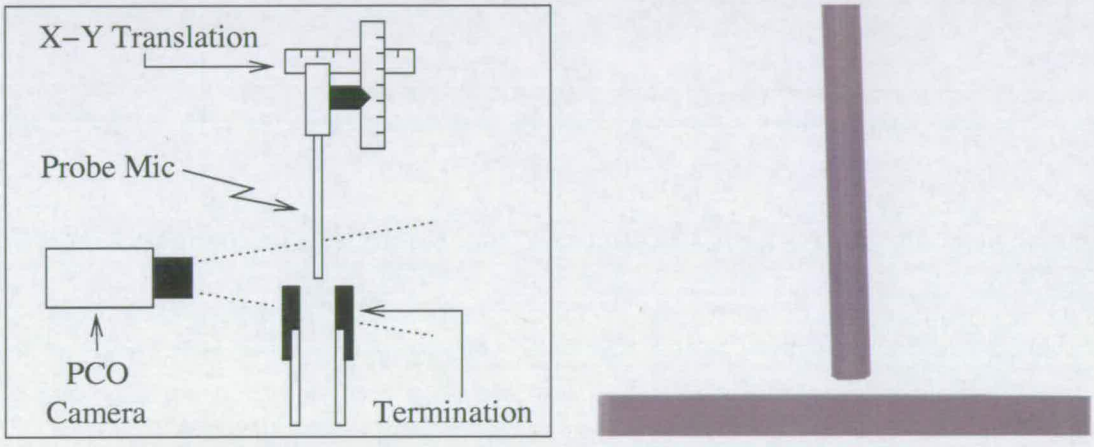


Figure 6.4: Left: microphone positioning setup. Right: photograph showing silhouette of probe microphone positioned above the tube termination.

was mounted vertically on an X-Y translation stage with the probe aligned with the copper tube as depicted in figure 6.4. The position of the probe tip was adjusted until it was located at the centre of the termination at a distance corresponding to two interrogation areas (32 pixels) above the open end. It was important to be able to measure both the pressure and velocity at the same spatial position and this distance was chosen after inspection of trial PIV vector maps and noting that glare problems caused the PIV analysis software to produce anomalous vectors close to the open end. At a distance of 32 pixels (approximately 0.7mm) the vectors were reliable. Adjustments to the horizontal and vertical position of the probe tip were made by making small changes with the X-Y translation stage, and monitored by taking digital photographs using the PCO camera. An example photograph is shown on the right hand side of figure 6.4. The distance in pixels from the open end of the termination to the probe tip could then be measured from the digital images and the probe adjusted

accordingly until the correct position was achieved. Once in the correct position the digital images of the probe in location were retained for future reference.

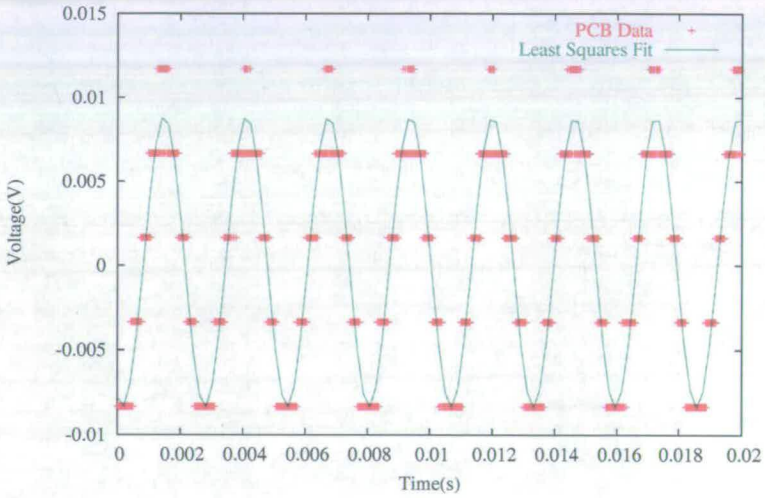


Figure 6.5: Least Squares fit of PCB signal at 136.7dB for the R = 0mm termination.

The sound pressure level within the tube was adjusted to the required level as previously described (section 4.3.3). Labview was then used to simultaneously output a sine wave to the loudspeaker to set up the sound field and record three separate input signals. The three input signals were: 1) the reference input signal to the loudspeaker (before passing through the amplifier); 2) the conditioned output voltage signal from the PCB pressure transducer located 160mm from the open end; 3) the conditioned voltage signal from the probe microphone located 0.7mm outside the open end.

Once acquired, the signals were analysed in Matlab using self-written software to measure the amplitudes and phases of first harmonic components of each of the reference and probe microphone voltage signals. The Probe microphone voltage amplitude was measured and converted into pressure amplitude and the phase difference ϕ_p between the reference input signal and the pressure signal from the probe microphone measured.

For the PCB transducer, the signal amplitude was estimated using an unweighted non-linear least squares method [Press *et al* 92] in GNUPLOT to fit the amplitude and phase of a 380Hz sine wave to the measured data. The decision to use this technique was based on the fact that the PCB signal conditioner is designed for high amplitude measurements and the lowest amplitude measurements in this work were just above the lowest level of its operating range and showed high levels of quantisation.

Figure 6.5 shows a fit with data measured at 136.7dB. The data is highly quantised and this is clearly not an ideal fit of the data. However, since the data gathered from

the PCB transducer was used only to give a reference pressure amplitude, and was not used in any calculations, this was not considered to be a significant problem. The amplitude (the essential piece of information needed from this procedure) appears to be slightly underestimated at this sound level. The level of quantisation in the recorded signal reduces rapidly as the sound pressure level increases, so the underestimation was only really a problem at the lowest level.

A second problem with the recorded PCB signals was discovered (that was not observed on the oscilloscope trace during the course of the experimental work) at sound pressure levels above 165dB. Figure 6.6 shows a comparison of the simultaneously measured signals from the probe microphone and the PCB transducer at 168dB. A significant distortion in the decelerating positive part of the PCB signal near the maxima is observed, whereas only slight distortion is observed in the probe microphone signal near the minima.

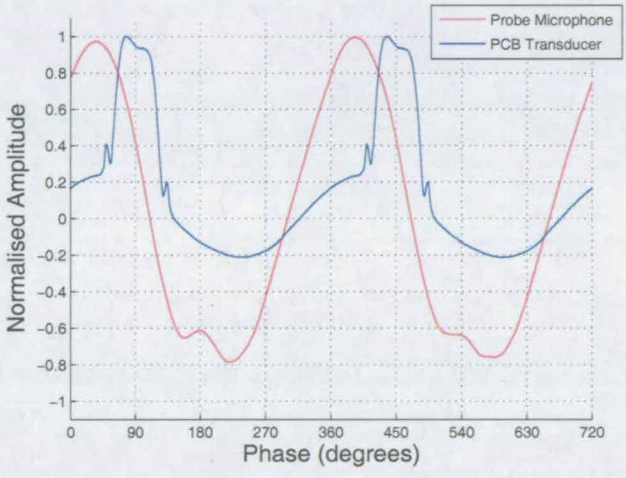
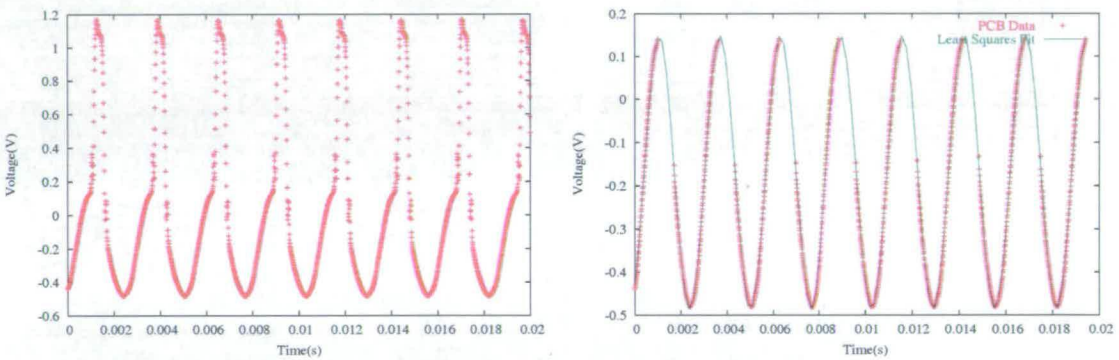


Figure 6.6: Normalised PCB transducer and Probe microphone signals at 168dB for the R = 0mm termination

This distortion may be an indication of non-linear propagation within the tube. However, the pressure field measured with the probe microphone and PIV observations of the velocity field for the R=4mm termination (figure 5.17) both suggest that the acoustic field at the tube termination will still (under the correct termination conditions) behave in an essentially linear manner at 168dB. This has the implication that the sound field within the tube is also essentially linear at 168dB and leads the author to the conclusion that the problem may not be with the sound field, but rather with the PCB transducer itself, or the way in which it is mounted onto the apparatus. It may be that at such high amplitudes structural vibrations either within the transducer

or in its surroundings cause unwanted contact with the diaphragm which results in the observed distortion.

If it is then assumed that the PCB transducer measures correctly at all times except when the distortion is present, it is possible to reconstruct an approximation to the signal that would be measured in the ideal case with no distortion. To do this the distorted parts of the problem signals are disregarded and the least squares method is used to fit the amplitude and phase of a sine wave with an additional DC offset to the remaining data. The signal is then reconstructed and the voltage amplitude estimate used to calculate the pressure. The original and reconstructed PCB signals at 168dB are shown in figure 6.7. The data from the reconstructed signals agree with the measurements made from the oscilloscope readings at the time of the experiment, and give sensible values for the pressure and linear velocity amplitude within the tube. The signals reconstructed in this way were therefore considered acceptable for reference purposes.



(a) (b)

Figure 6.7: (a) Original PCB transducer signal at 168dB for the R = 0mm termination. (b) Corrected signal and non-linear least squares fit of corrected PCB signal

The PCB voltage amplitude was converted to a pressure amplitude simply by using the sensitivity data given by the manufacturer. This was then converted to SPL using equation 2.6. In all instances within this work when a measurement is said to have been made at a certain SPL, unless otherwise stated, it has been calculated using this method.

An estimate of the acoustic velocity amplitude $|u_{ac}|$ at the open end of the tube was made using the pressure signal measured by the PCB transducer located within the tube at a distance of 16cm from the open end. For the simplified case of a standing wave in a lossless tube open at both ends with plane wave propagation and perfect reflection at each end the following equation can be used to calculate the maximum

acoustic velocity amplitude at the open end:

$$|u_{ac}| = |p|/\rho_0 c. \tag{6.9}$$

where $|p|$ is the maximum pressure amplitude measured at a position half way along the tube length. The half length of the tube used in this study was 23cm whereas the PCB transducer was located at a distance of 16cm from the open end. This means that the PCB is not measuring the maximum pressure amplitude within the tube, but a value slightly lower. Figure 6.8 shows the pressure amplitude as a percentage of the maximum amplitude within the tube as a function of distance from the open end for this simplified case. The pressure measured by the PCB transducer at 16cm from the open end is just over 10% lower than that as would be measured if it were located at the centre of the tube (23cm). This corresponds to a difference in the sound pressure level of less than 1dB between the pressure measured at the position of the PCB sensor and the maximum pressure within the tube. The acoustic velocity amplitudes calculated using equation 6.9 are therefore also about 10% too low. These measurements are used to ensure consistency in the sound level within the tube between experiments and are not used in any calculations. Time did not permit correction to these values.

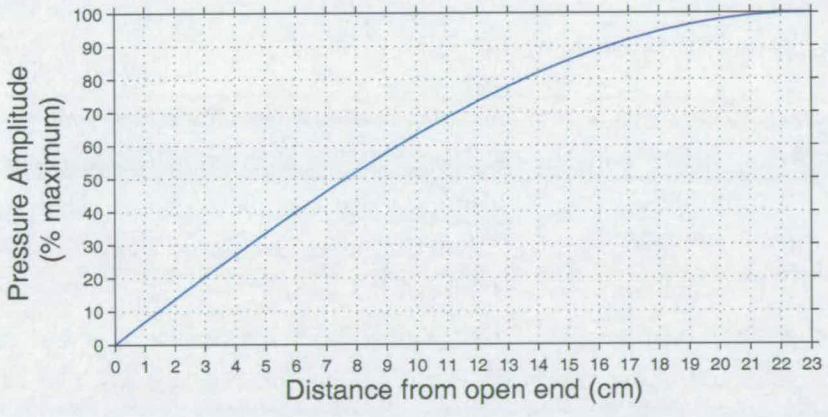


Figure 6.8: Pressure amplitude as a percentage of the maximum amplitude as a function of distance from the open for a standing wave in a 46cm tube open at both ends with zero impedance at the open ends.

For the probe microphone the voltage signal remained well conditioned throughout the range of measurements. The amplitude and phase of the first harmonic component of the signal were measured by using some basic functions in Matlab to calculate the Fast Fourier Transform (FFT) of the signal and to extract the magnitude and phase of the peak located at 380Hz in the resultant frequency domain data (for the present work

this was always the largest peak, as expected). Once the magnitude (in Volts) of the first harmonic of the probe microphone signal was established a corresponding pressure amplitude was calculated by using the gain setting from the conditioning amplifier (as noted at the time of measurement) and equation 4.6 along with magnitude calibration data (see section 4.4) to calculate the overall sound pressure level measured by the probe microphone SPL_{probe}. The acoustic pressure amplitude $|p|$ at the probe tip was then calculated by rearranging equation 2.6 in conjunction with equation 2.2 to give:

$$|p| = \sqrt{2} p_0 10^{\frac{SPL_{probe}}{20}} \tag{6.10}$$

An FFT of the reference sinusoid was taken and the phase of the first harmonic was established in the same way as for the probe microphone. The phase difference ϕ_p between the first harmonics of the probe microphone and reference sinusiod signals was then calculated by subtracting the phase of the probe microphone signal from that of the reference signal. It was important to take into account the phase correction to the phase of the probe microphone at 380Hz before subtraction. In addition, consideration of the effect of the reverse-biased nature of Brüel and Kjær microphones was taken into account. This is explained in more detail in section 4.4.

6.3.2 Volume velocity measurements

For the purpose of this study it was assumed that the flow from the exit of the tube is cylindrically symmetric about the tube axis. Using this assumption it was possible to calculate the volume flux passing through a plane a short distance from the open end of the tube from the velocity maps. Outliers associated with glare limit how close to the open end these calculations can be made. From inspection of the PIV data, vectors at a distance of 32 pixels (approx 0.7mm) from the open end of the tube were not significantly affected and could be used for the calculation.

Calculation method

Before calculating the volume velocity, the situation is simplified by making use of the axial symmetry and taking the average of velocity values at measurement points on symmetrically opposite sides of the tube axis. This reduces the data by half and leaves a set of velocity data consisting of a discrete series of points radially outwards from the tube axis (figure 6.9). These points are labelled $1, 2, 3, ..., n$ in the direction away from the tube axis and the vertical component of velocity associated with each point is v_n. The separation in mm of each measurement point is Δx and the distance from the tube axis to each measurement point is x_n. The volume velocity U_n through each

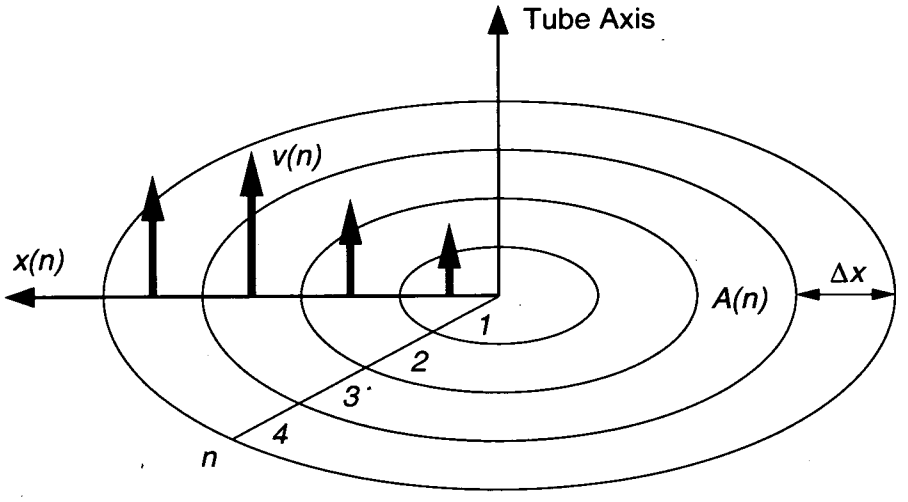


Figure 6.9: Volume velocity calculations for axially symmetric flows

area element A_n associated with each measurement point n is:

$$U_n = A_n v_n \tag{6.11}$$

The area A_n is just the difference in area between two concentric circles of radii $n\Delta x$ and $(n-1)\Delta x$:

$$\begin{aligned} A_n &= \pi \left(n^2 - (n-1)^2\right) \Delta x^2 \\ &= \pi(2n-1)\Delta x^2 \end{aligned} \tag{6.12}$$

In the situation where the tube passes through the centre of one particular interrogation area, then to calculate the volume velocity through a circular plane at the open end of the tube, the equation for the volume velocity is changed slightly. The sum over n is from 0 to n with n=0 being the index referring to the interrogation area containing the central axis, and the area is:

$$A_n = \begin{cases} \frac{1}{4}\pi\Delta x^2 & : n = 0 \\ 2\pi n \Delta x^2 & : n > 1 \end{cases} \tag{6.13}$$

The total volume velocity U was evaluated across the exit of the tube for each of the 10 PIV measurements through the acoustic cycle at each sound level using either equation 6.12 or equation 6.13, depending on the situation. This analysis was performed

using Matlab by summing U_n over n from the tube axis to the tube wall:

$$U = \sum_n U_n \tag{6.14}$$

Error analysis

The error in the above calculation was obtained by using the standard error on the mean associated with the velocity measurements at each point in the averaged vector maps. The standard error on the mean was calculated during the post-processing of the PIV data at the same time as the averaging process whereby the 25 (or so) velocity vector maps at each phase step were reduced to one averaged velocity vector map. Therefore each measurement point n on each vector map consists of a mean velocity $\bar{v_n}$ with an associated standard error on the mean Δv_n

$$v_n = \bar{v_n} \pm \Delta v_n \tag{6.15}$$

The error in the volume velocity at each measurement point in a vector map ΔU_n is given by standard error combination methods as:

$$\Delta U_n = U_n \frac{\Delta v_n}{v_n} = A_n \Delta v_n \tag{6.16}$$

where it has been assumed that the error in the area calculation is negligible in comparison to the velocity error (since the error in dr is of the order of one hundredth of a millimetre). The error in the total volume velocity ΔU at a particular phase is then obtained by summing ΔU_n in quadrature:

$$\Delta U = \left\{ \sum_n (A_n \Delta v_n)^2 \right\}^{\frac{1}{2}} \tag{6.17}$$

Curve fitting

To obtain a value for the amplitude, $|U|$ and phase ϕ_U of the first harmonic of the volume velocity, with associated error estimates, a weighted non-linear least squares fit of the volume velocity and error data was made. The function fitted to the data was a sine wave of frequency (ν) 380Hz:

$$f(t) = A sin(2\pi\nu t + B) \tag{6.18}$$

where A and B are the parameters to be fitted, namely the amplitude and phase of the signal. Gnuplot was chosen to perform the curve fitting procedure which uses

the Marquard-Levenberg algorithm [Press *et al* 92] to help prevent divergent estimates. From initial guesses for the values of A and B the software iteratively computes improved estimates and continues until the estimates converge to the final value. Gnuplot also provided information about error estimates in the amplitude and phase as well as giving the reduced chi-square value, χ^2_R, of the final estimate as a measure of the goodness of fit.

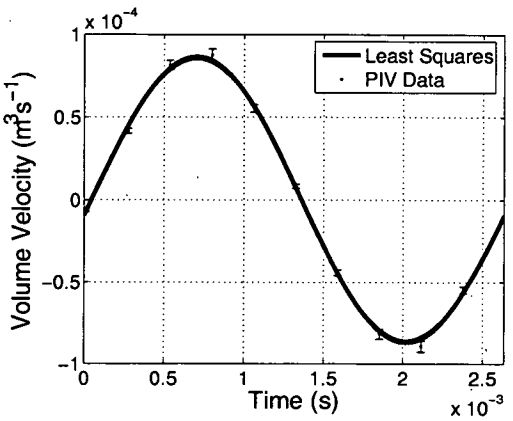
In the ideal case χ^2_R should be of order 1, with values much larger than 1 indicating a number of possible problems with the fit: underestimated errors, errors that are not normally distributed, outliers present in the data, or a poorly chosen fitting function. A value of χ^2_R much less than 1 indicates that the error estimates may be too large or that the statistical assumptions about the data are not justified.

The curve fitting procedure used here is not expected to produce reduced chi-square values of order 1 once the onset of non-linear flow effects is observed since the procedure only fits a single harmonic component to the volume velocity data and it is well known that such non-linear effects can be associated with the generation of upper harmonics. The reduced chi-square value from the sinusoidal least-squares fit does, however, give an indication of the linearity of the volume velocity signal and hence can be used as a qualitative measure of the non-linearity of the flow. It is also interesting to note the points in the acoustic cycle at which the measured volume velocity departs from the idealised linear acoustic behaviour.

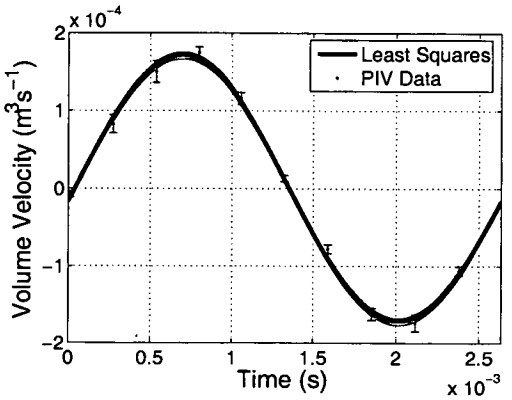
Volume velocity results

Plots of the variation of volume velocity over one acoustic cycle are shown in figures 6.10 to 6.14 for each of the five terminations studied. The solid black line represents the line of best fit from the non-linear least-squares curve fitting procedure, with the maximum and minimum error bounds from the fitting procedure shown in red. Volume velocity data measured from the PIV vector maps is shown in blue with errorbars showing the standard error on the mean for each data point. The reduced chi-square value for the least squares fit is given beneath each plot. In the following text the reduced chi-square shall be referred to simply as chi-square to avoid confusion.

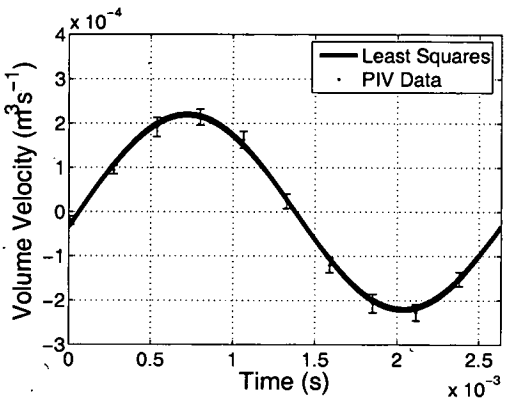
Volume velocity curves for the sharp edged termination are shown in figure 6.10. As can be seen the least-squares results appear to represent the data well, especially below 145.8dB. Above this level non-linear flow phenomena begin to increase in importance and the fit appears to becomes less good with outliers resulting in an increase in the chi-square value. Observations from the PIV vector maps suggest that these outliers can be attributed to the onset of vortex shedding on the outflow part of the acoustic cycle and from inspection of the waveform can be expected to contribute to the generation



(a) $\chi^2_R = 1.03$



(b) $\chi^2_R = 0.89$



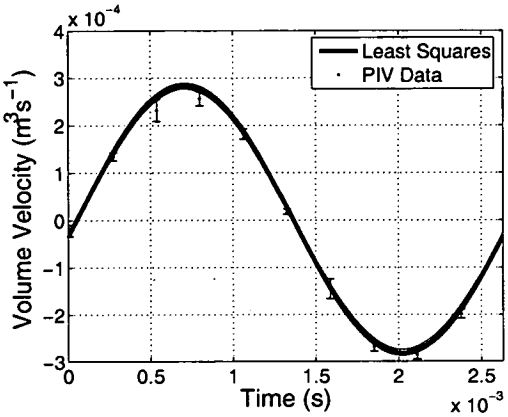
(c) $\chi^2_R = 0.44$

Figure 6.10: Volume velocity data and least-square fit results for sharp ended termination at a number of sound pressure levels: (a)136.8dB (b)141.9dB (c)143.8dB.

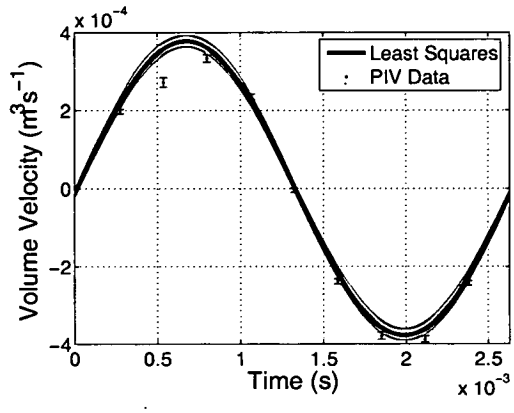
of higher harmonics.

After an initial increase in the chi-square value with increasing sound pressure level there is a reduction which correlates with an increased relative error associated with the value of the outlier (compared with other data points). This suggests that just above the vortex shedding threshold random fluctuations in the velocity field as a whole are comparable with those within the localised vortex structures generated on outflow. At increased sound levels random fluctuations due to the presence of vortices are much greater than those in the bulk of the flow, indicating a generally stable flow regime with periodic strongly turbulent events. This is as observed on the PIV vector maps.

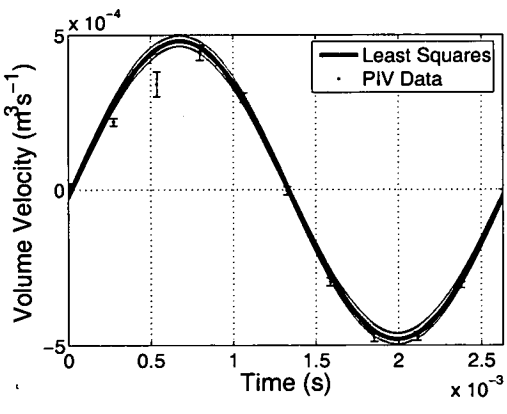
Below 168dB, there is a good fit with the data on inflow, suggesting that the flow remains essentially linear in nature during the suction part of the acoustic cycle. At 168dB outliers associated with vortices generated on both outflow and inflow are observed and result in a large chi-square value.



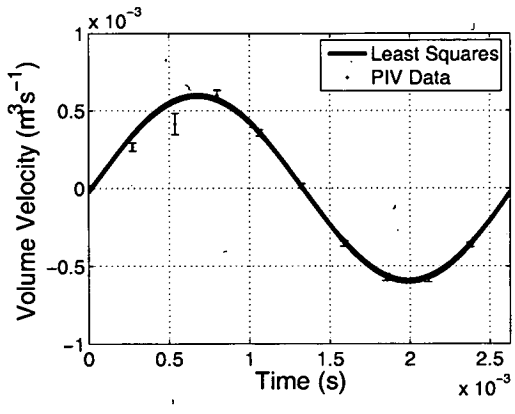
(d) $\chi^2_R = 1.11$



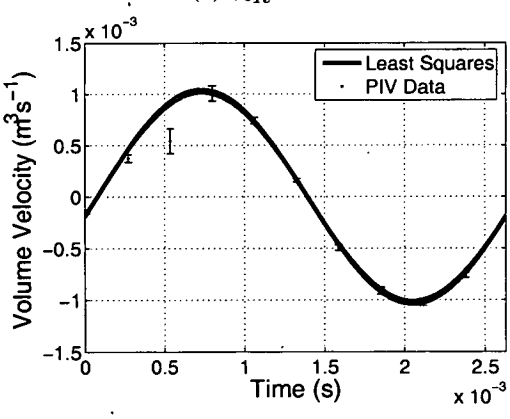
(e) $\chi^2_R = 13.74$



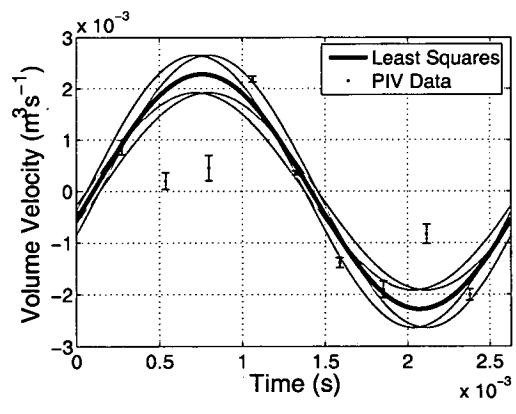
(f) $\chi^2_R = 5.58$



(g) $\chi^2_R = 2.04$

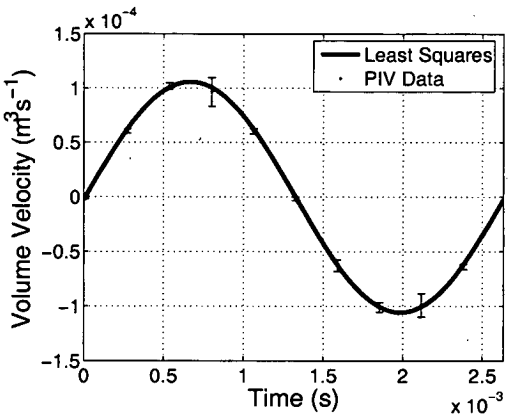


(h) $\chi^2_R = 2.44$

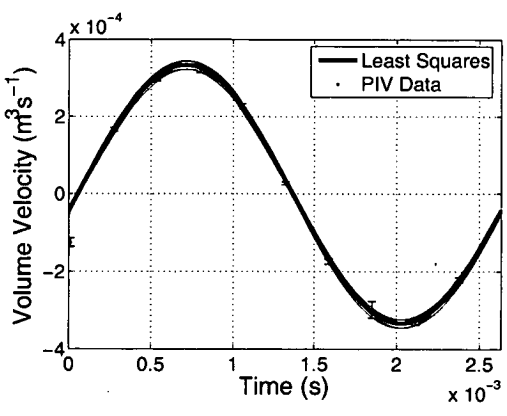


(i) $\chi^2_R = 37.13$

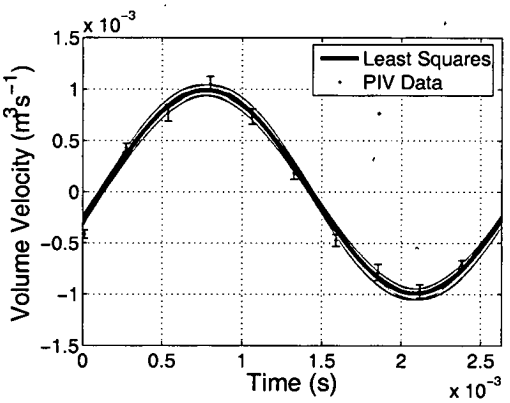
Figure 6.10 continued: (d)145.8dB (e)148.0db (f)150.0dB (g)152.0dB (h)157.2dB (i)168.0dB.



(a) $\chi^2_R = 0.30$



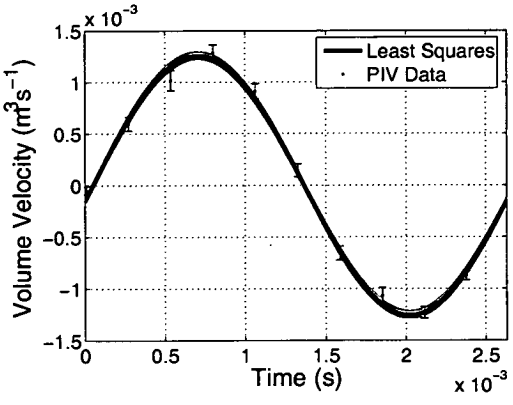
(b) $\chi^2_R = 8.00$



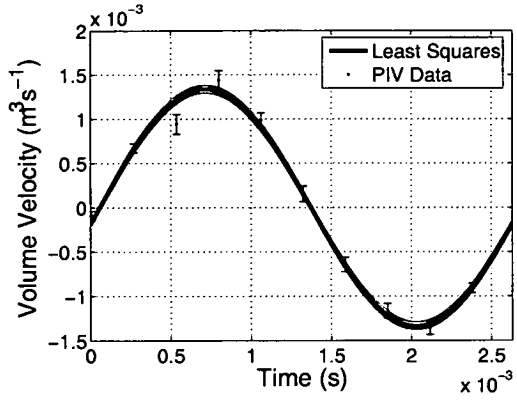
(c) $\chi^2_R = 3.12$

Figure 6.11: Volume velocity data and least-square fit results for R = 0mm termination at a number of sound pressure levels: (a)136.7dB (b)146.9dB (c)157.2dB.

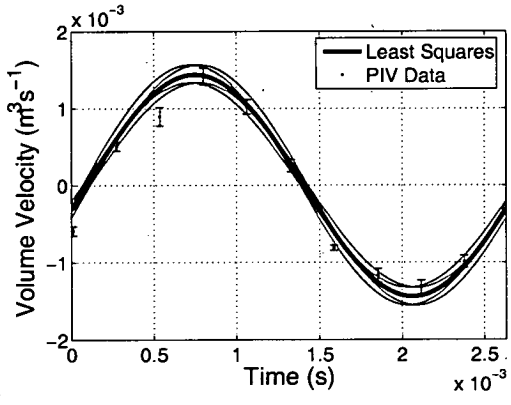
For the R = 0mm and R = 0.3mm terminations (figures 6.11 and 6.12) again a good fit with the volume velocity data is observed below the vortex shedding threshold (at approximately 161.2dB and 166.7dB respectively), after which outliers on the outflow part of the acoustic cycle affect the chi-square value dramatically, especially in the case of the R = 0mm termination. Outliers at the first measurement are observed below the vortex shedding threshold only for the R = 0mm termination at sound pressure levels in the range 146.9dB to 157.2dB and for the R = 0.3mm termination in the range 146.9dB to 162.3dB. These outliers result in an increased chi-square value. From observations of the PIV maps this flow behaviour appears to be related to entrained inflow at the edges of the tube entrance and in both cases this behaviour ceases at around 4dB below the transition to vortex shedding. The least-squares fit generally appears to be a good representation of the volume velocity on inflow.



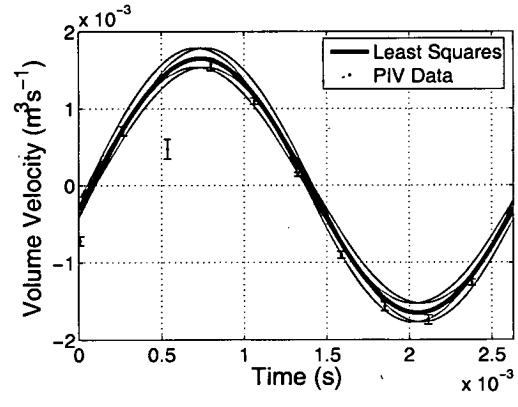
(d) $\chi^2_R = 1.15$



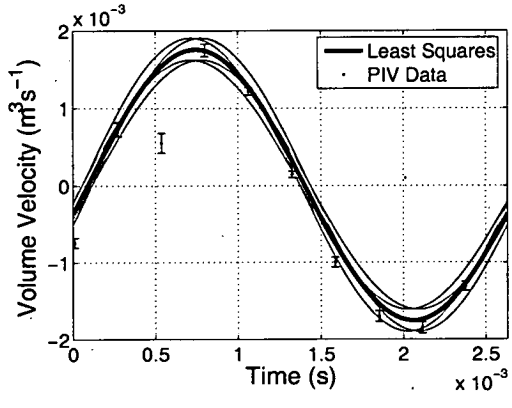
(e) $\chi^2_R = 1.22$



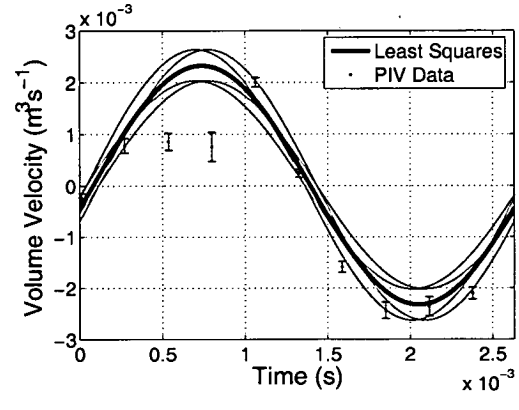
(f) $\chi^2_R = 8.02$



(g) $\chi^2_R = 18.44$

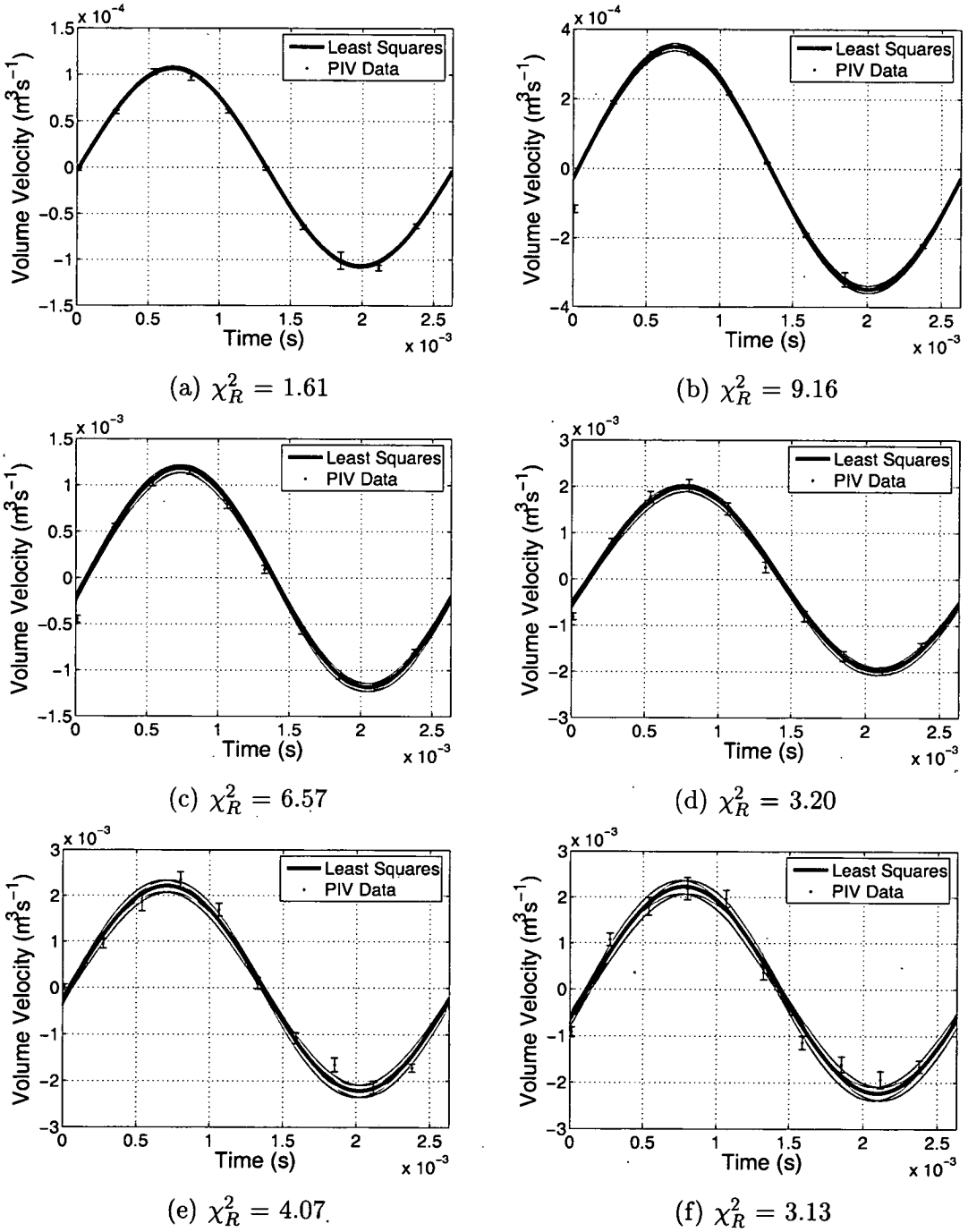


(h) $\chi^2_R = 15.77$



(i) $\chi^2_R = 17.28$

Figure 6.11 continued: (d)158.2dB (e)159.2dB (f)160.2dB (g)161.2dB (h)162.3dB (i)168.0dB



(a) $\chi^2_R = 1.61$

(b) $\chi^2_R = 9.16$

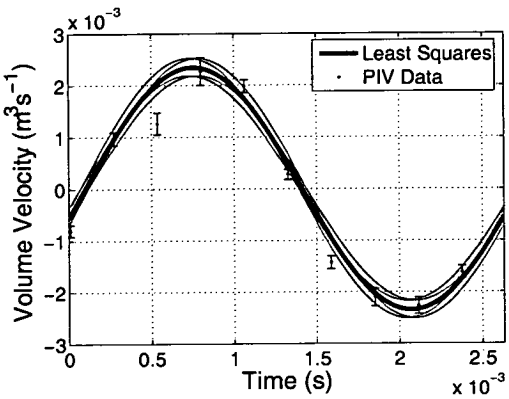
(c) $\chi^2_R = 6.57$

(d) $\chi^2_R = 3.20$

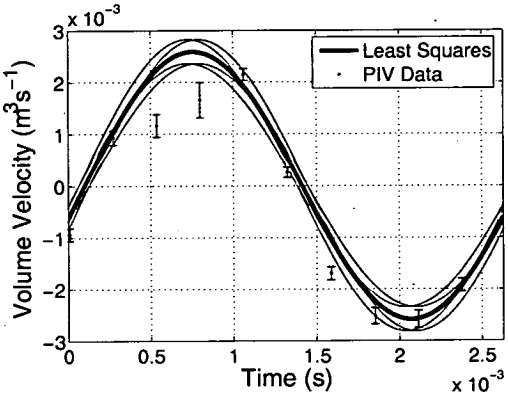
(e) $\chi^2_R = 4.07$

(f) $\chi^2_R = 3.13$

Figure 6.12: Volume velocity data and least-square fit results for R = 0.3mm termination at a number of sound pressure levels: (a)136.3dB (b)146.9dB (c)157.1dB (d)162.3dB (e)164.5dB (f)165.6dB.



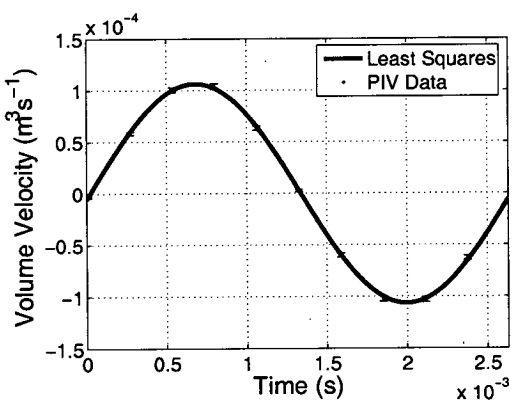
(g) $\chi^2_R = 4.68$



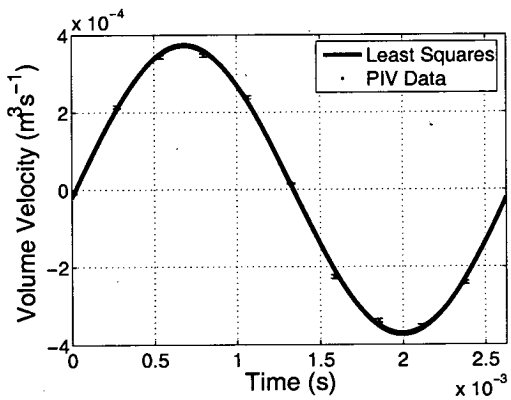
(h) $\chi^2_R = 8.47$

Figure 6.12 continued: (g)166.7dB (h)168.0dB.

The least-squares fit with the R = 1mm termination is good for all of the measured sound pressure levels with chi-square values in the range 0.61 to 5.73 (figure 6.13). The highest chi-square values of 4.89 and 5.73 at 147.0dB and 152.2dB appear to be due to slightly underestimated errors. Vortex shedding begins at 169.1dB for this termination and the associated outliers on outflow are observed at this level and at slightly lower levels in the build up to the transition.

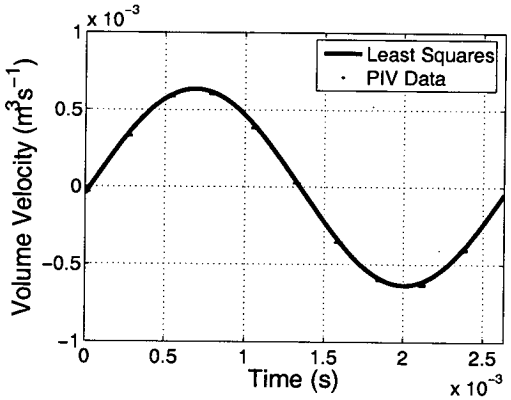


(a) $\chi^2_R = 0.68$

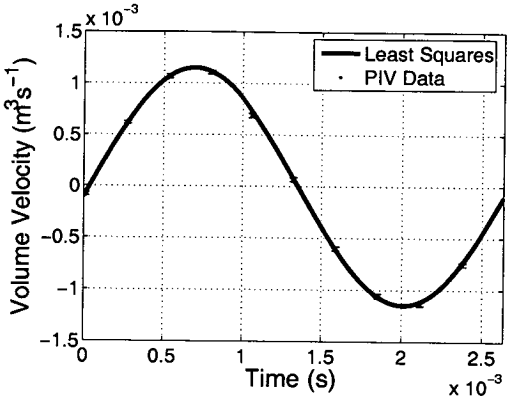


(b) $\chi^2_R = 4.89$

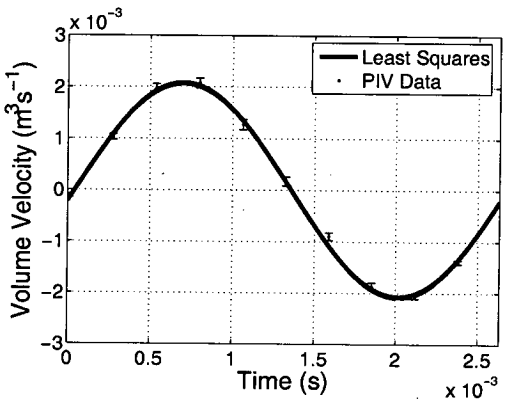
Figure 6.13: Volume velocity data and least-square fit results for R = 1mm termination at a number of sound pressure levels: (a)136.6dB (b)147.0dB.



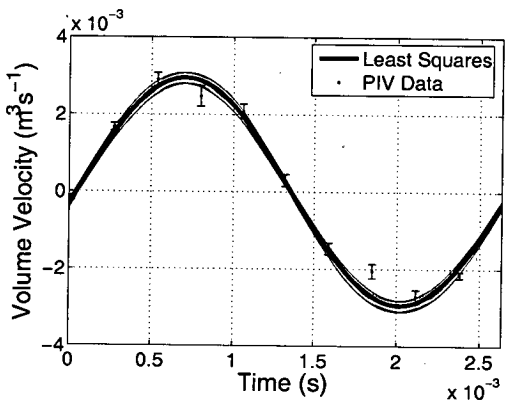
(c) $\chi^2_R = 5.73$



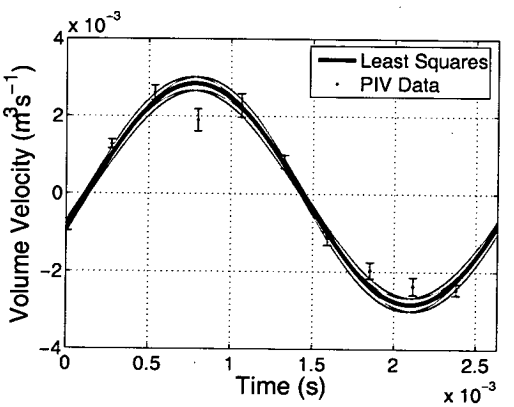
(d) $\chi^2_R = 0.61$



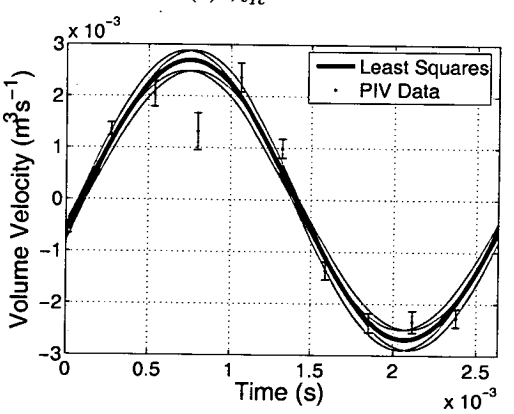
(e) $\chi^2_R = 1.57$



(f) $\chi^2_R = 3.33$

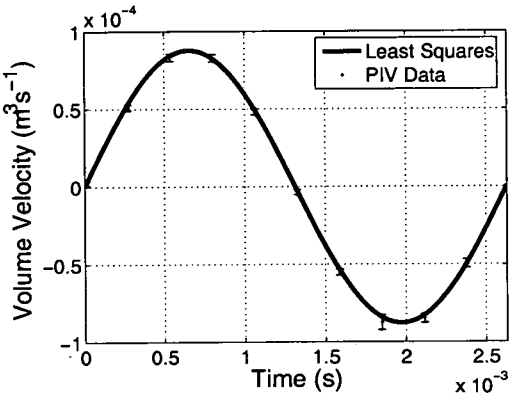


(g) $\chi^2_R = 3.37$

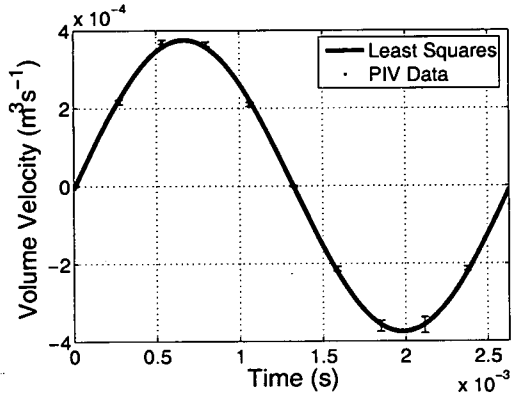


(h) $\chi^2_R = 3.83$

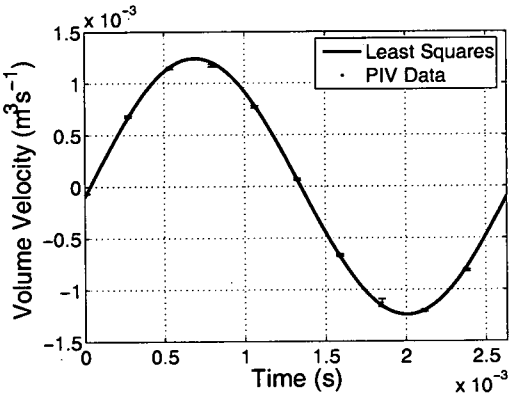
Figure 6.13 continued: (c)152.2dB (d)157.1dB (e)162.3dB (f)166.6dB (g)167.9dB (h)169.1dB.



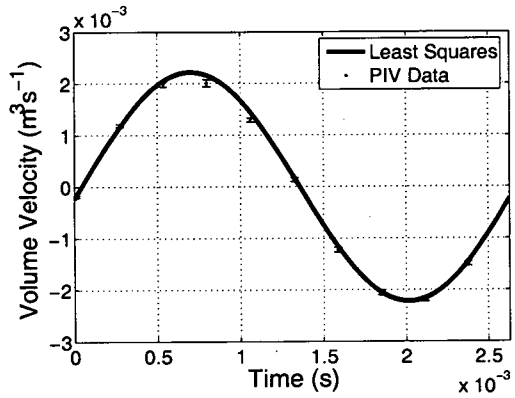
(a) $\chi^2_R = 0.50$



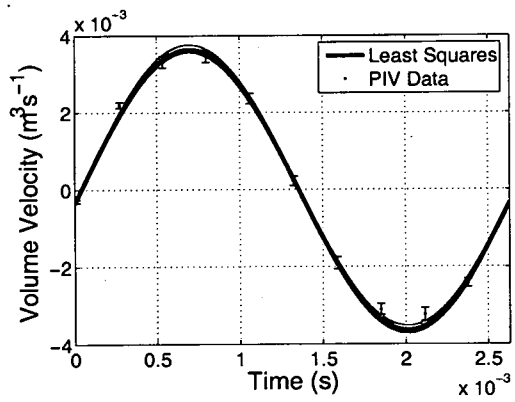
(b) $\chi^2_R = 1.39$



(c) $\chi^2_R = 1.49$

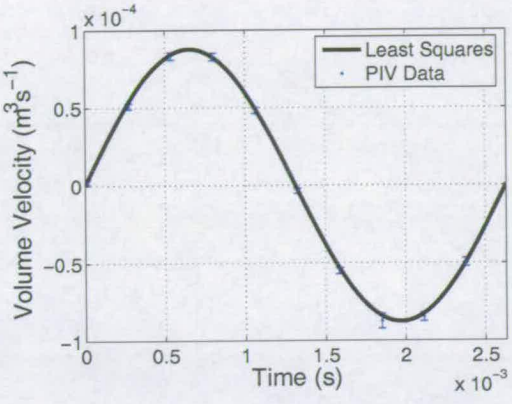


(d) $\chi^2_R = 1.61$

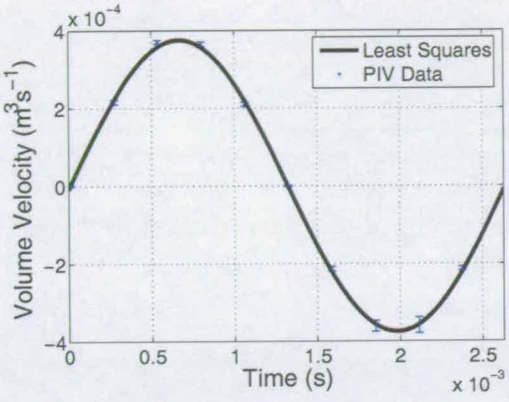


(e) $\chi^2_R = 1.83$

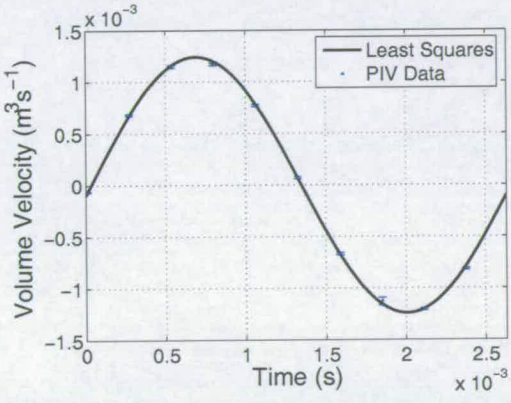
Figure 6.14: Volume velocity data and least-square fit results for R = 4mm termination at a number of sound pressure levels: (a)137.3dB (b)146.9dB (c)157.1dB (d)162.3dB (e)167.9dB.



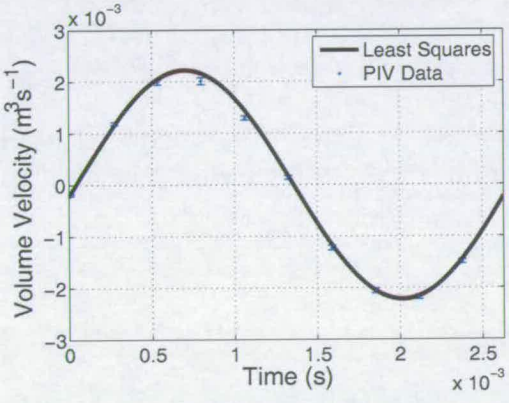
(a) $\chi^2_R = 0.50$



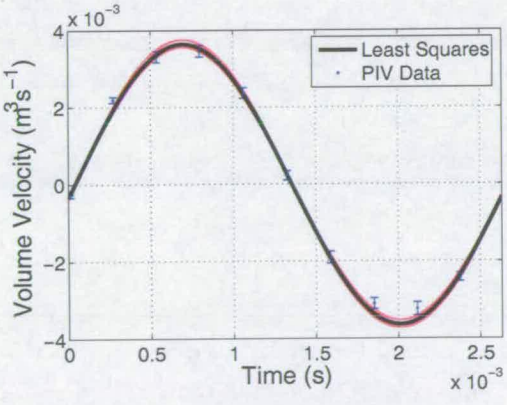
(b) $\chi^2_R = 1.39$



(c) $\chi^2_R = 1.49$



(d) $\chi^2_R = 1.61$



(e) $\chi^2_R = 1.83$

Figure 6.14: Volume velocity data and least-square fit results for R = 4mm termination at a number of sound pressure levels: (a)137.3dB (b)146.9dB (c)157.1dB (d)162.3dB (e)167.9dB.

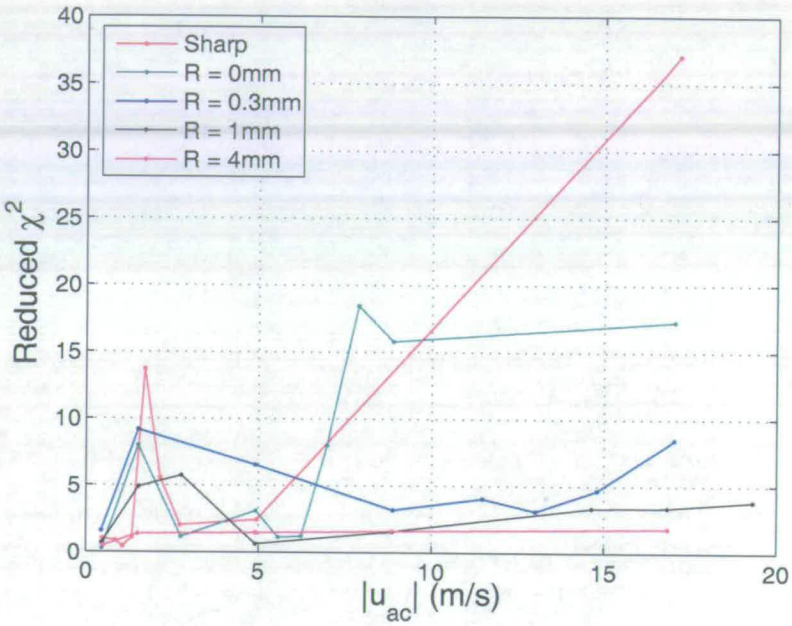


Figure 6.15: Reduced chi-square values for non-linear least squares volume velocity fit as a function of the acoustic velocity amplitude $|u_{ac}|$.

The volume velocity data for the R = 4mm termination is shown in figure 6.14 and shows high levels of linearity with chi-square values mainly between 1 and 2. The reduced chi-square value of 0.5 at 137.3dB may be due to overestimated errors, but the fit with the data still appears to be representative. The linearity observed here is backed up with observations from the PIV vector maps where non-linear flow effects are minimal and the velocity field bears close resemblance to potential flow up to much higher acoustic amplitudes.

The reduced chi-square values for the least-squares fit of the volume velocity data for each of the tube terminations is plotted as a function of acoustic velocity amplitude (calculated from the PCB transducer using equation 6.9) in figure 6.15. The main features discussed above can be clearly seen. For the sharp termination a peak in the chi-square value coincides with the transition to vortex shedding. For the R = 0mm termination a dramatic increase in chi-square occurs after the transition. The general trend appears to be towards linearity as the radius of curvature of the inner edge of the termination increases.

6.3.3 Termination impedance error analysis

The termination impedance is in general a complex quantity and is a function of the pressure and volume velocity amplitudes and of the phase difference θ between them. If we define Z_n as the normalised termination impedance by dividing equation 6.7 by the characteristic impedance Z_c we get:

$$Z_n = \frac{Z_t}{Z_c} = \frac{1}{Z_c}\frac{|p|}{|U|}e^{i\theta} \tag{6.19}$$

Taking the real and imaginary parts of equation 6.7 we get the normalised acoustic resistance R_n and acoustic reactance X_n:

$$R_n = \Re(Z_n) = \frac{1}{Z_c}\frac{|p|}{|U|}cos(\theta) \tag{6.20}$$

$$X_n = \Im(Z_n) = \frac{1}{Z_c}\frac{|p|}{|U|}sin(\theta) \tag{6.21}$$

If we assume that the error in the pressure amplitude is negligible (since it is calculated using a calibrated microphone and the FFT analysis used essentially calculates an average amplitude value from over 380 cycles with a very small error in this value) then we can calculate the error in the real part of the termination impedance ΔR_n due to errors in θ and $|U|$. The error ΔR_θ in the real part of the impedance due to errors in theta is:

$$\Delta R_\theta = \frac{\partial R_n}{\partial \theta}\Delta\theta \tag{6.22}$$

where $\Delta\theta$ is the error in the phase difference between the pressure and volume velocity. Taking the derivative of R_n with respect to θ we get:

$$\Delta R_\theta = -X_n\Delta\theta \tag{6.23}$$

Similarly, the error ΔR_U in the real part of the impedance due to errors in the volume velocity $\Delta|U|$ is:

$$\Delta R_U = \frac{\partial R_n}{\partial |U|}\Delta|U| = -\frac{R_n}{|U|}\Delta|U| \tag{6.24}$$

The combined error in the real part of the impedance is then calculated as:

$$\Delta R_n = \left\{\Delta R_\theta^2 + \Delta R_U^2\right\}^{\frac{1}{2}} \tag{6.25}$$

6.4 Termination impedance results

Once the least-squares curve fitting procedure was complete and the amplitude and phase of the volume velocity signal determined, the phase difference between the first harmonic components of pressure and volume velocity for each sound level and termination was evaluated, allowing the termination impedance to be calculated using equation 6.7. The normalised acoustic resistance of the termination was then deduced using equation 6.8 and plotted against the idealised linear acoustic velocity amplitude $|u_{ac}|$ at the open end of the tube as measured by converting the pressure measurement made at the location of the PCB transducer using equation 6.9. It should be recalled from section 6.3.1 that the sound pressure level measured by the PCB transducer is around 1dB too low. Therefore the linear acoustic velocity amplitude $|u_{ac}|$ at the open end is underestimated by about 10%. As the PCB transducer was only used to ensure consistency in the acoustic amplitude within the tube between experiments, and not used in the impedance calculations, this does not significantly affect the results. Time did not allow correction to the value of $|u_{ac}|$, but the effect of this correction would be a minor reduction in the gradient of results. Errors in the normalised acoustic resistance were calculated as described in section 6.3.3.

Figure 6.16 shows the results of the acoustic resistance calculations for each of the five terminations studied. Also shown for comparison are the linear predictions of Levine & Schwinger [Levine 48] for an unflanged tube and of Nomura *et al.* [Nomura 60] for a tube with an infinite flange.

At low acoustic amplitudes it can be seen that there is a convergence towards a value slightly higher than the linear predicted result of Nomura *et al.* [Nomura 60] for all terminations except the R=4mm termination. There is no obvious explanation for this problem of the but it may be associated with convection currents within the PIV enclosure being of comparable magnitude to the acoustic velocity amplitude causing a slight but significant disturbance of the velocity field at low amplitudes. The R=4mm termination tends towards a value just above the Levine & Schwinger [Levine 48] result for an unflanged tube as expected. Dalmont [Dalmont 01] found the effect of a finite circular flange was to raise the termination impedance slightly above the unflanged linear prediction. The observed convergence for the R=4mm termination is in agreement with expectations since the tube terminations used are of finite width and cannot be considered truly unflanged.

It can be seen that the linear predictions no longer hold when the acoustic amplitudes are as high as those found in the range of measurements made in this study (equivalent to those found within real woodwind instruments playing fortissimo) and that the acoustic resistance is dependent on the acoustic velocity amplitude within

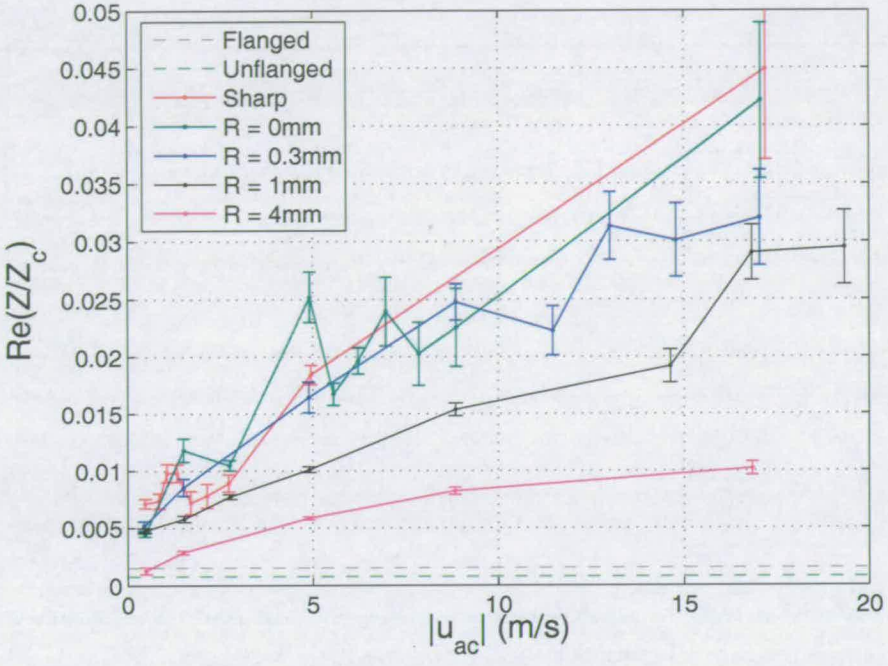


Figure 6.16: Real part of the normalised termination impedance for five termination geometries as a function of the acoustic velocity amplitude $|u_{ac}|$.

the tube. The general trend is for the rate of increase of the acoustic resistance with acoustic velocity amplitude to reduce with increasing radius of curvature.

For the sharp termination there is an initial sharp increase then sudden drop in the acoustic resistance. The peak value corresponds to the transition to the first regime of vortex shedding, described in section 5.3.2, in which vortex rings from previous acoustic cycles diffuse and propagate slowly. The drop in the acoustic resistance occurs at the same acoustic amplitude as the second regime of vortex shedding described in section 5.3.2. After this initial peak the acoustic resistance continues to rise steadily but at a lesser rate than in the initial rise.

The shape of the plot for the R = 0mm termination is rather complicated and there is no obvious single marker of such a transition, although such a transition can be clearly observed in the PIV velocity maps for an acoustic velocity amplitude of 7.87ms^{-1}. The scatter observed in the data for the R = 0mm termination is most likely to be due to the instability of the velocity field at acoustic amplitudes close to the threshold at which the transition to vortex shedding occurs. As the acoustic velocity amplitude increases towards the threshold the flow undergoes a series of significant changes from simple linear behaviour. Observations of the velocity profile at the tube termination at increasing sound levels show marked deviation from the idealised plane wavefronts. The

PIV vector maps show that the effects of jet formation and vortex generation at the tube edges increasingly disturbs the velocity field in this region. This will be discussed further in section 6.6.

An approximately linear increase in the real part of the terminating impedance is observed for the R = 0.3mm termination up to an acoustic velocity amplitude of $12ms^{-1}$ where there is a slight dip followed by a continued rise at a lesser rate. The PIV vector maps show an increase in non-linear flow phenomena for this termination in the vicinity of this dip; however, the flow does behave in a more linear fashion over a larger range of velocities than for the terminations with a sharper inner edge. Jet flow and vortices generated at the inner edges of the tube exit are observed to increase in strength with increasing acoustic velocity amplitude (as observed with the sharp and R = 0mm terminations), but the development from simple linear flow through to vortex shedding is more gradual and takes place over a wider dynamic range.

The data for the R = 1mm termination show an increase in the real part of the termination impedance in proportion to the acoustic velocity amplitude up to about $15ms^{-1}$. Above this level the PIV vector maps show an increase in non-linear flow behaviour indicating the start of the transition to vortex shedding. These measurements are at the upper end of the range of acoustic amplitudes physically possible to study with the apparatus used, and it was only possible to view the completed regime transition for one sound level for this termination.

The vector maps for the R = 4mm termination show much more potential flow-like behaviour over the whole range of measurements made. This is in qualitative agreement with the impedance data, with values closest to the linear predictions. PIV vector maps show the presence of vortex generation at high acoustic velocity amplitudes, but no transition to vortex shedding was observed for this termination over the range of measurements made.

6.5 Comparison with two microphone method results

Figures 6.17 to 6.21 show a comparison of the normalised termination resistance results calculated using PIV with those calculated by Atig [Atig 03, Atig 04] using the two microphone method for each of the tube terminations. As can be seen, the measurements made using PIV are of the same order of magnitude and are in general higher than those estimated using the two microphone technique.

The PIV results for the sharp termination (figure 6.17) are in close agreement with the results of Disselhorst and van Wijngaarden [Disselhorst 80] calculated using equation 6.4, with most of the data falling between the extreme values calculated with $\beta = 0.6$ and $\beta = 1$. At acoustic amplitudes below the transition to vortex shedding

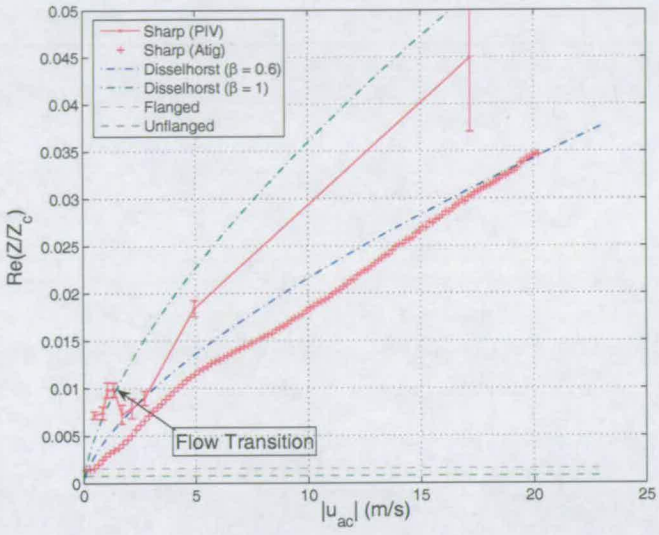


Figure 6.17: Comparison of the real part of the termination impedance as a function of acoustic velocity amplitude $|u_{ac}|$ calculated using two methods for the sharp termination: PIV measurements (solid lines); Two microphone method (Atig [Atig 03, Atig 04]) (+). The linear predictions for flanged and unflanged tubes are shown (- - -). Sharp termination. For comparison the results calculated using equation 6.4 are shown (- · -) with $\beta = 0.6$ and $\beta = 1$.

the PIV results are in agreement with the $\beta = 1$ result of Disselhorst. At the acoustic velocity amplitudes above the flow transition, and below 5ms^{-1}, the impedance results agree best with equation 6.4 with $\beta = 0.6$.

Atig observed the presence of discontinuities in some of his measurements, notably at 10.5ms^{-1} for the R=0mm termination (figure 6.18), at 15.4ms^{-1} for the R=0.3mm termination (figure 6.19)and at around 20.5ms^{-1} for the R=1mm termination (figure 6.20). It was suspected that the cause of these discontinuities could be connected with a change in flow regime. The PIV velocity vector maps obtained in chapter 5 indeed confirm the presence of a transition to a vortex shedding regime. The velocity amplitudes at which these flow regime changes occur is observed to be significantly lower than those observed by Atig for the R = 0mm termination, but appears to be slightly lower but in good agreement for the R = 0.3mm and R = 1mm terminations. For the R=0mm termination the flow regime transition occurs at an acoustic velocity amplitude (measured at the PCB transducer) of 7.87ms^{-1}, for the R=0.3mm termination at 14.8ms^{-1} and for the R=1mm termination the flow regime change begins at 19.3ms^{-1}.

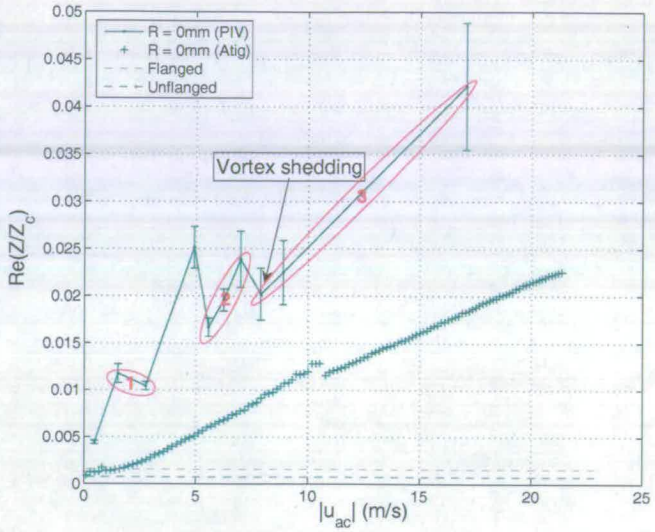


Figure 6.18: Comparison of the real part of the termination impedance as a function of acoustic velocity amplitude $|u_{ac}|$ calculated using two methods for the R=0mm termination: PIV measurements (solid lines); Two microphone method (Atig [Atig 03, Atig 04]) (+). The linear predictions for flanged and unflanged tubes are shown (- - -). Flow regimes are highlighted in red.

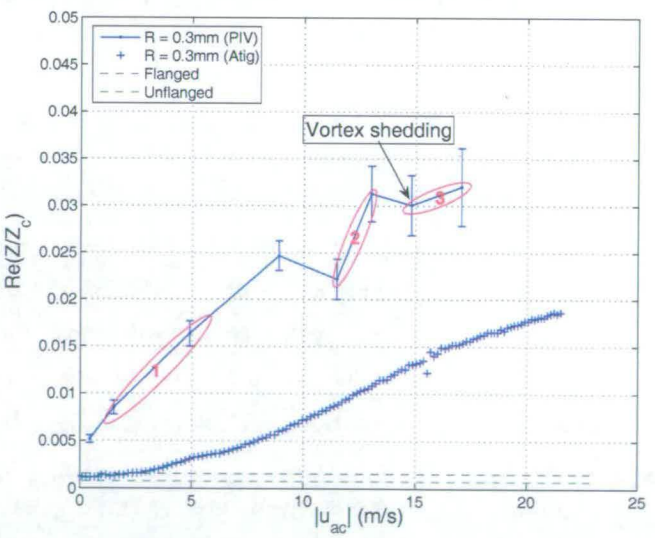


Figure 6.19: Comparison of the real part of the termination impedance as a function of acoustic velocity amplitude $|u_{ac}|$ calculated using two methods for the R=0.3mm termination: PIV measurements (solid lines); Two microphone method (Atig [Atig 03, Atig 04]) (+). The linear predictions for flanged and unflanged tubes are shown (- - -). Flow regimes are highlighted in red.

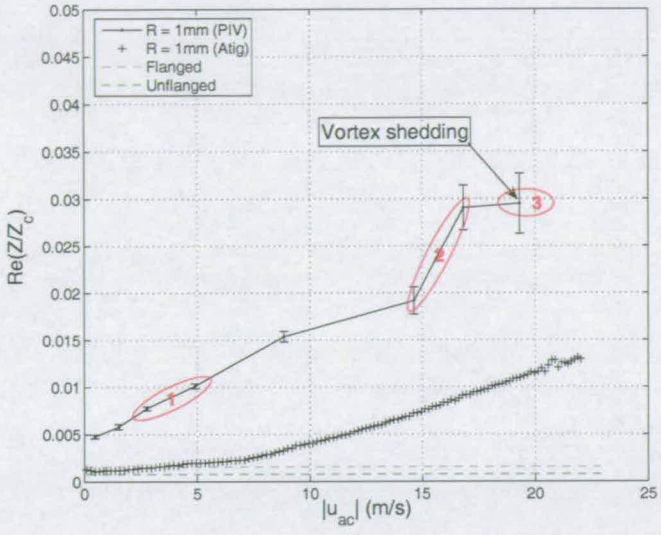


Figure 6.20: Comparison of the real part of the termination impedance as a function of acoustic velocity amplitude $|u_{ac}|$ calculated using two methods for the R=1mm termination: PIV measurements (solid lines); Two microphone method (Atig [Atig 03, Atig 04]) (+). The linear predictions for flanged and unflanged tubes are shown (- - -). Flow regimes are highlighted in red.

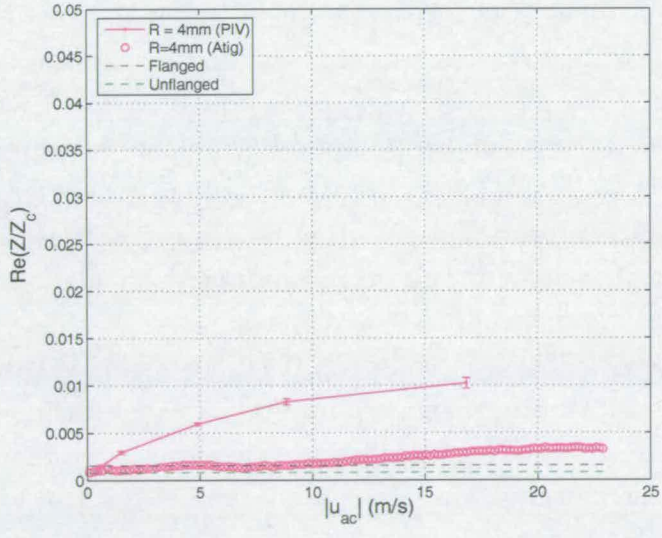


Figure 6.21: Comparison of the real part of the termination impedance as a function of acoustic velocity amplitude $|u_{ac}|$ calculated using two methods for the R=4mm termination: PIV measurements (solid lines); Two microphone method (Atig [Atig 03, Atig 04]) (+). The linear predictions for flanged and unflanged tubes are shown (- - -).

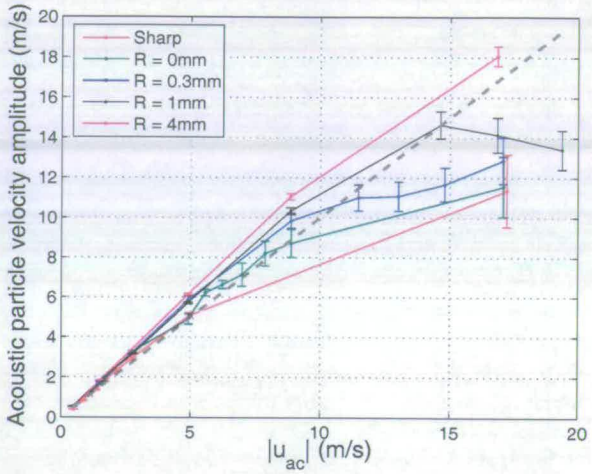
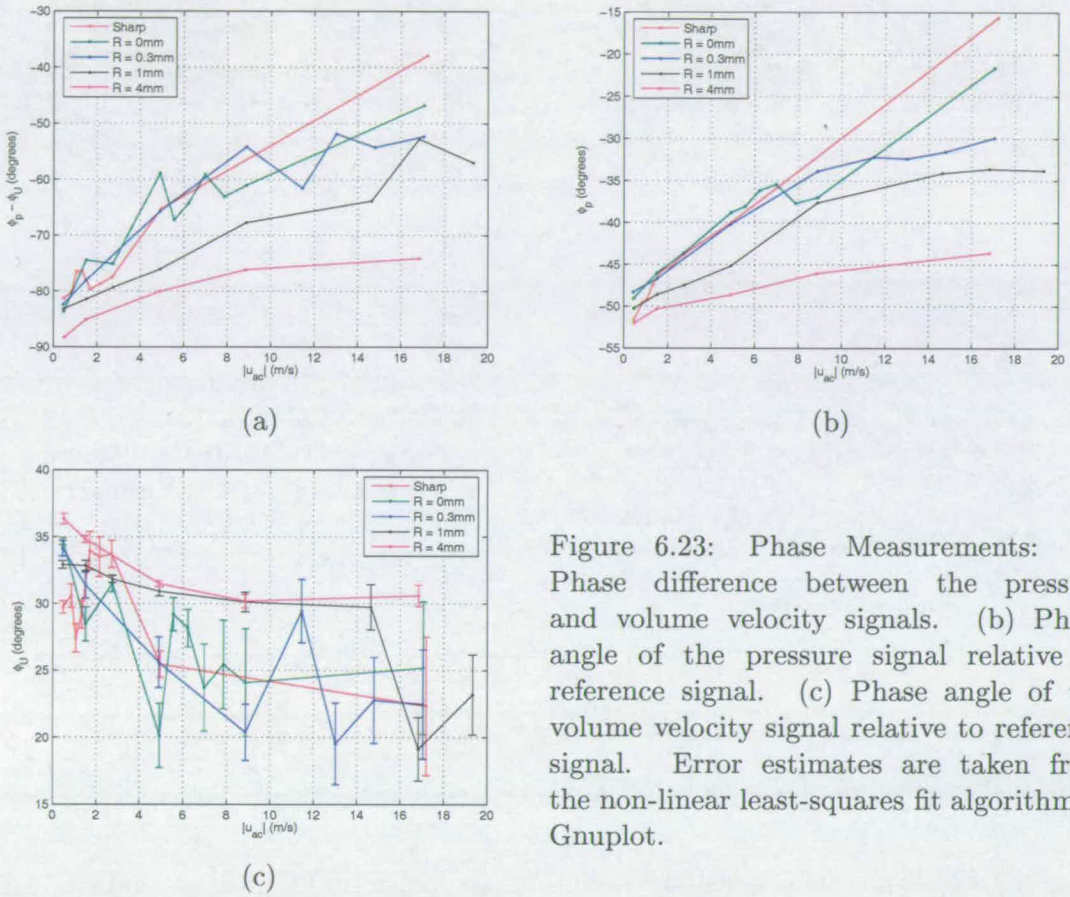


Figure 6.22: Comparison of the acoustic particle velocity measured with PIV (vertical axis) with the acoustic velocity amplitude $|u_{ac}|$ measured with the PCB transducer (horizontal axis) using the linear approximation. The grey dashed line represents equal PIV and PCB measurements.

In the experiments carried out by Atig [Atig 03, Atig 04], the acoustic particle velocity was calculated from the pressure signal measured by a PCB transducer (identical to the one used in this study and mounted at the same position along the length of the tube) with the assumption of plane wave propagation using equation 6.9. Figure 6.22 shows a plot of the acoustic particle velocity averaged over the area of the open end of the tube calculated from the PIV volume velocity measurements (as described in section 6.3.2) as a function of the acoustic particle velocity $|u_{ac}|$ calculated from the pressure measurements made by the PCB transducer using equation 6.9. As can be seen, the method assuming plane wave propagation underestimates the acoustic velocity amplitudes below about 5ms^{-1} and overestimates or underestimates for higher amplitudes by a varying degree depending on the tube termination used and whether or not non-linear loss mechanisms are important. For example, a PCB measurement giving an acoustic velocity of 10ms^{-1} underestimates the acoustic velocity for the R=4mm termination by approximately 2ms^{-1} and overestimates the acoustic velocity for the sharp termination by the same amount. This may have a small but noticable affect on the results produced by Atig and may help to partially explain the discrepancy between the results measured by the two different methods.

Possibly of more importance in determining the termination impedance is the effect of direct measurement of the phase of the acoustic volume velocity. Figure 6.23 shows the three phase measurements needed to calculate the termination impedance as a function of acoustic velocity amplitude. Morphologically, the graph of the phase

difference between pressure and volume velocity shown in figure 6.23(a) is very similar to graph of the termination impedance calculated using PIV (figure 6.16) suggesting that the phase measurement plays a determining role on the observed scatter of the data.



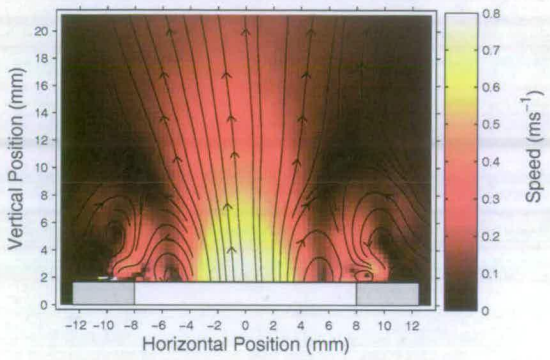
(a)

(b)

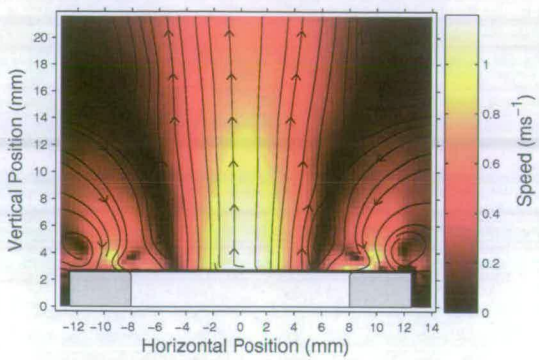
(c)

Figure 6.23: Phase Measurements: (a) Phase difference between the pressure and volume velocity signals. (b) Phase angle of the pressure signal relative to reference signal. (c) Phase angle of the volume velocity signal relative to reference signal. Error estimates are taken from the non-linear least-squares fit algorithm in Gnuplot.

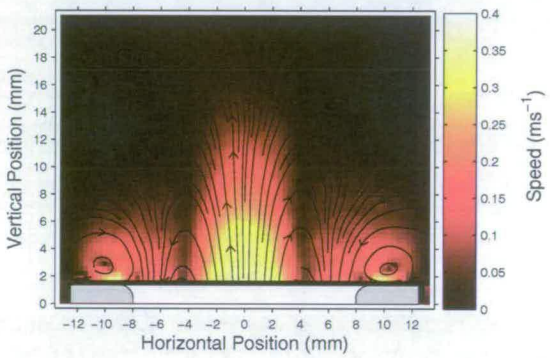
Figures 6.23(b) and (c) show the pressure and volume velocity phase measurements relative to the reference signal, respectively. These graphs illustrate that it is fluctuations in the measured phase of the volume velocity due to the development of non-linear flow phenomena that determine the scatter of the impedance data measured by PIV. It is of note that the pressure phase measurement for the R=0mm termination appears morphologically very similar to the impedance curve measured for the same termination by Atig with a smooth rise with a discontinuity at the location of the vortex shedding transition. It appears that indirect measurement of the volume velocity phase by use of pressure signals alone cannot fully take into account the effects of non-linear flow phenomena. It is then expected that this issue is the major cause of discrepancy between the results measured with the two different methods.



(a)



(b)



(c)

Figure 6.24: Flow regime 1. Averaged velocity magnitude contour maps with streamlines: (a) R = 0mm termination at $|u_{ac}| = 2.75ms^{-1}$. (b) R = 0.3mm termination at $|u_{ac}| = 4.89ms^{-1}$. (c) R = 1mm termination at $|u_{ac}| = 2.76ms^{-1}$.

6.6 Comparison with PIV streaming vector maps

Irregularities in the impedance measurements made using PIV in figures 6.18 to 6.20 can be seen at acoustic velocities lower than those at which the transition to vortex shedding occurs. These appear to indicate the presence of non-linear flow phenomena below this transition. By examination of streaming velocity vector maps (velocity vector maps time-averaged over one acoustic cycle) in conjunction with particle velocity vector maps three main non-linear flow regimes have been identified for the R=0mm, 0.3mm and 1mm terminations which seem to correlate with the impedance irregularities. These regimes have been marked on the figures in red and are numbered 1 to 3.

Regime 1 occurs at velocity amplitudes of approximately 1.5ms^{-1} to 5ms^{-1}. The main features of this regime are a streaming jet from the centre of the termination and the presence of a weak inward circulating vortex ring just above the termination walls. This regime seems to correspond to region 3 described by Ingard and Labate [Ingard 50] (section 5.2.1). Typical streaming vector maps from this regime for the R = 0mm, 0.3mm and 1mm terminations can be seen in figure 6.24. On first inpressions

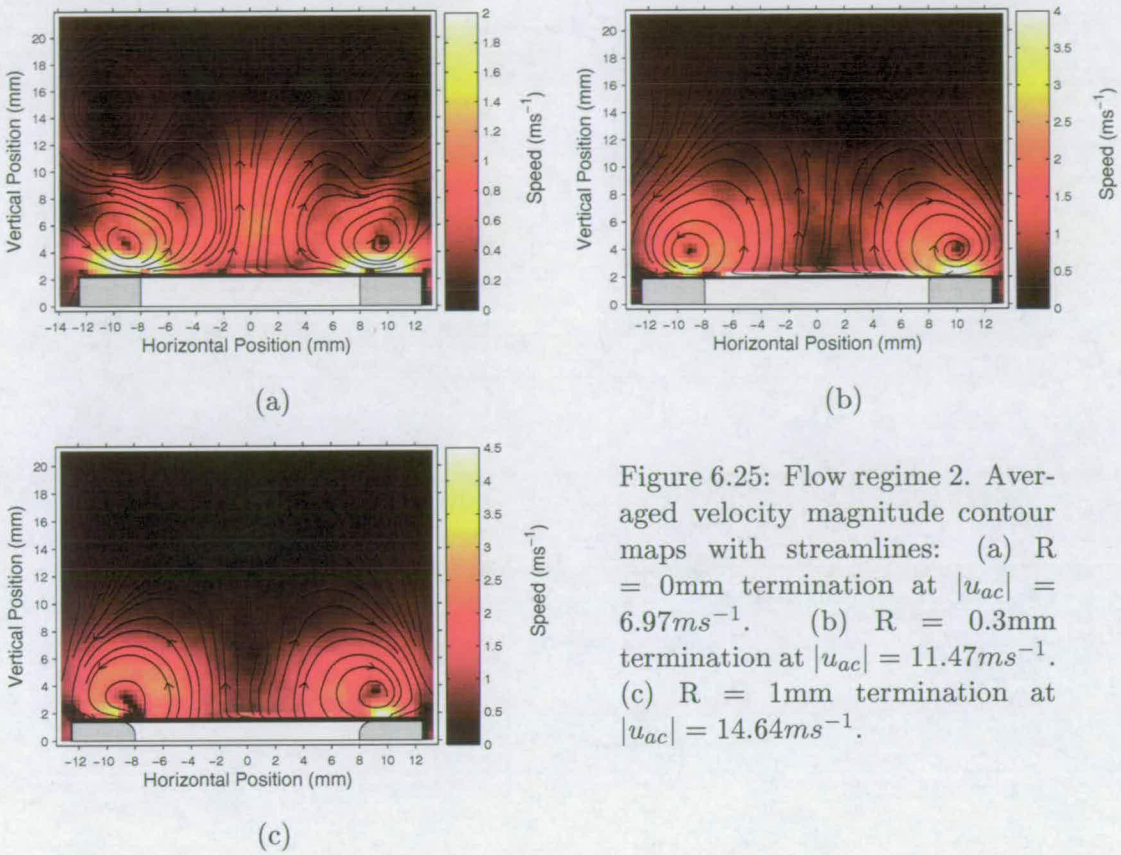
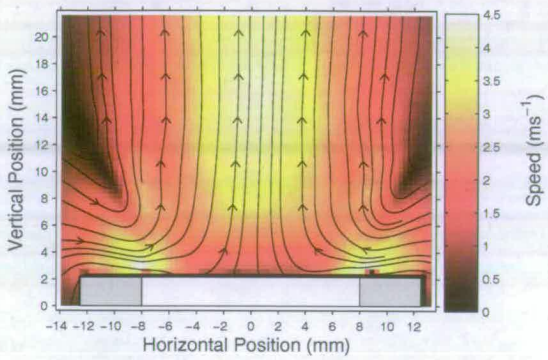


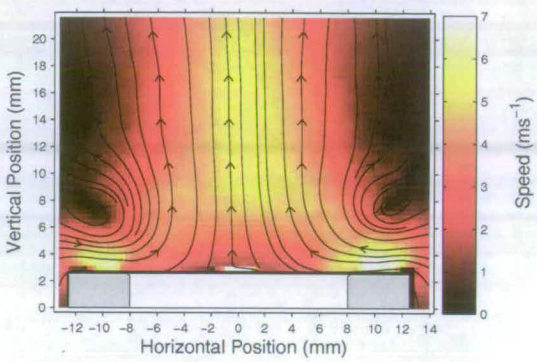
Figure 6.25: Flow regime 2. Averaged velocity magnitude contour maps with streamlines: (a) R = 0mm termination at $|u_{ac}| = 6.97ms^{-1}$. (b) R = 0.3mm termination at $|u_{ac}| = 11.47ms^{-1}$. (c) R = 1mm termination at $|u_{ac}| = 14.64ms^{-1}$.

it seems that this may be due to flow separation at the sharp outside edge of the termination during the inflow part of the acoustic cycle. Inspection of the PIV acoustic particle velocity data reveals, however, that the cause of the inward circulation is due to the vortex ring that is generated within the tube on inflow being expelled on outflow. This process has already been discussed in relation to the R=0.3mm and R=1mm terminations in section 5.3.4. Velocity magnitude and vorticity contour maps for each stage of the acoustic cycle corresponding to the streaming result shown in figure 6.24(b) can be seen in figure 5.16.

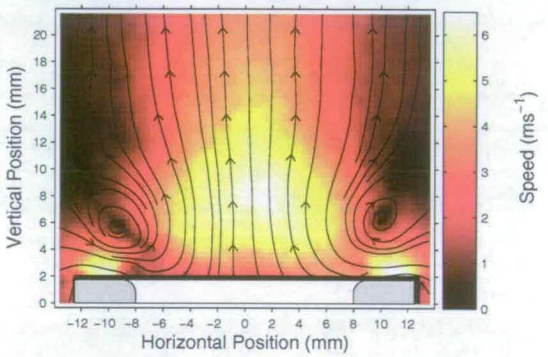
Acoustic flows in regime 2 consist of either a weak or insignificant jet with strengthening vortices generated due to boundary layer separation at the inside edge on outflow appearing outside the termination. These rotate in the opposite sense to those mentioned in regime 1 This regime occurs at velocity amplitudes between approximately 5.5ms^{-1} and 7ms^{-1} for the R=0mm termination, between 11.4ms^{-1} and 13.0ms^{-1} for the R=0.3mm termination and at between 14.6ms^{-1} and 16.8ms^{-1} for the R=1mm termination. Streaming velocity vector maps for regime 2 for the R=0mm, 0.3mm and 1mm terminations are shown in figure 6.25. This regime is the



(a)



(b)



(c)

Figure 6.26: Flow regime 3. Averaged velocity magnitude contour maps with streamlines: (a) R = 0mm termination at $|u_{ac}| = 7.87ms^{-1}$. (b) R = 0.3mm termination at $|u_{ac}| = 14.80ms^{-1}$. (c) R = 1mm termination at $|u_{ac}| = 19.33ms^{-1}$.

same as the vortex generation regime described in relation to the R = 0mm termination in section 5.3.3. Typical PIV results showing the acoustic particle velocity and vorticity fields corresponding to this flow regime can be seen in figure 5.12.

Between regimes 1 and 2 is a transitional flow regime where characteristics of both regimes are present. Jet production is observed, vortex rings generated on outflow at the inner edge become stronger and inflow generated vortex rings are observed, but to a lesser extent. This flow regime could perhaps have been separately classified, but as it appears to be a transition between two regimes with characteristics of both it was decided not to. The transitional stage is observed at 4.9ms^{-1} for the R=0mm termination and at 8.9ms^{-1} for both the R=0.3mm and 1mm terminations. After this transitional stage the termination resistance drops or the rate of increase reduces significantly. This may be related to the cessation of the jet streaming effect as the flow jumps to a regime in which vortex generation becomes a more efficient loss mechanism.

Regime 3 is characterised by strong jet formation and periodic vortex shedding and has already been discussed (for example in section 5.3.3). The interaction between the

jet and vortices is strong in this regime. Example streaming vector maps for this regime are shown in figure 6.26. This flow regime is observed at velocity amplitudes in excess of 7.9ms^{-1} for the R=0.mm termination, 14.8ms^{-1} for the R=0.3mm termination and 19.3ms^{-1} for the R = 1mm termination. This flow regime corresponds to the vortex shedding regime described in section 5.3.3. Typical PIV results showing details of the acoustic particle velocity and vorticity fields corresponding to this flow regime can be seen in figure 5.14.

It appears that it is possible to group the terminations in terms of the types of flow regimes observed. As discussed above, the acoustic flows associated with the R = 0mm, 0.3mm and 1mm terminations share a series of characteristic non-linear flow patterns over the range of sound levels studied. It is not possible, however, to place either the sharp termination or the R = 4mm termination in the same group since the termination geometries are significantly dissimilar.

As might be expected, the R = 4mm termination shows the greatest similarity to those already mentioned. Indeed flow patterns similar to regimes one and two are observed. However, as the extent of the rounding of the inner edge is such that there is only one edge at which boundary layer separation can occur the details of these regimes are somewhat different to those associated with less rounded terminations. For example, a flow similar to regime 1 is observed, with vortices generated on inflow at the outside edge but with no jet, and a flow similar to regime 2 is observed, with vortices generated on outflow at the outside edge and a jet. The jet and vortices in this case are quite separate in space and do not interact strongly. This is the result of a phenomenon known as the Coanda effect or the tendency of a boundary layer to remain attached to a convex surface. Figure 6.27 illustrates the effect of edge roundness on flow separation.

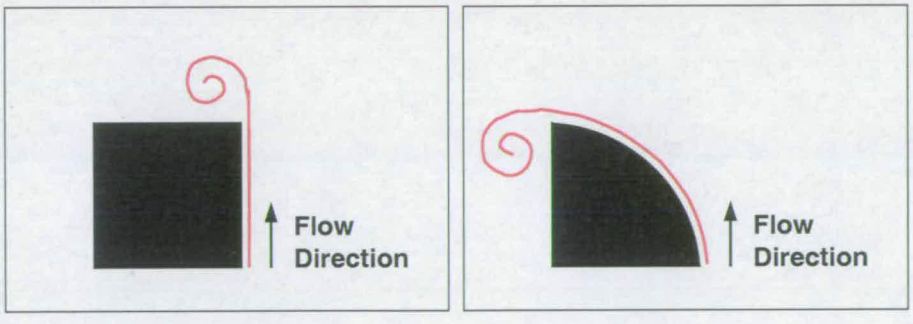


Figure 6.27: Effect of edge roundness on flow separation

The sharp termination also undergoes a series of flow regime changes which ultimately lead to a transition to vortex shedding and jet production as in regime 3, although there are some significant differences. There is a similarity with the R =

4mm termination in that there is only one edge at which flow separation can occur, although the edge sharpness leads to quite different behaviour. As previously discussed in section 5.3.2 flow separation occurs at a relatively low acoustic amplitude and three main vortex shedding regimes are observed.

6.7 Conclusions

It seems clear that the shape of the termination plays an important role in determining the level of energy loss due to the production of non-linear flow phenomena at high acoustic amplitudes. An increased impedance at the termination will reduce the proportion of acoustical energy reflected back down the tube to maintain the standing wave. Hence, in the case of a real instrument played by a musician, the the amount of energy introduced at the input end of the instrument must be proportionally more for an instrument with sharp edges than one with rounded edges to maintain a given sound level within the bore of the instrument. In other words, an instrument with rounded edges will play more efficiently and can therefore be played more loudly with less effort than one with sharp edges.

The PIV technique provides an invaluable tool for measuring the termination impedance at the open end of a resonant tube. Important information about the volume velocity amplitude and, most importantly, phase (that cannot be inferred from pressure measurements with linear approximations) is measured directly. Comparison between measured impedance data and velocity vector maps gives an essential understanding of the physical flow phenomena responsible for the non-linear losses observed.

Chapter 7

Evaluation of Acoustical Losses using Vortex Sound Theory

7.1 Introduction

The termination impedance of an open ended tube at high sound levels can be evaluated using PIV by direct measurements of acoustic particle velocity in conjunction with pressure measurements, as shown in the previous chapter. This method gives a measure of the strength of the acoustical losses at the open end of a tube but on its own does not give any information about the physical mechanisms which are the cause of the observed losses. PIV vector maps assist by allowing a qualitative assessment of the flow and can allow the main loss mechanisms to be identified visually (chapter 5). This chapter examines a method for the numerical evaluation of non-linear acoustical losses due to vortex generation at the open end of a tube in which a high amplitude sound field has been generated using a loudspeaker. The effect of the geometry of the termination of the tube on these losses is examined.

It is the aim of this chapter to apply the vortex sound analysis method to the PIV data gained in chapter 5 to demonstrate the flexibility of the PIV technique and to compare the impedance results calculated using this method with those calculated by direct measurements of velocity and pressure.

Periodic vortex shedding induced by an acoustic field has been observed by several authors at orifices and at the open ends of tubes [Ingard 50, Ingard 67, Peters 93a, Peters 93b] and is a well known dissipative mechanism [Salikuddin 83, Disselhorst 80, Howe 80]. To quantify the losses associated with vortex generation and shedding at the open end of a tube a method for the evaluation of PIV velocity maps using vortex sound theory (section 2.6) is outlined. Comparison between the results of the vortex sound calculations and the vorticity fields measured from the PIV vector maps allow both qualitative and quantitative descriptions of the acoustical effect of vortex shedding on losses over the acoustic cycle.

The sound production mechanism in a variety of so called 'air reed' or 'flue' musical

wind instruments such as the flute or the recorder has long been attributed to the presence of flow separation and vortex generation as a thin air jet impinges on an edge. It is a matter of debate as to whether the vorticity generated acts as a sound source or as a loss mechanism, or if it acts solely as a perturbation to the air jet acting to produce the instability that drives the initial jet oscillation.

Extensive recent work by Bamberger has investigated the sound generation mechanism at the labium in the head joint of a flute using PIV [Bamberger 01, Bamberger 02, Bamberger 04, Bamberger 05]. Application of vortex sound theory (section 2.6) to the measured PIV data has allowed the vortex sound power density to be calculated, leading to the conclusion that the sound production mechanism in flue instruments results solely from the vortex sound produced by the jet. To enable such a calculation, Bamberger makes two separate sets of PIV measurements. Firstly, the velocity field produced by an air jet impinging on the labium of a flute is measured. Secondly, a measurement of the acoustic velocity field is made at the labium with the sound field generated by a loudspeaker to represent an irrotational acoustic reference flow.

As described in section 2.6, to calculate the acoustic power generation or dissipation using vortex sound theory it is necessary to know both the velocity field associated with the vorticity distribution and the (theoretical) reference acoustic (potential) velocity field that would be present in the absence of any vorticity. To facilitate these requirements in this study PIV measurements were made of the open end of the tube at a range of acoustic amplitudes with five different tube termination geometries (section 4.3.2). At low acoustic velocity amplitudes the vorticity field is negligible and the velocity field can then be used as an approximation to the reference potential flow (section 5.3.1). As the acoustical velocity amplitude increases the vorticity field becomes non-negligible and begins to play an important role in determining the structure of the flow field, fulfilling the first requirement.

For comparison, a second method was used to derive a representation of the reference acoustic velocity field. By making the assumption that the flow field outside the open end of the tube is equivalent to that above a plane piston located in the plane of the open end it was possible to calculate an approximation to the potential velocity field numerically. In the simplest case the piston is represented mathematically as an array of oscillating point sources for which the velocity field is well known. The vortex sound calculation was then repeated using the numerically calculated data in conjunction with the PIV data.

The assumption of an axisymmetric flow field is made in the evaluation procedure to allow the net acoustical power loss in a three dimensional measurement volume surrounding the end of the tube to be calculated from two dimensional PIV data.

Analysis was carried out using Matlab with various customised programmes (m-files) written by the author.

7.2 Vortex sound analysis of PIV maps

7.2.1 Analysis method

As described in section 2.6.2, when vortices are present in a sound field there is an energy transfer back and forth between the rotational energy of the vortex and the acoustical energy of the sound field. Acoustical power P is transferred to and/or from the reference acoustic velocity field $\vec{u}$ by the vorticity $\vec{\omega}$ associated with the solenoidal velocity field $\vec{v}$. The PIV data is comprised of a grid of discrete measurement points at coordinates (i,j) where i and j are indices referring to the horizontal (x) and vertical (y) positions of the interrogation areas. To enable calculation of the power dissipation from PIV vector maps, it is useful to express equation 2.62 in a discrete form:

$$P = -\rho_0 \sum_{i,j} \{\vec{\omega}(i,j) \times \vec{v}(i,j)\} \cdot \vec{u}(i,j) dV(i,j) \tag{7.1}$$

where $dV(i,j)$ is the infinitessimal volume associated with the rotation of a finite interrogation area at a position (i,j) about the central tube axis by an infinitessimal angle $d\phi$.

The situation measured in this study is cylindrically symmetric so a simplification in the calculation procedure can be made. Data reduction is carried out by taking an average value of velocity data at equal distances on either side of the central axis of the tube. The resulting two dimensional data has one component in the radial direction (x) and another in the axial direction (y). By symmetry an extension from two to three dimensions can be made by a rotation of the data about the tube axis. Each measurement point (i,j) thereby has an associated volume $V(i,j)$ (the size of which depends on its distance from the tube axis). The mass $M(i,j)$ contained within this discrete measurement volume is $\rho_0 V(i,j)$. The vortex power in the cylindrical volume associated with the interrogation area at position (i,j) is then:

$$P(i,j) = -\{\vec{\omega}(i,j) \times \vec{v}(i,j)\} \cdot \vec{u}(i,j) M(i,j) = \vec{F}_c(i,j) \cdot \vec{u}(i,j) M(i,j) \tag{7.2}$$

where $\vec{F}_c(i,j) = -(\vec{\omega}(i,j) \times \vec{v}(i,j))$ is the coriolis volume force per unit mass due to the rotational vortex motion associated with the interrogation area at grid position (i,j).

The mass within each volume $V(i,j)$ is calculated using the axisymmetry of the situation, in a similar way to the volume velocity calculation described in section 6.3.2.

comprised entirely of uncorrelated data. This is produced in the PIV analysis procedure by the image of the tube termination itself. Additionally, glare and reflections from surfaces close to the open end of the tube occasionally result in the presence of outliers.

For visualisation purposes the first problem of uncorrelated data due to the termination image is easily dealt with by removing the offending area completely by setting the velocity of each vector within the problem area to zero. For the calculation of vorticity, however, this approach can result in highly overestimated measurements due to the creation of velocity gradients which may or may not be present in the real flow. In the present situation it is valid to completely remove some of the data by zeroing the velocity: in regions where the tube walls are located it is natural to set the velocity to zero due to the no slip condition. Vorticity produced at the edges imposed by the velocity zeroing at the tube wall locations is not unrealistic, since in the physical flow the same velocity gradient is present due to the solid walls of the termination. In the region between the walls, within the space at the open end where no velocity data is available, the case is not as simple. Instead, to minimise the addition of non-physical velocity gradients data was copied from just outside the open end of the tube and used to replace the missing data just inside the open end. This procedure results in the measurement of a minimal amount of spurious vorticity.

Any outliers in the vicinity of the open end in the low amplitude PIV measurements (used to represent the potential flow) were manually removed and replaced by trial and error with neighbouring data to achieve a result which appeared more realistic. This was done because any small imperfections in this data could result in spurious results which would consequently be amplified significantly in scaling to higher acoustic amplitudes.

7.2.2 Potential velocity field - PIV

As previously stated, two methods to evaluate the potential flow have been used in this study. The first of these, from here onward termed the Low Amplitude Potential Method (LAPM), uses a set of low velocity amplitude PIV measurements, made at ten phase steps through the acoustic cycle, to approximate the potential flow field for each of the tube terminations. The sound pressure level measured within the tube at a distance of 160mm from the open end using the PCB transducer is approximately 136.5dB. At this sound level the acoustic velocity amplitude $|u(0)|$ (calculated from the volume velocity measured in section 6.3.2 by dividing by the area of the open end) is between 0.43ms^{-1} and 0.53ms^{-1}, depending on which tube termination is used, and negligible vorticity is observed. A streaming velocity map, time-averaged over one acoustic cycle, is calculated from this data and is subtracted from each of the velocity maps at each phase step. This helps to remove any unwanted circulations or mean flow

patterns that were occasionally observed in the low amplitude PIV measurements, due to convection currents as previously described in section 5.3.1.

The reference potential acoustic velocity field $\vec{u}(n)$ at a sound pressure level $SPL(n)$, where n is an index to the experimental measurement set, is then obtained by assuming a linear relationship between velocity and pressure amplitudes and multiplying the low amplitude (potential) measurement by a scaling factor $\alpha(n)$. This scaling factor relates to the increase in dB between the low and high amplitude (non-linear) measurements:

$$\alpha(n) = 10^{\frac{SPL(n)-SPL(0)}{20}} \tag{7.7}$$

where $SPL(0)$ is the sound pressure level of the low amplitude (potential) measurement. This gives for the reference acoustic velocity field:

$$\vec{u}(n) = \alpha(n)\vec{u}(0) \tag{7.8}$$

where $\vec{u}(0)$ is the potential velocity field measured at low amplitude. Example low amplitude PIV results are shown in figures 5.2 and 5.3.

7.2.3 Potential velocity model - Pistonic flow

The second method of determining the potential field uses a simple model in which the flow field at the open end of the tube is approximated by the flow above an oscillating piston located in the plane of the open end with the same radius a as the tube. A piston can be mathematically represented by an array of acoustic point sources located in a circular plane. For each point source the velocity field in three-dimensions can be calculated using the following equation [Pierce 81]:

$$\vec{u} = \frac{Q(t)}{2\pi|r|^3}\vec{r} \tag{7.9}$$

where $\vec{r} = x\vec{e_x} + y\vec{e_y} + z\vec{e_z}$ is the vector displacement from a point source located at the origin to an arbitrary point in three-dimensional space. The distance from the source is then $|r| = \sqrt{x^2 + y^2 + z^2}$ where x, y and z are cartesian coordinates of the point in question and $\vec{e_x}$, $\vec{e_y}$ and $\vec{e_z}$ are unit vectors in the x, y and z directions.

The volume velocity $Q(t)$ of the source is given by:

$$Q(t) = |Q|\sin(\omega_0 t + \phi_Q) \tag{7.10}$$

where $|Q|$ is volume velocity amplitude of the source, ϕ_Q is, in this study, the phase of the volume velocity measurement taken from the low amplitude PIV measurement

and ω_0 is the radian frequency of the source. The value of $|Q|$ was arbitrarily chosen as 1 in the calculation since subsequent normalisation and scaling procedures meant that the value chosen was not important.

The procedure of calculating the velocity field for a single point source using equation 7.9 was executed in Matlab. A three-dimensional grid of measurement points was used with the same grid spacing as the PIV vector map data. The plane of the PIV data was used to define the x-y plane, the piston surface is then in the x-z plane and the y-z plane is the remaining plane required to define the calculation volume (figure 7.1).

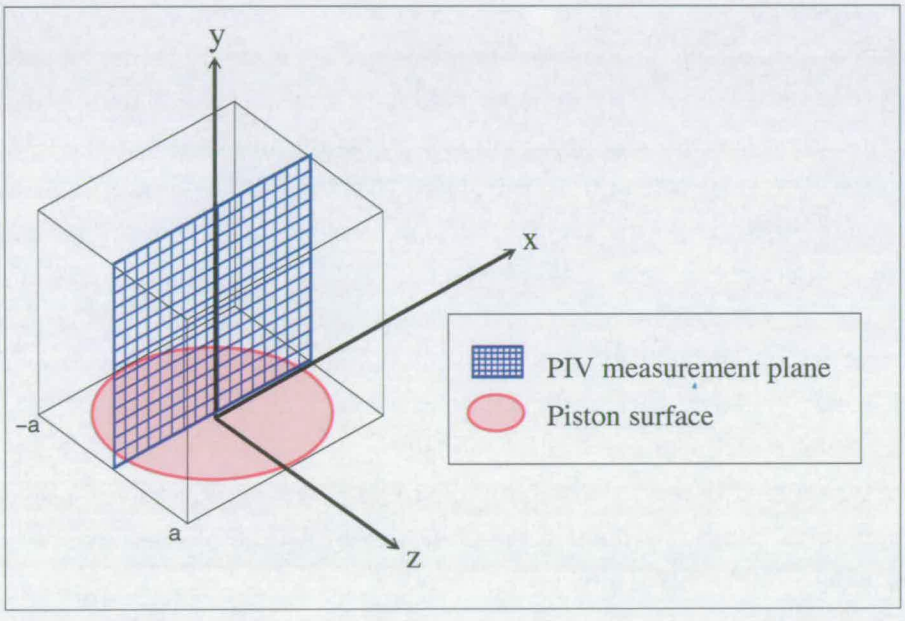


Figure 7.1: Schematic showing the orientation of reference planes used in the pistonic modelling procedure.

The location of the piston in three-dimensions was defined as follows. The vertical position for the piston was chosen based on the experimental case to be modelled depending on the positional requirements of the PIV data for each termination and sound level. The grid locations of the outer edges of the piston were identified in the x-y plane by measuring the positions of the inner edges of the tube terminations from the raw PIV images. From this the location of the central axis was determined. The depth of the calculation volume (in the z-direction) was chosen to be equal to the diameter of the open end and extend from -a to a.

The three-dimensional velocity field above a circular piston was then calculated by the summation of a series of single point sources in the plane of the open end of the

tube with origins at grid locations less than one tube radius from the central axis. Each point source had a velocity field defined by equation 7.9 with $Q = 1$ for simplicity. Only two-dimensional velocity data in the x-y plane through the central axis (z = 0) was needed to correspond to the PIV data. The remaining data was therefore disregarded to speed up the calculation. Also, the z-component of velocity is zero by symmetry in the x-y plane and so its calculation was unnecessary.

A single vector map showing flow away from the piston resulted from this process. The pistonic velocity field was then normalised by dividing by the maximum velocity magnitude within the data set to allow the data to be scaled to the required velocity amplitude. It was chosen to scale the pistonic data to correspond to the average velocity over the open area of the tube in low amplitude PIV measurements. A sinusoidally oscillating time series of potential velocity field data was then calculated by multiplying the normalised and scaled data by equation 7.10 taking into account the phase of the corresponding PIV measurement. This ensured that the modelled data represented the same ten time steps through the acoustic cycle as the low amplitude PIV measurements. Cylindrical symmetry was taken into account for the vortex sound calculation and the full field data was reduced by half.

The same scaling method for high amplitude potential velocity fields was used as is described in section 7.2.2, with scale factors given by equations 7.7 and 7.8.

Typical results of the pistonic flow modelling procedure are shown in figures 5.4 and 5.5. As discussed in section 5.3.1, the pistonic potential flow model appears to be a good representation of the flow at the open end of a tube at the lowest amplitudes measured using PIV in this study.

7.3 Results and discussion

In this section vortex sound results for three measurement areas are presented as a function of amplitude for each of the potential models used. The variation with time will be discussed for the specific case of the R = 0mm termination. Finally, contour maps showing the spatial distribution of vortex sound power as it evolves over the course of an acoustic cycle at a single sound level will be presented.

The vortex sound calculation procedure described in section 7.2.1 was repeated for the two methods of representing the potential velocity field for each of the terminations and sound levels studied. The level of sound power production or absorption by vortices in three areas of the flow was then compared. These three areas are indicated as areas 1,2 and 3 in figure 7.2. Area 1 is the entire region of the measured data and so includes both areas 2 and 3. Areas 2 and 3 are spatially independent from each other and were chosen after inspection of vortex power contour maps revealed spatially distinct vortex

power behaviour in each region, most notably for the slightly flanged terminations. Area 2 can be considered to represent free space with no opportunity for interaction with solid boundaries. Area 3, conversely, represents an area spatially restricted on one side by solid walls and edges. The vortex power in each of these areas was calculated by limiting the sum in equation 7.5 to the boundaries describing each area.

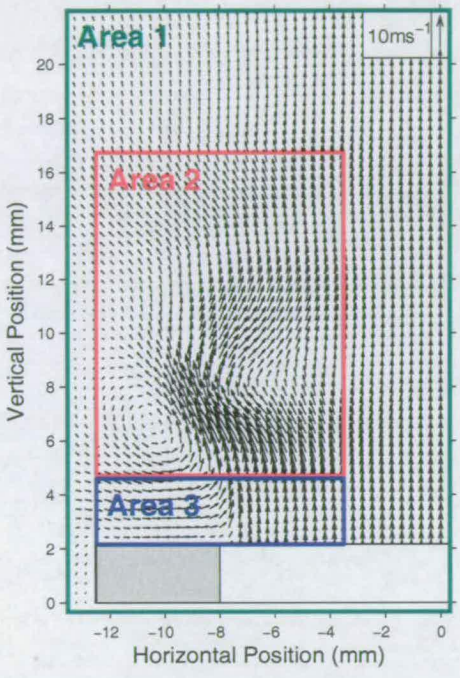


Figure 7.2: Vortex sound measurement areas. Area 1 encompasses the whole vector field. Area 2 represents an area of free space. Area 3 is an area bounded by a wall on one side. The grey area represents the position of the tube wall. The blank white area represents the tube opening for which there is no data.

The normalised acoustic resistance was then calculated from the average power over one acoustic cycle using equation 2.63 and plotted for each measurement area as a function of the linear acoustic velocity amplitude $|u_{ac}|$ as estimated using the PCB microphone[2]. By presenting the results in terms of a normalised acoustic resistance a comparison with the termination impedance findings of the previous chapter (figure 6.16) can be made. Equation 2.63 was also used to evaluate the acoustic resistance in each measurement area as a function of the time. This allows a general examination of the power transmission to and from the acoustic field as the acoustic cycle progresses.

[2]Here the linear acoustic velocity is calculated from the PCB transducer using equation 6.9. Further details are given in sections 4.3.3 and 6.3.1.

7.3.1 Velocity amplitude dependence

The results of the normalised acoustic resistance calculated using vortex sound theory for each of the three measurement areas are given in figures 7.3 to 7.5 as a function of the linear acoustic velocity for each of the five tube terminations studied (figure 4.8). There is notably different behaviour in each of the different regions of the flow field.

Area 1

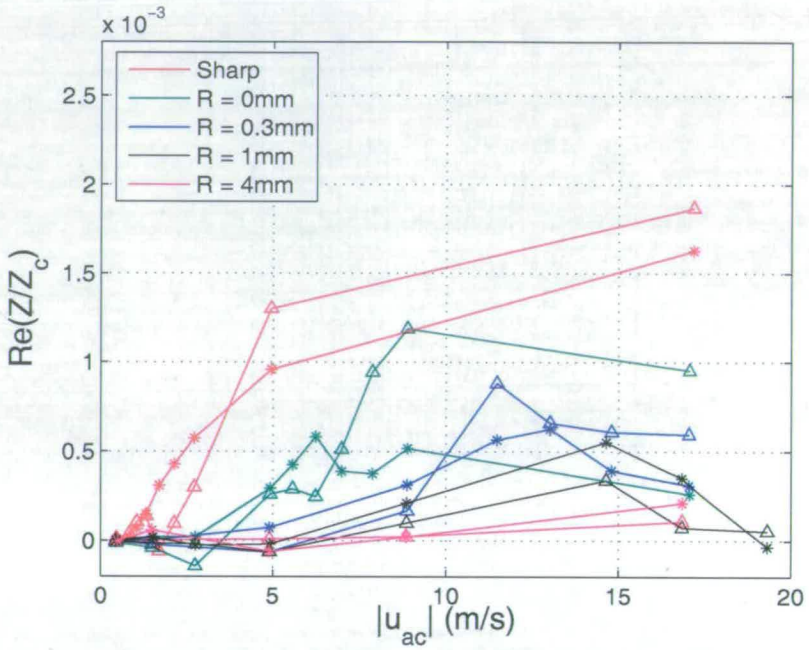


Figure 7.3: Acoustic resistance as a function of the acoustic velocity amplitude $|u_{ac}|$ - Area 1. The results of the vortex sound calculation using two determinations of the potential field: ($\triangle$) PIV data; ($*$) Pistonic potential model.

The results gained in area 1 (figure 7.3) show that there is a net acoustical loss due to a transfer of acoustical energy into generation of vorticity over the acoustic cycle when the entire measurement area is taken into account. The rate of acoustical loss clearly depends on both the geometry of the tube termination and on the acoustic amplitude of the standing wave within the tube. The sharp termination incurs energy loss at a significantly higher rate as the amplitude is increased than each of the flanged tubes. The rate of increase and level of the acoustic resistance reduces for each of the flanged terminations as the radius of curvature of the inner edge increases. As the velocity amplitude increases the rate of increase of acoustical loss in general appears to reduce. The acoustical loss due to generation of vorticity appears to be negligible in

the case of the most rounded termination. It is of note that the net acoustical losses over the acoustic cycle due to vortex generation estimated using vortex sound theory are an order of magnitude smaller than the acoustical losses calculated in the previous chapter by direct impedance measurements.

There appears to be good agreement in the magnitudes of the losses calculated using vortex sound theory with both methods of potential field estimation, although there are some notable differences in the detailed behaviour. The Pistonic potential method result for the tube R = 0mm termination, for example, shows good agreement between methods in the level of acoustical loss up to about 7ms^{-1}. Above this level the acoustic losses calculated using the pistonic potential method are more than a factor of two smaller than the results calculated using the low amplitude PIV method. The point at which the two methods diverge coincides with the velocity amplitude at which the transition to vortex shedding occurs.

Area 2

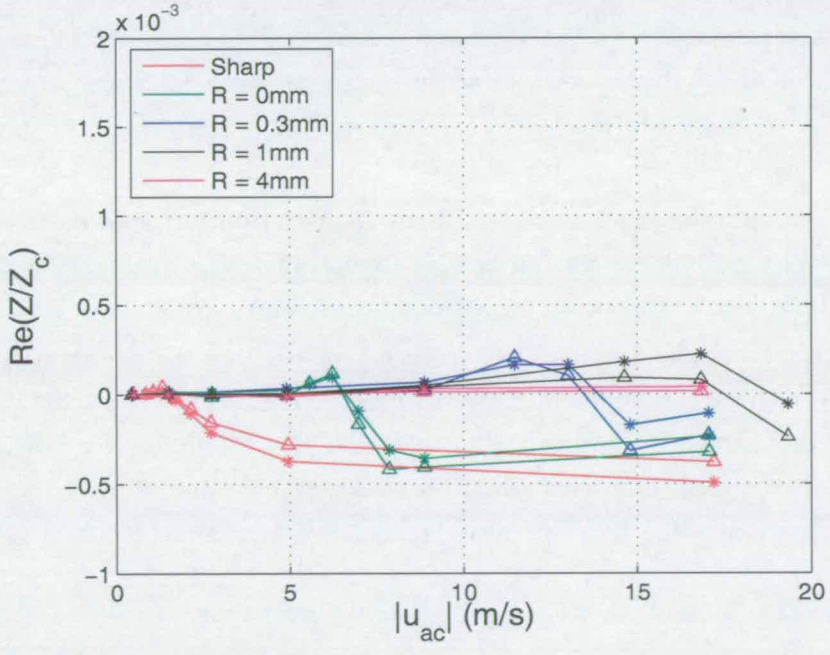


Figure 7.4: Acoustic resistance as a function of the acoustic velocity amplitude $|u_{ac}|$ - Area 2. The results of the vortex sound calculation using two determinations of the potential field: ($\triangle$) PIV data; ($*$) Pistonic potential model.

Clear evidence of sound production by vortices in the region of free space represented by area 2 can be seen in figure 7.4. A negative value of the acoustic resistance indicates

a net transfer of power over the acoustic cycle from the vortices to the acoustic field in this region. The magnitude of the net production in area 2 is clearly less than than the net absorption in area 1. Some interesting points arise on examination of this figure. Firstly there is excellent agreement between the PIV and modelled potential results. This indicates that the flow fields away from the open end in both models are very nearly equivalent. This justifies the determination that the low amplitude PIV results are a good representation of a potential flow in this region. Also, it is clear that the model of a potential flow above a piston is a good representation of the flow at the open end of a tube in this distance from the open end.

The amplitude at which the acoustic resistance becomes negative for each of the terminations coincides with the vortex shedding threshold. This makes sense since only at amplitudes above this level do any significant vortex structures enter this area. Vortices are in general confined to the region close to the open end of the tube at lower amplitudes. For the sharp edged termination there is a more gradual increase in the level of sound production than the other terminations. This is because the vortices generated with this termination are initially much smaller and move more slowly. With the other terminations vortex shedding occurs at a significantly higher velocity amplitude by which point the vortices are stronger and considerably larger. There appears to be a saturation in the level of energy production attained at a normalised acoustic resistance of approximately -5$\times$ 10^{-4}.

There is no vortex shedding associated with the R=4mm termination in the range of acoustic velocity amplitudes measured. The results for this termination in area 2, indicating a negligible contribution, confirm this.

There is a region of slight energy loss in area 2 just before the transition to vortex shedding. Before the transition occurs vortices are generated in area 3 which cling to the outside walls of the open end of the termination. As the sound level increases, so does the spatial extent of these vortices. This observed loss is most likely to be due to part of the vortex extending into the measurement region of area 2.

Area 3

The normalised acoustic resistance results shown in figure 7.5 for area 3 show a great deal of similarity with the results in area 1. The magnitude of the net loss in this region is higher than in the entire vector field, indicating that the majority of the acoustical losses are associated with this region close to the wall. This is not unexpected since the presence of the wall imposes a large permanent velocity gradient on this region of the flow. This results in high levels of vorticity and hence power loss.

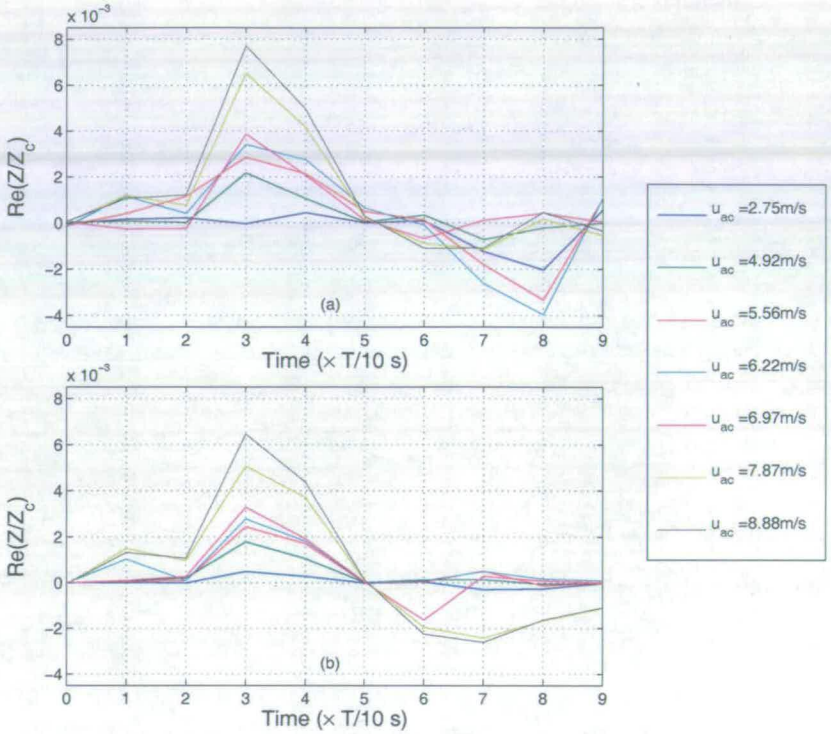


Figure 7.6: Acoustic resistance as a function of time - Area 1. The results of the vortex sound calculation using two determinations of the potential field for the R = 0mm termination: (a) PIV data. (b) Pistonic potential model.

losses at the fourth time step (at Time = 3 × T/10 seconds, where T is the period of the acoustic cycle) for all sound levels above 4.92ms^{-1}. This peak coincides with maximum outflow. At Time = 0 and Time = T/2 seconds the potential velocity magnitude is approximately zero. At these points the reference potential field changes from inflow to outflow and vice-versa.

The only notable discrepancy between the results obtained using the two methods is observed during the inflow part of the acoustic cycle. For the PIV result on inflow there is in general sound production for most acoustic velocity amplitudes although there is a clear change in behaviour for velocity amplitudes above $|u_{ac}| = 7.87\text{ms}^{-1}$. Up to an acoustic velocity amplitude of 6.22ms^{-1} a peak in the sound production is observed at Time = 8 × T/10 seconds. Above this level the magnitude of the loss reduces significantly and the peak shifts to an earlier stage of inflow. The results using the pistonic potential model, however, show negligible sound production on inflow below the same threshold velocity amplitude. Above this level sound production is observed on inflow with a larger magnitude than observed using the PIV data. The

threshold velocity at which this change in behaviour is observed corresponds to a velocity amplitude at which the vortex shedding transition occurs.

Area 2

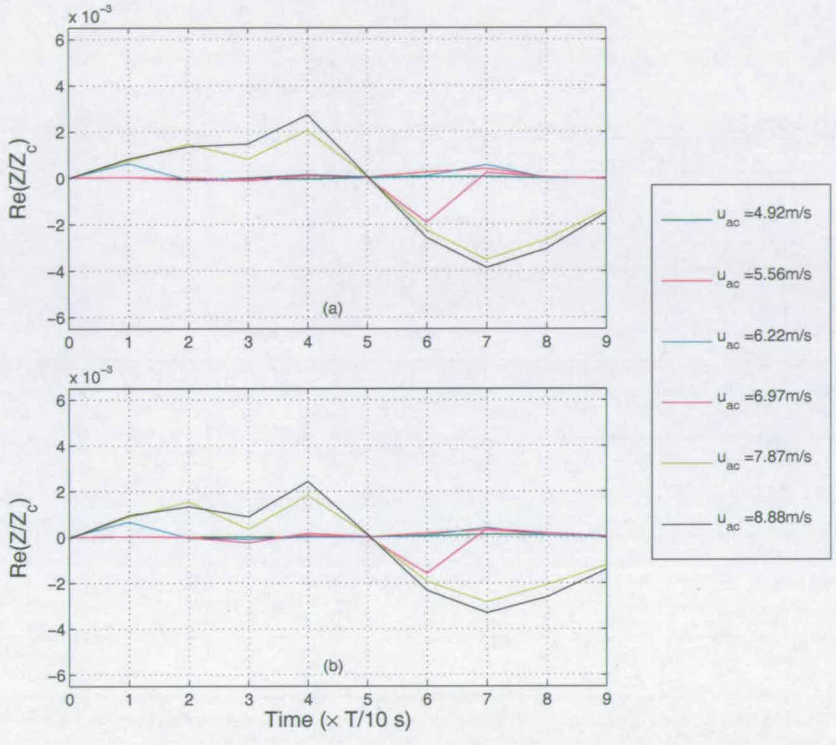


Figure 7.7: Acoustic resistance as a function of time - Area 2. The results of the vortex sound calculation using two determinations of the potential field for the R = 0mm termination: (a) PIV data. (b) Pistonic potential model.

The results for area 2 are shown in figure 7.7. There is excellent agreement between the different potential representations used, with an almost exact reproduction between results, although the pistonic potential results are slightly lower in magnitude. In area 2 both methods indicate that there is no significant acoustic power production or absorption on either inflow or outflow below an acoustic velocity amplitude of 6.22ms^{-1}. No vortices enter this area until the vortex shedding regime which occurs at an acoustic velocity amplitude of 7.87ms^{-1}, so this is as expected. Above 7.87ms^{-1} vortex shedding begins and the behaviour changes dramatically. There is acoustic power absorption on outflow indicated by positive values of the contribution to the acoustic resistance, peaking at Time = 4 × T/10 seconds. Acoustic power production is observed on inflow which has a peak at Time = 7 × T/10 seconds. There is slight production at 6.97ms^{-1}

at the beginning of the inflow stage. The PIV vector maps indicate that at this level, which is just prior to the vortex shedding regime, the flow is slightly unstable in this region and some vorticity is momentarily shed before being drawn back toward the open end.

Area 3

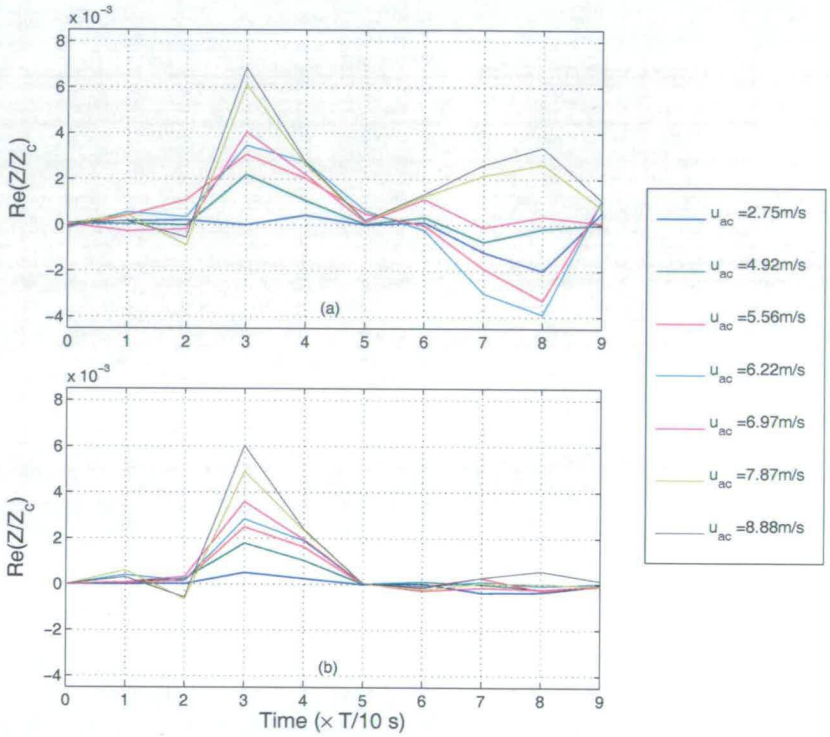
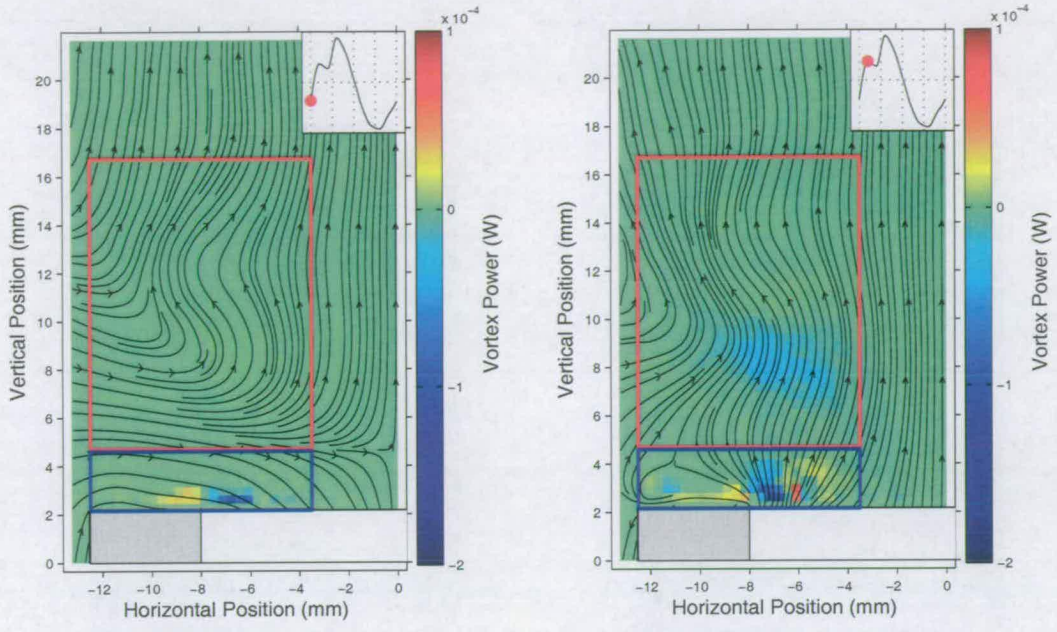


Figure 7.8: Acoustic resistance as a function of time - Area 3. The results of the vortex sound calculation using two determinations of the potential field for the R = 0mm termination: (a) PIV data. (b) Pistonic potential model.

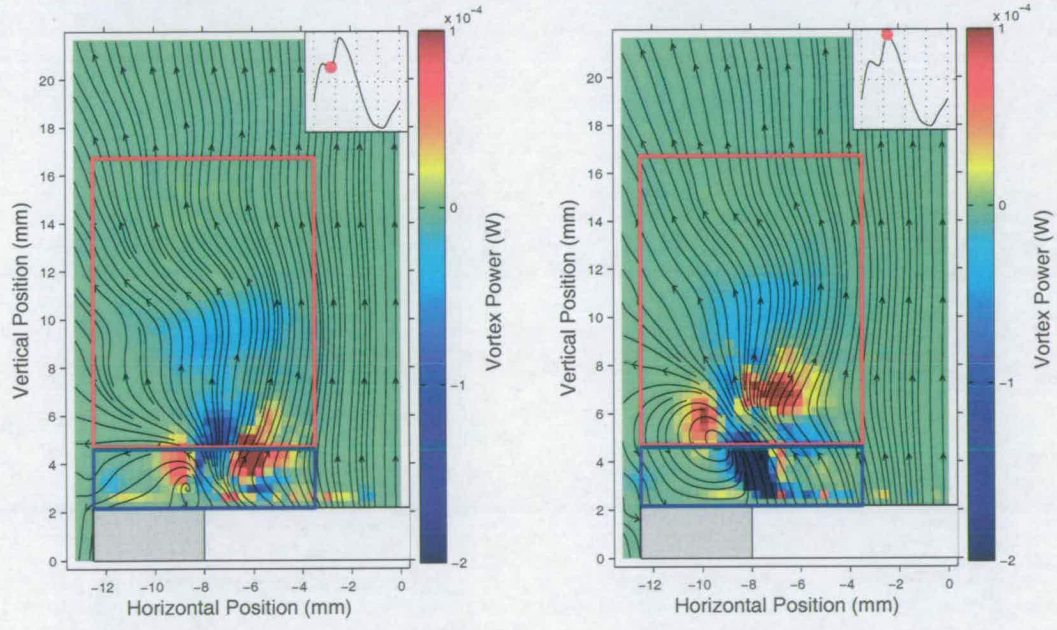
In area 3 acoustical power loss is observed for the outflow part of the acoustic cycle and the results calculated using both potential models are in good agreement. The peak loss occurs at Time = 3 × T/10 seconds, just prior to the peak loss in area 2. On inflow, there is a striking difference between the two methods. For the results calculated using the LAPM data there is acoustic power production on inflow up to an acoustic velocity amplitude of 6.22ms^{-1}. Above 6.97ms^{-1} there is power absorption on inflow. The pistonic potential method shows no acoustic power production or absorption at all on inflow.

Comparison of the results measured at a velocity amplitude of 8.88ms^{-1} in areas 2



(a) Time $= 0\ (\times \frac{T}{10})s$

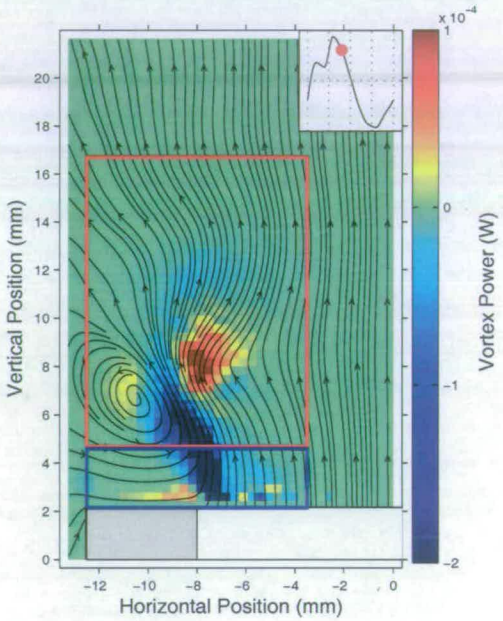
(b) Time $= 1\ (\times \frac{T}{10})s$



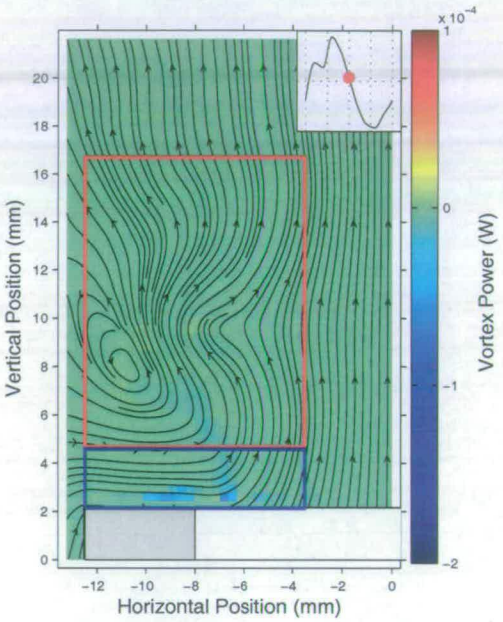
(c) Time $= 2\ (\times \frac{T}{10})s$

(d) Time $= 3\ (\times \frac{T}{10})s$

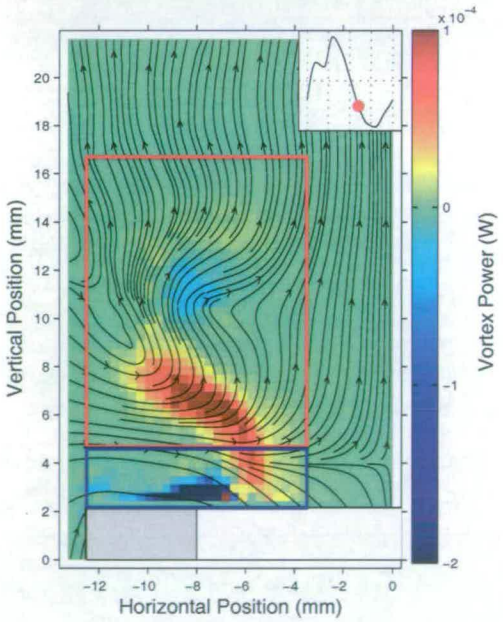
Figure 7.9: Vortex sound power contours for the the R=0mm termination at an SPL of 162.3dB ($|u_{ac}| = 8.88ms^{-1}$). Time is with respect to the trigger point. Grey areas represent the termination wall locations. The red and blue boxes indicate the boundaries of areas 2 and 3 respectively. Blue areas represent acoustic power loss. Red areas represent acoustic power production. The waveform in the upper right corner of each image indicates the point in the acoustic cycle at which the contour map is taken.



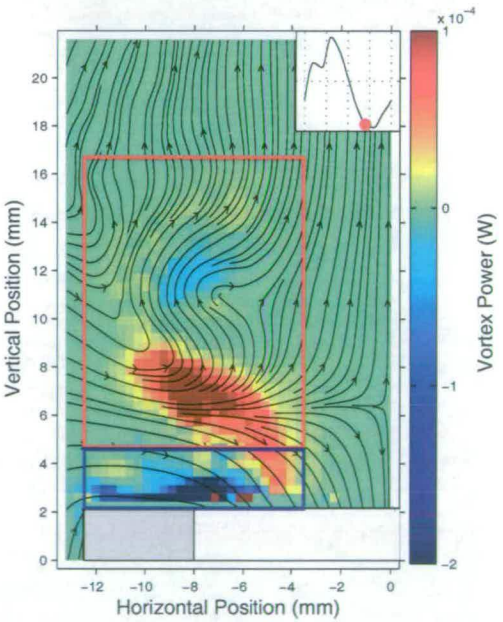
(e) Time $= 4\ (\times \frac{T}{10})s$



(f) Time $= 5\ (\times \frac{T}{10})s$

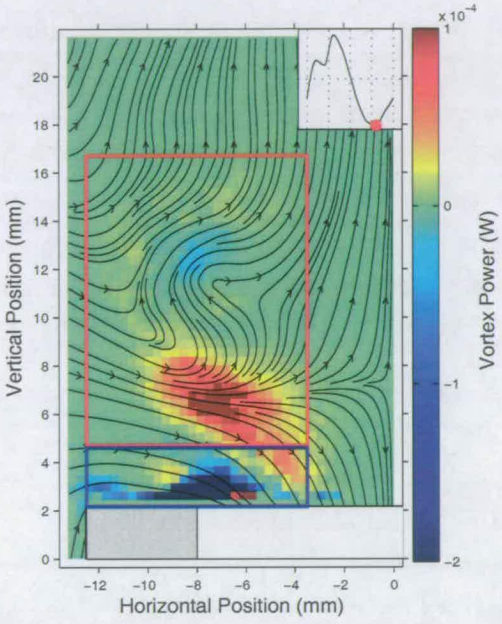


(g) Time $= 6\ (\times \frac{T}{10})s$

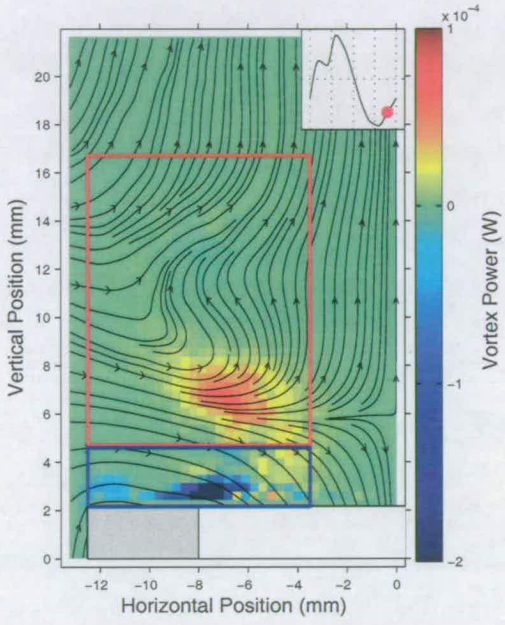


(h) Time $= 7\ (\times \frac{T}{10})s$

Figure 7.9 continued.



(i) Time $= 8\ (\times \frac{T}{10})s$



(j) Time $= 9\ (\times \frac{T}{10})s$

Figure 7.9 continued.

(figure 7.7) and 3 (figure 7.8) with the vortex power contour maps in figure 7.9 helps to identify several features[3]. As the acoustic cycle progresses, an anti-clockwise circulating vortex structure can be seen being ejected from the open end of the tube. This shall be referred to as the major vortex. As this vortex is ejected on outflow it carries with it a region of vorticity which acts to strongly absorb energy from the acoustic field. The major vortex is accompanied by a smaller counter-rotating vortex which was generated on the inflow part of the previous acoustic cycle and which acts as a source on outflow but is much weaker. This shall be referred to as the minor vortex.

In figure 7.9(d) the area of absorption associated with the major vortex can be seen to be almost entirely within the boundaries of area 3. There are no other significant losses within this area at this stage. Comparison with the results for area 3 in figure 7.8 reveals that the peak in the acoustic resistance on outflow corresponds to this stage of the acoustic cycle. The observed absorption on outflow within area 3 appears to be solely due to the passage of the major vortex through area 3 into area 2. The peak power absorption in area 2 in figure 7.7 is observed at the time at which the major vortex enters this area, at one time step ($T/10$) later than the peak result for area 3. The power dissipation observed on outflow for area 2 appears mainly to be due to a dispersed area of power absorption (shown in light blue) which is caused by the remnant of the major vortex produced by the previous acoustic cycle.

When the acoustic potential field changes from inflow to outflow or vice-versa there is negligible power production or loss as the entire potential field is approximately zero. This is seen in figure 7.9(a) and (f) for the changes from inflow to outflow and from outflow to inflow respectively. Once the inflow part of the cycle commences, the function of the major vortex changes from power absorption to production, and the weak minor vortex changes from production to absorption. During inflow the major vortex, which is now acting as an acoustic source, is entirely contained within the boundaries of area 2. This correlates with the observation of sound production on inflow in area 2 in figure 7.7 (page 177).

During inflow the flow close to the tube wall in area 3 shows high levels of acoustic power loss. This is the source of the energy dissipation on inflow for the PIV results in figure 7.8(a). This dissipation is not observed in the vortex sound contour maps produced using the pistonic potential model as the reference flow. This is due to the fact that in the pistonic model does not accurately describe the flow around walls and edges.

[3]Additionally, comparison with the corresponding vector and vorticity contour maps in figure 5.14 also helps to identify flow features.

7.3.3 Interpretation of vortex sound theory

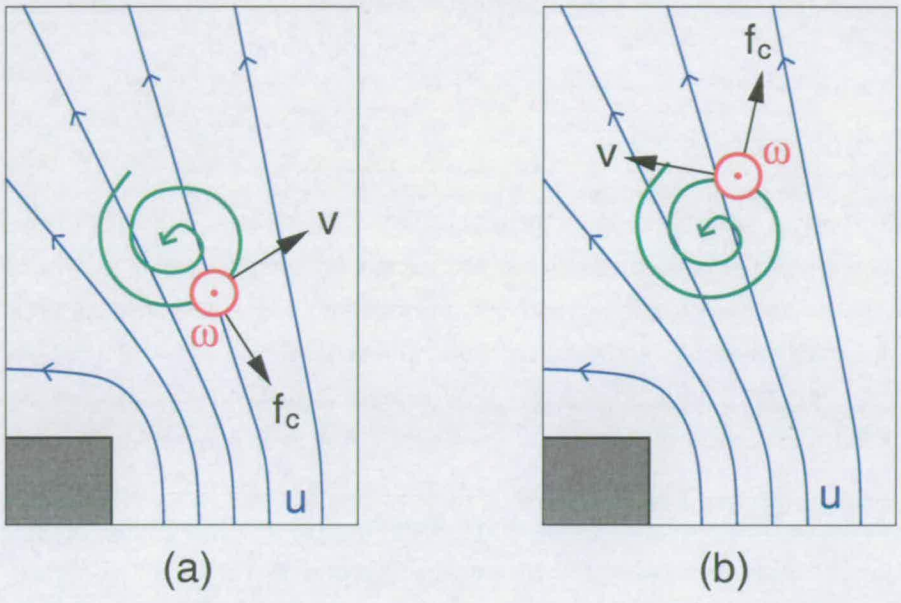


Figure 7.10: Schematic representation showing a vortex in a potential flow u. The vortex is circulating in an anti-clockwise sense with vorticity ω directed out of the page. The local vortex velocity is v and the resultant coriolis force is f_c. (a) Coriolis force opposes motion of the potential flow resulting in power loss. (b) Coriolis force reinforces the motion of the potential flow resulting in power production.

As was shown in the previous section, the distribution of the vortex sound power field of a vortex in the presence of a potential field is not constant over the vortex structure. Different areas of the vortex contribute more or less to the acoustic field than others. Whether an area of the vortex will act as an acoustic source or loss mechanism (and the extent to which it does) depends on the orientation of the local velocity field associated with the vortex, relative to the direction of the acoustic potential field. Figure 7.10 schematically illustrates the case for two spatial positions on the same vortex structure in a potential field. The local velocity of the vortex is tangential to the edge of the vortex and the vorticity is directed out of the page. The associated coriolis force is always perpendicular to the edge of the vortex and directed outward.

Figure 7.10(a) examines the effect at a point on the lower right hand edge of the vortex structure. In this case the coriolis force vector has a component acting in the opposite direction to the acoustic potential flow, and acts as a drag force, transferring power from the potential field to the vortex. In figure 7.10(b) a point on the upper right hand edge of the vortex is examined. Here the coriolis force vector has a component in the same direction as the acoustic potential flow and so reinforces and transfers energy

to the flow.

These effects can be seen in detail in the vortex sound contour maps and velocity streamlines in figure 7.9 for the case of the R=0mm termination.

7.4 Conclusions

The work in this chapter has shown that it is feasible to use the vortex sound analysis method in association with PIV measurements by using a low amplitude measurement to represent the acoustic potential flow. Comparison with vortex sound results calculated using a theoretical model of the acoustic potential flow above a piston confirm that this is a valid approach. The acoustic resistance results measured using the vortex sound method indicate that losses due to vortex generation account for only approximately 10% of the losses calculated in the previous chapter. This is expected to be an underestimation since measurements were only made outside the open end of the tube. It is highly likely that the interaction of vortices with the tube walls will be a significant loss mechanism within the open end. This, however, seems to indicate that another mechanism is responsible for the losses observed by Atig [Atig 04] and in the previous chapter.

The results in section 7.3.2 show that the net acoustical losses due to the interaction of vorticity with the acoustic field are most significant in a region within 2.5mm of the open end. Outwith this region vortices act as a net source of sound over an acoustic cycle, but are of lesser magnitude. The results have shown that the pistonic model of the flow above the open end of a tube is appropriate for distances greater than 2.5mm from the open end, but significant differences in the region closer than this are detected.

Chapter 8

Conclusions

A summary of the conclusions reached in this work are presented in this chapter. Some recommendations for future work are then made.

8.1 Non-linear effects in acoustically generated flows at the open ends of tubes

The first aim of this study was to investigate the presence of non-linear effects in high amplitude acoustically generated flows using PIV to measure the velocity field at the open ends of tubes with various termination geometries.

In chapter 5 PIV measurements of the open end of a tube in which a high amplitude sound field was generated by a loudspeaker were described. Five interchangeable termination geometries were used to investigate the effect of varying the geometry of the open end on the flow field at a number of sound levels.

The PIV results in chapter 5 show that a range of non-linear flow effects are present that depend on the geometry of the termination. At low sound levels it has been shown that non-linear effects are negligible and the velocity field can be described as a potential flow. As the acoustic velocity amplitude increases a number of distinct non-linear flow regimes are observed, as described in a number of previous studies [Sivian 35, Ingard 50]. The results for the sharp edged termination show that non-linear behaviour becomes important at much lower acoustic amplitudes than for the terminations with a slight flange. Also a range of different vortex shedding regimes are observed for the sharp edged terminations. The most rounded termination showed minimal non-linear behaviour even at the highest sound levels measured.

The three slightly flanged terminations with a rounded inner edge (with radii of curvature R = 0mm, 0.3mm and 1mm) show the closest similarity to one another in their observed non-linear flow behaviour. A distinct transition from a flow regime where vortices are generated on outflow but remain in the close vicinity of the termination to a regime in which vortex shedding and jet formation become important is observed. The acoustic amplitude at which this transition occurs depends strongly on the radius

of curvature of the inner edge of the open end of the tube. Terminations with a less rounded inner edge undergo the transition to vortex shedding at a lower acoustic amplitude.

8.2 Termination impedance measurements at high acoustic amplitudes

The second aim of this study was to obtain termination impedance measurements using the velocity information provided by the PIV results from chapter 5 in conjunction with pressure measurements made at the open end of the tube using a probe microphone. A secondary aim was to compare these with results with those obtained in a separate study using a two-microphone method by Atig [Atig 04].

A method of obtaining the termination impedance from PIV velocity and pressure measurements was described in chapter 6. The volume velocity was obtained from measurements in a plane just outside the open end of the tube. A curve fitting procedure was used to determine the amplitude and phase of the volume velocity. These results were analysed in conjunction with the amplitude and phase of the first harmonic component of the pressure signal and the termination impedance was thus obtained and plotted against the linearised acoustic velocity amplitude at the open end.

It was found that the shape of the tube termination plays an important role in determining the level and rate of increase of energy loss associated with the production of non-linear flow phenomena at high acoustic amplitudes. Comparison with the results of Atig [Atig 04] showed that results measured with the two methods were of the same order of magnitude and showed essentially the same trends with slight differences in detailed behaviour. Differences were attributed to direct rather than linearly inferred measurements of the phase of the volume velocity.

Three distinct flow regimes were recognised for the slightly flanged terminations by comparison of the termination impedance results with time-averaged acoustic velocity data. These flow regimes were found to correspond to flow regions observed by Ingard and Labate [Ingard 50].

8.3 Losses associated with acoustically generated vortex structures

The final aim of this work was to evaluate the acoustical losses associated with the production of vortices using vortex sound theory.

Chapter 7 outlined a method of post-processing the PIV data obtained in chapter

5 using vortex sound theory to obtain a measure of the acoustical energy loss caused by vortex generation, in terms of a normalised acoustic resistance. Two methods were used to determine a representative reference acoustic potential flow. The first method made use of low amplitude PIV data and the second used a theoretical model which represented the flow at the open end of a tube as that above an oscillating piston.

The results show that the two representations of the potential field are comparable for distances greater than 2.5mm from the open end. For distances less than this the agreement is not as good. The pistonic model of the flow fails to predict any sound loss on inflow due to the fact that the model does not correctly represent flow around edges and corners. The low amplitude PIV measurements are shown to be a good representation of the acoustic potential flow indicating that the method used was justified.

The acoustic resistance results measured using the vortex sound method for the region outside the tube indicate that losses due to vortex generation account for only approximately 10% of the losses calculated in chapter 6. It is expected that since losses within the open end of the tube are not taken into account that this is an underestimation although this cannot be confirmed. This seems to indicate that another loss mechanism may be responsible for the losses observed by Atig [Atig 04] and in chapter 6.

8.4 Future work

A number of extensions and improvements to this work could be made. PIV measurements at a larger number of phase steps would allow an improved determination of the phase of the volume velocity data. The range of terminations could be extended to include those with larger flanges or with rounded outer edges, for example.

To fully evaluate the non-linear acoustical losses at the open end of a tube a number of steps could be taken. Firstly, the losses associated with vortex generation inside the open end of the tube could be evaluated. This would require PIV measurements within the open end and could be achieved in a number of ways. Secondly, it would be of interest to evaluate the energy loss associated with jet streaming and to compare this with the losses measured using vortex sound theory and by direct measurement. Also, different potential models incorporating tube walls would be of benefit both for comparison with PIV data and in the vortex sound calculation, especially in the region close to the open end.

Although this study has estimated the losses associated with non-linear acoustic flows at the open end of a representation of a woodwind instrument, the method does not give an indication of the what the resulting effect on the timbre of a real

woodwind instrument would be. It would be of great interest to woodwind instrument manufacturers to know what effect this has.

Experiments could be extended to the measurement of real instruments. One problem with this would be in the excitation mechanism used. Since there are safety issues associated with the PIV technique it may be difficult to safely use human players and an artificial means of excitation would then be essential.

Some technical issues could be solved using a laser capable of a shorter time between light pulses than the one used in this study. This would allow higher acoustic velocity amplitudes to be measured and would allow flow regions to be measured with higher magnification to obtain more detailed information about the flow close to the tube walls, for example. A high speed camera could be used for the study of transient behaviour or the development of acoustic flows during the course of a single acoustic cycle.

The techniques used in this study have demonstrated that PIV is highly suited to the measurement of acoustic fields. It is an extremely flexible technique and can potentially be applied to any situation in which non-linear acoustic fields are present, not just in the field of musical acoustics.

Appendix A

Limitations of PIV in acoustic particle displacement measurement

A.1 Maximum Displacement: Nyquists Theorem

An object is imaged onto an array of pixels using a ccd camera. The object is of known physical size L (measured in metres) in the plane of the image and the corresponding size of the object, in pixels, measured from the image is σ. These two sizes could, for example, be the size of the entire field of view and the resolution in pixels of the image, respectively, or simply the size in metres and pixels of an object placed in the field of view (see figure A.1). To carry out a PIV analysis of the pixel array (image) it is divided into a grid of smaller *interrogation areas*. The width of the interrogation area is typically 32 pixels and is here denoted I. The physical size (in metres) of the interrogation area is given by: LI/σ. Nyquist's sampling theorem limits the maximum resolvable spatial displacement of a particle in the flow to 50% of the interrogation width, or $I/2$ [Dewhirst 98] (although an optimal value of 30% was found in [Keane 90]). The maximum allowable displacement s_{max} of a particle for a given field of view and resolution is then:

$$s_{max} = \frac{LI}{2\sigma} \tag{A.1}$$

It should be noted that although Nyquist's theorem limits the maximum resolvable displacement to 50% of the interrogation width, the displacement should in reality be smaller than this (optimally about 30% [Keane 90]) to prevent a reduction in the signal to noise ratio.

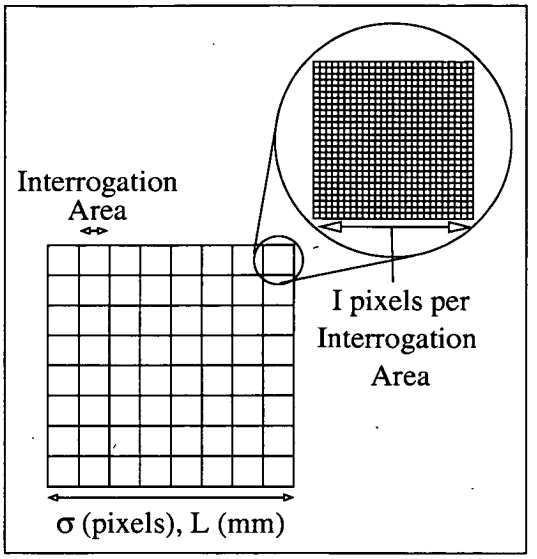


Figure A.1: Image array showing interrogation areas and pixels

A.2 Acoustic Particle Displacement and Frame Capture Rate

The acoustic particle velocity is of the form:

$$\frac{ds}{dt} = v_0 sin(\omega t)$$

where s is the particle displacement, v_0 is the particle velocity amplitude, ω is the radian frequency and t is time.

If a series of images are captured using a high speed camera with a frame capture rate of ϵ Hz, then there will be ϵ/f captured images per acoustic cycle and a time interval between frames of $\tau = 1/\epsilon$. The particle displacement per image, Δs, is calculated by integrating the acoustic particle velocity between time intervals t_1 and t_2. This gives for the magnitide of the displacement:

$$|\Delta s| = \frac{v_0}{\omega}\{cos(\omega t_1) - cos(\omega t_2)\} \qquad \text{(A.2)}$$

The maximum value of this quantity is found over an interval τ centered on the zero crossings of the particle displacement(where $\omega t = \pi/2, 3\pi/2 \ldots$), where the gradient is at its greatest (see figure A.2). This gives for t_1 and t_2:

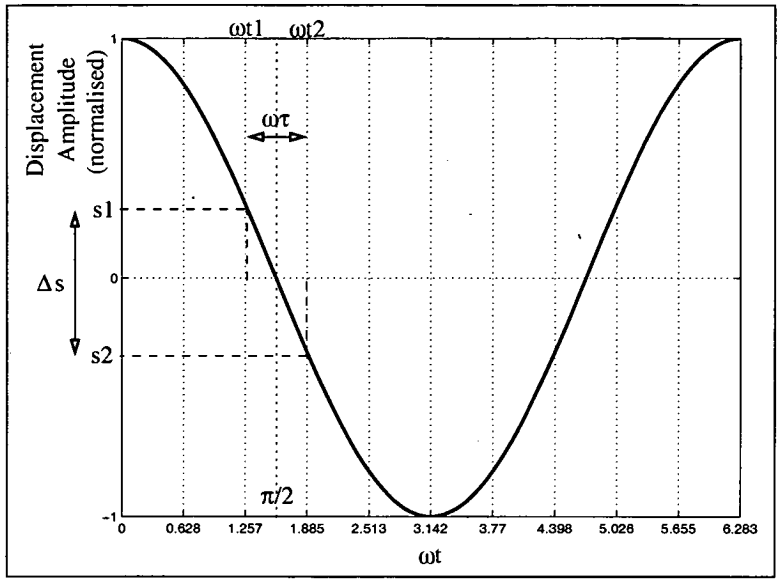


Figure A.2: Particle Displacement

$$\omega t_1 = \frac{\pi}{2} - \frac{\omega\tau}{2}$$
$$\omega t_2 = \frac{\pi}{2} + \frac{\omega\tau}{2} \tag{A.3}$$

Combining equations (A.2) and (A.3), and using the trigonometric identity:

$$2sinAsinB = cos(A-B) - cos(A+B) \tag{A.4}$$

We arrive at the following equation for the maximum particle displacement per image:

$$|\Delta s| = \frac{2v_0}{\omega} sin(\frac{\omega\tau}{2}) \tag{A.5}$$

For $\omega\tau/2 \ll 1$ (low frequencies and/or high camera frame capture rates) we can make use of the small angle approximation (for small θ, $sin\theta \approx \theta$) to write:

$$|\Delta s| \approx v_0\tau \tag{A.6}$$

To comply with Nyquist's theorem this quantity should be less than or equal to s_{max}.

$$\Delta s \leq s_{max} \tag{A.7}$$

Therefore, combining equations (A.1), (A.6) and (A.7), we get:

$$v_0 \tau \leq \frac{LI}{2\sigma} \tag{A.8}$$

Using this inequality we can determine minimum values for the field of view size, for example, given that we know the upper limit of the particle velocity magnitude that we want to measure, and that we know and can adjust the camera resolution, frame rate (or time between frames given by $\tau = 1/\epsilon$), and interrogation size.

$$L \geq \frac{2v_0\sigma}{I\epsilon} \tag{A.9}$$

Table A.1 shows values calculated for the minimum size of the field of view using I = 32pixels, v_0 = 30m/s with values for the resolution and frame capture rate of the Phantom v5.0 high speed camera.

Resolution σ (pixels)	Frame Rate ϵ (Hz)	Field of View Size L (m)
1024	1000	1.92
512	3800	0.25
256	11900	0.04

Table A.1: Field of view sizes for several resolutions and frame rates of the Phantom v5.0 high speed camera. Values were calculated using v_0 = 30m/s and I = 32pixels.

Perhaps more useful is the ability to calculate maximum time intervals between images (for the PCO camera used in this study, for example) and to identify suitable frame capture rates for use with a high speed camera. The maximum time interval is given by:

$$\tau \leq \frac{LI}{2\sigma v_0} \tag{A.10}$$

Table A.2 shows maximum τ and minimum ϵ values for a range of field of view sizes and camera resolutions with an interrogation size of 32 pixels. For a laser providing light pulses with a time interval between pulses of 100μs it can be seen that there are only a few configurations that will allow velocity measurements in a field of view of 5cm that are high enough to be useful.

A.3 PIV Measurement of Resonant Tubes

For PIV measurements of particle velocity at the end of a resonating tube it is possible to calculate a suitable time interval between images if the sound pressure level as measured in the region of interest is known. In the linear regime, the acoustic impedance

L = 0.05m, v_0 = 30m/s			
Resolution σ(pixels)	1024	512	256
Inter-Frame Time $\tau(\mu s)$	26	52	104
Frame Rate ϵ(Hz)	38500	19200	9600
L = 0.05m, v_0 = 10m/s			
Resolution σ(pixels)	1024	512	256
Inter-Frame Time $\tau(\mu s)$	78	156	312
Frame Rate ϵ(Hz)	12800	6400	3200
L = 0.01m, v_0 = 10m/s			
Resolution σ(pixels)	1024	512	256
Inter-Frame Time $\tau(\mu s)$	15	31	62
Frame Rate ϵ(Hz)	64000	32000	16000

Table A.2: Time intervals between frames and image capture rates at various image resolutions for different sized fields of view and maximum velocity

at a cross-section of tube is:

$$Z = \frac{p}{U} = \frac{\rho_0 c}{S} \tag{A.11}$$

where p is the pressure, $U = u_0 S$ is the volume velocity (with u_0 the average velocity across the cross-section) and S is the cross-sectional area of the tube. The pressure (in Pascals) can be written as:

$$p = \rho_0 c u_0 \tag{A.12}$$

The sound pressure level (SPL) is given by:

$$SPL = 20 \log \left(\frac{p}{p_{ref}} \right) = 20 \log \left(\frac{\rho_0 c u_0}{p_{ref}} \right) \tag{A.13}$$

where $p_{ref} = 2 \times 10^{-5}$. Rearranging for u_0 gives:

$$u_0 = \frac{p_{ref}}{\rho_0 c} 10^{\left(\frac{SPL}{20}\right)} \tag{A.14}$$

Putting $u_0 = v_0$ and combining equations A.10 and A.14 gives for τ:

$$\tau \leq \left(\frac{LI\rho_0 c}{2\sigma p_{ref}} \right) 10^{\left(-\frac{SPL}{20}\right)} \tag{A.15}$$

Figure A.3 shows a plot of τ with increasing SPL for three camera resolutions ($\sigma = 1024, 512, 256$) with $L = 0.05m$ and $I = 32$pixels.

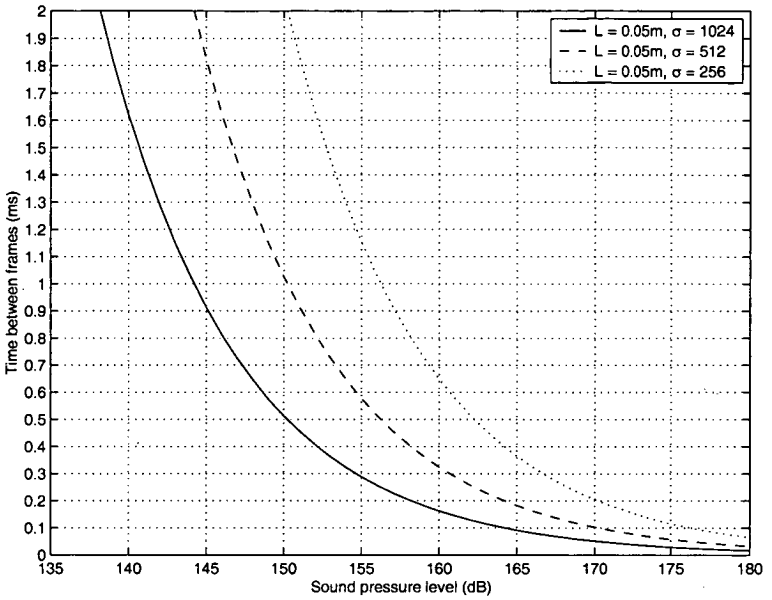


Figure A.3: Image separation time and sound pressure level

A.4 Errors

Figure A.4 shows three curves, one representing equation A.5 and two others representing its first and second order approximations for a typical driving frequency of 500 Hz and maximum particle velocity of 30 m/s. The size of the percentage error in Δs due to use of the first order (small angle) approximation can be seen in figure A.5. At an image capture rate of 3.8kHz, $\omega\tau/2 \approx 0.4$, corresponding to an error in Δs of about 3% or 0.25mm. Lower frame capture rates lead to an unacceptably large error, so a second order approximation should be used instead.

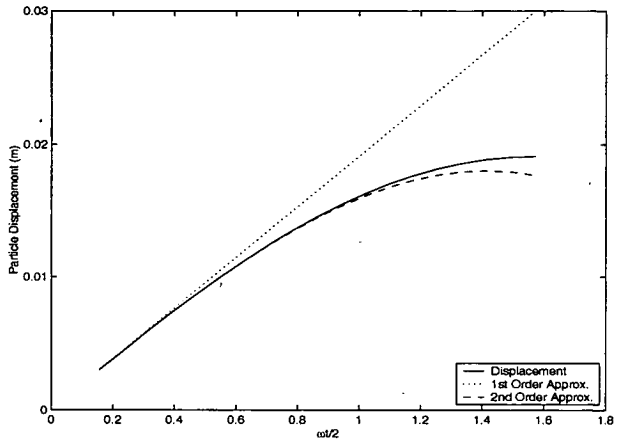


Figure A.4: Particle displacement and its first and second order approximations

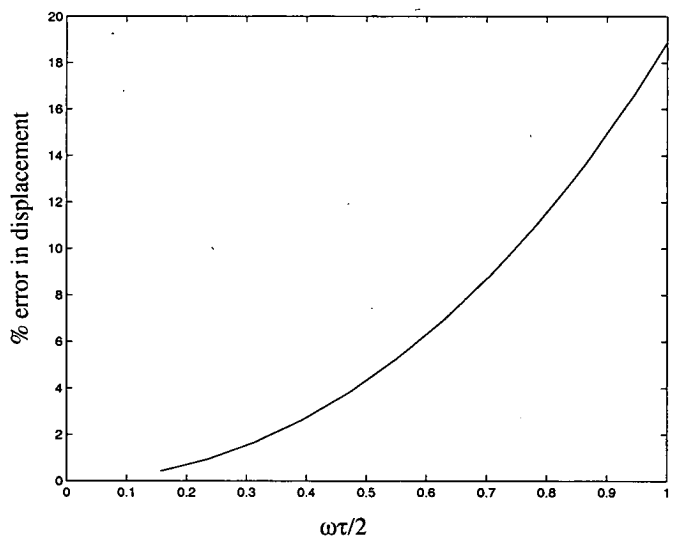


Figure A.5: First order error in particle displacement due to small angle approximation

Bibliography

[Adrian (Editor) 93] R.J. Adrian (Editor). Selected papers on laser doppler velocimetry. New York: SPIE, 1993.

[Adrian 91] R.J. Adrian. *Particle-imaging techniques for experimental fluid mechanics.* Ann. Rev. Fluid Mech., vol. 23, pages 261–304, 1991.

[Agüi 87] J.C. Agüi & J Jiménez. *On the performance of particle tracking.* J. Fluid Mech., vol. 185, pages 447–468, 1987.

[Atig 01] M. Atig. *Non-linéarités acoustiques localisées. Exemple du rayonnement d'un tube.* D.E.A report, Académie du Nantes, Université du Maine, 2001.

[Atig 03] M. Atig, J.-P. Dalmont & J. Gilbert. *Impedance of pipe ends at high sound pressure levels.* Compte Rendus de l'Academie des Sciences - Mechanique, 2003.

[Atig 04] M. Atig. *Non-linéarité acoustique localisée a l'extrémité ouverte d'un tube.* PhD thesis, Université du Maine, Le Mans, 2004.

[Bachelor 02] G.K. Bachelor. An introduction to fluid dynamics. Cambridge University Press, 2002.

[Bamberger 01] A. Bamberger & A. Orth. *Fluid dynamical investigation of the intonation roll with particle image velocimetry.* In Proceedings ISMA, 2001.

[Bamberger 02] A. Bamberger. *Investigations and recent results on flutes with* PIV. In Proceedings of Forum Acusticum Conference, Sevilla, Spain, 2002.

[Bamberger 04] A. Bamberger. *Vortex sound of flutes observed with Particle Image Velocimetry.* In Proceedings of the 18th International Conference on Acoustics, Kyoto, Japan, 2004.

[Bamberger 05] A. Bamberger. *Vortex sound of flutes using flow determination with Endo-PIV.* In Proceedings of Forum Acusticum, Budapest, Hungary, 2005.

[Barker 77] D.B. Barker & M.E. Fourney. *Measuring fluid velocities with speckle patterns.* Optics Letters, vol. 1(4), pages 135–137, 1977.

[Boucheron 04] R. Boucheron, H. Bailliet & J.-C. Valière. *Beyond laminar regime in acoustic wave guides.* In Proceedings of the 18th International Conference on Acoustics, Kyoto, Japan, 2004.

[Bruecker 04] C. Bruecker, M Treip & M. Kob. *Study of the vortex dynamics in a mechanical model of the vocal folds using Particle Image Velocimetry.* In Proceedings of the International conference on Voice Physiology and Biomechanics, Marseille, France, 2004.

[Brunn 95] H.H. Brunn. Hot-wire anemometry - principles and signal analysis. Oxford University Press, 1995.

[Campbell 00] D.M. Campbell, J.A. Cosgrove, C.A. Greated, S. Jack & D. Rockliff. *Review of LDA and PIV applied to the measurement of sound and acoustic streaming.* Optics and Laser Technology, vol. 32, pages 630–639, 2000.

[Dalmont 01] J.-P. Dalmont, C.J. Nederveen & N. Joly. *Radiation impedance of tubes with different flanges: numerical and experimantal investigations.* J. Sound Vib., vol. 244(3), pages 505–534, 2001.

[Dantec 98] Dantec. *Safex Fog Generator - User's guide.* Dantec Measurement Technology A/S, October 1998.

[Dantec 05] Dantec. Private communication. September 2005.

[de Bree *et al* 96] H.-E. de Bree *et al.* *The Microflown: a novel device for measuring acoustical flows.* Sensors and Actuators: A, Physical, vol. SNA054/1-3, pages 552–557, 1996.

[de Bree 03a] H.-E. de Bree. *The Microflown, an acoustic particle velocity sensor.* Australian Acoustics, vol. 31(3), pages 91–94, 2003.

[de Bree 03b] H.-E. de Bree. *An overview of Microflown Technologies.* Acta Acustica, vol. 89, pages 163–172, 2003.

[Dewhirst 98] T. Dewhirst. *Multiple CCD Array Digital Particle Imaqge Velocimetry.* PhD thesis, University of Edinburgh, 1998.

[Disselhorst 80] J.H.M. Disselhorst & L. Van Wijngaarden. *Flow in the exit of open pipes during acoustic resonance.* Journal of Fluid Mechanics, vol. 99(2), pages 293–319, 1980.

[Dracos (Editor) 96] Th. Dracos (Editor). Three-dimensional velocity and vorticity measuring and image analysis techniques. Kluwer Academic Publishers, Dordrecht, 1996.

[Dufford 02] S. Dufford, D. Marx & P. Blanc-Benon. *Détermination de la vitesse acoustique instantané par PIV dans un stack thermoacoustique.* In Proc. 6th French Conference on Acoustics, Lille, France, 2002.

[Durst 80] F. Durst, A. Melling & J.H. Whitelaw. Principles and practice of laser doppler anemometry. Academic Press, 1980.

[Esposito 03] E Esposito & M. Marassi. *Quantitative assessment of air flow from professional bass reflex systems ports by Particle Image Velocimetry and laser doppler anemometry.* In Proceedings of the Stockholm Musical Acoustics Conference, 2003.

[Grant (editor) 94] I. Grant (editor). Selected papers on particle image velocimetry. SPIE Optical Engineering Press (Milestone Series), 1994.

[Grant 97] I. Grant. *Particle image velocimetry: a review.* Proc. Instn. Mech. Engrs., vol. 211(C), pages 55–76, 1997.

[Hann 95] D.B. Hann. *Simultaneous measurement of acoustic fields and flow fields using optical methods.* PhD thesis, University of Edinburgh, 1995.

[Hann 97a] D.B. Hann & C.A. Greated. *The measurement of flow velocity and acoustic particle velocity using particle image velocimetry.* Meas. Sci. Technol., vol. 8, pages 1517–1522, 1997.

[Hann 97b] D.B. Hann & C.A. Greated. *Measurement of the acoustic particle velocity using particle image velocimetry.* Acustica, vol. 83, pages 354–358, 1997.

[Hirschberg 95] A. Hirschberg, J. Kergomard & G. Weinreich. Mechanics of musical instruments - cism courses and lectures no.355. Springer - Verlag, Wein, New York, 1995.

[Hirschberg 96] A. Hirschberg, J. Gilbert, R. Msallam & Wijnands A. P. J. *Shock waves in trombones.* J. Acoust. Soc. Am., vol. 99(3), pages 1754–1758, 1996.

[Hirschberg 97] A. Hirschberg. *Selfsustained aeroacoustic oscillations in gas transport systems: a prediction method for pulsations induced by closed pipe segments.* Rapport technique TUE NT R-1428-D, Eindhoven University of Technology, 1997.

[Hoffmans 99] G.C.J. Hoffmans. *Vortex sound in confined flows.* PhD thesis, Eindhoven University of Technology, 1999.

[Holder 63] D.W. Holder. Schlieren methods. H.M. Stationary Off. London, 1963.

[Howe 75] M.S. Howe. *Contributions to the theory of aerodynamic sound, with application to excess jet noise and the theory of the flute.* J. Fluid Mech., vol. 71(4), pages 625–673, 1975.

[Howe 80] M.S. Howe. *Dissipation of sound at an edge.* J. Sound Vib., vol. 70(3), pages 407–411, 1980.

[Ingard 50] U. Ingard & S. Labate. *Acoustic circulation effects and the nonlinear impedance of orifices.* Journal of the Acoustical Society of America, vol. 22(2), pages 211–218, 1950.

[Ingard 67] U. Ingard & H. Ising. *Acoustic nonlinearity of an orifice.* Journal of the Acoustical Society of America, vol. 42(1), pages 6–17, 1967.

[Keane 90] R.D. Keane & R.J. Adrian. *Optimisation of particle image velocimeters part1: double pulsed systems.* Meas. Sci. Technol., vol. 1, pages 1202–1215, 1990.

[Keefe 83] D.H. Keefe. *Acoustic streaming, dimensional analysis of nonlinearities, and tone hole mutual interactions in woodwinds.* J. Acoust. Soc. Am., vol. 73(5), pages 1804–1820, 1983.

[Lauterborn 84] A. Lauterborn & A. Vogel. *Modern optical techniques in fluid mechanics.* Ann. Rev. Fluid Mech., vol. 16, pages 223–244, 1984.

[Levine 48] H. Levine & J. Schwinger. *On the Radiation of Sound from an Unflanged Circular Pipe.* Phys. Rev, vol. 74, pages 383–406, 1948.

[Lighthill 52] M.J. Lighthill. *On sound generated aerodynamically I.* In Proceedings of the Royal Society of London Series A 211, 1952.

[Maynart 83] R. Maynart. *Speckle velocity study of vortex pairing an a low-Re unexcited jet.* Physics of Fluids, vol. 26(8), pages 2074–2079, 1983.

[Melling 97] A. Melling. *Tracer particles and seeding for particle image velocimetry.* Meas. Sci. Technol., vol. 8, pages 1406–1416, 1997.

[Moreau 05] S. Moreau, H. Bailliet & J.-C. Vallière. *Entering Length due to pipe termination of unsteady acoustic flow.* In Proceedings of Forum Acusticum Conference, Budapest, Hungary, 2005.

[Nederveen 98] C.J. Nederveen. Acoustical aspects of woodwind instruments. Northern Illinois University Press, DeKalb, Illinois. 2nd Edition, 1998.

[Nomura 60] Y. Nomura, I. Yamamura & S. Inawashiro. *On the acoustic radiation from a flanged circular pipe.* J. Phys. Soc. Japan, vol. 15, pages 510–517, 1960.

[Peters *et al* 93] M.C.A.M. Peters *et al. Damping and reflection coefficient measurements for an open ended pipe at low mach and low helmholtz numbers.* J. Fluid Mech., vol. 256, pages 499–534, 1993.

[Peters 93a] M.C.A.M. Peters. *Aeroacoustic sources in internal flows.* PhD thesis, Eindhoven University of Technology, 1993.

[Peters 93b] M.C.A.M. Peters & Hirschberg A. *Acoustically induced vortex shedding at sharp edged open channel ends: simple vortex models.* J. Sound Vib., vol. 161(2), pages 281–299, 1993.

[Pierce 81] A.D. Pierce. Acoustics: An introduction to its physical principles and applications. McGraw-Hill Book Company, Inc., New York, 1981.

[Powell 64] A. Powell. *Vortex sound theory.* J. Acoust. Soc. Am., vol. 36, pages 177–195, 1964.

[Pratt 77] R.L. Pratt, S.J. Elliott & J.M. Bowsher. *the measurement of the acoustic impedance of brass instruments.* Acusica, vol. 38, pages 236–246, 1977.

[Press *et al* 92] W.H. Press *et al.* Numerical recipes in c: the art of scientific computing. Cambridge University Press, 1992.

[Raffel 98] M. Raffel, C. E. Willert & J. Kompenhans. Particle image velocimetry. Springer - Verlag, Berlin, Heidelberg, 1998.

[Rockliff 01] D. Rockliff, D.M. Campbell & J.-P. Dalmont. *Experimental Study of the Velocity Field at the Side Holes and Termination of a Tube.* In Proceedings of International Congress on Acoustics, Rome, Italy, 2001.

[Rockliff 02a] D. Rockliff. *Application of Particle Image Velocimetry to the Measurement of Non-Linear Effects generated by High-Intensity Acoustic Fields.* PhD thesis, University of Edinburgh, 2002.

[Rockliff 02b] D. Rockliff, D.J. Skulina, D.M. Campbell & C.A. Greated. *PIV Measurement of acoustic velocities at woodwind instrument toneholes.* In Proceedings of the Institute of Acoustics meeting, Salford, UK, 2002.

[Salikuddin 83] M. Salikuddin & K.K. Ahuja. *Acoustic power dissipation on radiation through duct terminations: experiments.* Journal of Sound and Vibration, vol. 91(4), pages 479–502, 1983.

[Schlicke 01] T. Schlicke. *Breaking waves and the dispersion of surface films.* PhD thesis, University of Edinburgh, 2001.

[Schram 03] C. F. Schram. *Aeroacoustics of Subsonic Jets: Prediction of the Sound Produced by Vortex Pairing Based on Particle Image Velocimetry.* PhD thesis, Eindhoven University of Technology, 2003.

[Settles 01] G.S. Settles. Schlieren and shadowgraph techniques: Visualising phenomena in transparent media. Springer, 2001.

[Sharpe 89] J.P. Sharpe, C.A. Greated, C. Gray & D.M. Campbell. *The measurement of acoustic streaming using particle image velocimetry.* Acustica, vol. 68, pages 168–172, 1989.

[Sivian 35] L.J. Sivian. *Acoustic Impedance of Small Orifices.* J. Acoust. Soc. Am., vol. 7, pages 94–101, 1935.

[Skulina 02] D.J. Skulina, D. Rockliff, D.M. Campbell & C.A. Greated. *Measurement of the acoustic velocities at woodwind instrument toneholes using particle image velocimetry.* In Proceedings of Forum Acusticum Conference, Seville, Spain, 2002.

[Skulina 03] D.J. Skulina, D.M. Campbell & C.A. Greated. *Measurement of the Termination Impedance of a Tube using Particle Image Velocimetry.* In Proceedings of the Stockholm Musical Acoustics Conference, 2003.

[Skulina 05] D.J. Skulina, R. MacDonald & D.M. Campbell. *PIV applied to the Measurement of the Acoustic Particle Velocity at the Side Hole of a Duct.* In Proceedings of Forum Acusticum Conference, Budapest, Hungary, 2005.

[Smith 03] B.L. Smith & G.W. Swift. *Power dissipation and time-averaged pressure in oscillating flow through a sudden area change.* J. Acoust. Soc. Am., vol. 113(5), pages 2455–2463, 2003.

[Stanislas 97] M. Stanislas & J.C. Monnier. *Practical aspects of image recording in particle image velocimetry.* Meas. Sci. Technol., vol. 8, pages 1417–1426, 1997.

[Thompson 05] M.W. Thompson & A.A. Atchley. *Simultaneous measurement of acoustic and streaming velocities in a standing wave using laser doppler velocimetry.* J. Acoust. Soc. Am., vol. 117 (4), pages 1828–1838, 2005.

[Tritton 99] D.J. Tritton. Physical fluid dynamics. Clarendon Press, Oxford, 1999.

[Tropea 95] C. Tropea. *Laser Doppler anemometry: recent developments and future challenges.* Meas. Sci. Technol., vol. 6, pages 605–619, 1995.

[van de Hulst 92] F.J.M. van de Hulst. Light scattering by small particles. Dover, 1992.

[van der Eerden 98] F.J.M. van der Eerden, H.-E. de Bree & H. Tijdemann. *Experiments with a new acoustic particle velocity sensor in an impedance tube.* Sensors and actuators, vol. 69, pages 126–133, 1998.

[van Lier 01] L. van Lier, S. Dequand & A Hirschberg. *Aeroacoustic diffusers: An experimental study of typical industrial diffusers at Reynolds numbers of* $O(10^5)$. J. Acoust. Soc. Am., vol. 109(1), pages 108–115, 2001.

[Vergez 05] P Vergez C. De la Cuadra. *Jet motion in flute-like instruments: experimental investigation through flow visualisation and image processing.* In Proceedings of Forum Acusticum Conference, Budapest, Hungary, 2005.

[Vignola 92] J.F. Vignola, S. Berthelot, S. Jones & J. Jarzynski. *Equation of motion of microparticles in suspension in an insonified medium.* J. Acoust. Soc. Am., vol. 1, pages 332–334, 1992.

[Westerweel 93] J. Westerweel. Digital particle image velocimetry. Delft University Press, 1993.

Publications

D. J. Skulina, R. MacDonald and D.M. Campbell. PIV applied to the measurement of the acoustic particle velocity at the side hole of a duct. In *Proc. Forum Acusticum 2005*, Budapest, Hungary, 2005.

D. J. Skulina, R. MacDonald and D.M. Campbell. Visualisation of acoustic flows around a square duct side hole using PIV In *Proc. Scottish Fluid Mechanics Meeting 2005*, Edinburgh, UK, 2005.

D. M. Campbell, D. J. Skulina and C.A. Greated, Particle image velocimetry applied to the study of wind instruments. In *Proc. ICA2004*, Kyoto, Japan, 2004.

D. J. Skulina, D.M. Campbell and C.A. Greated. Measurement of the termination impedance of a tube using particle image velocimetry. In *Proc. SMAC 2003*, Stockholm, Sweden, 2003.

D. J. Skulina, D. Rockliff, D.M. Campbell and C.A. Greated. Measuremento of the acoustic velocities at woodwind instrument side holes using particle image velocimetry. In *Proc. Forum Acusticum 2002*, Seville, Spain, 2002.

D. Rockliff, D.J. Skulina, D.M. Campbell and C.A. Greated. PIV Measurement of acoustic velocities at woodwind instrument toneholes. In *Proc. IOA, 2002*, Salford, UK, 2002.